Advancing the micro-EDM technique with powder-mixed dielectric and process modelling

Tan, Michael Peng Cheong

2010

Tan, M. P. C. (2010). Advancing the micro-EDM technique with powder-mixed dielectric and process modelling. Doctoral thesis, Nanyang Technological University, Singapore.

https://hdl.handle.net/10356/43562

https://doi.org/10.32657/10356/43562

(On the Spine)

ADVANCING THE MICRO ELECTRICAL DISCHARGE MACHINING TECHNIQUE WITH POWDER-MIXED DIELECTRIC AND PROCESS MODELLING

TAN P. C. M.

2010

NANYANG TECHNOLOGICAL UNIVERSITY

ADVANCING THE MICRO ELECTRICAL DISCHARGE MACHINING TECHNIQUE WITH POWDER-MIXED DIELECTRIC AND PROCESS MODELLING

TAN PENG CHEONG, MICHAEL

SCHOOL OF MECHANICAL AND AEROSPACE ENGINEERING

2010

ADVANCING THE MICRO ELECTRICAL DISCHARGE MACHINING TECHNIQUE WITH POWDER-MIXED DIELECTRIC AND PROCESS MODELLING

TAN PENG CHEONG, MICHAEL

School of Mechanical and Aerospace Engineering

A thesis submitted to the Nanyang Technological University
in partial fulfilment of the requirement for the degree of
Doctor of Philosophy

2010

To my wife and son…

Abstract

The electrical discharge machining (EDM) process possesses inherent characteristics that make it a promising micro-machining technique. However, micro electrical discharge machining (micro-EDM) is only used in niche applications due to the lack of an established knowledge base to facilitate process planning. The stochastic nature of material removal, sensitivity of process performance to process parameters and conditions and numerous process parameter permutations available for machining contribute to the difficulties in building a knowledge base for micro-EDM. Compounding to this complication, the process parameters and conditions in EDM and micro-EDM are distinctly different, thereby rendering limited transferability of knowledge base. Thus, focused studies on micro-EDM are needed to improve process reliability and controllability as well as to enhance process capabilities. This research has endeavoured to achieve advancement of the micro-EDM technique through a two-pronged approach of process performance enhancement and process modelling.

The proposed use of powder-mixed dielectric in micro-EDM (PMD micro-EDM) is a novel initiative to adopt this established technological development in EDM (PMD-EDM) for micro-EDM. By reproducing the effects of improved machined surface quality and enhanced machined surface functional properties of PMD-EDM in PMD micro-EDM, advancements to the micro-EDM process has been achieved. The realisation of PMD micro-EDM has been achieved through employing discharge energies less than 25 μJ with sub-microsecond pulse on time durations and complemented by the use of nano-powder additives of semi-conductive and non-conductive materials in concentrations below 1 g/l. Initial investigations on the unit removal characteristics of PMD micro-EDM have shown a distinct difference in the morphology of craters produced in a powder-free and powder-mixed dielectric, thereby proving the feasibility of PMD micro-EDM. Furthermore, the observation of craters having smaller peak-to-valley heights when generated under single electrical discharge conditions has been exhibited as reductions in arithmetical mean surface roughness of 14 % to 24 % when processing with PMD micro-EDM. Improvements in machined surface quality have also been displayed through reductions in recast layer thickness of between 15 % and 35 %.

A new multiple discharge approach (MDA) for micro-EDM process modelling and simulation has also been introduced to augment the single electrical discharge erosion models and offered fresh perspectives on the mechanism of overlapping crater profile and interconnecting crater recast region formation. The unique incorporation of a numerical approach for thermal conduction analysis, geometrical prediction of crater profile and classification of extremities in overlapping crater profiles and temperature distributions has allowed the application of heat fluxes to non-linear boundaries and prediction of upper and lower bounds of performance measure values, representing the stochastic nature of material removal. The MDA has been demonstrated through the development of models for R_{max} and recast layer thickness, which have been validated by experimental results. It has highlighted the influence of preceding crater profile and heat source location on resulting thermal distribution, crater profile and recast layer profile. During model development, values of heat flux fraction, plasma flushing efficiency (PFE) and recast PFE have also been determined.

The possibility of employing PMD micro-EDM for surface modification, as suggested by the presence of retained material within the crater, has also been alluded through preliminary studies which has revealed the deposition of nickel-titanium nano-powder additive material onto the machined surface. Further investigations into the use of powder-mixed dielectric for micro electrical discharge alloying (PMD micro-EDA) and micro electrical discharge coating (PMD micro-EDC) are needed to establish these processes for enhancement of machined surface functional properties.

Acknowledgements

My heartfelt gratitude goes to my mentor, A/P Yeo Swee Hock, for receiving me under his tutelage. Prof Yeo, thank you for exposing me to the many dimensions of academic research and for planting in me the good seeds of research aptitude. I am indeed fortunate to have a patient and conscientious supervisor who is so skilful at providing guidance without inhibiting the exploratory nature of research. I will sorely miss the research meetings that are always peppered with snippets of informal anecdotes and the sumptuous group lunches. Thank you for making my Ph.D. training so meaningful and wonderful.

My appreciation is extended to the technical staff of Metrology Laboratory, Precision Machining Laboratory, Precision Engineering Laboratory and Materials Laboratory 1 for their assistance in administrative and technical matters. Special mention to Ms Jacelyn Tan, Ms Esther Lim, Ms Yong Mei Yoke, Mr Martin Lim, Mr Ang Teck Meng, Mr Chang Set Chiang, Mr Kong Seng Ann and Mr Koh Wing Leong.

To my fellow friends from Metrology Laboratory, past and present, thank you for the research discussions, nonsense discussions, fun-filled parties and impromptu Japanese and Farsi lessons. You know who you are. A special thanks to Willy for being such an inspiration and for being my host when I was on exchange in Tokyo Institute of Technology under the Asia-Oceania Top University League on Engineering programme. These fond memories will be cherished dearly.

I am eternally grateful to my parents for their support and unconditional sacrifices. Thank you for taking us in and helping us care for Zachary when the demands of studies and research called us away for extended periods.

Finally, to the most important people of my life: my wife and son. To my son, thank you for being my greatest motivation. To my loving wife, thank you for egging me to further my studies and supporting me throughout this journey. WE DID IT!

Table of Contents

List of Figures

List of Tables

Nomenclature

C = capacitance (pF)

E = discharge energy (μJ)

F = fraction of heat flux distributed to the electrode

I = discharge current (A)

R = radius of circular heat source (μm)

Ra = arithmetical mean surface roughness (μm)

Rq = root mean square surface roughness (μm)

T = temperature (K)

V = discharge voltage (V)

c = specific heat (J/kg·K)

f = fraction of increase in heat source radius

i = time step number

j = location number for surface roughness measurement lay

k = thermal conductivity (W/m·K)

m = total number of elemental strips

n = total number of time steps

p = total number of elemental strips

q = heat flux (W/m^2)

r = radial coordinate

s = unit distance around element boundary

t = time (μs)

u = factor determining shape of Gaussian distribution

w = weight function

z = axial coordinate

A_{recast} = measured area of recast layer (μm^2)

B_{upper} = upper bound of simulated recast layer thickness (μm)

C^e = element specific heat (J/kg·K)

E_{in} = input discharge energy (μJ)

E_m = measured discharge energy (μJ)

E_0 = energy density (W/m^2)

I_{av} = average discharge current (A)

I_i = discretized discharge current (A)

I_{pk} = peak discharge current (A)

L_f = latent heat of fusion (kJ/kg)

Q_m = heat transmission rate from an annulus labelled m (W)

Q_w = heat absorption rate of the workpiece (W)

R_i = discretized heat source radius (µm)

R_{max} = maximum peak to valley surface roughness (µm)

$R_{max,sim}$ = simulated value for maximum peak-to-valley surface roughness (µm)

T_0 = ambient temperature (K)

T_b = boiling temperature of electrode material (K)

T_m = melting temperature of electrode material (K)

T^e = finite element approximation of temperature (K)

V_{av} = average discharge voltage (V)

V_i = discretized discharge voltage (V)

V_{OC} = open circuit voltage (V)

h_{av} = average height of measured recast layer (µm)

h_d = discharge gap distance (µm)

k_r = thermal conductivity in radial direction (W/m·K)

k_z = thermal conductivity in axial direction (W/m·K)

n_r = unit normal vector in radial direction

n_z = unit normal vector in axial direction

q_0 = maximum heat flux at radial coordinate $r = 0$ (W/m^2)

q_i = discretized heat flux (W/m^2)

q_m = heat flux at radial coordinate r_m (W/m^2)

q_n = heat flux normal to the element boundary (W/m^2)

r_m = radial coordinate of annulus labelled m (µm)

r_{mp} = radius of melt pool (µm)

t_1 = start of pulse on time (ns)

t_2 = end of pulse on time (ns)

t_{on} = pulse on time (ns)

Γ^e = element boundary

Ω^e = elemental unit

α = thermal diffusivity (m^2/s)

σ = electrical conductivity (S/m)

ρ = mass density (kg/m^3)

α' = adapted thermal diffusivity (m^2/s)

α_{error} = Type I error probability in ANOVA study

ϕ_1 = crater diameter measured in Direction 1 (μm)

ϕ_2 = crater diameter measured in Direction 2 (μm)

ϕ_{av} = average crater diameter (μm)

$I(t)$ = time dependent discharge current (A)

$R(t)$ = time dependent heat source radius (μm)

$R_p(t)$ = time dependent plasma channel radius (μm)

$V(t)$ = time dependent discharge voltage (V)

$q(r)$ = radial coordinate dependent heat flux (W/m^2)

$q(t)$ = time dependent heat flux (W/m^2)

Δt = duration of one load step (ns)

Δx = width of one vertical elemental strip (nm)

$[B]$ = shape function derivative matrix evaluated at integration points

$[K]$ = conductivity matrix

$\{L\}$ = vector operator

$\{N\}$ = element shape function vector

$[C^e]$ = element specific heat matrix

$[K^e]$ = element diffusion conductivity matrix

$\{N\}^T$ = transpose of shape function vector $\{N\}$

$\{T^e\}$ = element nodal temperature vector

$\left\{\dot{T}^e\right\}$ = time derivative of element nodal temperature vector

$\{q^e\}$ = element heat flux vector

List of publications

JOURNALS

1. Yeo S.H., Tan P.C. and Kurnia W. 2007 Effects of powder additives suspended in dielectric on crater characteristics for micro electrical discharge machining. *Journal of Micromechanics and Microengineering*. **17**(11) p. N91-N98.
2. Tan P.C., Yeo S.H. and Tan Y.V. 2008 Effects of nanopowder additives in micro-electrical discharge machining. *International Journal of Precision Engineering and Manufacturing*. **9**(3) p. 22-26.
3. Tan P.C. and Yeo S.H. 2008 Modelling of overlapping craters in micro-electrical discharge machining. *Journal of Physics D: Applied Physics*. **41**(20) p. 205302 (12 pp.).
4. Yeo S.H., Tan P.C., Aligiri E., Tor S.B. and Loh N.H. 2009 Processing of zirconium-based bulk metallic glass (BMG) using micro electrical discharge machining (micro-EDM). *Materials and Manufacturing Processes*. **24**(12) p. 1242 - 1248.
5. Tan P.C. and Yeo S.H. 2010 Modeling of recast layer in micro-electrical discharge machining. *Journal of Manufacturing Science and Engineering*. **132**(3) p. 031001 (9 pp.).
6. Tan P.C. and Yeo S.H. 2010 Investigation of recast layers generated by a powder-mixed dielectric micro electrical discharge machining process. *Proceedings of the Institution of Mechanical Engineers, Part B, Journal of Engineering* Manufacture. Accepted manuscript.

CONFERENCES

1. Tan P.C., Yeo S.H. and Tan Y.V. 2008 Effects of nanopowder additives in micro-electrical discharge machining. *Proceedings of the Asian Symposium for Precision Engineering and Nanotechnology 2007 (ASPEN 2007)* (GIST, Gwangju, Korea, 6-9 Nov 2007) Korean Society for Precision Engineering, (CD-ROM).
2. Yeo S.H., Tan P.C., Aligiri E., Tor S.B. and Loh N.H. 2009 Processing of Zirconium-Based Bulk Metallic Glass (BMG) Using Micro Electrical Discharge Machining (Micro-EDM). *Proceedings of the 13th International Conference on Machine Design and Production (UMTIK 2008)*. (Istanbul, Turkey, 3-5 Sep 2008).

Chapter 1
Introduction

This chapter presents a brief introduction to the research and outline of the report. As shown in Figure 1.1, the background of the research area is provided followed by the research motivation, research objectives and originality of the research. Finally, the report outline is included.

Chapter 1: Introduction
1.1 Background
1.2 Motivation
1.3 Objectives
1.4 Scope of research
1.5 Originality of research
1.6 Outline of the thesis

Figure 1.1 Overview of Chapter 1

1.1 Background

The use of micro-parts and components with micro-features has become indispensable in many industries, such as medical, automotive, biotechnology and electronics. It has been highlighted that microsystem-based products represent key value-added elements for many sectors of industry and are important contributors to a sustainable economy [1]. In order to keep abreast with the increasing sophistication of micro-component design, the capabilities of micro-manufacturing processes have to be continuously enhanced to produce the required micro-products economically and reliably. Therefore, there is a need for continuous research to improve existing micro-machining techniques and develop novel micro-machining techniques that can cater to the future micro-manufacturing needs.

The earliest micro-machining processes are those employed in micro electro-mechanical systems (MEMS) technologies, such as photolithography on silicon substrate [2]. The techniques used are, however, limited to the fabrication of quasi three-dimensional structures with low aspect ratios and only applicable to a limited selection of working materials [3]. To address the limitations of MEMS-based machining processes, the use of traditional material removal methods such as drilling, grinding, milling and turning for micro-machining has also evolved [4-6]. Apart from the machining of holes by micro-

drilling [7] and cylindrical shapes by micro-turning [8], micro-milling [9] and micro-grinding [10] techniques are also used in the fabrication of complex three-dimensional structures and profiles. Although the introduction of traditional machining methods brought about an improvement in machining versatility over MEMS-based methods, these traditional machining processes also have limitations. Issues related to the machining of advanced materials with high hardness, chemical incompatibility of the workpiece and cutting tool materials [11] and fabricating of micro parts with increased complexity in shapes and lower rigidity are typical. An avenue for addressing these limitations is through the use of non-traditional machining techniques for micro-machining [12]. Some of these techniques include laser beam machining (LBM) [13], focused ion beam machining (FIBM) [14], ultrasonic machining (USM) [15] and electrical discharge machining (EDM) [16-18]. Each of these techniques possesses unique process characteristics that enable them to perform better at specific micro-machining processes. For example, USM is a mechanical machining process where material is removed by mechanical abrasion and is more suited for processing hard and brittle materials. On the other hand, EDM is a thermal machining process utilising electro-thermal effects for material removal and is more appropriate for machining electrically conductive materials regardless of hardness. The underlying factors that make EDM a good micro-machining technique (micro-EDM) are the absence of physical contact and significant machining forces between the tool and workpiece during material removal. This enables the use of tools with finer form and lower rigidity for machining and more intricate parts to be produced without significant tool and workpiece deflection. Although LBM and FIBM are also thermal machining processes that are suitable for micro-machining, the attractiveness of micro-EDM over these machining techniques is its relatively simple equipment set up and low capital equipment cost. The ease of implementing the micro-EDM technique has made it the most widely adopted non-traditional machining technique, outselling all other processes excluding milling, turning and grinding [19]. The micro-EDM technique is applied in specialized processes such as the fabrication of high aspect ratio micro-holes in inkjet nozzles and fuel injection nozzles as well as the manufacture of micro-moulds used in the mass production of micro-parts. While developments in the micro-EDM technique have made it a reliable process in these applications, outstanding process shortcomings have limited its ability to attain a wider range of utilization [17]. These shortcomings stem from an insufficient degree of reliability in machine tools and process characteristics that are currently available. As shown in Figure 1.2, the

problematic areas have been broadly classified into electrode and workpiece handling and preparation, machining process and measurement of end product.

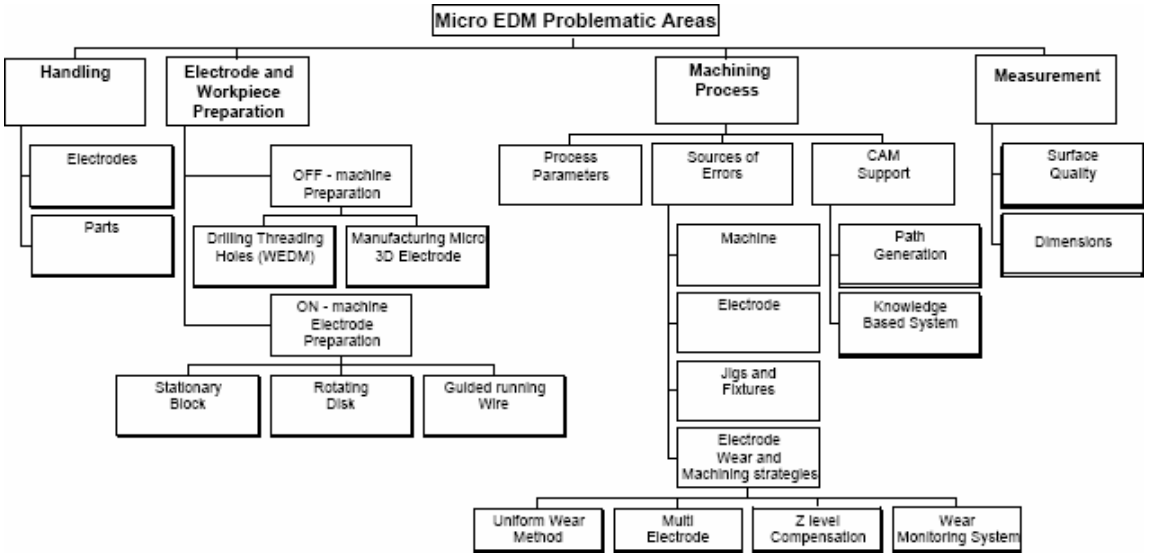

Figure 1.2 Problematic areas in micro-EDM [17]

The concern about machining process lies in the need for careful process planning for micro-EDM, since both feature sizes and machined tolerances are very small. However, the ability to process plan is hindered by an underdeveloped knowledge-based system due to a lack of process characteristics data. The shortage of data arises from difficulties in understanding the effects of process parameters on performance measures fully due to the stochastic nature of material removal in EDM. As a result, process characteristics are established based on studies to determine the influence of each process variable on the desired process characteristic. While efforts in the optimization of process parameters for EDM have managed to address issues related to material removal, tool wear and machined surface quality [20], research in micro-EDM is still not as well documented. One of the research tracks that has received considerable research in EDM, but only limited studies in micro-EDM, is the use of powder-mixed dielectrics [21]. Process characteristics resulting from the use of powder-mixed dielectric in EDM (PMD-EDM) are potentially beneficial to micro-EDM and studies are required to ascertain the feasibility of PMD micro-EDM and to draw out its benefits for micro-machining.

It has been reported that the introduction of minute amounts of foreign particles in the dielectric helped to promote dielectric breakdown and minimise the spatial concentration of discharge such that the improved discharge transitivity across the spark gap improved process stability [22]. As a result, process characteristics of PMD-EDM included

increases in material removal rate (MRR), reductions in wear ratio (WR) and improvements in surface quality (SQ) [23-25]. The improvements in MRR and WR were attributed to enhancements in machining stability caused by a reduction in the occurrence of arcing and short-circuiting as debris is more easily removed from the discharge gap, which may be widened by three folds due to the presence of conductive particles [26]. In the same light, the discharge gap enlargement and presence of powder additives reduced discharge intensity to generate machined surfaces with reduced recast layer, lower micro-crack density and better surface finish [27]. It has been observed that a near mirror surface finish was characterized by shallower, more regularly shaped and uniformly sized craters [28]. The machined surfaces of the PMD-EDM process may also be imparted with improved mechanical properties such as wear resistance [29] and high hardness [30] through surface modification. These attributes are beneficial to micro-EDM since it may lead to enhancements in process characteristics that satisfy micro-machining requirements, realization of performance measures that addresses service-life concerns of micro-parts and improvements in process reliability and repeatability. Thus, a realization of these potentials will further enhance the role of EDM in micro-machining to meet the growing needs of the micro-manufacturing industry.

1.2 Motivation

The process characteristics of EDM make it a suitable micro-machining technique. In addition, the relatively simple equipment set up and low capital equipment cost makes it more affordable and more readily accepted for implementation. With the increased sophistication in micro-part design and usage of a greater variety of materials, there is a fast growing need for manufacturing processes that are equipped to produce the next generation of micro-products. EDM has already carved a niche for itself as a reliable micro-manufacturing process for high aspect ratio micro-holes and micro-moulds. However, its range of application is limited due to insufficient knowledge on process characteristics and effects of process parameters on performance measures. In order to enhance the micro-EDM technique so that it can be applied to a broader range of processes, existing process characteristics have to be refined to satisfy micro-machining requirements and new process characteristics have to be engineered to augment process capabilities. In this way, a fresh lease of life may be given to an affordable and widely utilised machining process.

A study on the use of powder-mixed dielectric for micro-EDM was initiated given that an assessment of PMD-EDM process characteristics and performance measures indicated some attributes that are potentially beneficial to the micro-EDM technique. The use of PMD-EDM was reported to reduce the roughness of machined surfaces. This is beneficial to micro-EDM since roughness should be reduced in proportion to the size of the micro-product [31]. The inspection of a surface machined by PMD-EDM revealed the presence of shallow, more regularly shaped and uniformly sized craters [28]. This process characteristic may enhance the micro-EDM technique since unit removal must be small and repeatable to ensure high machining accuracy [32]. The machined surface quality of the PMD-EDM process was reported to improve, in that the density of micro-cracks is minimised, recast layer thickness is reduced [25] and the machined surface is imparted with functional properties [33-35] such as wear resistance, corrosion resistance and reduced friction coefficient. The reduction in defects and residual stresses at the machined surface can improve the fatigue strength of machined components [36] while the improved attributes of the machined surface allow machined components to be tailored for specific applications [37]. Considering that changes to the properties of the machined surface affect the component more significantly as component size is reduced, these process characteristics should be considered for micro-EDM. Therefore, the compelling results from PMD-EDM studies that indicate multiple benefits for micro-EDM warrant investigations into the PMD micro-EDM technique.

1.3 Objectives

The research work is conducted with the following underlying objectives:

a) To investigate the material removal characteristics of a single electrical discharge in the PMD micro-EDM process
b) To study the effectiveness of PMD micro-EDM for surface quality improvement applications
c) To propose a new process modelling and simulation approach for prediction of machining performance measures in micro-EDM

1.4 Scope of research

The research on powder-mixed dielectric focuses on its use under micro-EDM process parameters and conditions. The process parameters such as micro-joule discharge energy magnitudes and sub-microsecond range pulse on time durations as well as process

conditions such as discharge gap distances of a few micrometers and flushing only through tool rotation are unique to micro-EDM. Moreover, to adapt the use of powder-mixed dielectrics for micro-EDM, changes in powder characteristics are also required. These new combinations of process parameters and conditions will create new process characteristics, which need to be studied and understood. The conduct of single discharge experiments to study the unit removal characteristics of PMD micro-EDM will provide a controlled testing environment where the effects of nano-powder additives can be discerned. The conduct of machining experiments will then assess the effectiveness of PMD micro-EDM in improving machining performance measures of micro-machining. To conduct the single discharge and machining experiments, purpose-built test rigs based on the resistance-capacitance pulse generator architecture were developed. The test rigs enabled the generation of single electrical discharges as well as the adjustment of pulse on time durations with minimal changes to peak discharge current.

The research on process modelling and simulation focuses on the use of theoretical modelling for micro-EDM process performance predictions. The majority of theoretical models available for machining performance measure prediction rely on the single electrical discharge approach, which does not consider the multiple discharge nature of material removal in EDM. A new process modelling and simulation approach will be developed to extend the use of single electrical discharge erosion models to the modelling of multiple discharges. It will then be illustrated through the modelling of various machining performance measures.

1.5 Originality of research

The originality of the proposed areas of research is supported through a review of related literature. The justification for each research area is as follows:

1. Material removal characteristics of a single electrical discharge in the PMD micro-EDM process. The amount of material removed by a single electrical discharge has been termed unit removal [31]. The unit removal characteristics of a machining process are essential for studying its material removal mechanism and understanding its process characteristics. While unit removal studies have been conducted for EDM and investigations on the process characteristics of PMD-EDM have been reported, works related to the proposed PMD micro-EDM technique are limited. Results from the unit removal study would help to identify

changes in process characteristics and possible improvements to performance measures. Furthermore, the outcome of such fundamental studies would be useful as a basis for future developments in PMD micro-EDM.

2. Surface quality improvement with PMD micro-EDM. The results of unit removal studies on PMD micro-EDM suggested the possibility of achieving improvements in certain performance measures during actual machining operations, which had to be verified. The outcome of these machining studies demonstrated the feasibility of performing PMD micro-EDM and the positive effects it has on enhancing the micro-EDM technique.
3. New process modelling and simulation approach for micro-EDM. The existing models developed for EDM and micro-EDM are based on the material removal characteristics of a single electrical discharge. These single electrical discharge erosion models (SEDEMs) do not take into account the multiple discharge nature of EDM process, the overlapping nature of crater formation and interconnecting nature of crater recast regions. The proposed process modelling and simulation approach, called the multiple discharge approach (MDA), extended the use of SEDEMs to multiple discharge modelling. To demonstrate the MDA, performance measures were modelled and validated with experimental results. The models also enabled the formulation of expressions suitable for micro-EDM process control.

1.6 Outline of the thesis

Following the introduction in Chapter 1, literature reviews on EDM process modelling and the concept and application of PMD-EDM are presented in Chapter 2. Then, Chapter 3 will cover the experimental methodology and characterization techniques used. After which, experimental results of the unit removal study are presented in Chapter 4. Chapters 5 and 6 report the findings of machining experiments on surface quality improvement, namely, surface roughness and recast layer thickness, respectively. Next, process modelling and simulation for micro-EDM are reported in Chapter 7. Finally, Chapter 8 will present the conclusion and future work.

Chapter 2
Literature Review

This chapter reviews electrical discharge machining (EDM) as a technique for micro-machining. With reference to Figure 2.1, the discussion is divided into three sections, comprising basics of EDM, technological developments in EDM and outcome of the literature review. The basics of EDM will cover the evolution of EDM, theory of EDM process and a comparison between EDM and micro-EDM. The review on technological developments in EDM will include the use of powder-mixed dielectrics for EDM and process modelling in EDM and micro-EDM. The final section presents a summary of the literature review outcome.

Figure 2.1 Overview of Chapter 2

2.1 Basics of EDM

The basics of EDM are first covered in the literature review prior to a critical literature review on technological developments made in the EDM technique. This section provides a general understanding of EDM by presenting a brief history of EDM followed by theory of the EDM process and then makes a distinction between EDM and micro-EDM. In the

coverage of EDM process theory, the mechanism of electro-thermal material removal, description of EDM process parameters and performance measures are touched on.

2.1.1 Evolution of EDM technique

The origins of EDM can be dated back to the early 1940s with the works of Russian scientists Boris Lazarenko and Natalya Lazarenko [38]. The Lazarenkos developed a spark machining process based on the resistance-capacitance (RC) circuit, which became the foundation for future RC-type pulse generating systems in use for EDM.

The pulse generating system affects the speed and reliability of the machining process as well as the quality of the finished product [39]. Generally, two types of pulse generators are commercially used, namely, the transistor-type and the RC-type pulse generators. Transistor-type generators are used to produce higher frequency isopulses, that is, repeated pulse discharges with identical duration and magnitude that improved the reliability of the machining process and allowed the production of machined surfaces with controlled finishes. RC-type generators are employed in fine-finishing machining [40] and micro-machining [16] where small discharge energies with sub-microsecond range discharge durations are required. While transistor-type isopulse generators for micro-machining have been developed [41, 42], RC-type pulse generator are still more commonly employed due to the simplicity of design. Furthermore, while studies into a new capacity-coupled pulse generator have been reported to deliver discharge energies for nano-metric material removal [43], it is still not commercially available.

The development of EDM as a reliable machining technique also involved improvements in generating consistent machining performance outcomes and achieving accurate control of the machining process. These are attained through adopting sound process planning strategies, which requires the availability of process characteristic knowledge. Thus, considerable research is done in establishing process characteristics, optimising process parameters [44, 45], advancing process modelling [46-48], monitoring, control and automation [49-51].

As research focus in EDM shifted from basic research to applied research [52], there was growing research interest in new EDM techniques such as micro-machining [53-55], machining of insulating ceramic materials [56-58], EDM using a powder-mixed dielectric

[23-25], combining EDM with other machining methods in hybrid processes [59-61], dry EDM [62-65] and near-dry EDM [66, 67]. In addition, attempts at widening the scope of EDM application to green-related industries have led to studies in the fabrication of fuel cell [68] and solar cell [69] components.

2.1.1.1 Application of EDM in micro-machining

The application of EDM in micro-machining is termed micro-EDM. The attractiveness of micro-EDM is attributed to the following process characteristics.

- Ability to machine any electrically conductive and semi-conductive material
- No mechanical contact between tool electrode and workpiece
- Negligible machining forces exerted between tool electrode and workpiece
- Ability to machine high aspect ratio features
- Ability to machine three-dimensional features
- Ability to machine complex profiles in a single workpiece setting
- Ability to machine with minimal formation of burrs at machined edges
- A relatively versatile and cost effective machining method

Micro-EDM is able to machine any material with electrical resistivity up to 100 Ωcm [16], regardless of hardness and without additional workpiece conditioning [70]. The absence of physical contact and significant machining forces between the tool and workpiece during material removal allows the use of slender tools for machining intricate features with minimal tool and workpiece deflection. Micro-sized rods can be used to drill high aspect ratio holes [71] and mill three-dimensional profiles [72] without repositioning the workpiece to ensure minimal positioning errors. With minimal burrs on the machined surface [73] the need to perform deburring processes, which increases manufacturing time and may damage the micro-features, is reduced. Given the relatively simple equipment set up and low capital equipment cost, micro-EDM is a cost effective micro-machining method that can be easily adopted.

In a review of developments in three-dimensional micro-machining using machine tools [31], it was suggested that micro-EDM was the best means of producing concave shapes due to the negligible machining forces and the ease of implementing on-the-machine tool making solutions. In addition, a review of the state of the art and future trend of EDM [20,

74] identified micro-EDM as a feasible area of expansion for EDM application. Based on the success of machining insulating ceramics with EDM, the technique was extended to the fabrication of micro-holes [75]. The versatility of micro-EDM over MEMS-based micro-machining techniques in three-dimensional micro-structuring of silicon was demonstrated through the fabrication of various micro-features [76-79]. Furthermore, new hybrid processes relying partly on micro-EDM have also evolved [80, 81]. The ease of applying EDM as a micro-machining technique has led to the development of various types of micro-EDM processes such as die-sinking [82, 83], drilling [84, 85], milling [86, 87], wire cutting [88, 89], wire grinding [53] and turning [90]. However, the commercial application of these processes have so far been confined to niche areas, such as the drilling of high aspect ratio micro-holes for inkjet nozzles [91], tapered holes for diesel fuel injection nozzles [92] and the fabrication of micro-moulds for mass replication processes [93, 94]. In order to enhance the competitiveness of micro-EDM as a micro-manufacturing technology, it is necessary to advance the micro-EDM technique by improving machining performance and providing process capabilities for new areas of application. Generally, the development of new micro-EDM applications requires an understanding of EDM process characteristics, determining process characteristics that are potentially beneficial to micro-EDM and modifying process conditions to suit the micro-machining application.

2.1.2 Theory of EDM process

After about 70 years of being used as a commercial machining technique, the theory of the material removal mechanism during EDM is still varied [95]. The various theories that were proposed to describe the material removal process can be broadly categorised into two modes [96], namely, an electro-thermal mechanism [97-106] and an electro-mechanical mechanism [107]. In the electro-thermal mechanism, it is proposed that the electrode material is removed through thermal melting and vaporization as a result of a superheated and highly pressurised plasma channel formed between the electrodes during an electrical discharge [108]. On the other hand, the electro-mechanical mechanism proposed that for discharge durations less than 5 μs, electrostatic forces acting on the electrode surface generated stresses within the electrode such that regions subjected to stresses higher than the material yield strength are removed. Of these two modes, the more widely used electro-thermal mechanism is discussed further in the following section.

2.1.2.1 The electro-thermal mode of material removal

The electro-thermal material removal mechanism is classified into three phases, namely, pre-discharge phase, discharge phase and post-discharge phase. Referring to Figure 2.2, the electro-thermal mode of material removal undergoes the following stages:

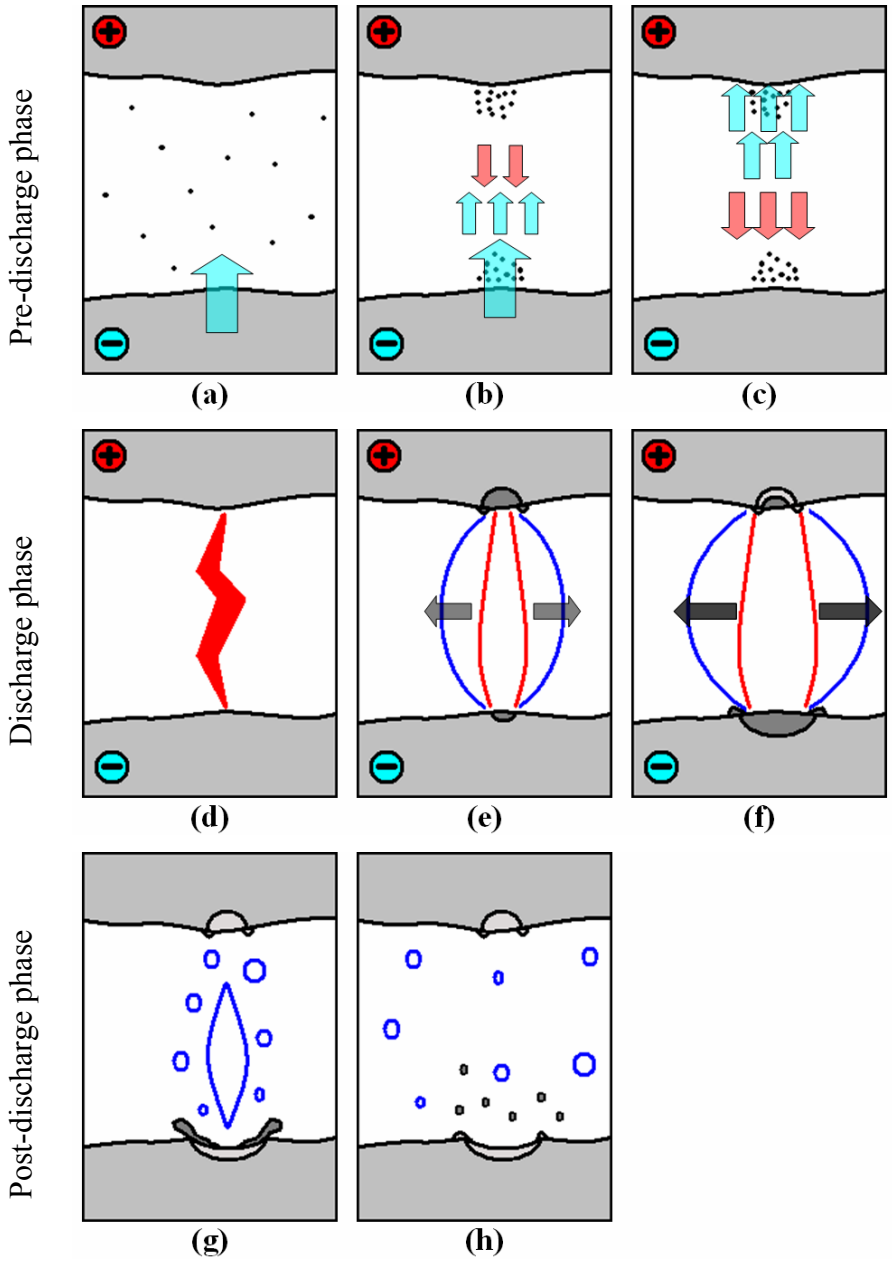

Figure 2.2 Electro-thermal material removal mechanism [95]

b) In a typical EDM process, electrical discharges are generated in a dielectric medium, between a positively-charged anode and a negatively-charged cathode. Under the influence of a voltage applied across the cathode and anode, electrons are emitted from the cathode.

c) The electrons emitted into the dielectric collide with neutral atoms and particles in their path causing the formation of more electrons and ions. In some cases conductive particles, such as the debris of preceding discharges, are polarised and attracted to areas with high electric field strength. The accumulating particles create a bridging effect that reduces the inter-electrode gap and facilitate discharge initiation.

d) The newly formed electrons move towards the anode quickly while the ions move towards the cathode at a slower speed due to their relatively larger mass. In the process they collide with more neutral atoms and particles. This avalanche-like formation of electrons and ions is known as impact ionisation. When the moving electrons eventually bridge the inter-electrode gap, dielectric breakdown occurs and the discharge phase begins.

e) Upon breakdown, the ensuing conductive channel allows electrons emitted from the cathode to move easily towards the anode and intensifies impact ionisation. The impact ionisation forms a plasma channel having a very high current density which generates a high heat flux that melts the electrodes. The temperature of the plasma channel has been measured experimentally using spectroscopy and results ranged between 4000K to 8000K [109, 110] and 8000K to 10000K [110].

f) As the plasma channel expands with continued electron emission, the high temperature vaporises, disassociates and ionises the dielectric at the plasma channel and dielectric interface and causes the formation and growth of a gas bubble [106]. The pressure within the bubble builds up to a range between 6bars and 14bars [111, 112] due to the viscosity and inertia of the dielectric [113]. It supports superheating of the molten material with minimal vaporisation [103], thereby forming a pool of molten material, called a melt pool. The pressure within the bubble also pushes some molten material out of the melt pool. It was suggested that the anode melts before the cathode due to the speed difference in electron and ion movement [104], thereby creating a larger melt pool at the anode during the initial stages of discharge. In micro-EDM, where discharge durations are in the sub-microsecond range, the workpiece is set as the anode so that material removal is greater than tool wear.

g) Further plasma channel expansion causes a reduction in heat flux density at the anode which aids resolidification of molten material as heat is conducted away from the melt pool via the base material. On the other hand, the molten material at

the cathode increases due to the impact of slower moving positive ions [104]. As in the case of the anode, molten material is also pushed out of the cathode melt pool due to the bubble pressure. The discharge phase ends when the voltage applied across the electrodes is removed or discharge current ceases.

h) With the removal of applied voltage or cessation of discharge current, the plasma channel collapses and bubble implodes. The implosive force from the sudden pressure drop causes the molten material in the melt pool to be partially expelled. At the anode, minimal expulsion of molten material may occur when a majority of the molten material resolidifies before collapse of the plasma channel.

i) The dielectric cools and solidifies the expelled molten material and molten material retained in the melt pool. The retained molten material resolidifies as a recast region of the resulting crater.

2.1.2.2 Process parameters and performance measures in EDM

The process parameters in EDM are used to control the performance measures of the machining process. Process parameters are generally controllable machining input factors that determine the conditions in which machining is carried out. These machining conditions will affect the process performance result, which are gauged using various performance measures. Table 2.1 lists some of the common process parameters and their effects on the machining condition. Table 2.2 lists the various performance measures used to gauge performance results.

Table 2.1 Effects of process parameters on machining condition

Process parameter	Effect on machining condition
Pulse on time	The pulse on time (t_{on}) represents the duration of discharge and is the time during which the electrode material is heated by the high temperature plasma channel. A longer pulse on time will increase the discharge energy.
Pulse off time	The pulse off time (t_{off}) represents the duration when no discharge exists and the dielectric is allowed to deionise and recover its insulating properties. A longer pulse off time improves machining stability as arcing is eliminated.

Process parameter	Effect on machining condition
Voltage	The input voltage applied across the tool electrode and workpiece is called the open circuit voltage (V_{OC}). The amount of V_{OC} influences the spark gap distance. During discharge, V_{OC} drops to the discharge voltage (V_d) which is influenced by the strength of the dielectric. A larger V_d will increase the discharge energy. As V_d varies during t_{on}, its magnitude may be expressed as an average discharge voltage (V_{av}).
Current	The discharge current (I_d) is a measure of the amount of electrical charges flowing between the tool and workpiece electrode. As the flow of electrical charges is the primary heating mechanism in electro-thermal erosion, a higher I_d will increase the discharge energy. As I_d from an RC-type pulse generator is not constant during t_{on}, the magnitude of I_d may be expressed as a peak current (I_{pk}) or average discharge current (I_{av}).
Discharge energy	This is the electrical energy that is available for material removal. It may be expressed as input discharge energy (E_{in}) or measured discharge energy (E_m). In an RC-type pulse generator, E_{in} depends on the applied capacitance and V_{OC}. The magnitude of E_m is calculated from measured pulse on time, discharge voltage and discharge current values.
Electrode polarity	Electrode polarity is chosen based on the requirement of electrode wear dominance at a given pulse on time. In micro-EDM, the tool electrode has negative polarity so that wear of the workpiece dominates.
Discharge gap distance	This is the maximum distance separating the anode and cathode at which sustainable discharge is possible. It is influenced by the open circuit voltage and strength of dielectric.
Dielectric	The dielectric serves as a medium in which controlled electrical discharges may be generated. It restricts plasma channel growth and influences the force of plasma channel implosion and expulsion of molten material. The dielectric cools expelled molten material into debris while its flow through the discharge gap aids in

Process parameter	Effect on machining condition
	debris flushing and cools the electrode by drawing heat away from the discharge location.
Flushing method	Flushing refers to the process of clearing machining debris from and suppling fresh dielectric to the discharge gap. Inadequate flushing causes accumulation of debris within the discharge gap that will lead to unstable machining. The method of flushing used largely depends on the tool electrode and machined feature dimensions. In micro-EDM, flushing effects are typically generated by a rotary electrode while jet flushing is seldom used as excessive unsymmetrical flushing forces may cause bending or breakage of tool or feature.

Table 2.2 Performance measures used to gauge performance results

Performance measure	Process performance result
Material removal rate (MRR)	MRR is a performance measure for the erosion rate of the workpiece and is typically used to quantify the speed at which machining is carried out. It is expressed as the volumetric amount of workpiece material removed per unit time.
Tool wear rate (TWR)	TWR is a performance measure for the erosion rate of the tool electrode and is a factor commonly taken into account when considering the geometrical accuracy of the machined feature. It is expressed as the volumetric amount of tool electrode material removed per unit time.
Wear ratio (WR)	WR is the ratio of TWR/MRR and is used as a performance measure for quantifying tool-workpiece material combination pairs since different material combinations gives rise to different TWR and MRR values. A material combination pair with the lowest WR indicates that the tool-workpiece material combination gives the optimal TWR and MRR condition.
Surface quality (SQ)	Surface quality is a broad performance measure used to describe the condition of the machined surface. It comprises components such as surface roughness (SR), extent of heat

Performance measure	Process performance result
	affected zone (HAZ), recast layer thickness and micro-crack density.
Surface roughness (SR)	SR is a classification of surface parameter used to describe an amplitude feature, which translates to roughness of the surface finish. Of the many parameters available to quantify SR, the most commonly used in EDM are arithmetical mean surface roughness (*Ra*), maximum peak-to-valley surface roughness (R_{max}) and root mean square surface roughness (*Rq*).
Heat affected zone (HAZ)	HAZ refers to the region of a workpiece that did not melt during electrical discharge but has experienced a phase transformation, similar to that of heat treatment processes, after being subjected to the high temperatures of electrical discharge.
Recast layer thickness	The recast layer refers to the region of resolidified molten material occurring as the topmost layer of the machined surface. The recast layer is usually located above the heat affected zone.
Micro-crack density	Micro-crack density is a performance measure that describes the extent of micro-cracks existing on the machined surface. Micro-cracks are typically found in the recast layer, seldom crossing into the HAZ.

The relationship between process parameters and process performance is complex in that performance measures are usually affected by a combination of process parameters and process parameter magnitudes. While discharge energy magnitude influences MRR, SR, recast layer thickness, HAZ and micro-crack density [114-117], recast layer thickness has been reported to be influenced more by pulse on time duration than peak current, while micro-crack density has been reported to be influenced by discharge current and pulse on time combination pairs, rather than discharge energy [118]. The sensitivity of process performance to process parameters coupled with the large number of process parameter combination permutations is one of the reasons for compilations of machining technologies and also one of the driving forces behind studies on optimal process parameter combinations [119-121]. In addition, expressions relating process performance

to process parameters were also formulated through process modelling studies so as to better control the EDM process and predict its performance results [122-124].

2.1.3 Comparison of EDM and micro-EDM

There are generally two ways of distinguishing EDM and micro-EDM, namely, by the feature size produced [125] and by the machining parameter magnitude used [126]. In this research, EDM and micro-EDM are differentiated by their process parameter magnitude since it is used as the primary means for controlling unit removal in EDM [127] and hence the machinability of micro-features [128]. Thus, to be classified as a micro-EDM process the process parameter magnitudes used had to fall in the range shown in Table 2.3, which were chosen based on the operating window of a commercial micro-EDM system, Panasonic MG-ED72W [129-131].

Table 2.3 Range of process parameter magnitudes for micro-EDM

Process parameter	Value
Open circuit voltage, V_{OC}	≤ 110 V
Peak current, I_{pk}	< 3.5 A
Pulse on time, t_{on}	< 1 μs
Discharge energy, E	≤ 25 μJ
Tool electrode size	≤ 300 μm in diameter
Tool electrode polarity	Negative
Flushing technique	Electrode rotation

The process conditions under which machining occur in EDM and micro-EDM are distinctively different due to the unique process parameter magnitudes employed for micro-machining. In order to satisfy micro-machining requirements, small discharge energies are used to generate a small unit removal [127] and to reduce surface roughness [31]. This is typically achieved by lowering discharge current, pulse on time and open circuit voltage. The discharge current and pulse on time are lowered by using a smaller capacitance, in the RC-type pulse generator, for machining. As a result, unlike the transistor-based pulse generators used in EDM, discharge current and pulse on time from the RC-type pulse generator cannot be adjusted independently. Furthermore, while the discharge voltage and current are controlled at predefined levels in the isopulse discharge,

those in the RC discharge are not controlled but affected by the capacitor charge state. Thus the use of different pulse generators will cause variations in heat input incident on the electrode, especially at short pulse on time durations [112]. The open circuit voltage is kept low to minimise discharge gap distance and lower discharge energy [132]. As a result, discharge gap distances are significantly smaller in micro-EDM, measuring between 1.5 μm and 5 μm [126]. The small discharge gap creates a higher back pressure within the gap, which inhibits dielectric flow and debris removal from the gap [28] as well as restricts widening of the plasma channel [133]. In addition, the need to machine micro-features requires tool electrode dimensions in the micrometer range, which limits the use of jet flushing methods typically employed in EDM and favours the use of electrode rotation to generate flushing effects. The jet flushing effects in EDM are easily controlled by flow pressure and flow rate while the flushing effects from a rotating electrode in micro-EDM are derived from Taylor-Couette flow and centrifugal forces. Therefore, these factors contribute to variations in inter-electrode conditions between EDM and micro-EDM. The smaller discharge energies in micro-EDM also means that the influence of dielectric viscosity, surface tension and mass transfer at the plasma channel to dielectric interface may have a more significant effect on the growth of plasma channel and material removal than in conventional EDM [96]. Moreover, given the smaller discharge energies in micro-EDM, a more significant proportion of discharge energy may be used for plasma growth, thereby leaving a smaller fraction for material removal. In micro-EDM, the electrode polarity setting used is opposite that of EDM due to the difference in electron and ion mobility [104] and difference in pulse on time durations adopted by each process [134]. Thus, the greater amount of discharge energy distributed to the anode [135] coupled with the small pulse on time cause larger craters at the anode than the cathode [136], thereby creating more material removal from workpiece than tool wear in micro-EDM. The electrode polarity has been reported to influence the nature of heat input used in EDM process modelling [104, 105].

The sensitivity of process performance to process parameters coupled with the distinct differences in process conditions between EDM and micro-EDM indicate that their process characteristics and performance are also diverse. It was suggested that the crack formation mechanism in EDM and micro-EDM are different since cracking still occurred in micro-EDM even though the discharge energy and pulse on time duration used were far from the crack susceptibility region defined in EDM [137]. Also, while jet flushing

was suggested to affect recast layer thickness in EDM [138], the flushing conditions from electrode rotation and dissimilar inter-electrode conditions in micro-EDM may create differing process performance results. In process modelling, differences in electrical discharge characteristics were shown to generate contrasting results between EDM and micro-EDM [134]. This highlights the need for individual process control and performance prediction models for EDM and micro-EDM [139-141]. Therefore, although results of EDM investigations may be relied to suggest similar trends in micro-EDM, specific studies on micro-EDM should still be performed under micro-EDM process conditions to elucidate the actual process characteristics.

Nevertheless, EDM and micro-EDM still share a similar electro-thermal material removal mechanism, which implies that certain process performance results are common for the two processes. Material removal is brought about by repeated electrical discharges, which cause the machined surface to be covered by overlapping craters of randomly varying depths and positions [142]. This effectively limits the minimum surface roughness achievable of which an arithmetical mean surface roughness between 0.2 μm and 0.4 μm have been reported [143]. The incomplete expulsion of molten material from the melt pool is another process characteristic that is common to both processes. This generates a recast layer on the machined surface, which contains residual-stresses [144, 145] and is susceptible to micro-cracking [146]. These surface imperfections are considered to reduce the fatigue strength, wear resistance and corrosion resistance of machined components [147, 148].

Although these surface defects are encountered in both EDM and micro-EDM, their effects are more severe in micro-EDM due to the relatively smaller size difference between defect and micro-feature. Moreover, there is also a need to reduce surface roughness in proportion to feature size when attempting to perform micro-machining [31]. The ability to control and predict the performance of micro-EDM process is also more crucial due to the minute tool and feature sizes and small discharge gap distances. Thus, improvements to the micro-EDM technique requires advancements that enable reductions in surface defects, enhancement of surface functional properties as well as allow better control and prediction of process performance. The following literature review of technological developments focused on the use of powder-mixed dielectrics in EDM and process modelling for EDM and micro-EDM with the intent of addressing these issues.

2.2 Technological developments

A review of the application of powder-mixed dielectrics for EDM process was conducted as performing EDM in a powder-mixed dielectric was reported to reduce surface roughness, recast layer thickness and micro-crack density [25] as well as enhance the machined surface with functional properties [149]. Then a review of process modelling for EDM and micro-EDM was performed to ascertain the advancements made in process modelling so that improvements to available process modelling approaches may be proposed.

2.2.1 Application of powder-mixed dielectrics for EDM

The use of powder-mixed dielectrics for EDM either involves the direct addition of powder additives into the dielectric (PMD-EDM) or the use of powder compact tool electrodes such that the dielectric is saturated with powder additives of tool electrode material resulting from high tool wear (PCT-EDM). Generally, most studies on PMD-EDM focused on the improvements in MRR, WR and SQ with some studies extending towards the imparting of functional properties to machined surfaces. On the other hand, the majority of investigations concerning PCT-EDM concentrate on the enhancement of machined surface functional properties, such as wear resistance, corrosion resistance and reduced friction coefficient, through surface modification. This distinction in process application may be due to the precedence of results concerning these two processes. One of the earliest studies on PMD-EDM [150] was conducted in 1965 from which it was reported that erosion rate increased when machining with conductive powder mixed in the dielectric. In contrast, the possibility of surface modification using PCT-EDM probably originated when studies into electrical discharge machined surfaces showed the incorporation of traces of tool material on the machined surface [151] and when the analysis of spark phenomena indicated the presence of gases in the anode phase zone rushing towards the cathode, thereby bringing about anodic material transfer to the cathode [152]. The significance of depositing material using EDM over other material deposition techniques such as electroplating, physical and chemical vapour deposition is the ability to perform material deposition during the actual machining operation [153]. The PCT-EDM process has been applied to coating and cladding repairs of aerospace components [154].

2.2.1.1 Powder-mixed dielectric EDM (PMD-EDM)

In PMD-EDM, powder additives are mixed directly into the dielectric to change the electro-thermal properties of the dielectric. The presence of conductive and semi-conductive powder additives within the discharge gap aids dielectric breakdown at larger gap distances [155] while the absorption of thermal energy by the powder additives alter the material removal mechanism [156]. In PMD-EDM studies, the common variables used include powder material, powder granularity and powder concentration. Furthermore, the process parameters and conditions employed were mostly suitable for EDM, such as microsecond range pulse on time and jet flushing [28, 157, 158]. While the process performance measures assessed in the studies included MRR, TWR, WR, SR, recast layer thickness and micro-crack density, the review focused on SR, recast layer thickness and micro-crack density since they are factors that affect SQ and the minimum machinable size of micro-features. Furthermore, a review on the use of PMD-EDM for surface modification was done to assess the possibility of enhancing the machined surfaces of micro-components with functional properties through PMD micro-EDM.

It is generally agreed that the use of PMD-EDM helped to reduce SR because the presence of powder additives within the discharge gap caused discharge gap enlargement, which brought about favourable conditions for generation of craters with lesser undulations and shallower troughs. The presence of overlapping craters with lesser undulations around the crater rims and flatter crater bottoms was reported to be a characteristic of a fine finish surface machined by EDM, which resulted in a surface roughness R_{max} of less than 2 μm [159]. To appreciate the physics of gap enlargement caused by the powder additives [26], the perturbations to electrical field intensity caused by conductive and non-conductive particles were theoretically calculated and shown that these particles promoted the initiation of electrical discharges at larger gap distances than that without the presence of particles. In a study on the mechanism by which debris particles assisted discharge ignition [160], it was proposed that the formation of particle bridges between the electrodes shortened discharge distances and created higher field strengths which facilitated discharge ignition at larger gap distances. The movement of debris in the discharge gap were studied and the results used to develop theoretical models for the reciprocating motion of debris particles under the influence of electrostatic forces in the discharge gap [161]. This allowed the estimation of time taken for debris to

form chains due to electrophoresis and in turn provided information on discharge delay time and gap distance. Another experiment to observe the behaviour of particles in an electrical field generated between parallel electrodes reported four distinct behaviours, namely, reciprocating motion between electrodes, adhesion on either electrode, clustering in the gap and chain formation that bridged the electrodes [30].

The enlarged discharge gap was suggested to help lower the electrostatic gap capacitance [162] so that discharge energy is lowered [37] through the discharge of micro-currents [28] and smaller craters are produced. In a study using silicon (Si) powder additive of granularity less than 20 μm in radius at a concentration of 20 g/l [37], it was suggested that the powder additives helped to disperse the discharges over the machined area and produce a more uniformly machined surface. The dispersion of discharges may be characterized by an absence of arc discharges which is a concentration of discharges that leads to a deterioration in SQ [22]. In the same light, it was shown that the introduction of Si powder helped to reduce the occurrence of abnormal discharges of which arcing was a main component [162]. Furthermore, it was suggested that the more even distribution of discharges in the gap region was due to a less significant difference in electric field between micro-peaks as a result of a wider inter electrode gap [28]. It was proposed that the widened discharge gap reduced back pressure, which promoted the flow of fresh dielectric into the work area so that more effective debris removal was achieved. In the study, powder concentration was kept at 2 g/l while various powder granularities and materials were used, such as, 38 μm graphite particles, 45 μm silicon particles and 3 μm molybdenum sulphide particles. However, a wider discharge gap translates to a large overcut which should be minimised, especially in micro-machining, so that machining accuracy is more controllable. Furthermore, an excessive overcut would limit the size of producible micro-holes and create more pronounced side wall tapers [163]. To minimise discharge gap enlargement, smaller sized powder additives were recommended, based on studies that used Al particle granularities of 70~80 nm, 10~15 μm and 100 μm [164]. Moreover, it was reported that the more conductive Al particles produced a larger channel expansion and more pronounced side wall tapers compared to the semi-conductive silicon carbide (SiC) particles when Al and SiC powders were used in micro channel machining of titanium alloy [163]. To address the issue of gap enlargement, a non-conductive alumina (Al_20_3) powder of granularity 1 μm, concentration of 4 g/l and tool electrode

rotation at 60 rev/min was used to machine SKD11 steel [165]. Results showed that surface roughness and recast layer thickness were reduced without a change in gap distance.

The interaction effects of powder material, granularity, concentration and discharge parameters on SR and recast layer thickness was reported in a study using Al powder with granularities of 70~80 nm, 10~15 µm and 100 µm, in concentrations between 0 cm^3/l and 1.0 cm^3/l, with discharge currents of 1.5 A and 4 A and pulse on time of 25 µs [158]. It was shown that the smallest *Ra* on SKD-11 mould steel was achieved at 1.5 A, 70~80 nm granularity and 0.25 cm^3/l powder concentration. Moreover, recast layer thickness was lower at larger granularities of Al powder and Al powder was also reported to be the most effective in reducing recast layer thickness, followed by chromium (Cr) and SiC. The effects of powder material property on the distribution of discharge energy should also be considered since the amount of discharge energy available directly influences crater formation and the resulting crater size [166]. In this aspect, another study observed differences in light intensities emitted by the Si and Al particles during electrical discharge as well as differences in resulting plasma channel sizes of discharges in Si-mixed and Al-mixed dielectrics [156]. Through photographic evidence from a high speed framing camera, it was suggested that the Si particles had higher energy storage abilities due to the higher intensity of light emission and the narrower plasma channel formed in Si-mixed dielectric. Thus, it was also proposed that the thermal material removal characteristics of PMD-EDM are influenced by the energy storage properties of the powder additives. Given that the distribution of discharge energy to the anode and cathode are different, the effects of electrode polarity on surface roughness in PMD-EDM were also studied [167]. The study suggested that the smaller craters and fewer micro-cracks produced in Al powder-mixed dielectric were attributed to the discharge distribution effect brought about by the Al powder.

The presence of powder additives within the discharge gap does not automatically reduce SR, recast layer thickness and micro-crack density. An excessive concentration of powder additives was reported to reduce SQ due to the more frequent occurrence of undesirable discharges [25]. Using aluminium (Al) powder in concentrations between 0.1 g/l and 2 g/l with discharge power of 150W and pulse on time of 800 µs [155], it was reported that SR increased due to the generation of deeper craters. Similarly, using Al powder with 10 µm

granularity in a concentration of 40 g/l and pulse on time of 150 µs caused SR to increase with increasing discharge current [133]. A similar outcome was also recorded when an additive concentration of 0.5 g/l was used with a discharge current of 7 A at a pulse on time of 260 µs [25]. However, surface roughness was lowered when either the additive concentration was increased to 1.5 g/l or when discharge current was lowered to 2.5 A at a pulse on time of 50 µs. Through the use of Si powder additives with 10 µm granularity in concentrations between 0 g/l and 20 g/l [157], it was reported that a concentration of 2 g/l produced the smallest R_{max}. However, the improvement in surface roughness was affected by the jet flushing flow rate and electrode area. In addition, while the recast layer was denser, more homogeneous and thinner, its variation with powder concentration was not evident. On the other hand, another study reported that when concentration of nickel (Ni) powder having 5 µm granularity was increased in 10 g/l increments up to 40 g/l and machining was performed at 3 A discharge current and 2 µs pulse on time[29], the recast layer thickness increased and the machined surface became crack free. In the same study, when carbon powder of 30 µm granularity was used in concentrations up to 15 g/l with 3 A discharge current, the recast layer thickness was constant regardless of concentration but increased when pulse on time was increased from 2 µs to 200 µs. The benefit of inhibiting a reduction in recast layer thickness becomes evident when PMD-EDM is used in surface modification applications.

After conducting PMD-EDM in the nickel-mixed dielectric [29], it was reported that the machined surface hardness produced in 40 g/l Ni powder concentration was higher than that of the recast layer produced in a powder-free dielectric, which was in turn harder than the base material. It was concluded that a recast layer containing nickel could be generated by the PMD-EDM process. In a follow up to the study [33], a titanium (Ti) tool electrode and carbon powder were employed to generate a titanium carbide (TiC) machined surface with increased wear resistance. It was reported that the machined surface hardness increased with pulse on time and powder concentration. Using a different approach involving powder accretion without material removal [30], another study employed Ti powder of 36 µm granularity and concentration of 50 g/l to accrete a hard TiC layer on the workpiece. To promote accretion open circuit voltage of 320 V, discharge current of 2 A, pulse on time of 2 µs and negative tool polarity were used, while a pulse off time of 1024 µs ensured minimal material removal. In addition, various tool electrode configurations were explored to maintain a high powder concentration

within the discharge gap. A reduced machined surface friction coefficient was also reported after PMD-EDM was performed with molybdenum disulphide-mixed dielectric to deposit a lubricant layer on carbon steel and stainless steel [37]. The process parameters employed included open circuit voltage of 320 V, discharge current of 2 A and pulse on time of 2 μs [168]. In a recent study, it was reported that the combination pair of discharge current and pulse on time determined the nature of material removal and deposition [169].

Thus, the successful reduction of surface defects and enhancement of surface functional properties in PMD-EDM are strongly influenced by both powder properties and process parameters. Furthermore, process performance results are highly dependent of process parameters used and process conditions involved.

2.2.1.2 Powder-compacted tool EDM (PCT-EDM)

In PCT-EDM, powder-compact tool electrodes are prepared using powder metallurgy techniques and used for machining. Generally, the tool electrodes are made up of micro-sized powder additives having powder material that is intended to be deposited onto the machined surface. The selected material and a binder material, both in powder form, are mixed together and sintered or partially-sintered to form powder-compacted electrodes [170-175]. Then during the PCT-EDM process, the alloying powders are released into the dielectric through the disintegration of the tool electrode by electro-thermal effects. The main purpose of using powder-compacted tool electrodes is to lower the apparent thermal conductivity of the material [175] so that a higher electrode wear rate is achieved and an adequate concentration of powder additives is supplied to the discharge gap for deposition. As in the case of surface modification with PMD-EDM, PCT-EDM may be performed with material removal or without material removal. The combined mode of machining and material deposition by PCT-EDM is called electrical discharge alloying (EDA) by some researchers [171, 172] while material deposition by PCT-EDM is called electrical discharge coating (EDC) [173, 174]. With reference to Figure 2.3, the EDA and EDC processes both require a high tool electrode wear to introduce particles of tool electrode material into the discharge gap. These particles are combined with the pyrolytic carbon particles, from hydrocarbon dielectric fluid decomposition, under high temperatures and are alloyed onto the machined surface. Typically the EDA process involves considerable

workpiece material removal while the EDC process involves minimal workpiece material removal.

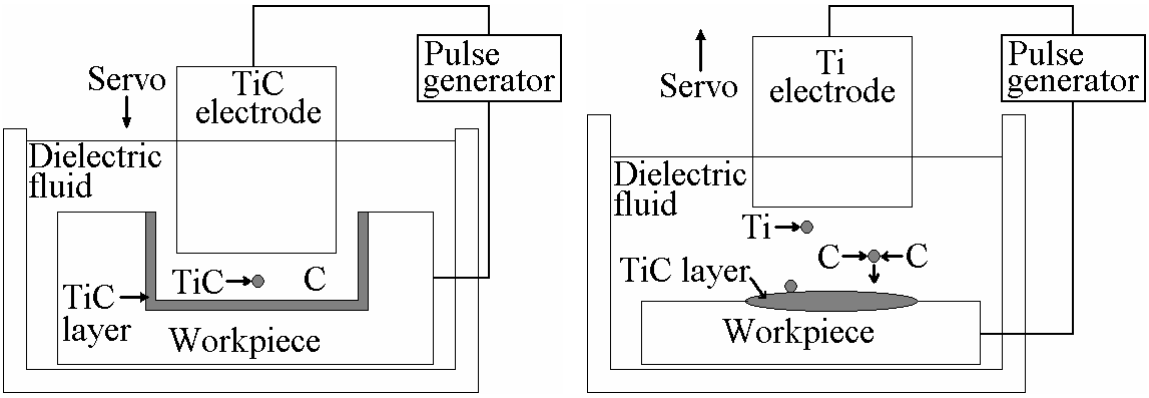

(a) Electrical discharge alloying (b) Electrical discharge coating

Figure 2.3 Schematic representation of various PCT-EDM processes [172, 173]

In an EDA study that used copper powder with 50 μm granularity to produce electrodes at various forming pressures [176], their performance compared to a solid copper electrode were assessed through machining with 270 V open circuit voltage, 2.9 A discharge current and 100 μs pulse on time. While the solid tool electrode showed the highest ratio of recast layer thickness to tool wear, the percentage concentration of deposited material was higher for the powder-compacted electrodes. Furthermore, with observations of the direct adhesion of 50 μm powder additives to the workpiece surface machined using the powder-compacted electrodes it was suggested that, from the perspective of alloying, surface roughness and discharge gap dimension, finer particles should be used. In an EDA/EDC investigation that used copper (Cu) and tungsten (W) powders [177], powder granularity of 45 μm were mixed in a wt.% ratio of 3:1 to produce semi-sintered electrodes. Applying open circuit voltages in the range of 60 V to 100 V, discharge currents in the range of 3 A to 16 A and pulse on time durations in the range of 50 μs to 400 μs, it was shown that the electrode wear rate was more than three times the surface deposition rate. The EDC of a carbon steel workpiece was also performed using a tungsten carbide – cobalt (WC-Co) composite tool electrode for deposition of WC layer onto the workpiece [175]. The deposition process was performed with negative electrode polarity to promote high electrode wear and peak current of 25 A, with pulse on and off times of 16 μs and 512 μs respectively.

2.2.1.3 Concluding remarks

The PMD-EDM process is mostly used in the improvement of machined surface quality while dominance of the PCT-EDM process is in the imparting of functional properties to machined surfaces. Nevertheless, the potential of PMD-EDM in surface modification has been revealed in some investigations and a review of the process characteristics in PMD-EDM and PCT-EDM shows the former being more conducive for implementation in micro-EDM. Through this review, it is found that the principle of PMD-EDM can be more readily applied to micro-EDM as changes to process parameters are more manageable and process requirements are more conducive for micro-machining. On the other hand, the implementation of PCT-EDM to micro-machining requires a number of major issues to be addressed first. The process parameter magnitudes employed to promote tool wear may not coincide with those used for micro-EDM. The requirement for high tool wear may affect machining accuracy and efficiency while the need to fabricate powder-compacted micro-electrodes may heighten process complexity. The relatively small size of tool electrode to volume of dielectric may limit the achievable powder concentration.

In the PMD-EDM process, as in the case of EDM and micro-EDM, process performance is sensitive to process parameters and process conditions. However, unlike EDM and micro-EDM, additional considerations related to powder properties are needed in PMD-EDM. To better appreciate the technological evolution of the PMD-EDM technique and identify its state-of-the-art, a chronologically-arranged list of PMD-EDM studies was drawn, as presented in Table 2.4 to Table 2.7. The list was based on selected studies [23-26, 28-30, 133, 155, 156, 158, 163-165, 169, 178, 179] which highlighted key research parameters and findings relevant to the research presented in this thesis.

Table 2.4 Technological development of PMD-EDM

Year	Researcher(s)	Experimental parameters	Research findings
1981	Erden, A. and Bilgin, S.	Powder material (concentration): Cu (2.5 g/l to 50 g/l), Al (0.1 g/l to 2 g/l), Fe (0.2 g/l to 7.5 g/l) and C (0.05 g/l to 1.0 g/l) Pulse on time: 60 µs to 2000 µs	The machining rate increased with increase in powder concentration due to the decrease in time lag. High powder concentration decreased machining rate due to the occurrence of short circuits. The discharge gap increased with increase in powder concentration.
1981	Jeswani, M.L.	Powder material (granularity, concentration): Graphite (10 µm, 0.25 g/l to 6 g/l) Pulse on time: 5 µs to 40 µs Discharge energy: 1 mJ to 500 mJ Tool shape and movement: Rod, vertical vibration at 40 Hz	At the powder concentration of 4 g/l, MRR increased by 60 %, TWR increased by 15 % and WR decreased by 28 %. The breakdown voltage at 4 g/l was about 30 % less than in powder-free dielectric. The reduction in breakdown voltage increased discharge frequency, which consequently increased MRR.
1991	Mohri, N., Saito, N. and Higashi, M.	Powder material (granularity, concentration): Si (less than 20 µm, 20 g/l) Pulse on time: 2 µs Discharge current: 1 A Tool shape and movement: Rod, planetary motion with radius of 125 µm and speed of 3000 rev/min	The discharge gap in powder-mixed dielectric was more than several times larger than in powder-free dielectric. The discharges were dispersed over the gap region such that machined surface roughness was not strongly dependent on working area. The machined surface had strong corrosion resistance.
1994	Yan, B.H. and Chen, S.L.	Powder material (granularity, concentration): Al_2O_3 (0.05 µm to 5 µm, 2 g/l to 12 g/l) Pulse on time: 5 µs to 300 µs Discharge current: 1.5 A to 6 A Tool shape and movement: Rod, rotation at 60 rev/min	The machined surface roughness and recast layer thickness were reduced without a change in discharge gap distance.
1995	Ming, Q.Y. and He, L.Y.	Powder material (granularity, concentration): Conductive and inorganic oxide (0.01 µm to 10 µm, less than 4 g/l) Pulse on time: 32 µs to 260 µs Discharge current: 0.5 A to 7 A	The surface roughness decreased with increase in powder concentration, but increased with excessive powder concentration. The tendency for crack inception and extent of crack propagation on the machined surface was reduced. The recast layer was thinner and denser.

Table 2.5 Technological development of PMD-EDM (continued)

Year	Researcher(s)	Experimental parameters	Research findings
1998	Wong, Y.S., Lim, L.C., Rahuman, I. and Tee, W.M.	Powder material (granularity, concentration): Graphite (35 µm to 41 µm, 2 g/l), Si (42 µm to 48 µm, 2 g/l), Al (42 µm to 48 µm, 2 g/l), SiC (2.28 mm to 2.44 mm, 2 g/l), MoS_2 (1 µm to 3 µm, 2 g/l) Pulse on time: 7.5 µs to 27 µs Discharge current: 1 A to 2 A	The reduction in breakdown voltage allowed discharges to occur at wider discharge gap distances which facilitated debris removal and improved machining stability. The wider discharge gap reduced back pressure and facilitated the flow of dielectric into the gap. The wider discharge gap reduced electrostatic capacity and resulted in smaller discharge currents so that smaller craters are produced. The discharges were dispersed which generated well-formed and small overlapping craters on the machined surface.
2000	Chow, H.M., Yan, B.H., Huang, F.Y. and Hung, J.C.	Powder material (granularity, concentration): Al (1 µm, 2.5 g/l to 75 g/l), SiC (1 µm, 2.5 g/l to 75 g/l) Pulse on time: 2 µs to 20 µs Discharge current: 0.1 A to 1 A Tool shape and movement: Disc, rotation at 150 rev/min	PMD-EDM was applied to the fabrication of micro-slits. The effects of disc rotation in a powder-mixed dielectric enabled multiple discharging within a single input pulse. The multiple discharging dispersed discharge location and divided discharge energy to generate machined surfaces with reduced surface roughness. Aluminium powder material produced a larger gap expansion than silicon carbide.
2001	Furutani, K., Saneto, A., Takezawa, H., Mohri, N. and Miyake, H.	Powder material (granularity, concentration): Ti (36 µm, 50 g/l) Pulse on time: 2 µs to 1024 µs Discharge current: 1 A to 20 A Tool shape and movement: Rod, vertically reciprocating; Gear-shaped, periphery velocity of 0.63 m/s to 6.3 m/s	PMD-EDM was applied to accretion process. The accretion of titanium carbide using a thin electrode to keep powder concentration within the discharge gap high produced a column structure. A gear shaped rotating electrode was used to deposit a uniform thickness over a wider area.
2001	Tzeng, Y.F. and Lee, C.Y.	Powder material (granularity, concentration): Al (70 nm to 100 µm, 0.7 g/l to 2.7 g/l), Cr (10 µm to 15 µm, 1.8 g/l to 7 g/l), Cu (10 µm to 15 µm, 2 g/l to 9 g/l), SiC (10 µm to 15 µm, 0.8 g/l to 3 g/l) Pulse on time: 6 µs to 75 µs Discharge current: 1.5 A to 4 A	The discharge gap distance and material removal rate increased as powder granularity was increased. Of the powder materials capable of remaining in suspension during machining, aluminium produced the largest discharge gap enlargement and silicon carbide produced the smallest.

Table 2.6 Technological development of PMD-EDM (continued)

Year	Researcher(s)	Experimental parameters	Research findings
2001	Uno, Y., Okada, A. and Cetin, S.	Powder material (granularity, concentration): C (30 µm, 1 g/l to 15 g/l), Ni (5 µm, 2 g/l to 40 g/l) Pulse on time: 2 µs to 200 µs Discharge current: 3 A	Most of the molten material within the crater generated in powder-mixed dielectric was not expelled due to the smaller expulsion force caused by a larger gap distance. As carbon powder concentration increased, recast layer undulation and non-uniformity were reduced. The presence of cracks and pores were also reduced. As nickel powder concentration increased, recast layer thickness increased and layer uniformity improved.
2002	Zhao, W.S., Meng, Q.G. and Wang, Z.L.	Powder material (granularity, concentration): Al (10 µm, 40 g/l) Pulse on time: 150 µs Discharge current: 15 A to 23 A	PMD-EDM was applied to improving the efficiency of rough machining. PMD-EDM enabled a 70 % improvement in machining efficiency over EDM in powder-free dielectric while achieving similar machined surface roughness.
2003	Kozak, J., Rozenek, M. and Dabrowski, L.	Powder material (granularity, concentration): Al (84 µm, 10 g/l), SiC (84 µm, 0.2 g/l and 2 g/l), Al_2O_3 (2 µm to 22 µm, 10 g/l) Pulse on time: 9 µs to 200 µs Discharge current: 1 A to 12 A	PMD-EDM using kerosene and deionized water were compared. The surface roughness of PMD-EDM with Al_2O_3 in water was higher than that of EDM with kerosene at discharge currents below 11 A. Generally, a higher surface roughness was generated when Al_2O_3 powder granularity of 14 µm was used compared to 22 µm.
2004	Klocke, F., Lung, D., Antonoglou, G., and Thomaidis, D.	Powder material (granularity, concentration): Al (less than 10 µm, 2 g/l to 6 g/l), Si (less than 10 µm, 2.5 g/l to 10 g/l) Pulse on time: 10 µs Discharge current: 10 mA to 65 mA	The powder additives caused greater expansion of plasma channel compared to a powder-free dielectric. The powder additives changed the thermal material removal mechanism and affected the composition and morphology of the recast layer.

Table 2.7 Technological development of PMD-EDM (continued)

Year	Researcher(s)	Experimental parameters	Research findings
2005	Tzeng, Y.F. and Chen, F.C.	Powder material (granularity, concentration): Al (70 nm to 100 µm, 0.7 g/l to 2.7 g/l), Cr (10 µm to 15 µm, 1.8 g/l to 7 g/l), Cu (10 µm to 15 µm, 2 g/l to 9 g/l), SiC (10 µm to 15 µm, 0.8 g/l to 3 g/l) Pulse on time: 6 µs to 75 µs Discharge current: 1.5 A to 4 A	The presence of powder additives reduced the recast layer thickness. The surface roughness decreased when aluminium powder granularity was decreased. The recast layer thickness decreased when aluminium powder granularity was increased. Aluminium powder material produced the smallest surface roughness and thinner recast layer.
2008	Chow, H.M., Yang, L.D., Lin, C.T. and Chen, Y.F.	Powder material (granularity, concentration): SiC (3 µm and 5 µm, 25 g/l) Pulse on time: 2 µs to 20 µs Discharge current: 0.1 A to 1 A Tool shape and movement: Disc, rotation at 20 rev/min	PMD-EDM using pure water was applied to the fabrication of micro-slits. Using SiC increased the electrical conductivity of water which increased discharge gap and dispersed the discharge energy. PMD-EDM produced a larger slit expansion and electrode wear but a smaller amount of machined burr compared to powder-free dielectric.
2008	Kansal, H.K., Singh, S. and Kumar, P.	Powder material (granularity, concentration): Graphite (30 µm, 2 g/l) Pulse on time: 100 µs to 300 µs Discharge current: 3.2 A to 12 A	Numerical simulation of PMD-EDM using finite element methods. The effects of powder additives on crater geometry were attributed to discharge frequency and breakdown voltage, which were factored in the model through the use of a new parameter. The parameter introduced a constant factor to the determination of heat flux to the workpiece.
2009	Furutani, K., Sato, H. and Suzuki, M.	Powder material (granularity, concentration): Ti (38 µm, 50 g/l) Pulse on time: 2 µs to 128 µs Discharge current: 2 A to 17 A	PMD-EDM was applied to accretion process. Deposition of TiC was possible at discharge energies below 5 mJ under certain discharge current and pulse on time combinations. There existed a maximum discharge current for deposition. The larger the discharge current, the smaller the range of pulse on time durations available for deposition.

With reference to selected studies on PMD-EDM [23, 24, 26, 28-30, 133, 156, 158, 163-165, 167, 169, 178, 180, 181], Figure 2.4 shows the coverage of PMD-EDM research conducted in terms of powder properties and electrical process parameter, specifically, pulse on time. Pulse on time was chosen as it was the most consistently used process parameter in the references reviewed. Moreover, it is one of the key electrical process parameters that control discharge energy.

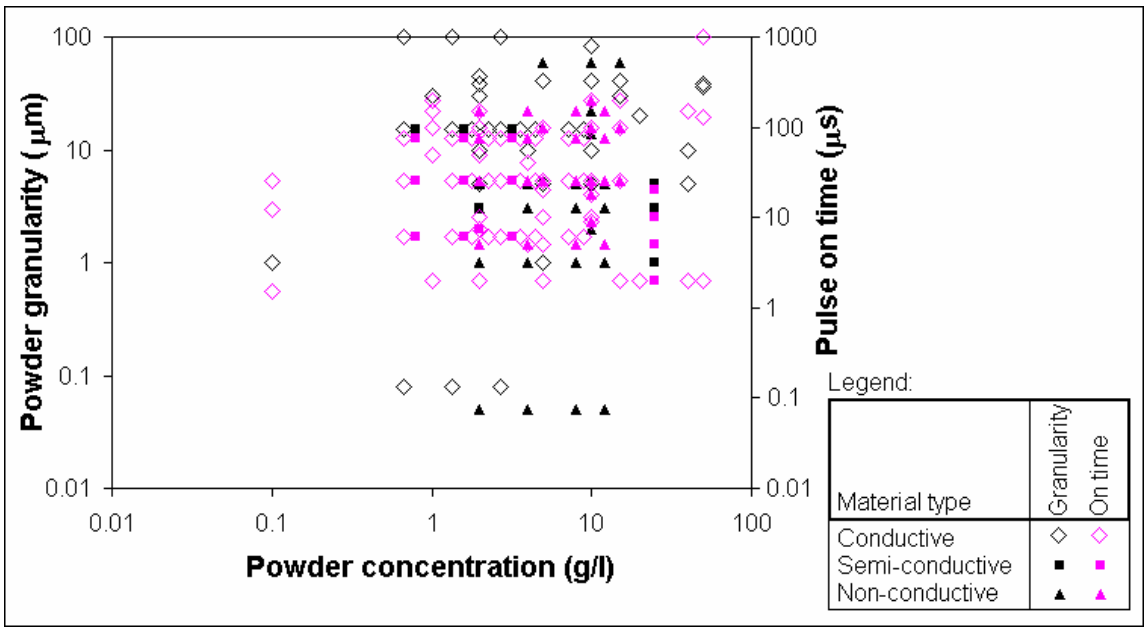

Figure 2.4 Coverage of PMD-EDM research

Figure 2.4 revealed a gap in PMD-EDM research for powder granularity less than 1 µm, powder concentration below 1 g/l and pulse on time less than 1 µs. This is primarily because most research was conducted for EDM process conditions in which pulse on time durations were more than 1 µs and the use of micro-sized powders in concentrations of more than 1 g/l were appropriate. Thus, despite the availability of studies for a wide range of process parameters, a set of process parameters applicable to PMD micro-EDM is unavailable. Consequently, the effectiveness of employing a powder-mixed dielectric with discharge energies less than 25 µJ and pulse on time durations in the sub-microsecond range for the purpose of reducing surface defects and enhancing surface functional properties is unclear. To address this, there is a need to conduct research on the use of powder-mixed dielectrics using electrical process parameters and process conditions associated with micro-EDM.

Micro-machining requires precision machining principles to be followed strictly, such as machining units and small unit removal. A machining unit is the minimum controllable amount of material that can be removed or added with high repeatability. Since a small machining unit is necessary for improving machining precision, studies into machining unit for various machining methods have been conducted, such as micro-turning [182], micro-milling [183] and laser beam machining [184]. In EDM and micro-EDM, the unit removal is a crater produced by one discharge pulse and the limit of unit removal depends on the discharge energy [31]. While single discharge experiments for EDM with an RC-type pulse generator [185] and for PMD-EDM [29] have been conducted, the feasibility of PMD micro-EDM should also be determined through similar experiments. Then, observations from single discharge experiments can be related to actual machining conditions through the conduct of machining experiments on PMD micro-EDM. In the conduct of experiments for PMD micro-EDM, the following process parameters should be considered:

- Using powder granularities in the nanometre range. The use of finer sized particles is intended to facilitate powder entry into the discharge gap. Moreover, it was reported that using finer particles could minimise surface roughness, which is important in micro-EDM. In addition, nano-sized particles may be more readily processed given the small discharge energy and pulse on time.
- Using powder concentrations less than 1 g/l. The purpose of using small powder concentrations is to minimise gap enlargement and prevent arc discharges across the small discharge gap, which can damage the machined surface. Furthermore, the tendency for particle flocculation will also be minimised.
- Using semi-conductive and non-conductive powder materials. The use of conductive powder materials gives the largest discharge gap enlargements. Through the use of semi-conductive and non-conductive powder materials, gap enlargement may be reduced. This will facilitate attempts to control machining accuracy.

2.2.2 Process modelling in EDM and micro-EDM

In order to better understand the process characteristics of EDM and micro-EDM for process optimisation and control, both theoretical and empirical studies have been conducted to study the influence of process parameters on process performance. These studies may allow process models to be formulated, which are useful for EDM

practitioners in selection of parameters according to desired machining outcomes [48] and as quantitative relations for on-line adaptive control of the EDM process [47]. The theoretical approach formulates models based on universal principles such as the law of energy conservation. The conservation equation is then coupled with equations of state that are approximated based on empirical data. On the other hand, the empirical approach formulates models based only on empirical data using statistical approaches, such as Taguchi method [45], response surface methodology [186], regression modelling [123] and factorial studies [118], and forecasting models, such as artificial neural network [187] and residual grey dynamic model [124]. While theoretical and empirical models are both developed for process optimisation, performance prediction and process control applications, only theoretical models have the added advantage of providing an insight into the physics behind the material removal mechanism. Thus, a theoretical process modelling approach was taken in this research and a review on theoretical modelling was done.

The multi-disciplined considerations involved in analysing an electrical discharge and the stochastic nature of material removal in EDM presents difficulties in process modelling [188]. To address this, simplifications to thermal loading and boundary conditions are usually made during the model development. While it is possible to obtain sufficiently reliable models after such simplifications, these models may neglect certain aspects of the electrical discharge erosion process, which when considered may provide new insight into the material removal process. The theoretical models that were proposed to describe the material removal process in EDM are generally based on the electro-mechanical mechanism [107] and the electro-thermal mechanism [134]. As the electro-mechanical mechanism proposed that the effects of electrostatic forces on material removal is more significant at pulse on time durations below 5 μs and considers thermal melting effects at short pulse durations insignificant [107], the model can only be used to describe the material removal mechanism in micro-EDM. On the other hand, the electro-thermal mechanism has been adopted to model the micro-EDM process with pulse on time durations up to 1 μs [134] and allows the effects of flushing efficiency on material removal and recast layer generation to be considered. Of the theoretical models based on the electro-thermal mode of material removal, three regions of interest concerning the electrical discharge erosion process are evident, namely, cathode erosion [104], anode erosion [105] and plasma channel development [106]. As the models describing the

cathode and anode erosion are based on the same thermal conduction principles, a distinction between cathode and anode is sometimes not made during the initial model development [97]. Instead, a distinction between cathode and anode erosion is made only when the models are solved after substitution of specific material properties. The existing theoretical models for the electrical discharge erosion process are also differentiated between EDM [104-106] and micro-EDM [112, 134]. This distinction may be attributed to the differences in electrical discharge characteristics, such as the range of discharge energy, pulse on time and time-variation of discharge voltage and current. Thus although the theoretical models for both processes share similar underlying principles, there are variations in thermal loading characteristics, boundary conditions and equations of state, which consequently influence the results obtained.

In the development of single electrical discharge erosion models (SEDEMs) for cathode and anode erosion prediction, a heat conduction analysis due to heat input from a single electrical discharge is performed to determine the unit amount of material removal. Solutions to the heat conduction analysis are obtained either analytically [189-192] or numerically [193-195]. The numerical approach allows greater flexibility in the application of thermal loads, boundary conditions and material properties [196-198]. Nevertheless, both approaches require fundamental parameters, such as the characteristics of heat source and heat flux, time duration of heat application and material properties, to be considered during the analysis of the heat conduction model. Most SEDEMs are used to predict single crater geometries [44] and performance measures that can be derived from the electro-thermal erosion of one crater, such as volumetric wear ratio [44] and distribution of induced thermal stress [199]. However, given the multiple discharge nature of the machining process, SEDEMs are not well suited to predict performance measures of EDM and micro-EDM. As a result various approaches have been taken to extend the use of SEDEMs for more accurate performance measure predictions.

Using the SEDEM as a base, the thermal conduction equation was solved analytically at various process parameter settings, within the range of 5 μJ to 150 μJ, to determine theoretical MRR, TWR and surface roughness values based on the geometry of one crater [141, 200]. Then, by comparing the theoretical performance measure values with corresponding empirical values, correction factors were determined. These correct factors could then be used to recalibrate any theoretical performance measure values, determined

within the range of 5 μJ to 150 μJ, to analytical performance measure values that closely approximate empirical values. Taking a different approach, an empirical expression was integrated to the heat conduction equation through a stochastic methodology called Data Dependent Systems [142]. The resulting hybrid model was solved for a transient temperature distribution. The material melting temperature isotherm, identified from the temperature distribution, represented the geometry of the characteristic crater, which is used to predict material erosion rate per discharge. Recently, various multiple discharge approaches were proposed to extend the SEDEM to performance measure prediction [201, 202]. In these approaches the resulting temperature distributions of heat fluxes from electrical discharges were determined numerically. The numerical approach allowed the application of heat flux boundary condition on any surface profile, which makes it ideal for simulation of overlapping craters. In one of the multiple discharge approaches taken to estimated the recast layer and HAZ thickness [201], two consecutive discharges on a flat boundary were modelled. The discharges were located next to each other so that their recast layer and HAZ could merge. To improve the agreement between simulated and measured crater dimensions, the second discharge was assumed to occur at a higher initial temperature than the first. In the other multiple discharge approach adopted for EDM modelling [202], a probability distribution function of discharge occurrence at various inter-electrode gap distances was used to determine the locations of consecutive discharges. In this way, the machined surface profile was simulated so that surface roughness and MRR values could be extracted. As part of model development discharge properties, such as percentage of energy distribution, equivalent temperature defining crater shape and coefficient determining the growth law of plasma channel, were estimated by comparing simulated and empirical surface roughness and MRR values [203].

To appreciate the various methods of extending SEDEM for process performance prediction, a consideration of the basic SEDEM formulation process is needed. This may be categorised into thermal conduction model, heat source, heat flux and material properties.

2.2.2.1 Thermal conduction model

Generally, the differential equation for heat transfer without internal heat generation is used as the underlying thermal model in the SEDEM. Given the axisymmetric nature of

the heat flux on the electrodes and the subsequent heat transfer process, the heat transfer equation in usually expressed in cylindrical coordinates as:

$$\frac{1}{r}\frac{\partial}{\partial r}\left(r\frac{\partial T}{\partial r}\right)+\frac{\partial^2 T}{\partial z^2}=\frac{1}{\alpha}\frac{\partial T}{\partial t} \tag{2.1}$$

where T represents the temperature, r the radial coordinate, z the axial coordinate, t the time and α the thermal diffusivity, which is expressed as

$$\alpha=\frac{k}{\rho\cdot c} \tag{2.2}$$

where k represents the thermal conductivity of the electrode material, ρ the mass density of the electrode material and c the specific heat capacity of the electrode material.

The initial and boundary conditions associated with the model were expressed as follows:

$$IC \quad : T(r,z,0)=T_0 \tag{2.3}$$

$$BCs \quad : -k\frac{\partial T(r,0,t)}{\partial z}=\begin{cases} q, & 0<r\le R \\ 0, & r>R \end{cases} \tag{2.4}$$

$$: \frac{\partial T(0,z,t)}{\partial r}=0, \qquad |z|>0 \tag{2.5}$$

$$: T(\infty,\infty,t)=T_0 \tag{2.6}$$

where T_0 represents the ambient temperature, q the heat flux and R the heat source radius.

In addition, the following assumptions are made:

- The electrode is considered a semi-infinite body since the volume of material removed is much smaller than the volume of the electrode.
- The electrode surfaces, with the exception of the portion subjected to the heat source, are completely insulated so that thermal exchanges at the electrode surface outside the heat source are neglected.
- The heat flux incident on the electrode is dissipated by conduction into the electrode with negligible thermal exchanges due to radiation and convection.
- The removal of electrode material through vaporization is negligible.
- There is only one spark per electrical discharge.
- The heat source is active for a known finite interval of time.
- The shape of the heat source is known and defined.
- The heat flux distributed uniformly within the heat source is known and defined.

2.2.2.2 Heat source

The heat sources used in existing theoretical models differ in their shape, size and time dependent characteristic. The typical heat source shape is circular [105, 134], although hemispherical [99, 101] and point [104] heat sources have also been proposed. The size of a circular heat source is either selected to represent an equivalent heat flux area [105, 195] or determined from the estimated size of the plasma channel [112], which is assumed to have a circular cross-section. For a circular heat source, both a fixed-size circular heat source [102, 134] and time dependent expanding circular heat source [103, 105] have been studied.

Various approaches have been used to estimate the size of the circular heat source. One approach suggested that the discharge channel was influenced by the dielectric and electrode materials [204]. It was proposed that the heat source radius was a function of discharge power and time according to the relationship

$$R(t) = L \cdot Q^{x} \cdot t^{y} \qquad (2.7)$$

where $R(t)$ represents the time dependent heat source radius, Q the discharge power and L, x and y are empirically determined constants. In addition, it was also suggested that the discharge radius was equal to the crater radius. Adopting the approximation of equality between crater radius and plasma channel radius, another study also suggested that it gave a realistic representation of plasma channel growth for the transient thermal model [192]. On the other hand, a study on a proposed first-stage expansion model for plasma growth suggested that the crater and plasma radii were unequal since the latter stopped expanding within a few microseconds after breakdown while the former continued to grow after that [196].

In yet another approach, the temperature at the heat source was assumed constant and equal to the boiling temperature of the electrode material [103]. The approach proposed that the heat source radius could be approximated as a function of time using the expression

$$T_b = \frac{E_0 \cdot R(t)}{k \cdot \sqrt{\pi}} \tan^{-1}\left(\sqrt{\frac{4 \cdot \alpha \cdot t}{R(t)^2}}\right) \qquad (2.8)$$

where T_b represents the boiling temperature of the electrode material and E_0 the energy density.

Using an approach that referenced studies on the plasma radius growth of exploding wires in water [105], it was suggested that $R(t) \propto t^{0.8\pm0.1}$. According to the report, the suggested expression for rate of plasma radius growth provided an energy flux consistent with experimental conditions and related the heat source radius to pulse on time as

$$R(t) = 0.788 \cdot t^{0.75} \qquad (2.9)$$

Expressions of the form similar to (2.9) were also proposed for electro-thermal modelling of anode and cathode erosion in micro-EDM [134]. Yet another approach proposed the estimation of heat source radius based on discharge current characteristics [198].

When a fixed-size heat source is considered, the heat source radius typically used corresponds to that at the final pulse on time [134, 197]. On the other hand, when an expanding circular heat source is considered, the heat source radii at specified time intervals throughout the pulse on time are calculated and used in a superposition scheme [98, 105, 193]. In studies related to the comparison of theoretical models for EDM [205], it has been reported that the circular heat source is preferred for prediction of crater shapes and that the dynamic feature of heat source diameter growth should be considered for more precise simulation of the spark erosion process.

2.2.2.3 Heat flux

The heat flux characteristics considered in the modelling of electrical discharges include the time dependence of heat flux magnitude, fraction of heat flux distribution to the electrodes and dielectric as well as heat flux distribution within the heat source. One of the methods to approximate the characteristics of the heat flux is through a modelling of the plasma channel development during electrical discharge [106, 112]. On the other hand, an empirical method that utilizes measured discharge voltage and current waveforms has also been used to acquire information that is used to characterize the heat flux [104, 105, 134]. The measured discharge voltage and current waveforms are typically used to estimate the power of the discharge, which is related to the magnitude of heat flux from the discharge. In conventional EDM, the average discharge voltage and current values estimated from these waveforms provide an appropriate approximation of the heat flux magnitude and its time dependence. This is because the use of iso-pulse generators produces relatively constant voltage and current values and a relatively longer pulse on time improves approximation of the time-averaged discharge voltage and current values.

However, the discharge voltage and current values under micro-EDM conditions vary with time due to the use of RC pulse generators. Furthermore, the relatively shorter pulse on time may introduce more errors in the time-averaged values. Thus, using time dependent discharge voltage and current values may provide a better approximation of heat flux to the electrode. When considering the magnitude of heat flux, the fraction of heat flux distribution should also be taken into account.

Being an empirically determined constant, the distribution fraction used are varied and have been suggested to be influenced by the dielectric as well as tool electrode to workpiece material combination. Under conventional EDM conditions, it was reported that the fraction of heat going to the cathode and anode were 18 % and 8 %, respectively, with the remainder lost to the dielectric [104, 105]. On the other hand, in a study on energy distribution in the EDM process [206], a distribution of 34 %, 48 % and 18 % to the cathode, anode and dielectric, respectively, was reported. For micro-EDM, a fraction of 14 % and 39 % to the cathode and anode, respectively, was proposed [134]. However, these fractions accounted for the combined effects of fraction of energy distributed to the electrode as well as fraction of molten material expelled from the electrode at the end of discharge. Although the combined fraction addresses the variances between predicted and actual crater volumes, such a consideration does not allow the fraction of energy distributed and fraction of molten material to be studied as separate parameters.

The fraction of molten material expelled at the end of discharge is termed plasma flushing efficiency (PFE) and defined as the ratio of the actual volume of the material removed to the total volume of the theoretically predicted molten pool in the electrode [104]. It was applied to address the variances between the theoretical and actual MRR and TWR values in conventional EDM [105] and varied according to experimental parameters as shown in table 1. Generally, a reduction in discharge current and pulse on time decreases PFE. At the lowest current and pulse on time of 2.34 A and 5.6μs, respectively, a PFE of 15 % and 2 % were reported for the anode and cathode, respectively.

When considering the spatial distribution of heat flux over the heat source area, the simplest heat flux is a uniformly distributed heat flux with constant magnitude [102]. A uniform heat flux with time dependent magnitude has also been adopted [105] although in

the same report it was suggested that a Gaussian-distributed heat flux provided a more accurate approximation. The Gaussian heat flux with constant magnitude during the pulse on time has been used in a finite element based calculation [197].

2.2.2.4 Material properties

The thermo-physical material properties used in the analytical solution of heat conduction models are assumed to be independent of temperature and usually averaged to account for their variations from ambient to melting temperatures [104, 105, 134]. In some cases, an adapted thermal diffusivity (α') is used to account for the melting process [97, 98, 102]. The adapted thermal diffusivity is calculated using the formula

$$\alpha' = \frac{k}{\rho}\left(c + \frac{L_f}{T_m}\right)^{-1} \qquad (2.10)$$

where L_f represents the latent heat of fusion and T_m the melting temperature of the electrode material.

Using the numerical approach to solve the heat conduction model, temperature-dependent material properties may be specified [207]. In addition, the influence of latent heat effects due to melting may also be considered [197].

2.2.2.5 Concluding remarks

The development of process models using the theoretical approach not only provides relations between process parameters and performance measures for process control and performance prediction, it also aids better understanding of the electrical discharge material removal mechanism. The applicability of the electro-thermal material removal mechanism in describing the electrical discharge process leading to material removal and recast layer generation makes it a more appropriate approach for this research. While the single electrical discharge erosion model (SEDEM) offers an adequate representation of crater generation by one electrical discharge, the multiple discharge approach presents a more appropriate description of the material removal characteristics in EDM, which involves repetitive electrical discharges. Based on results of studies conducted, the multiple discharge approach shows potential in extending SEDEMs towards better prediction of performance measures and in estimating discharge properties, such as percentage of energy distribution and plasma flushing efficiency. Thus, further studies on

the multiple discharge approach are needed to fully exploit the potential of this modelling approach.

2.3 Outcome of literature review

The electrical discharge machining (EDM) technique possesses process characteristics that make it suitable for micro-machining. However, the application of micro-EDM has so far been restricted to niche industries. In order to equip the process for greater conformance to fundamental precision machining principles and broaden its scope of application for more diverse range of micro-machining capabilities advancements to the micro-EDM technique, such as in minimisation of machining defects, enhancement of machined surface functional properties, process control and performance prediction, are required. This literature review revealed that the use of powder-mixed dielectrics in EDM (PMD-EDM) can bring about improvements in machined surface quality and imparting of functional properties to machined surfaces. However, the process parameters and conditions employed in these studies do not coincide with those in micro-EDM. Given the sensitiveness of process performance to the process parameters employed and process conditions involved, investigations into representative PMD micro-EDM process parameters and conditions are required. Furthermore, the review of process modelling in EDM and micro-EDM highlighted the shortage of modelling approaches that enable clearer understanding of the multiple discharge material removal mechanism, better prediction of performance measures and formulation of process relations for control and performance prediction.

To address the gaps in PMD micro-EDM, a feasibility study is conducted through single discharge experiment that enables the study of unit removal characteristics. Following which, machining experiments on PMD micro-EDM are conducted to assess the improvements in machined surface quality, which were suggested by results of the single discharge experiment. For process modelling, an investigation on a multiple discharge approach for micro-EDM process modelling and simulation is performed. The multiple discharge approach is demonstrated in the modelling of surface roughness and recast layer thickness in the micro-EDM process. Finally, preliminary investigations into the application of PMD micro-EDM for surface modification are also conducted.

Chapter 3
Experimental Methodology and Characterization Techniques

This chapter first covers the experimental setup for studies on PMD micro-EDM and micro-EDM. Experiments on PMD micro-EDM included the single discharge experiment and machining experiments for surface roughness and recast layer thickness investigations. In addition, micro-EDM experiments were also performed as part of the development of semi-empirical models for micro-EDM. The coverage of experimental setup encompasses experimental test rig, workpiece, tool electrode, dielectric and powder additives used. Next, the methods adopted in the preparation of workpiece samples and powder-mixed dielectrics are presented. Finally, various techniques used in the characterization of crater morphologies, machined surfaces and recast layers are covered. As shown in Figure 3.1, this chapter is divided into four sections comprising details on the experiment setup, preparation methods, characterization techniques and summary.

Chapter 3: Experimental Methodology and Characterization Techniques
3.1 Experiment setup
    3.1.1 Experimental test rig
        3.1.1.1 Single discharge experiment
        3.1.1.2 Surface roughness studies
        3.1.1.3 Recast layer thickness studies
    3.1.2 Workpiece and tool electrode
    3.1.3 Dielectric and powder additive
3.2 Preparation methods
    3.2.1 Workpiece
    3.2.2 Powder-mixed dielectric
3.3 Characterization techniques
    3.3.1 Voltage and current probes with oscilloscope
    3.3.2 Confocal optical profiler
    3.3.3 Optical microscope
3.4 Summary

Figure 3.1 Overview of Chapter 3

3.1 Experimental setup

The experimental setup includes equipment and materials used in the conduct of PMD micro-EDM and micro-EDM experiments. The equipment and materials were chosen based on the experimental objectives.

3.1.1 Experimental test rig

A total of 3 experimental test rigs were used for studies on PMD micro-EDM and micro-EDM. The test rig for PMD micro-EDM single discharge experiment was developed as the commercial micro-EDM system was not equipped with single discharge capabilities. However, the commercial micro-EDM system was used for surface roughness studies in PMD micro-EDM to demonstrate the feasibility of adapting the existing micro-EDM equipment for PMD micro-EDM applications. The third test rig was developed for studies on recast layer thickness in which more independent control of peak discharge current and pulse on time of electrical discharges from the RC pulse generator is needed.

3.1.1.1 Single discharge experiment

The test rig for single discharge experiment allowed different machining parameters to be selected, such as discharge energy and discharge gap distance, so that a variety of single pulse discharges could be generated. It also allowed the positioning of discharge locations so that the positions of discharge craters produced were distinct and ordered. In addition, a data acquisition system was included to capture the electrical parameters of each discharge so that the resulting craters could be analyzed in relation to the machining and discharge parameters used. The circuit diagram of the experimental set up is shown in Figure 3.2.

The single pulse RC discharge circuit comprised a charging loop and a discharging loop. The charging loop consisted of a DC supply set to deliver a voltage of 100 V, resistor labelled R and three capacitors labelled C_1, C_2 and C_3 with capacitance values of 500 pF, 1000 pF and 5000 pF, respectively. The capacitance values were chosen so that with a supply voltage of 100 V, input discharge energies of 2.5μJ, 5μJ and 25μJ, which are within the discharge energy range typically used in micro-EDM applications, could be delivered. The discharging loop consisted of the three capacitors, the tool electrode and workpiece. Switches A, B and C were used to select the appropriate capacitance value,

while switch D was used to toggle between the charging and discharging loop and also served as the trigger for single pulse discharge.

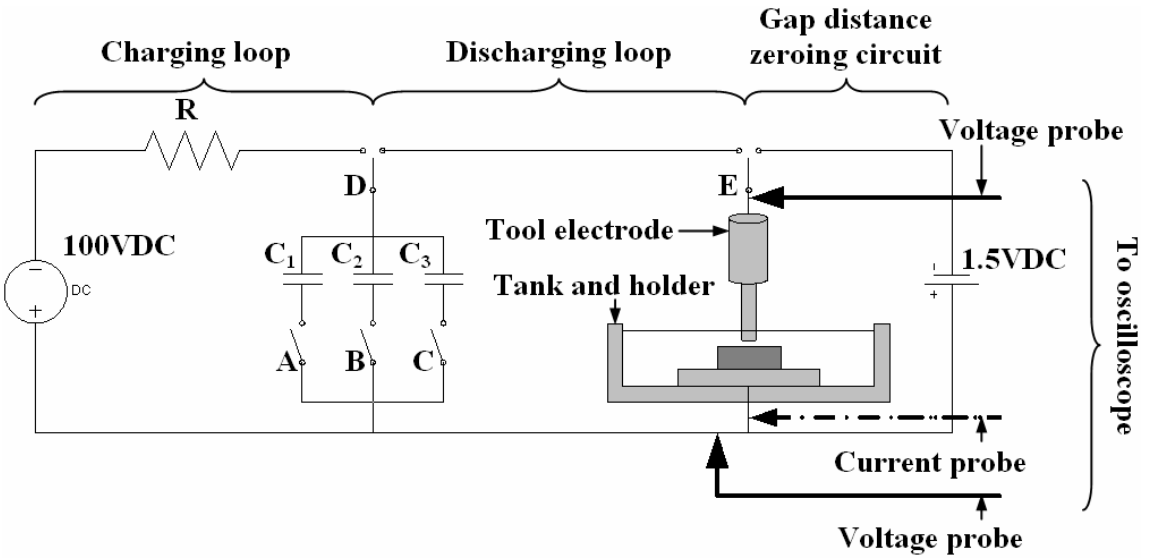

Figure 3.2 Circuit diagram of single discharge experimental test rig

In addition, switch E was used to toggle between the RC discharge circuit and gap distance zeroing circuit. The gap distance zeroing circuit comprised a 1.5 VDC battery source connected to the tool electrode and workpiece. With the gap distance zeroing circuit activated, current would flow through the closed loop once the tool electrode touched the workpiece. The tool electrode position corresponding to the initiation of current flow was set as zero gap distance. The electrode positioning system consisted of a 3-axis linear stage driven by Newport 850G-LS linear actuators via a Newport ESP 6000 motion controller. The electrode positioning system, which has an encoder resolution of 0.008 μm and a cumulative accuracy of < 0.1 % of travel, allowed the location of each discharge to be recorded as well as the appropriate discharge gap to be set. The dielectric tank and workpiece holder ensured that the workpiece was submerged in the dielectric and kept the workpiece in a fixed position. The data acquisition system comprised a Tektronix P5205 differential voltage probe, Tektronix A6302 current probe and Tektronix TDS2022 oscilloscope with sampling frequency of 2 giga-samples per second. The voltage probe was connected across the discharge gap to measure the discharge voltage while the current probe was connected to the wire from the workpiece to measure the discharge current and gap distance zeroing current. All discharge voltage and current waveforms were displayed and recorded on the oscilloscope.

3.1.1.2 Surface roughness studies

The test rig for surface roughness studies was modified from a commercial micro-EDM system, Panasonic MG-E72W, as shown in Figure 3.3.

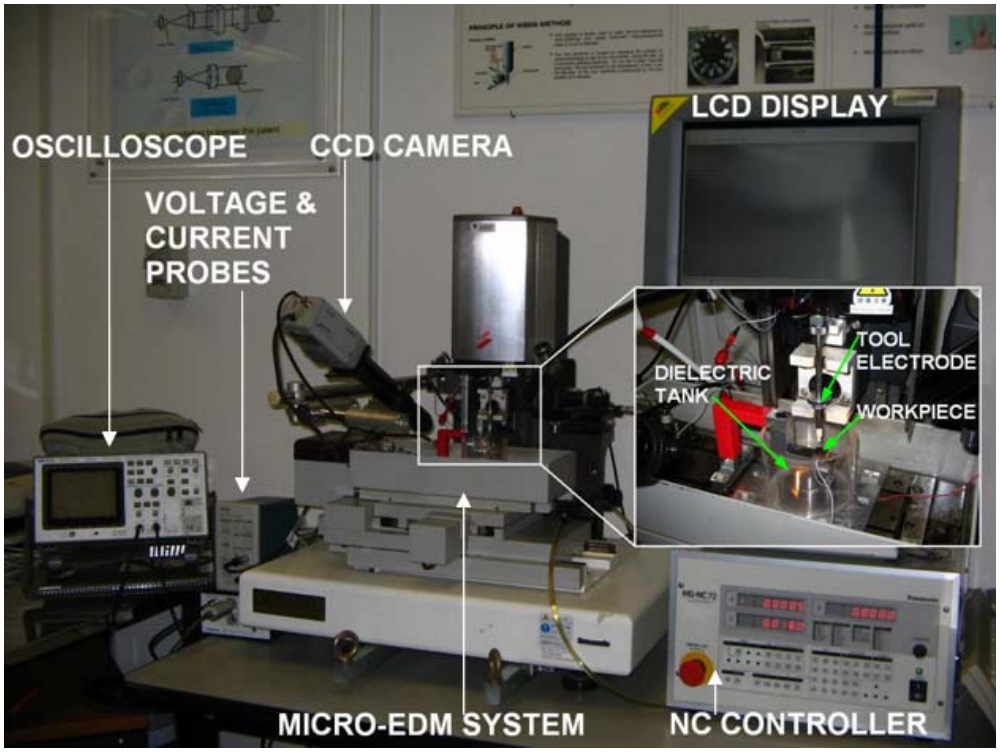

Figure 3.3 Experimental test rig for surface roughness studies

The micro-EDM system was equipped with a RC pulse generator having four capacitance settings of 3300 pF, 220 pF, 100 pF and 10 pF. The open-circuit voltage could be set from 0 V to 110 V. Tool electrode movement comprised vertical translational motion and tool electrode rotation at a fixed speed of 3000 rev/min. The tool electrode rotation is achieved through a spindle system. The spindle system comprised a DC motor that was used to rotate the tool electrode, which was supported on V-shaped ceramic bearings, via a belt drive connection. The horizontal translational motion of the workpiece and vertical translational motion of the tool electrode were manipulated by a numerical control (NC) controller (Model: MG-NC72) that was equipped with a minimum setting unit of 0.1 μm for all axes. The micro-EDM system was also fitted with a WEDG system for tool electrode dressing and a charge-coupled device (CCD) camera with a 5 times magnification lens for inspection of machining zone. In micro-hole drilling, the tool electrode first approached the workpiece in a vertical downward motion, at a traversing speed of 2 μm/s, until the initiation of electrical discharges. At this point, the Z-coordinate of the NC controller would be zeroed so as to register the electrode height as the entrance

of the micro-hole and the electrode was retracted by a distance of at least 30 μm. Next, the electrode was moved vertically downwards at a machining speed of 0.2 μm/s. During the drilling process, the tool electrode was retracted to break any short-circuits between tool electrode and workpiece. The micro-hole drilling process would terminate when the Z-coordinate of the NC controller registered a position equal to the programmed micro-hole depth. To demonstrate that an existing micro-EDM system could be adapted to perform PMD micro-EDM, modifications were made to the micro-EDM system which included a dielectric tank for powder-mixed dielectric and workpiece holder. In addition, the machining process was monitored through the discharge voltage and current waveforms captured using a voltage probe and current probe, and displayed on an oscilloscope.

3.1.1.3 Recast layer thickness studies

The test rig developed for studies on recast layer thickness in PMD micro-EDM allowed the control of peak discharge current, pulse on time and tool electrode rotation speed, which were suggested to be machining parameters that affected recast layer thickness. A modified RC pulse generator was used since a limitation of the RC circuit was a lack of independent control over peak discharge current and pulse on time. As shown in Figure 3.4, the pulse generator design was based on the relaxation-inductance-capacitance (RLC) circuit which included a variable capacitor and variable inductor. On their own, the capacitor determines the input energy for electrical discharge, while the inductor prolongs the pulse on duration with a reduction peak current. Used concurrently, the capacitor and inductor allowed pulse on time to be varied with minimal changes to peak current.

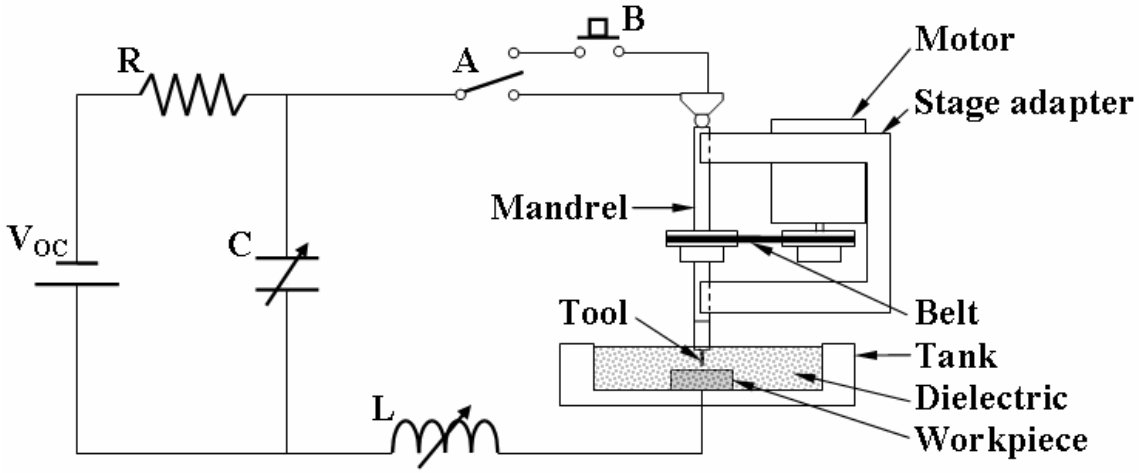

Figure 3.4 Circuit diagram of experimental test rig for recast layer thickness studies

The pulse generator circuit was connected to the tool electrode and workpiece such that the tool electrode was set as the cathode and the workpiece the anode, which is the conventional polarity arrangement in micro-EDM. The rod-shaped tool electrode was housed coaxially in a mandrel that was pulled against V-grooves of a stage adapter by a belt connection. The belt connection linked the mandrel to a variable speed motor, which was also attached to the stage adapter, to enable the rotation of tool electrode about its longitudinal axis. Tool electrode rotation was employed as the primary means of debris flushing during machining since it is a flushing method suitable for micro-EDM. The top of the mandrel was connected to the negative terminal of the pulse generator via a metal ball bearing so as to facilitate electrode rotation. The stage adapter was attached to a linear stage which was driven by a motion controller. The workpiece was directly connected to the positive terminal of the pulse generator and secured in a dielectric tank. The dielectric tank allowed the workpiece to be fully submerged in dielectric during machining. The toggle switch A is used to control the pulse generator for single discharge or multiple discharges, for machining purposes, while the trigger switch B is used to generate single discharges. Under the machining function, the test rig was designed to perform micro-hole drilling using a tool movement strategy similar to that adopted by the Panasonic micro-EDM system.

3.1.2 Workpiece and tool electrode

The workpiece materials used in the experiment were stainless steel AISI 301 and stainless mould steel AISI 420-MOD. Stainless steel AISI 301 was used for the initial studies to ascertain the feasibility of PMD micro-EDM given its ready availability and similarities in thermo-physical and electrical properties to stainless steel AISI 316L, which is commonly used as a tool insert material for moulding purposes. Subsequently, upon establishing the possibility of PMD micro-EDM, stainless mould steel AISI 420-MOD was used for machining experiments since the EDM process is widely used in the mould and die fabrication industry. The chemical compositions of the workpiece materials are shown in Table 3.1, while their thermo-physical properties are shown in Table 3.2. The dimension of AISI 301 workpiece samples used were thin plates measuring 20 mm X 20 mm X 1 mm while the AISI 420-MOD workpiece samples included 10 mm cubes and cuboids measuring 10 mm X 10 mm X 5 mm.

Table 3.1 Chemical composition of stainless steel materials [208, 209]

Workpiece material	Typical chemical composition (%)								
	C	Si	Mn	Cr	Ni	P	S	V	Fe
Stainless steel AISI 301	0.15	1	2	16-18	6-8	0.045	0.03	-	Bal
Mould steel AISI 420-MOD	0.38	0.9	0.5	13.6	-	-	-	0.3	Bal

Table 3.2 Thermo-physical properties of stainless steel materials [208, 209]

Property	Workpiece material	
	Stainless steel AISI 301	Stainless mould steel AISI 420-MOD
Density, ρ (kg/m^3)	8000	7800
Thermal conductivity, k (W/m·K)	21.5 (at 500 °C)	24.0 (at 400 °C)
Specific heat, c (J/kg·K)	500	460
Melting temperature, T_m (K)	1690	1720
Latent heat of fusion, L_f (kJ/kg)	285	-

The tool electrodes used were tungsten wire electrodes with diameters of 125 µm and 300 µm. The diameter 125 µm electrodes were used in the single discharge experiment to facilitate the locating of discharge craters. On the other hand, the diameter 300 µm electrodes were used in machining experiments to facilitate positioning of tool electrode at the mating line. While the tool electrode was not rotated in the single discharge experiment, the tool electrode in the machining experiments was rotated at speeds in the range of 1000 rev/min to 3000 rev/min to facilitate debris removal.

During the experiments, the tool electrode was set as the cathode, while the workpiece was set at the anode since this is the typical polarity configuration used in micro-EDM applications.

3.1.3 Dielectric and powder additive

The dielectric used was a synthetic electric spark oil from Idemitsu called Daphne® Cut HL-25. Two types of powder additive material (from Sigma-Aldrich, Singapore) were

used, namely, silicon carbide (SiC) and aluminium oxide (Al_2O_3). SiC was chosen for PMD micro-EDM due to its semi-conductive nature, which was reported to produce a smaller enlargement of discharge gap distance compared to conductive powder materials [163]. Similarly, Al_2O_3 was chosen due to its non-conductive nature that was suggested to improve surface finish without affecting gap distance [165]. The concern with an excessive enlargement of gap distance in PMD micro-EDM is the loss in geometrical accuracy due to the lack of compensation techniques available. The powder additives were made up of nano-powder additives with granularity of 40 nm ~ 47 nm and 45 nm ~ 55 nm for Al_2O_3 and SiC, respectively, as indicated in the manufacturer's material datasheet. Some selected properties of Al_2O_3 and SiC material are shown in Table 3.3.

Table 3.3 Properties of nano-powder additive materials

Property	Nano-powder additive material	
	Al_2O_3	SiC
Granularity (nm)	40 – 47	45 – 55
Density, ρ (kg/m^3)	3900	3100
Electrical conductivity, σ (S/m)	1×10^{-12}	1×10^{-4}
Specific heat, c (J/kg·K)	880	670

The use of nano-powder additives was intended to facilitate the entry of powder additives into the discharge gap, which measures a few microns in distance due to the use of small discharge energies. Various concentrations of powder additives were added to the dielectric, depending on the requirements of the experiment. Generally, the powder concentration was kept low to minimise the tendency of powder agglomeration and to ensure a homogeneous suspension during machining.

3.2 Preparation methods

Prior to the conduct of experiments, the workpiece samples and powder-mixed dielectrics had to be prepared. Furthermore, the characterization of certain features also required workpiece samples to be prepared before measurements could be conducted.

3.2.1 Workpiece

In the single discharge experiment, workpiece surfaces onto which electrical discharges would be subjected were pre-polished to achieve a mirror finish so that the effects from surface irregularities were minimized. The flat surface also allowed a reference plane,

from which measurements could be made, to be defined. In machining experiments for surface roughness and recast layer thickness investigations, the workpiece was formed by joining and holding two workpieces together in a way similar to the wringing of gauge blocks and described as wrung workpieces, as shown in Figure 3.5. Then by machining at predefined locations along the mating line, the cross-section of micro-holes could be revealed by exposing the mating faces of the wrung workpieces. The exposed cross-sections allowed machined surface roughness and recast layer thickness to be measured. After being wrung together, the top surfaces of both workpieces were also lapped to ensure that the surface to be machined was levelled and to remove crevices caused by rounded workpiece edges along the mating line.

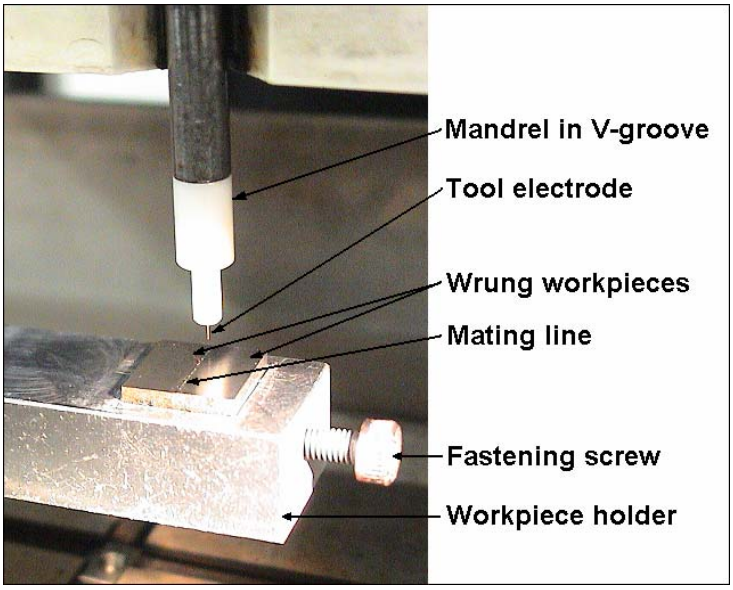

Figure 3.5 Arrangement of workpiece in machining experiments

Prior to characterization, the workpiece samples were cleaned in an ultrasonic bath. Furthermore, to measure the recast layer thickness of machined surfaces, the mating face of a workpiece sample was polished to a mirror-finish and subsequently etched to reveal the recast layer. Based on the recommended etching time of a few seconds to 15 minutes, the surface was etched for 10 seconds. The chemical composition of the etchant, called Vilella's reagent [210], is shown in Table 3.4. Vilella's reagent is one of the etchants suitable for revealing the general structure of stainless steels with grades in the AISI 300 series and AISI 400 series.

Table 3.4 Chemical composition of Vilella's reagent

Component	Quantity
Picric acid	1 g
Hydrochloric acid	5 ml
Ethanol (95 %)	100 ml

3.2.2 Powder-mixed dielectric

In the preparation of powder-mixed dielectric, the required amounts of powder additive and dielectric were measured separately before being mixed together and homogenised in an ultrasonic bath. A digital balance with resolution of 0.01 g was used to measure the required amounts of powder additive while a measuring flask with resolution of 1ml was used to measure the required amounts of dielectric. The use of ultrasonic agitation was reported to be an effective means of promoting de-agglomeration and achieving a uniform dispersion of powder additives in the preparation of nano-fluids [211]. Typically, a single batch of dielectric with required powder concentration was prepared and used throughout the experiment.

3.3 Characterization techniques

Characterization techniques refer to the methods by which features of interest are measured and/or inspected so that these features can be subsequently described in a quantitative or qualitative manner. Quantitative results are quantifiable measurements made with respect to a known scale of measurement, while qualitative results are more descriptive and pictorial by nature. The main purpose of conducting characterization is to allow features of interest to be compared so that variations and similarities between features can be revealed. This section covers various characterization techniques as well as methods of determining experimental performance measure values related to the research.

3.3.1 Voltage and current probes with oscilloscope

The voltage and current probes were used to capture the voltage and current variations during the duration of an electrical discharge. The acquired data were then displayed quantitatively on the oscilloscope. The electrical discharge data acquisition system comprised a Tektronix P5205 voltage probe, Tektronix A6302 current probe and a Tektronix TDS2022 oscilloscope with a sampling frequency of 2 giga-samples per second.

The high sampling frequency ensured that issues related to aliasing were minimized, especially when discharge durations were in the sub-microsecond range. The discharge voltage and current waveforms captured using the voltage and current probes and displayed on the oscilloscope allowed machining parameters such as breakdown voltage, average discharge voltage, peak discharge current, average discharge current and pulse on time to be known. A typical voltage and current waveform is illustrated in Figure 3.6, which also shows some of the useful information that could be extracted from the plots.

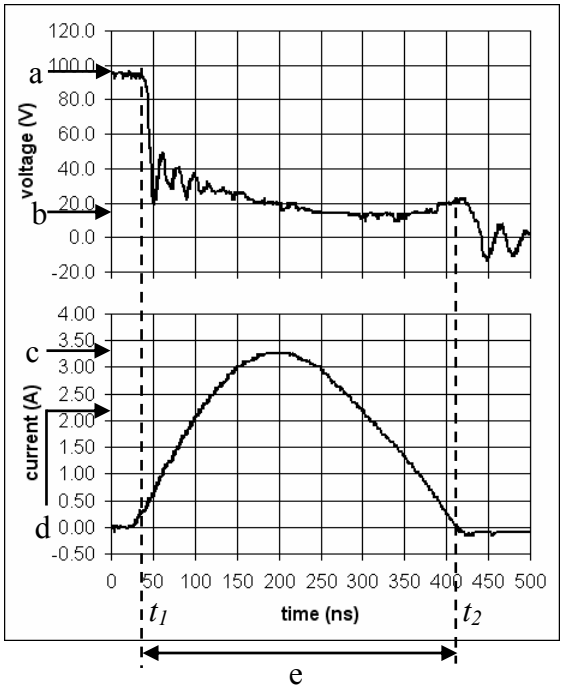

Legend:

a: Breakdown voltage

b: Average discharge voltage

c: Peak discharge current

d: Average discharge current

e: Pulse on time ($t_{on} = t_2 - t_1$)

Figure 3.6 Typical voltage and current waveforms

The breakdown voltage refers to the voltage measured across the discharge gap just before dielectric breakdown. The breakdown voltage is either equal to or smaller than the open circuit voltage (V_{OC}). The values of average discharge voltage and current are calculated by time averaging the total discharge voltage and current over the pulse on time using the following equations respectively:

$$V_{av} = \frac{1}{t_2 - t_1} \int_{t_1}^{t_2} V(t)dt \qquad (3.1)$$

$$I_{av} = \frac{1}{t_2 - t_1} \int_{t_1}^{t_2} I(t)dt \qquad (3.2)$$

where V_{av} represents the average discharge voltage, I_{av} the average discharge current, $V(t)$ the measured voltage as a function of time, $I(t)$ the measured current as a function of time, t_1 the start of pulse on time and t_2 the end of pulse on time.

In addition, the input discharge energy and measured discharge energy can be calculated using equations (3.3) and (3.4), respectively:

$$E_{in} = \frac{1}{2} \cdot C \cdot V_{OC}^2 \tag{3.3}$$

$$E_m = \int_{t_1}^{t_2} V(t) I(t) dt \tag{3.4}$$

where E_{in} represents the input discharge energy, E_m the measured discharge energy, C the selected capacitance and V_{OC} the open circuit voltage.

The measured discharge energy is typically calculated from the measured discharge voltage and current waveforms using equation (3.4) in the discretized form and expressed as:

$$E_m = \sum_{i=1}^{n} V_i \cdot I_i \cdot \Delta t \tag{3.5}$$

where

$$\Delta t = \frac{t_2 - t_1}{n} \tag{3.6}$$

and V_i represents the discretized discharge voltage at the i^{th} time step, I_i the discretized discharge current at the i^{th} time step and n the total number of time steps.

3.3.2 Confocal optical profiler

The confocal optical profiler is used in surface metrology applications for profile and topographical measurements as well as non-destructive 3D geometrical measurements of micro features. To measure a feature, light emitted from a point source is imaged into the object focal plane of the microscope objective. The reflected light is then detected by a photodiode located behind a pinhole. The pinhole is used to eliminate out of focus light that are reflected from beyond the range of the focal plane so that only shape images within the focal plane are captured. The individual images captured as the focal plane is moved vertically along the height of the feature are then reconstructed to form a complete feature measurement. The complete measurement can then be analyzed using tools from the associated software. The smallest measurement resolution of the profiler is dictated by the maximum objective lens available of which the 100X lens provides a spatial sampling distance of 0.18 μm and a minimum step height of 0.2 μm for vertical scanning.

The measurements taken from the confocal optical profiler were used to extract information on crater geometry in the single discharge experiment as well as surface roughness in the machining experiment. Figure 3.7(a) to (c) illustrate the various crater geometries that were measured for the single discharge experiment.

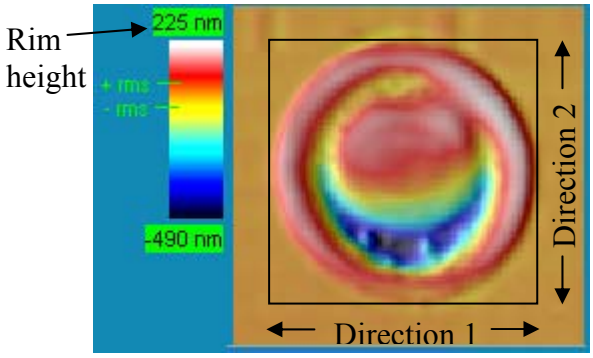

(a) Crater outer diameter and rim height

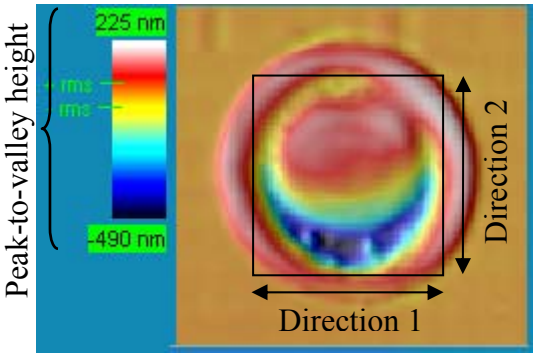

(b) Crater inner diameter and peak-to-valley height

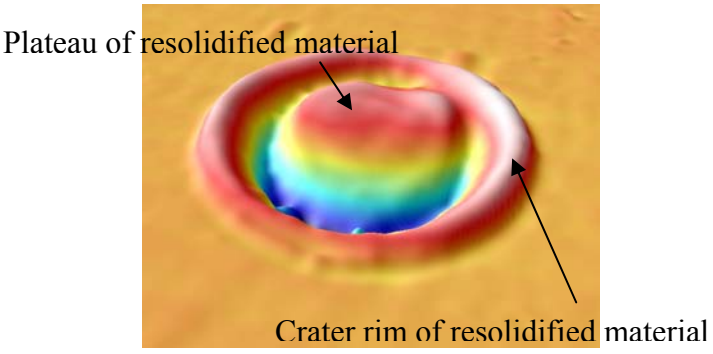

(c) Isometric perspective

Figure 3.7 Single crater geometries

To determine the crater outer and inner diameters measurements in orthogonal directions, labelled Direction 1 and Direction 2, were first taken. Then, the average crater diameter was calculated using the following equation:

$$\phi_{av} = \frac{\phi_1 + \phi_2}{2} \tag{3.7}$$

where ϕ_{av} represents the average crater diameter, ϕ_1 the diameter measured in Direction 1 and ϕ_2 the diameter measured in Direction 2. Using the height scale generated in the measurement, the crater rim height was taken as the highest measured point while the peak-to-valley height was taken as the difference between the highest and lowest measured points.

The confocal optical profiler was also used to determine the surface roughness of machined micro-holes. Figure 3.8 shows an image of the side wall of the machined micro-hole as measured by the optical profiler.

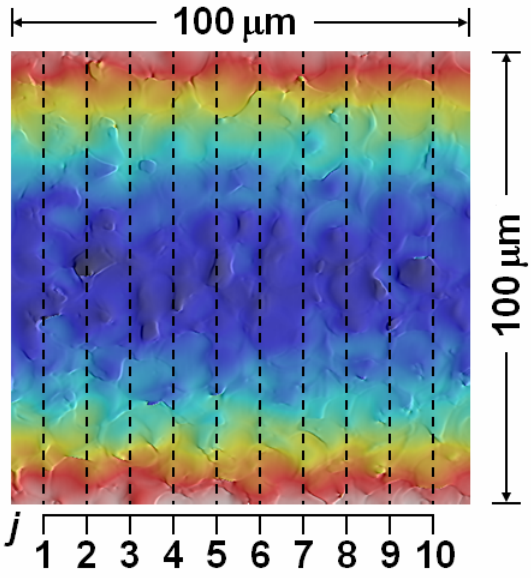

Figure 3.8 Surface roughness

The various coloured-bands represent different heights on the surface, thus revealing the side wall curvature and surface topography. The side wall curvature measurements were filtered from the surface profile measurement through software compensation using pre-measured side wall curvature values. As a result, the surface roughness measurements could be obtained. To determine the surface roughness of the machined surface, a sample area measuring 100 µm by 100 µm was captured. Next, a total of 10 surface roughness readings, using a cut-off value of 0.08 mm, were extracted from predetermined locations

within the sample area, represented by the index *j*. The 10 readings were then averaged to give a representative surface roughness. The typical surface roughness parameters that can be displayed include arithmetical mean surface roughness (*Ra*), maximum peak to valley surface roughness (R_{max}) and root mean square roughness (*Rq*).

3.3.3 Optical microscope and image processor

The optical microscope is used for both qualitative and quantitative assessment of machined features. While images captured by the optical microscope allow qualitative inspection of machined features, quantitative measurements are enabled through the use of image processing software. The assessment of recast layer thickness at the machined surfaces of micro-holes was conducted using the optical microscope. This is because the recast layer is known to be more resistant to etching than the base material and will thus appear as a white layer under the optical microscope due to its more reflective surface.

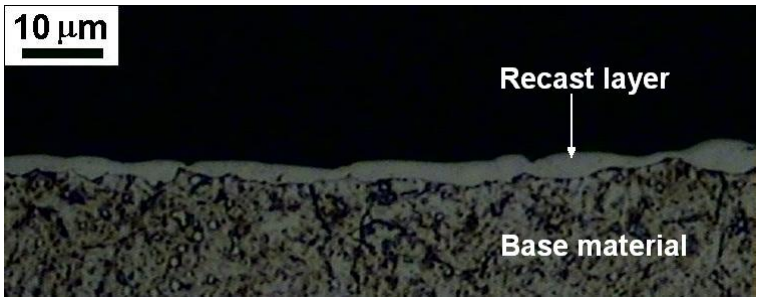

(a) Image from optical microscope

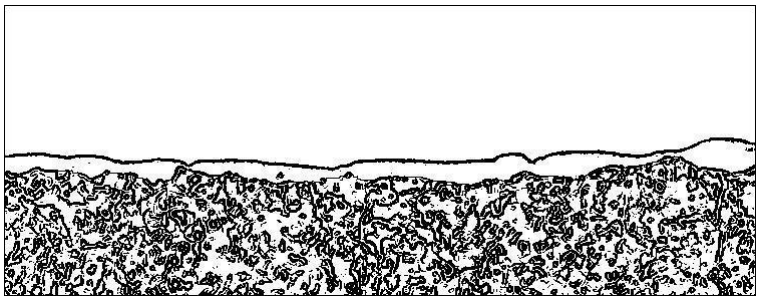

(b) Processed image

Figure 3.9 Images of recast layer

Figure 3.9(a) shows an image of a typical recast layer captured using the optical microscope, while Figure 3.9(b) shows a processed image with the recast layer outline. The image processor used to process images from the optical microscope was ImageJ, a public domain Java image processing and analysis program originally developed for use by the National Institutes of Health, USA. The ImageJ functions that were used included conversion to binary image, edge detection as well as length and area calculation. In the

conversion to binary image function, the threshold level to create the binary image is based on the IsoData method [212]. The edge detection function uses a Sobel edge detector to highlight sharp changes in intensity based on the gradient of the image intensity. The measurements of length and area are based on pixel counting of which each pixel in the image captured from the optical microscope with a magnification objective of 50X was 125 nm by 125 nm. As the outcome of these functions is influenced by image sharpness and contrast, a constant set of image capturing and processing parameters was consistently used for characterization. In this way, the tendency for random measurement errors may be minimised.

The recast layer thickness is estimated by measuring the area of the recast layer, discretizing the area by vertical elemental strips and applying the following equation:

$$h_{av} = \frac{A_{recast}}{\Delta x \cdot m} \tag{3.8}$$

where h_{av} represents the average thickness of the recast layer, A_{recast} the measured area of the recast layer, Δx the width of a vertical element strip measuring 125nm and m the total number of elemental strips spanning the recast layer. The average recast layer thickness as determined gives a closer estimate of recast layer thickness for each micro-hole. In this way, the average recast layer thickness may be used to study the variations in recast layer thickness across different micro-holes so that a more representative comparison of the effects of machining conditions on recast layer thickness may be done.

3.4 Summary

The experimental setups used for the single discharge and machining experiments are presented. In addition, workpiece sample and powder-mixed dielectric preparation methods were covered. Furthermore, the characterization equipment and techniques are explained. The following chapters cover the results and discussion of single discharge and machining experiments as well as numerical modelling and simulation conducted.

Chapter 4
Investigation on Material Removal by Single Electrical Discharge

This chapter covers results of the single discharge experiment conducted to investigate the unit removal characteristics of electrical discharges occurring in a powder-mixed dielectric. The electrical discharges are generated with input energies typically employed in micro-EDM, while the dielectric is mixed with nano-powder additives of silicon carbide material to suit the machining conditions in micro-EDM. In this chapter advantages of the single discharge experiment are explained, followed by a description of the experimental method. Then, a comparison of crater morphology, geometry and discharge waveforms due to the use of powder-free and powder-mixed dielectrics is presented. Furthermore, the factors affecting crater formation as well as mechanisms of crater formation in powder-mixed dielectric are proposed. An overview of the chapter is shown in Figure 4.1.

Figure 4.1 Overview of Chapter 4

4.1 Single discharge experiment

To understand the effects of employing a powder-mixed dielectric for micro-EDM, it is meaningful to investigate the unit removal characteristics of the process under representative machining conditions. The term unit removal or machining unit refers to the minimum controllable amount of material that can be removed with high repeatability. A small unit removal is necessary for improving machining precision, and in EDM the unit removal is a crater produced by one discharge pulse. Apart from representative machining conditions, it is useful to provide an experimental environment in which effects caused by the machining parameters under study can be singled out. The single

discharge experiment is conducted to produce non-overlapping craters on the workpiece surface and to allow the association of individual craters to the electrical discharges that created them. In this way, each recorded discharge voltage and current waveform may be related to the resulting crater morphology and geometry. By producing single craters on a smooth surface, the crater diameter may be easily identified and crater rim height may be measured from a defined reference plane. As a result, the crater diameter may be more accurately measured and the crater morphology more easily observed since the shape of a solitary crater is more clearly defined compared to multiple overlapping craters. In relation to the study of powder-mixed dielectrics, the single discharge experiment also provides a controlled machining environment in which the influence of powder additives may be singled out without other machining influences such as localized asperities on workpiece surface, air bubbles and machined debris. This will enable the effects of using powder additives to be more discernable so that findings may help elucidate the mechanism of crater formation and be used as a foundation for extension to sequential discharges as characterized in actual powder-mixed dielectric micro-EDM processes. Thus, the single discharge experiment was employed.

4.2 Experimental method

The single discharge experiment was performed using input energy settings of 2.5 μJ, 5 μJ and 25 μJ with the aim of studying the effects of nano-powder additives on resulting crater size and morphology that were produced with a range of input discharge energies typically employed in micro-EDM. In order to study the relationships between specific input parameters and outputs in the PMD micro-EDM process, a parametric investigation incorporating an analysis of variance (ANOVA) study was conducted. Of the complete set of experimental parameters used in the single discharge experiment, as shown in Table 4.1, the specific input parameters for parametric investigation were input energy and dielectric condition. As shown in Table 4.2, three input energies were used and the dielectric condition was categorised as powder-free and powder-mixed. Using the combination of input parameters shown in Table 4.3, 6 experimental runs comprising 30 replicates each were conducted under randomised conditions and outputs of crater geometry and discharge waveform were recorded.

Table 4.1 Experimental parameters for single discharge experiment

Parameter	Value
Open circuit voltage, V_{OC} (V)	100
Capacitance, C (pF)	500; 1000; 5000
Input energy, E_{in} (μJ)	2.5; 5; 25
Discharge gap distance, h_d (μm)	2.5
Workpiece material	Stainless steel, AISI 301
Tool electrode material	Tungsten
Tool electrode diameter (μm)	125
Dielectric	Idemitsu Daphne Cut HL-25
Powder material	Silicon carbide, SiC
Powder size (nm)	45 ~ 55
Powder concentration (g/l)	0; 0.02

Table 4.2 Input parameters for parametric investigation

Input parameter	Condition
Input energy, E_{in} (μJ)	2.5; 5; 25
Dielectric condition	Powder-free (0 g/l); Powder-mixed (0.02 g/l)

Table 4.3 Input parameters for each experimental run

Run	Additive	Capacitance (pF)	Input energy (μJ)
1	No	500	2.5
2	No	1000	5
3	No	5000	25
4	Yes	500	2.5
5	Yes	1000	5
6	Yes	5000	25

Prior to the start of the experiment, a single batch of powder-mixed dielectric was prepared and used for all 6 experimental runs. For each run, the appropriate capacitor was selected based on the required input discharge energy. To create a discharge crater, the gap distance zeroing circuit was activated and the tool electrode was lowered until a

contact with the workpiece was established. Next, the gap distance zeroing circuit was toggled to the RC discharge circuit and the tool electrode was raised by 2.5 μm. Then the powder-mixed dielectric was agitated to ensure a consistent suspension of powder additives before triggering a single electrical discharge between the tool electrode and workpiece. The discharge voltage and current waveforms were captured by the probes and recorded on the oscilloscope to verify the occurrence of a successful electrical discharge. The tool electrode was then moved to a new discharge location and the process repeated.

4.3 Results and discussion

The morphology and geometry of the resulting craters are compiled and compared qualitatively and quantitatively. In addition, observations on discharge current waveforms are discussed. The experimental results are also compared with those from existing literature and discussed.

4.3.1 Crater morphology

The morphology of craters produced in a given dielectric condition showed large similarities regardless of input energies. However, there were distinct differences in crater morphology between craters produced in powder-free and powder-mixed dielectrics. With reference to Figure 4.2, which shows SEM images of craters produced from the six discharge conditions, the obvious difference in morphology of these two types of craters lay in the form taken by the resolidified material. As shown in Figure 4.2(a) to (c), all the craters produced in powder-free dielectric have crater rims defined by a build up of resolidified material and the crater cavities with a depressed centre. This crater morphology may be created by superheating of molten material within the crater due to the high pressure of the plasma channel [103]. At the same time, the overpressure of the gas bubble enveloping the plasma channel may cause molten material to flow away from the interior of the melt pool and lead to the formation of crater rims. Then, upon the collapse of the plasma channel, the molten material within the melt pool is expelled due to the sudden drop in pressure and implosion of the gas bubble. Furthermore, the molten material at the crater rim may also experience the imploding force and cause the crater rim to have uneven edges. On the other hand the craters produced in powder-mixed dielectric, as illustrated in Figure 4.2(d) to (f), showed the presence of regularly-shaped crater rims defined by a build up of resolidified material and the occurrence of crater

cavities with plateaus of resolidified material within the boundaries of the crater rims. Thus, the characteristics of the recast region for both types of crater were distinctly different.

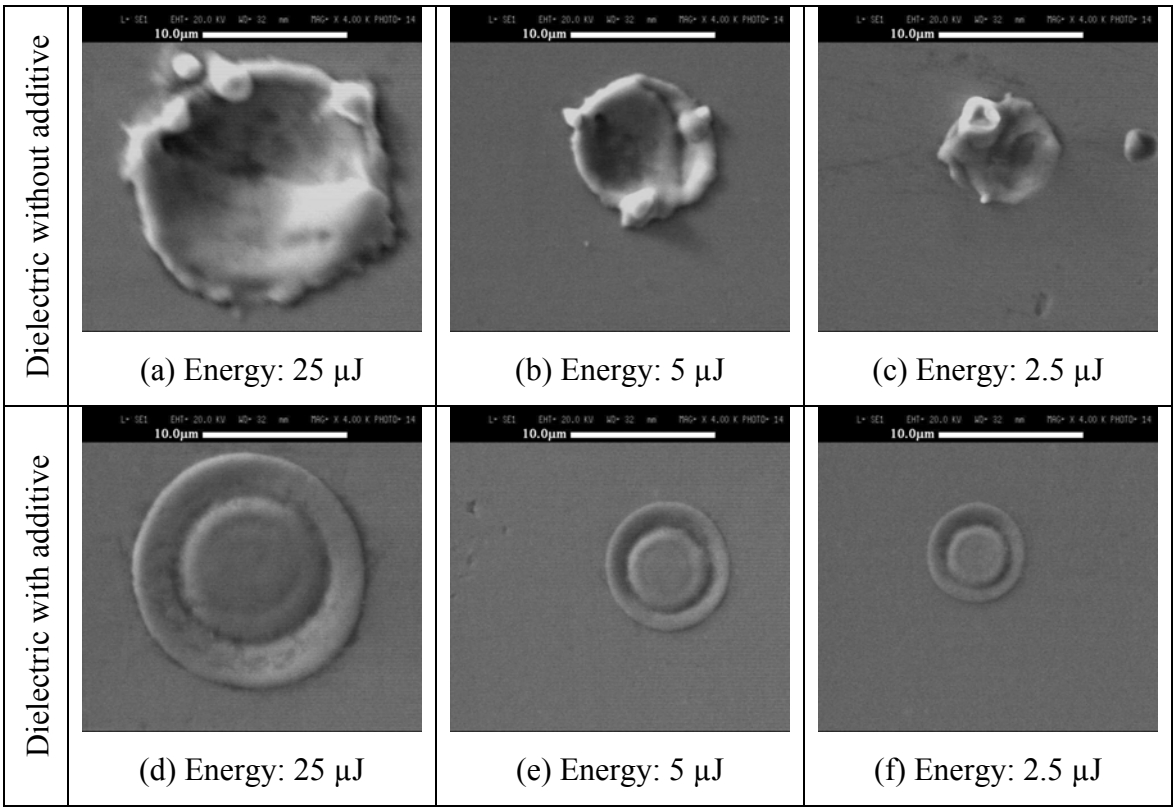

Figure 4.2 Morphology of craters produced in different dielectrics and at various input energies

The observation of craters with plateaus of resolidified material generated in a powder-mixed dielectric at discharge energies between 2.5 µJ and 25 µJ is a first for PMD micro-EDM. In a study on PMD-EDM [29], similar crater morphologies had been observed and the plateau were proposed as being formed by resolidified material after an examination of the crater cross-section. Moreover, it was suggested that formation of the centre resolidified material build up was due to a reduction in impact forces acting on the workpiece due to an enlargement in discharge gap. However, given that a constant discharge gap distance of 2.5 µm was maintained during the single discharge experiment, it may be possible that the increase in discharge gap is not the only factor responsible for lowering the molten material expulsion forces. In the absence of an enlargement in discharge gap, this crater morphology may suggest that the magnitude of pressure build-up by the plasma channel is lower in a powder-mixed dielectric than in a powder-free dielectric. Therefore, at the collapse of the plasma channel, forces from gas bubble implosion are not great enough to expel the molten material within the melt pool. As a

result, upon the collapse of the plasma channel molten material from the crater rim flow back into the crater cavity and solidify to form a plateau of resolidified material, while the remaining molten material at the crater rim solidify with even edges. The reduced overpressure from the plasma channel may be due to factors such as a lower amount of discharge energy available for the development of the plasma channel and a larger plasma channel expansion.

4.3.2 Crater geometry

The geometry of craters produced in both dielectric conditions showed a similar trend when input energy was varied at 2.5 μJ, 5 μJ and 25 μJ. Based on a qualitative assessment of the SEM images, the crater diameters were smaller when generated using lower input energies. To conduct a quantitative comparison on the geometry of the two types of craters, differentiated by the difference in dielectric conditions, the crater outer and inner diameters, crater rim height and crater peak-to-valley height were considered. The experimental data are shown in Appendix A.

A single-factor ANOVA study was conducted on the statistical significance of changes in average crater outer diameter, average crater inner diameter, crater rim height and crater peak-to-valley height due to the presence of powder additives in a dielectric. Results of the ANOVA study are tabulated in Appendix A of which Figure 4.3 gives a graphical illustration.

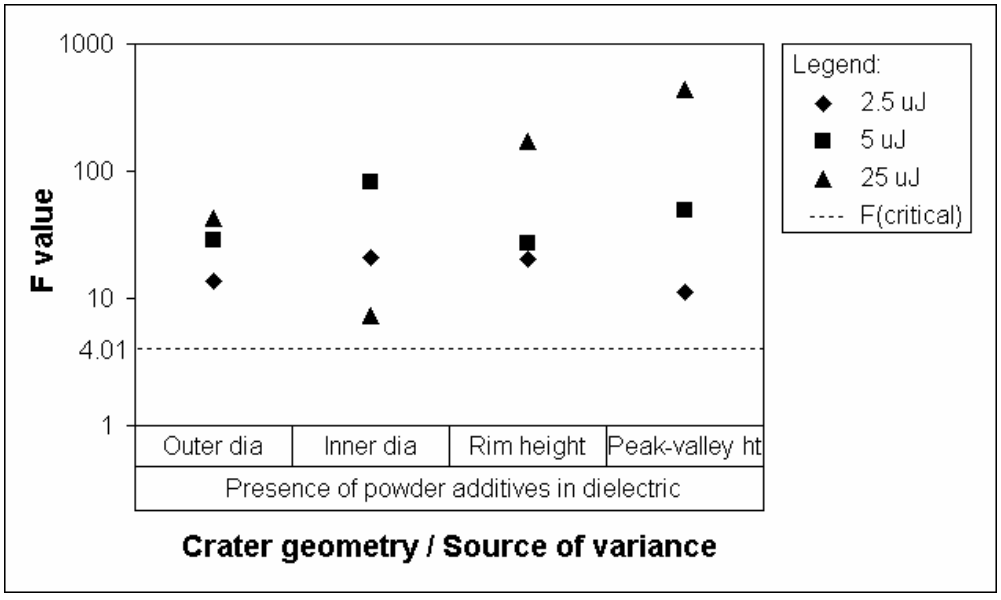

Figure 4.3 Results of ANOVA study for crater geometry

The ANOVA study assumes that the experimental data follows a theoretical F-distribution so that a test ratio for each source of variation can be determined and expressed as an F-value. The F-value is then compared with a control limit value F(critical) specified for type I error probability (α_{error} = 0.05). The source of variation is considered statistically significant when its F-value is greater than F(critical), while an F-value smaller than F(critical) implies an absence of statistically significant variance for the corresponding source of variation. It is evident that there was a statistically significant variation in crater geometries due to the use of a powder-mixed dielectric.

By comparing the crater outer diameters, an assessment of the final crater size may be done. While the ANOVA results in Figure 4.3 show that the difference in crater outer diameters of the two types of craters was statistically significant, Figure 4.4 show that the craters produced in powder-mixed dielectric were notably smaller in size than those produced in powder-free dielectric. The results, indicating the minimum, maximum and average values of 30 replicates at each machining condition, quantitatively show the increase in crater diameter as input energy was increased from 2.5 µJ, 5 µJ and 25 µJ. Furthermore, the deviations in average crater diameters were generally smaller for craters produced in powder-mixed dielectric compared to those produced in powder-free dielectric. This may suggest that a smaller and more repeatable unit removal is brought about by the introduction of powder additives into the dielectric.

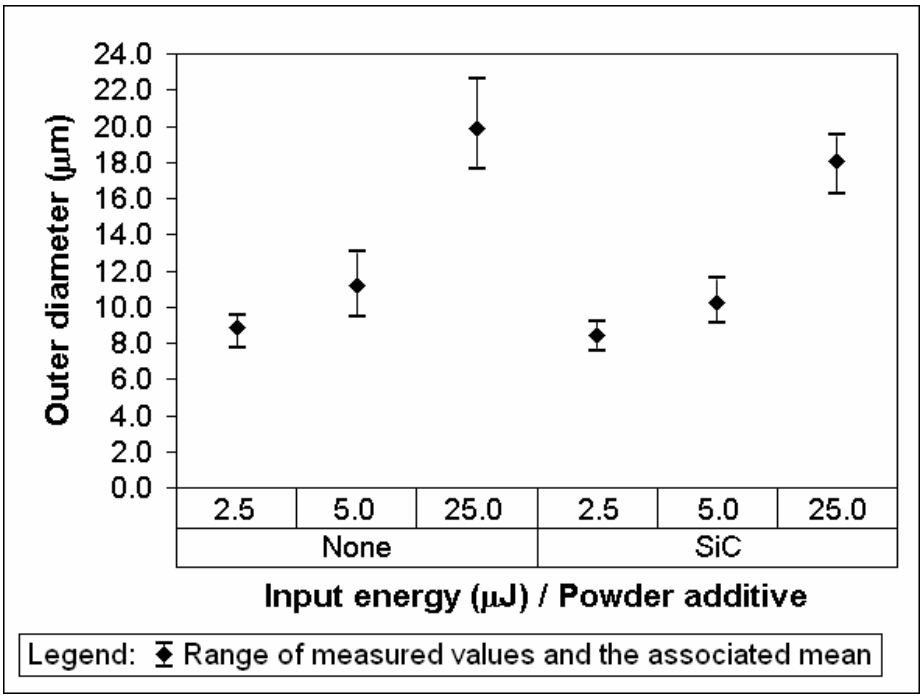

Figure 4.4 Average outer crater diameters for various machining conditions

Another property of the crater diameter was that it has been equated to the plasma channel diameter [204]. Thus the inner crater diameter was also compared since it may represent the boundary at which molten material within the melt pool is being pushed by the overpressure in the gas bubble and hence be indicative of the plasma channel size. Figure 4.5 shows the inner crater diameters of the two types of craters produced at input energies of 2.5 µJ, 5 µJ and 25 µJ.

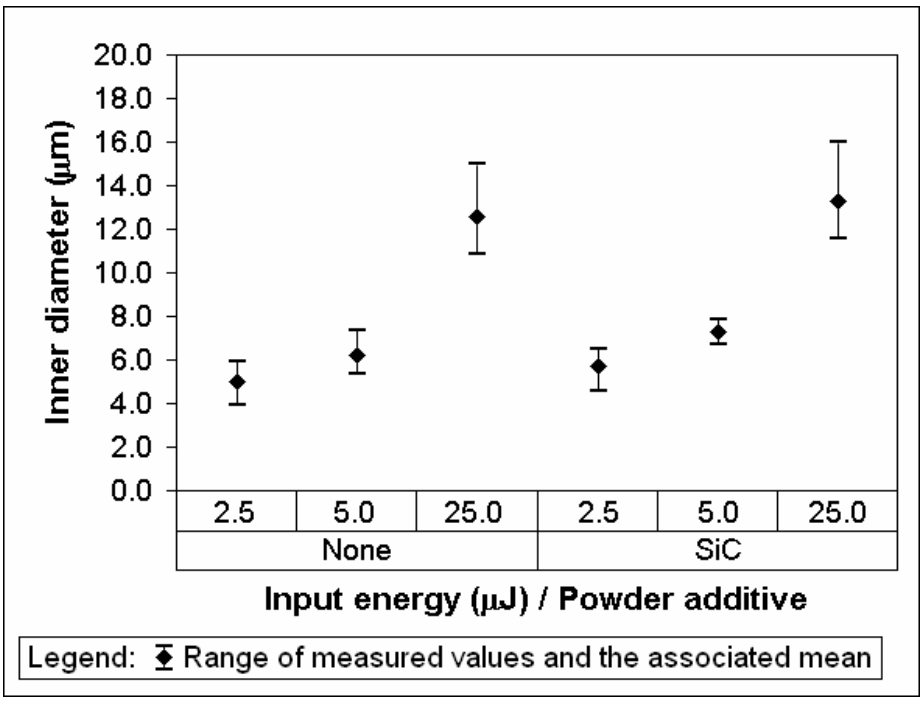

Figure 4.5 Average inner crater diameters for various machining conditions

The measurements of inner crater diameters showed that craters produced in powder-mixed dielectric had a larger inner diameter than craters produced in powder-free dielectric. However, measurements of outer crater diameters showed that craters produced in powder-mixed dielectric had a smaller outer diameter than those in powder-free dielectric. This may be caused by a reduction in discharge intensity of the larger plasma channel [156], which generates a smaller amount of molten material and causes the molten material to flow a shorter distance away from the interior of the melt pool. The presence of a larger inner diameter in powder-mixed dielectric was consistent with suggestions that powder additives caused a larger plasma channel expansion [156] and that the longer carrier movement routes brought about by the presence of powder additives created wider plasma channels [133]. Therefore, these results may suggest that

the use of nano-powder additives with input energies in the micro-EDM regime are also able to effect changes in the nature of plasma channel expansion.

To compare the rate of plasma channel expansion under the two dielectric conditions, regression lines were plotted through data points of inner crater radius versus pulse on time as shown in Figure 4.6. Power functions were used to describe the regression lines, as suggested by earlier studies [105, 134].

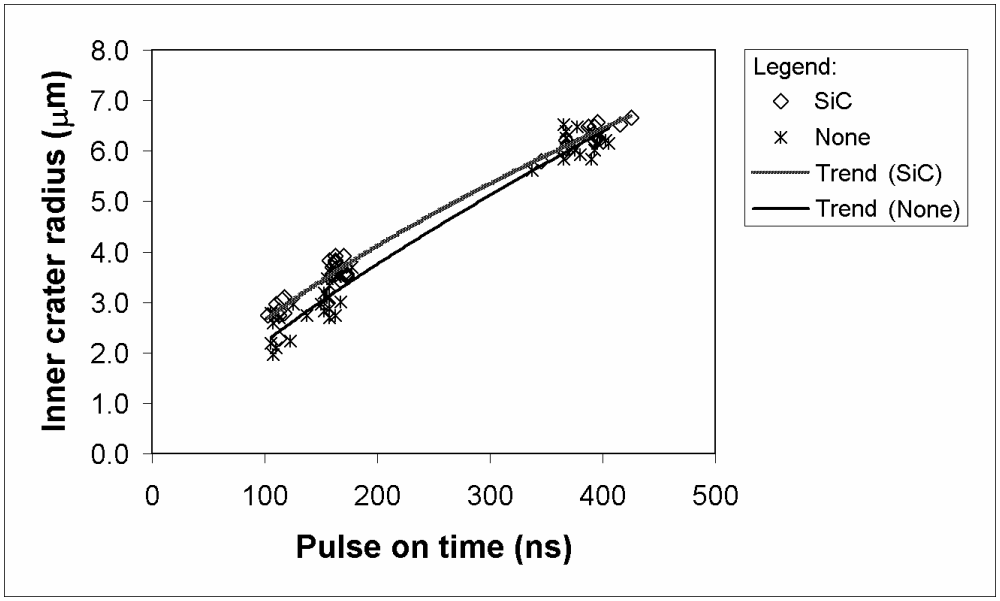

Figure 4.6 Rate of plasma channel expansion in power-mixed and powder-free dielectrics

The trend lines showed that the plasma channel in the powder-mixed dielectric was larger than that in the powder-free dielectric. Furthermore, the difference was more pronounced at shorter pulse on time durations, which was also highlighted by the ANOVA results in Figure 4.3. Also, while the rate of plasma channel expansion at shorter pulse on time durations was relatively similar in both dielectric conditions, at longer pulse on time durations the rate of expansion was relatively slower in the powder-mixed dielectric. Based on the trend lines the respective power functions for plasma channel expansion in powder-free dielectric and powder-mixed dielectric are

$$R_p(t) = 0.059 \cdot t^{0.79} \tag{4.1}$$

$$R_p(t) = 0.135 \cdot t^{0.65} \tag{4.2}$$

where $R_p(t)$ represents the time dependent plasma channel radius measured in micrometers and t the time measured in nanoseconds. The R^2 coefficient of determination for equations (4.1) and (4.2) are 0.953 and 0.971, respectively.

The height of crater rim was compared as it may be indicative of the intensity of gas bubble implosion since the amount of molten material pushed out of the melt pool by the gas bubble and the amount of molten material flowing back into the crater cavity at the end of discharge would change the crater rim height. Figure 4.7 shows the crater rim heights of the two types of craters produced at input energies of 2.5 μJ, 5 μJ and 25 μJ.

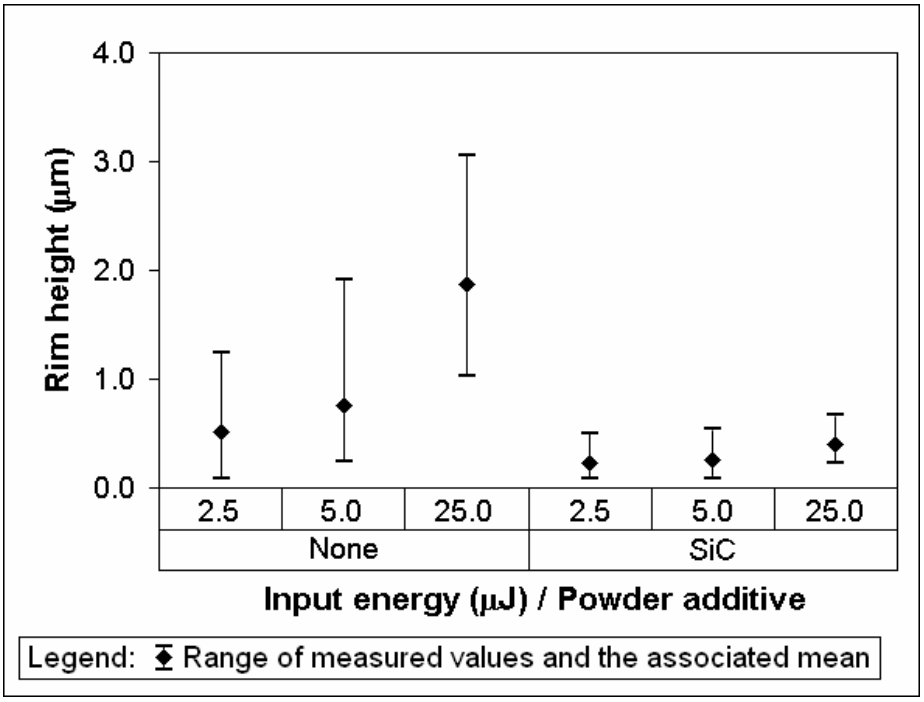

Figure 4.7 Crater rim heights for various machining conditions

The results showed that as input energy was increased, crater rim height also increased. This may suggest that with more molten material produced at a higher input energy, more molten material is pushed out of the melt pool thereby forming a taller crater rim. On the other hand, the crater rim heights of craters produced in powder-mixed dielectric were smaller than those produced in powder-free dielectric. This may suggest that a lesser amount of molten material is produced in a powder-free dielectric or that more molten material has flowed back into the crater cavity at the end of discharge in a powder-free dielectric or a combination of both factors. The depth of melt pool and flow of molten material around the crater may affect the recast layer thickness, which in turn influences the machined surface quality. In addition, the deviation in crater rim height was smaller for craters produced in powder-mixed dielectric compared to that produced in powder-free dielectric, which quantitatively showed the evenness of crater rims produced in powder-mixed dielectric.

By comparing the peak-to-valley heights, an assessment of the undulations in a crater may be done. Such undulations in crater geometry may be indicative of the eventual topography of the machined surface. Figure 4.8 shows the crater peak-to-valley heights of the two types of craters produced at input energies of 2.5 µJ, 5 µJ and 25 µJ.

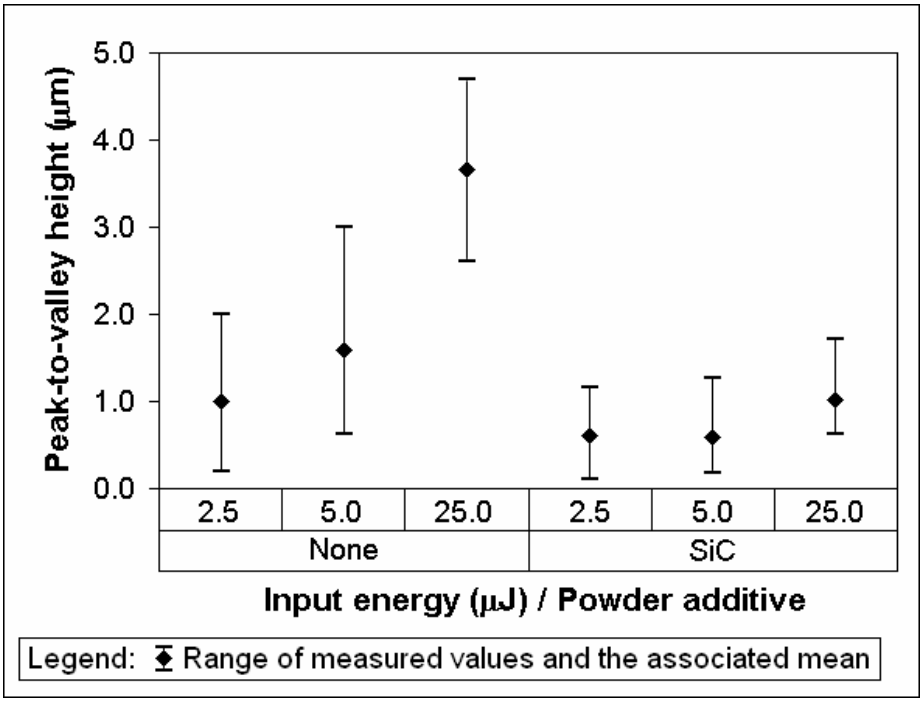

Figure 4.8 Crater peak-to-valley heights for various machining conditions

Results showed that the crater peak-to-valley heights increased as input energy was increased, which indicated that deeper craters were produced at higher input energies. Since deeper craters translated to a surface with greater undulations and hence a larger surface roughness, this observation was consistent with the general understanding that rougher machined surfaces are produced under larger discharge energies. On the other hand, the peak-to-valley heights as well as the deviation in peak-to-valley heights of craters produced in powder-mixed dielectric were smaller than those produced in powder-free dielectric. This may point to the possibility of producing smoother and more mirror-like surfaces in a powder-mixed dielectric under micro-EDM conditions.

4.3.3 Discharge waveforms

The voltage and current waveforms were captured for each single pulse discharge so that the electrical discharge information could be associated to the resulting crater morphology and geometry. The typical voltage and current waveforms at input energies of 2.5 µJ, 5 µJ

and 25 µJ for powder-free and powder-mixed dielectric are shown in Figure 4.9 and Figure 4.10, respectively. The captured voltage and current data are shown in Appendix A.

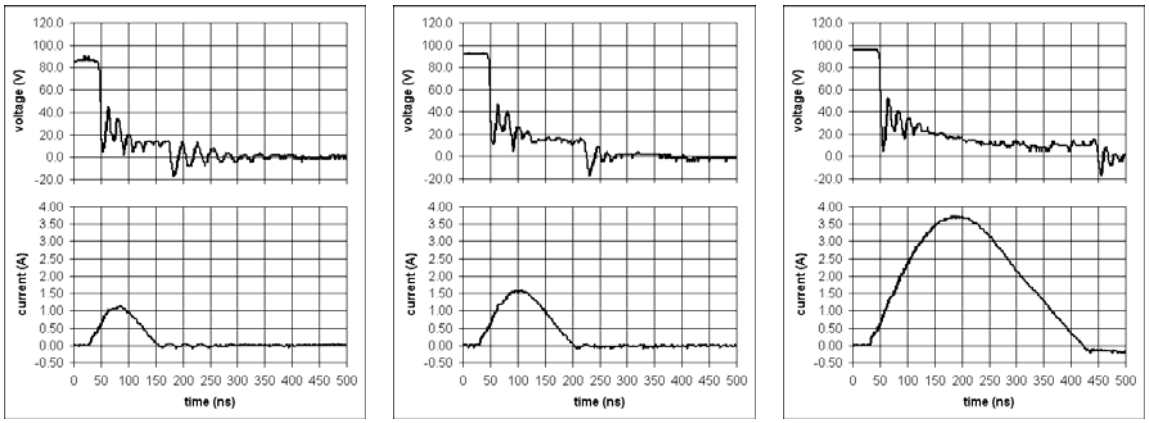

(a) 2.5 µJ (b) 5 µJ (c) 25 µJ

Figure 4.9 Comparison of waveforms at various input energies for powder-free dielectric

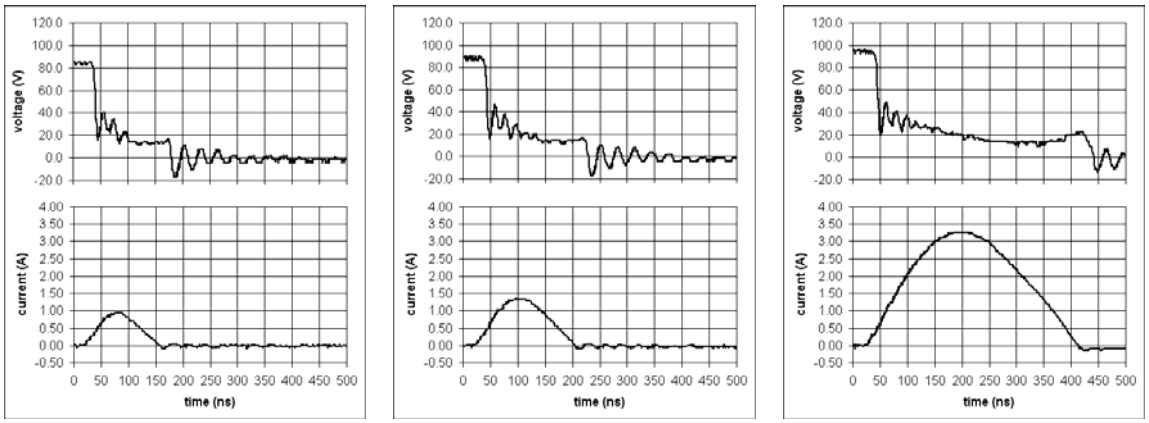

(a) 2.5 µJ (b) 5 µJ (c) 25 µJ

Figure 4.10 Comparison of waveforms at various input energies for powder-mixed dielectric

An inspection of the discharge waveforms showed similar trends for powder-free and powder-mixed dielectric. While discharge voltage was relatively constant during the electrical discharge, the discharge current and pulse on time increased as discharge energy was increased. It has been suggested that a long pulse on time and low peak current produced low temperature discharge channels with low power since more energy was lost through heat conduction into the workpiece during discharge [213]. This highlighted the significance of peak current and pulse on time on characteristics of the resulting plasma. Thus, a single-factor ANOVA study was conducted to examine the variations in peak discharge current and pulse on time due to the presence of additives in the dielectric. Results of the ANOVA analysis are tabulated in Appendix A of which Figure 4.11 gives a

graphical illustration. The results indicated that the influence of additives in the dielectric was statistically significant for peak discharge current and pulse on time.

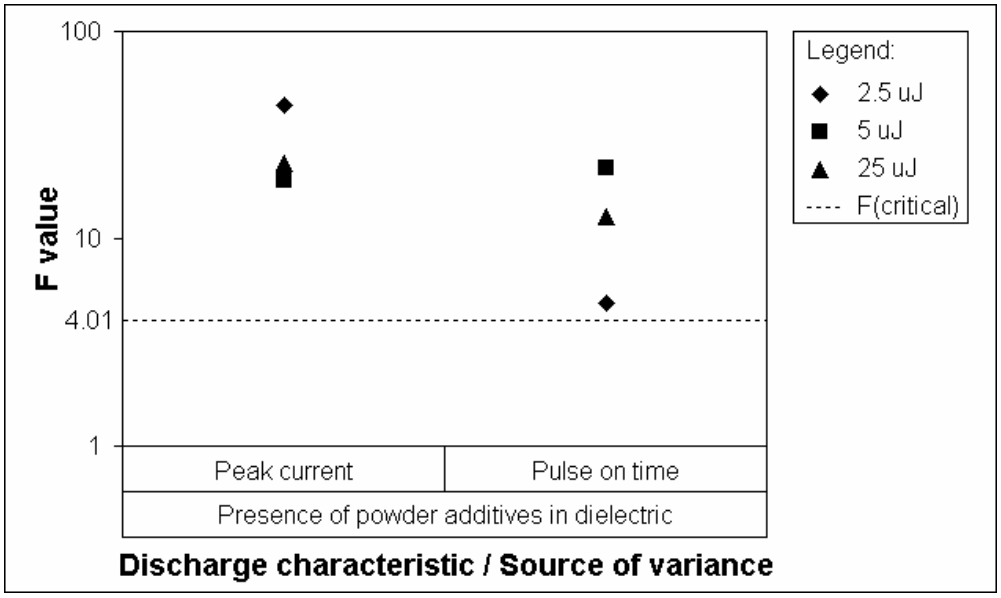

Figure 4.11 Results of ANOVA study for discharge characteristics

The value of peak current may give an indication of the movement of charge particles in the plasma channel since it represents the maximum amount of electrical charges flowing per second. The significance of the amount of charge particles movement during electro erosion is in the conversion of kinetic energy to thermal energy during bombardment of the electrode surface by the charge particles, namely, electrons and ions [112, 214].

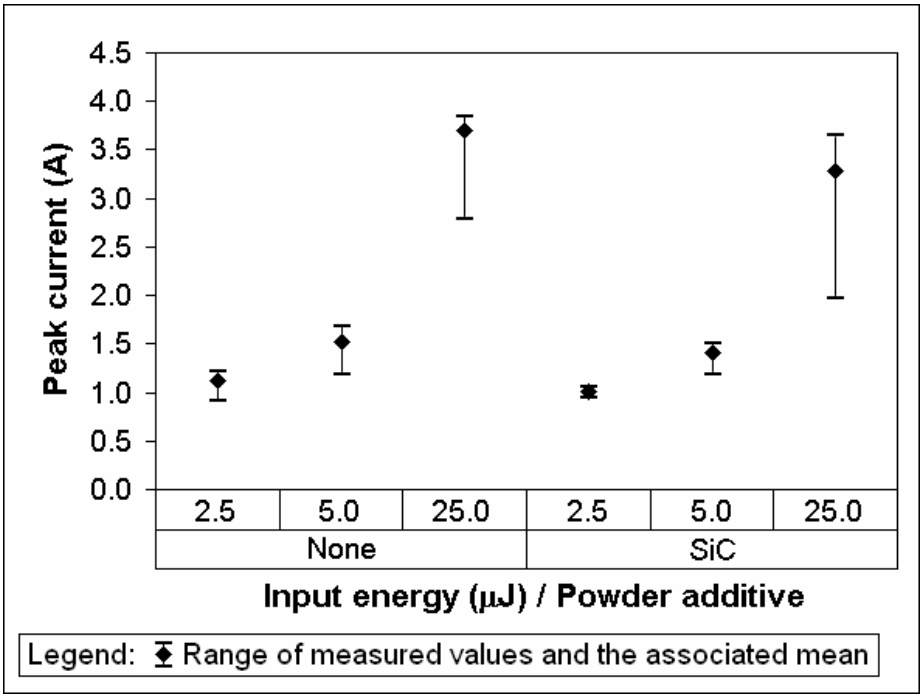

Figure 4.12 Peak discharge current for various machining conditions

Figure 4.13 shows the peak discharge currents produced at input energies of 2.5 μJ, 5 μJ and 25 μJ in the powder-free and powder-mixed dielectric. The results showed that the maximum flow rates of charges in the powder-mixed dielectric were notably lower than in the powder-free dielectric. In studies on PMD-EDM [156, 215], it was suggested that the additive particles within the discharge gap aided streamer propagation and dielectric breakdown. Furthermore, the additive particles also influenced the extent of plasma channel growth and stored energy from the electrical discharge [156]. Considering the interactions between additive particles and plasma channel, the lower peak discharge current in the powder-mixed dielectric may thus be caused by the presence of additive particles which inhibited the flow of charges across the discharge gap, thereby reducing discharge intensity.

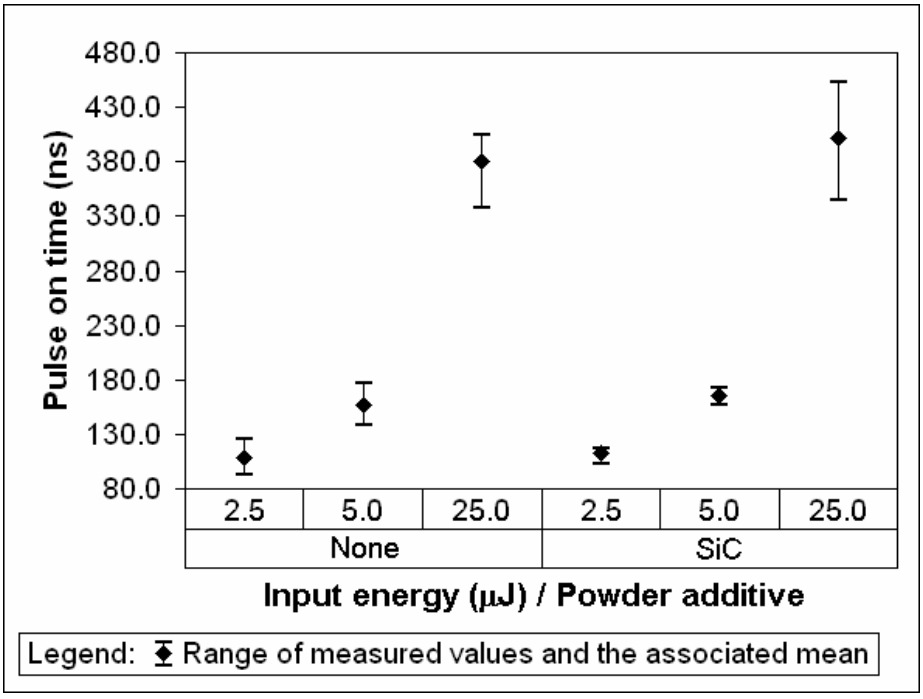

Figure 4.13 Pulse on time for various machining conditions

Figure 4.13 shows the pulse on time durations produced at input energies of 2.5 μJ, 5 μJ and 25 μJ in the powder-free and powder-mixed dielectric. The results showed that the pulse on time durations in the powder-mixed dielectric were longer than in the powder-free dielectric. The longer pulse on time would allow more energy to be lost through heat conduction into the workpiece [213] as well as to be consumed through the vaporisation, disassociation and ionization of the dielectric [106]. Thus, the combination of smaller peak discharge current and longer pulse on time would decrease the discharge intensity. The reduction in discharge intensity would cause a smaller fraction of heat flux to be

incident on the workpiece. As a result, a smaller area of the workpiece would be heated up and a shallower pool of molten material would be formed. The extent of plasma channel growth in a powder-mixed dielectric would also be greater than in a powder-free dielectric, given the larger inner crater diameters produced in powder-mixed dielectric as shown in Figure 4.5. A larger plasma channel would create a lower overpressure within the plasma channel compared to that in a powder-free dielectric. Thus, the smaller force of molten material expulsion would allow more molten material to be retained within the melt pool and would reduce the crater peak-to-valley height, as shown in Figure 4.8. With more resolidified material within the crater, less would be pushed to the crater rim. As a result, a lower crater rim height and smaller crater outer diameter would be formed, as illustrated in Figure 4.7 and Figure 4.4, respectively.

4.4 Summary

To explore the potential of PMD micro-EDM for micro-machining, the single discharge experiment was conducted to examine the unit removal characteristics of the process. Through the single discharge experiment conducted in powder-free and powder-mixed dielectric using input energies of 2.5 μJ, 5 μJ and 25 μJ, the following results were noted:

- A noticeable difference in crater morphology was seen between craters produced in powder-free and powder-mixed dielectric.
- The craters produced in powder-mixed dielectric were characterized by a plateau of resolidified material within an outer crater rim of resolidified material.
- The craters produced in powder-mixed dielectric had consistently smaller outer diameters.
- The craters produced in powder-mixed dielectric had larger inner diameters.
- The craters produced in powder-mixed dielectric had more even crater rims, smaller rim heights and smaller peak-to-valley heights.
- The peak discharge current, at 25 μJ input energy, in the powder-mixed dielectric is notably lower than in the powder-free dielectric.

The experimental observations allowed the following suggestions to be made regarding the PMD micro-EDM process:

- Additive particles within the discharge gap cause an over expansion of the plasma channel and the absorption of discharge energy from the plasma channel.

- The wider plasma channel and smaller discharge energy reduce the discharge intensity and pressure within the plasma channel.
- The reduced discharge energy generates a smaller amount of molten material within the melt pool.
- The overpressure within the gas bubble pushes molten material away from the interior of the melt pool to form the crater rim.
- Upon collapse of the plasma channel, the weaker flushing force is unable to expel the molten material significantly.
- The molten material flows back to the centre of the crater and resolidifies to form a plateau of resolidified material within a crater rim with even edges.

The single discharge experiment for PMD micro-EDM generated results showed that the use of nano-powder additives for micro-EDM led to a more consistent generation of craters that were smaller in size. This may prove beneficial in the attainment of a smaller and more repeatable unit removal. The plateau of resolidified material and smaller peak-to-valley height in the discharge crater may translate to smaller undulations on the machined surface and lead to a lower surface roughness. Moreover, the reduction in discharge intensity may limit the depth of melt pool and hence moderate recast layer thickness. Furthermore, the retention of resolidified material on the machined surface may be exploited in surface modification processes involving electrical discharge alloying.

Chapter 5
Investigation on Surface Roughness

This chapter covers the results of machining experiments conducted to investigate the effects of PMD micro-EDM on surface roughness. Results of single discharge experiment on the unit removal characteristics in PMD micro-EDM showed the generation of craters with smaller peak-to-valley heights. However, not only are discharge gap conditions in the machining process and single discharge experiment different, the machined surface is also characterized by overlapping craters. Therefore, while the single discharge experiment is useful for understanding the material removal mechanism, machining experiments are required to assess the actual changes to surface topography in PMD micro-EDM. In this chapter the rationale for conducting the machining experiment on PMD micro-EDM to investigate surface roughness is explained. Following which the experiment, involving various input energies, nano-powder additives and concentrations, is described. Next, a comparison of arithmetical mean surface roughness (*Ra*) measurements for surfaces machined in powder-free and powder-mixed dielectric is made. An overview of the chapter is shown in Figure 5.1.

Figure 5.1 Overview of Chapter 5

5.1 Machining experiment for surface roughness

Micro-EDM, being a micro-machining process, should satisfy precision machining considerations such as the use of small unit removal and the reduction in surface roughness in proportion to feature size [31]. The results of single discharge experiment conducted using powder-mixed dielectric in micro-EDM suggested the possibility of effecting such enhancements to the micro-EDM process. It was shown that the presence of powder additives within the discharge gap reduced crater outer diameter and produced more consistently-shaped craters, which translated to a smaller and more repeatable unit

removal. Furthermore, the reduction in peak-to-valley height may suggest a reduction in surface roughness resulting from the PMD micro-EDM process. However, since the machined surface comprises overlapping craters, the morphology of a single crater may not accurately represent the eventual machined surface topography. The machined surface topography is also affected by process stability such that increases in the frequency of short-circuiting and arcing may contribute to increased surface roughness. Process stability is highly dependent on discharge gap conditions of which the amount of suspended particles within the discharge gap is a significant factor [22]. Furthermore while the discharge gap conditions in single discharge experiment were controlled, such as the constant discharge gap distance and the absence of flushing effects from tool electrode rotation, the gap conditions during machining are not as regulated. Therefore, machining experiments on PMD micro-EDM are required to determine whether results of the single discharge experiment may translate to improvements in machining performance, such as the reduction in surface roughness, which can enhance micro-EDM for precision machining.

5.2 Experimental method

The machining experiment was performed on a commercially available micro-EDM system that was fitted with a separate dielectric tank for powder-mixed dielectric. Of the four input energies available from the micro-EDM system, two were used for the parametric investigation. The nano-powder additives used were silicon carbide (SiC) and aluminium oxide (Al_2O_3), which represented a semi-conductive and non-conductive material, respectively. The concentration of powder added to the dielectric was also varied to investigate the effects of powder concentration on surface roughness. Table 5.1 shows the range of machining parameters used in the experiment while Table 5.2 shows the specific machining conditions employed for individual experiments. By varying the combination of machining conditions, 14 experimental runs were conducted in which 3 micro-holes were machined for each run.

Prior to the start of the experiment, the 7 types of powder-mixed dielectric were prepared. The preparation of powder-mixed dielectric began with the largest required powder concentration for the given powder material. After the powder-mixed dielectric had been homogenized through ultrasonic agitation, the lower concentrations of powder-mixed dielectric were prepared through dilution with powder-free dielectric. For each run, the

appropriate capacitor was selected based on the required input energy. Before each hole was machined, the tool electrode was dressed to remove the effects of corner wear. Then the tool electrode was positioned above the mating line of two wrung workpieces. Next the powder-mixed dielectric was agitated with a stirrer and micro-hole drilling was performed. The micro-hole drilling was performed at a constant downward feed rate of 0.2 μm/s and ended when the motion controller registered the programmed machining depth. The tool electrode was rotated at 3000 rev/min throughout the machining process for debris flushing.

Table 5.1 Parameters for all machining experiments

Parameter	Value
Open circuit voltage, V_{OC} (V)	100
Capacitance, C (pF)	220; 3300
Input energy, E_{in} (μJ)	1.1; 16.5
Workpiece material	Stainless mould steel, AISI 420-MOD
Tool electrode material	Tungsten
Tool electrode diameter (μm)	300
Electrode rotation speed (rev/min)	3000
Hole depth (μm)	150
Dielectric	Idemitsu Daphne Cut HL-25
Powder material	SiC; Al_2O_3
Powder concentration (g/l)	0.02; 0.04; 0.08; 0.16

Table 5.2 Input parameters for individual experiments

Input parameter	Condition
Input energy, E_{in} (μJ)	1.1; 16.5
Powder material and concentration (g/l)	SiC: 0.02; 0.04; 0.08 Al_2O_3: 0.02; 0.04; 0.08; 0.16

5.3 Results and discussion

The arithmetical mean surface roughness (*Ra*) of the side wall of micro-holes was measured using the confocal optical profiler at a cut-off of 0.08 mm, compiled and compared. The variation of *Ra* values with respect to input energy and powder concentration are discussed.

5.3.1 Arithmetical mean surface roughness

The *Ra* value for each machining condition was derived from measurements of *Ra* from the 3 micro-holes machined. Furthermore, 10 measurements were taken at predetermined locations at the side wall of each micro-hole. The experimental data, tabulated in Appendix B, are plotted in graphs illustrated in Figure 5.2(a) and Figure 5.2(b), which show the *Ra* values for SiC and Al_2O_3 powder additives, respectively.

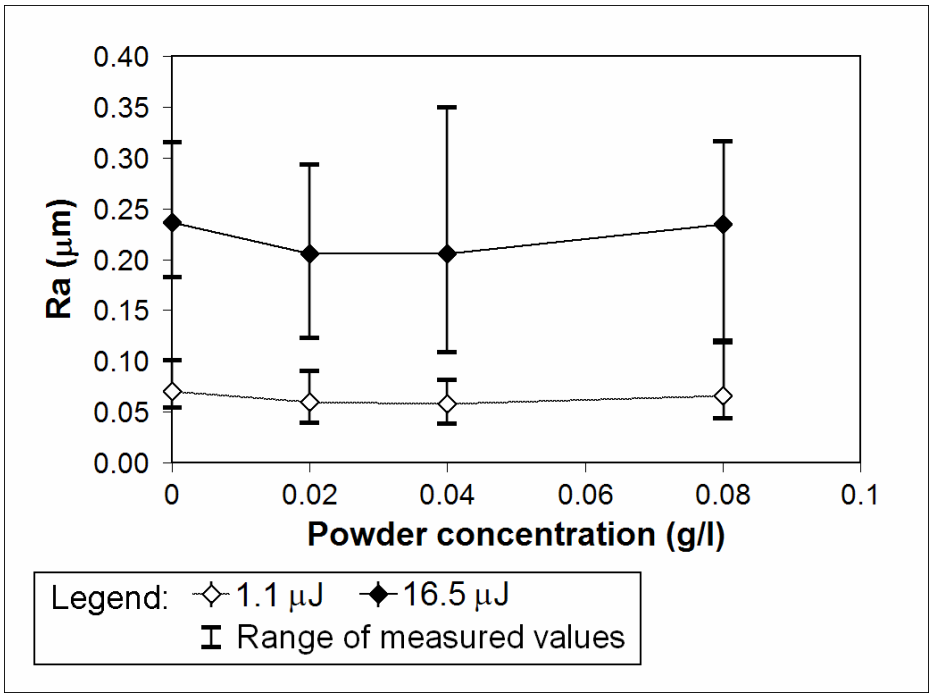

(a) Nano-powder additive: SiC

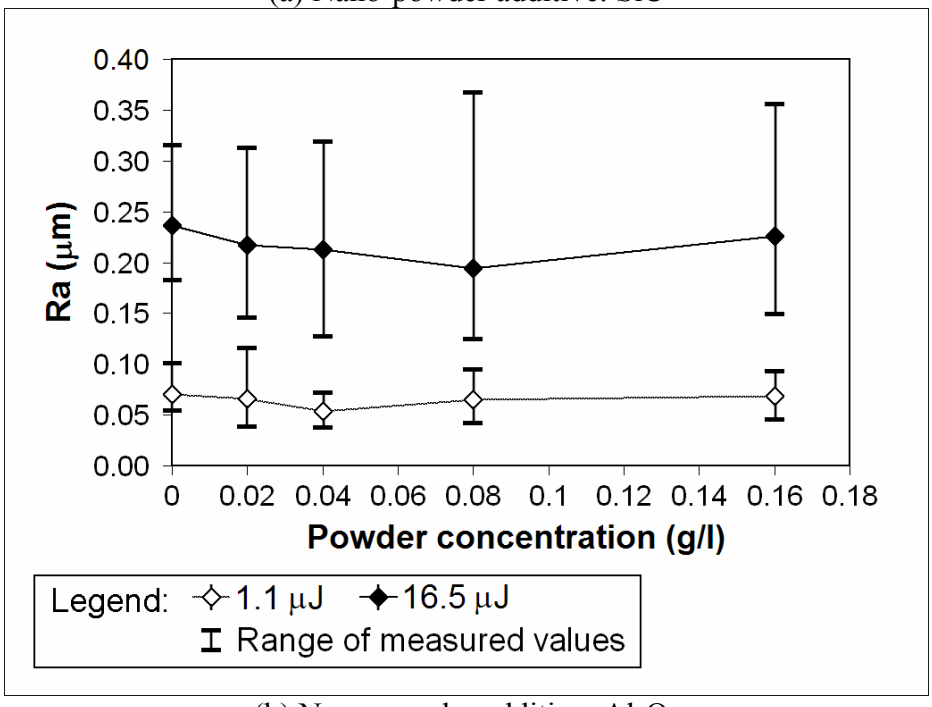

(b) Nano-powder additive: Al_2O_3

Figure 5.2 Arithmetical mean surface roughness at various parametric conditions

The results show that, regardless of input energy and powder material, the *Ra* value decreases for initial increases in powder concentration, reaches a minimum and then increases for further increases in powder concentration. It was suggested that while small amounts of suspended particles improved process stability through reduction in arcing frequency, an excessive amount of particles led to increased arcing and deterioration in surface finish [22]. Thus for PMD micro-EDM, powder concentrations between 0.02 g/l and 0.08 g/l were shown to generate the lowest surface roughness. On the other hand in PMD-EDM, it was reported that the lowest surface roughness was achieved at a powder concentration of 2 g/l when silicon powder of 10 μm average granularity was tested in concentrations of between 1 g/l and 20 g/l [157].

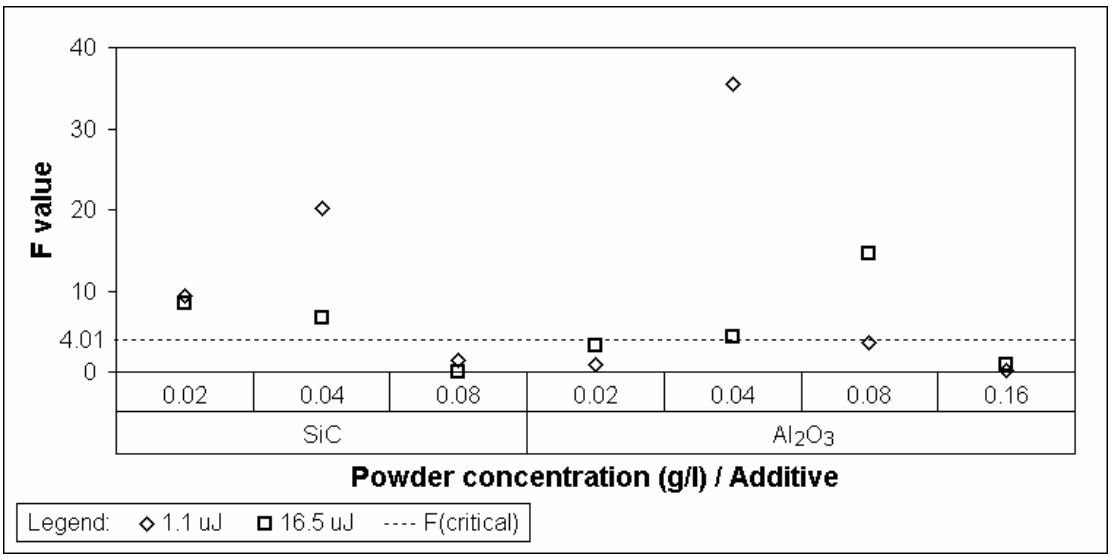

Figure 5.3 Results of ANOVA study for *Ra*

To determine whether a statistically significant reduction in surface roughness has been achieved by the PMD micro-EDM process, a single-factor ANOVA study was conducted. Based on the results shown in Figure 5.3, it is noted that only certain combinations of input energy, powder material and powder concentration were able to generate an evident reduction in surface roughness. The most significant reduction in surface roughness for SiC powder was achieved at 1.1 μJ input energy and 0.04 g/l powder concentration. For 16.5 μJ input energy, SiC powder produced the most significant surface roughness reduction at 0.02 g/l powder concentration. The most significant reduction in surface roughness for Al_2O_3 powder was also achieved at 1.1 μJ input energy and 0.04 g/l powder concentration. For 16.5 μJ input energy, Al_2O_3 powder produced the most significant surface roughness reduction at 0.08 g/l powder concentration.

The percentage reductions in *Ra* for various machining conditions that produced the most significant reduction in surface roughness are shown in Table 5.3.

Table 5.3 Percentage reductions in *Ra* for various machining conditions

Input energy (μJ)	Additive	Concentration (g/l)	*Ra* (μm)	Percentage reduction (%)
1.1	Nil	0	0.070	--
1.1	SiC	0.04	0.058	17
1.1	Al_2O_3	0.04	0.053	24
16.5	Nil	0	0.237	--
16.5	SiC	0.02	0.206	13
16.5	Al_2O_3	0.08	0.194	18

The results show that percentage reductions in *Ra* of between 13 % and 17 % were achieved for SiC powder additive material while reductions of between 18 % and 24 % were achieved for Al_2O_3 powder additive material. While a more electrically conductive powder material may cause an increase in discharge gap distance, affect the thermal material removal mechanism and hence the surface topography [133], a non-conductive powder material may engender a lower surface roughness through other effects. In a study on PMD-EDM with Al_2O_3 powder, it was reported that the powder had no effect on gap distance and suggested that the improvement in surface roughness was due to the suppressing of crater rim formation by minimising the reattachment of expelled molten material on the machined surface through attachment to the non-conductive powder additives [165].

5.3.2 Analysis of arithmetical mean surface roughness results

The presence of powder additives in the dielectric affects the mechanism of discharge crater formation, which consequently affects the machined surface roughness. In this study, the use of semi-conductive SiC and non-conductive Al_2O_3 powder additives has resulted in reductions in surface roughness. The resulting decrease in surface roughness originated from discharge gap enlargement which may be effected by both electrically conductive and non-conductive powder additives [26]. The enlarged discharge gap prevented intensive discharge and reduced discharge density [133]. As a result, smaller

and shallower craters were formed and contributed to the decrease in machined surface roughness [28]. The results also showed that, after reaching a minimum value at a particular powder concentration, surface roughness increased with increasing powder concentration. This is because the presence of excessive amounts of powder additives promoted the occurrence of short-circuiting which caused a deterioration in surface finish [157].

The experimental findings also revealed that the percentage reduction in *Ra* value for Al_2O_3 powder additive was larger compared to that for SiC powder additive. This could be partly attributed to the different amounts of heat energy absorbed from the plasma channel by the powder additives [156]. Given that the heat capacity of Al_2O_3 material is higher than SiC material, a greater proportion of heat energy would be absorbed and stored by Al_2O_3 powder additive, thereby availing a smaller proportion to be distributed to the workpiece. The larger percentage reduction in *Ra* value for input energy of 1.1 μJ could also be attributed to the greater proportion of heat energy absorbed by the powder additives with respect to the heat energy available. Thus, with a greater percentage reduction in the amount of heat energy distributed to the workpiece, there would be a greater percentage reduction in *Ra* value.

In general, it was proposed that the powder additives reduced the fraction of heat flux distributed to the workpiece by absorbing a portion of the heat energy from the plasma channel. Furthermore, it was proposed that the powder additives reduced the amount of molten material expelled from the melt pool at the end of discharge. This is because the powder additives would cause a discharge gap enlargement and more extensive expansion of the plasma channel. This would in turn reduce the overpressure within the plasma channel and consequently reduce its ability to expel molten material. As a result, a smaller and shallower discharge crater would be formed and *Ra* value would decrease. This mechanism of crater formation in powder-mixed dielectric will be further elaborated in the next chapter.

5.4 Summary

To demonstrate the feasibility of PMD micro-EDM with nano-powder additives made of semi-conductive and non-conductive powder materials, machining experiments using a commercial micro-EDM system was performed. Powder additives with granularity in the range of 40 nm to 55 nm were used in concentrations between 0.02 g/l and 0.16 g/l to minimise agglomeration of powder additives and facilitate their entry into the discharge gap. Using input energies of 1.1 μJ and 16.5 μJ, reductions in *Ra* values ranging between 13 % and 24 % were recorded. The largest percentage reduction in *Ra* was achieved at the input energy of 1.1 μJ and Al_2O_3 powder concentration of 0.04 g/l.

Based on the analysis of variations in *Ra* values with powder concentration and powder additive material, the mechanism of discharge crater formation in dielectric mixed with semi-conductive and non-conductive powder additives were proposed. Generally, both powder additives would absorb a portion of heat energy from the plasma channel and also effect an enlargement in discharge gap. Therefore, there would be a reduction in heat flux distributed to the workpiece as well as a reduction in expulsion force due to a larger extent of plasma channel expansion. Due to these effects, the smaller and shallower craters formed resulted in a decrease in surface roughness. In the case of SiC nano-powder additive, the increase in surface roughness at higher powder concentrations could be attributed to more frequent occurrences of short-circuiting due to the ease of particle bridge formation. On the other hand, the non-conductive property of Al_2O_3 nano-powder additive tended to form an insulating layer between the tool electrode and workpiece at higher powder concentrations. This inhibited discharge occurrence until the insulating layer was agitated by the relative movement of electrodes at small gap distances. The occurrence of discharges at these gap distances increased the chances of short-circuiting which increased surface roughness.

Chapter 6
Investigation on Recast Layer Thickness

This chapter covers the results of machining experiments conducted to investigate the effects of PMD micro-EDM on recast layer thickness. Results of the single discharge experiment showed that the craters generated in a powder-mixed dielectric had a different morphology compared to those generated in a powder-free dielectric. The difference in crater morphology may be caused by differences in electrical discharge intensity and flushing efficiency due to the presence of powder additives within the discharge gap. Moreover, changes in crater morphology reflect changes in geometry of the crater recast region which may translate to changes in recast layer thickness of the machined surface. In this chapter the purpose of conducting the machining experiment on PMD micro-EDM to study recast layer thickness is explained. Following which the experiment, involving various tool electrode rotation speeds, pulse on time durations and powder concentrations, is described. Then, a comparison of recast layer thickness generated using various combinations of machining parameters is presented. Finally, the factors affecting recast layer generation and mechanisms of recast layer generation are proposed. An overview of the chapter is shown in Figure 6.1.

Chapter 6: Investigation on Recast Layer Thickness
6.1 Machining experiment for recast layer thickness
6.2 Experimental method
6.3 Results and discussion
- 6.3.1 Tool electrode rotation without powder additives
- 6.3.2 Tool electrode rotation with powder additives
- 6.3.3 Concentration of powder additive
- 6.3.4 Mechanism of recast layer generation in PMD micro-EDM
  - 6.3.4.1 Qualitative description of recast layer generation in PMD micro-EDM
  - 6.3.4.2 Quantitative analysis of recast layer generation in PMD micro-EDM

6.4 Summary

Figure 6.1 Overview of Chapter 6

6.1 Machining experiment for recast layer thickness

The potential uses of PMD-EDM include the improvement of machined sub-surface quality in EDM, such as a reduction in cracking tendency and recast layer thickness [25, 157, 158] and the alloying of machined surface with elements of powder material in surface modification processes [24, 149]. In these applications, the recast layer thickness is a useful machining performance measure as it may be used to characterize the extent of surface damage or thickness of the functional layer, depending on the intended PMD-EDM application. The recast layer is essentially a collection of recast regions from individual craters. Thus factors such as fraction of energy transferred to the workpiece and discharge intensity, which affect the formation of recast region, may also influence recast layer thickness. Furthermore, due to the overlapping nature of crater formation on the machined surface the recast layer thickness is also influenced by the flow of molten material from the melt pool to neighbouring craters, which is affected by the flushing effects on the molten material. Results from the single discharge experiment showed that the morphology of craters generated in a powder-mixed dielectric consisted of a plateau of resolidified material within the boundaries of the crater rim. Although the forces from gas bubble implosion may not be great enough to expel the molten material, flushing effects from tool electrode rotation during machining may aid in the removal of molten material [138]. Moreover in a machining process the occurrence of overlapping craters may cause the molten material, which was initially pushed away from the interior of the melt pool by the overpressure in the gas bubble, to flow into neighbouring craters and not return to the newly formed crater cavity [216]. Therefore, while the observation of retained molten material within the crater is indicative of the potential of PMD micro-EDM for surface modification applications, machining experiments on recast layer thickness are required to advance its development.

6.2 Experimental method

As described in Section 3.1.1.3 and illustrated in Figure 3.4, the machining experiment was performed on a purpose-built test rig. The pulse generator design was based on the RLC circuit which allowed pulse on time to be varied with minimal changes to peak discharge current. Furthermore, the test rig was incorporated with a DC motor that enabled control of the tool electrode rotation speed. Pulse on time duration, tool electrode rotation speed and silicon carbide nano-powder additive concentration were chosen as

variables in the experiment. A constant peak discharge current of 1.45 A was used in combination with pulse on time durations of 166 ns, 362 ns and 606 ns to generate discharge energies of 5μJ, 11.7μJ and 21μJ, respectively, which are typical of the micro-EDM regime. The pulse on time duration was varied as it was noted to influence recast layer thickness more than peak discharge current [118]. Table 6.1 shows the complete set of machining parameters used during the experiment while Table 6.2 shows the specific parameters and values used in the three experiments conducted. Five holes were machined for each parametric condition. To machine a hole, the rod-shaped tool electrode was fed longitudinally towards the workpiece while being rotated about its longitudinal axis at the preset electrode rotation speed. The tool electrode was retracted upon detection of short-circuiting and resumed its downward feed when the short-circuit was broken. The machining process ended when the tool electrode reached the programmed depth of 150 μm and the tool electrode was retracted.

Table 6.1 Parameters for all machining experiments

Parameter	Value
Open circuit voltage, V_{OC} (V)	100
Pulse on time, t_{on} (ns)	166; 362; 606
Peak discharge current, I_{pk} (A)	1.45
Measured discharge energy, E_m (μJ)	5; 11.7; 21
Workpiece material	Stainless mould steel, AISI 420-MOD
Tool electrode material	Tungsten
Tool electrode diameter (μm)	300
Electrode rotation speed (rev/min)	1000; 3000
Hole depth (μm)	150
Dielectric	Idemitsu Daphne Cut HL-25
Powder material	Silicon carbide, SiC
Powder size (nm)	45 ~ 55
Powder concentration (g/l)	0; 0.02; 0.05; 0.1; 0.2; 0.5

Table 6.2 Input parameters for individual experiments

Experiment	Input parameter	Condition
Tool electrode rotation without powder additives	Pulse on time (ns)	166; 362; 606
	Rotation speed (rev/min)	1000; 3000
	Powder concentration (g/l)	0
Tool electrode rotation with powder additives	Pulse on time (ns)	166; 362; 606
	Rotation speed (rev/min)	1000; 3000
	Powder concentration (g/l)	0.5
Concentration of powder additives	Pulse on time (ns)	166; 362; 606
	Rotation speed (rev/min)	1000
	Powder concentration (g/l)	0; 0.02; 0.05; 0.1; 0.2

The first experiment on tool electrode rotation without powder additives was conducted to investigate the effects of tool electrode rotation speed on recast layer thickness since tool rotation is typically used in micro-EDM for flushing and flushing effects have been reported to affect recast layer thickness [138]. Flushing effects from tool electrode rotation may also cause powder additives to be expelled from the discharge gap since distinction between the powder additives and debris is not made. Thus, the effectiveness of PMD micro-EDM may be affected by the reduction of powder additives within the discharge gap. The second experiment on tool electrode rotation with powder additives was conducted to investigate this supposition. The powder concentration of 0.5 g/l was used to ensure that the influence from powder additives may be evident under all machining conditions. In the experiments on tool electrode rotation, two rotation speeds of 1000 rev/min and 3000 rev/min were used to assess the contrasting effects of electrode rotation speed on recast layer thickness. The rotation speed of 1000 rev/min was chosen as it corresponded to the maximum electrode rotation speed employed for studies on recast layer thickness in EDM [217] while 3000 rev/min was chosen at it is a representative tool rotation speed used in micro-EDM. The third experiment on concentration of powder additives was to study the effects of varying powder concentration on the enlargement in discharge gap and recast layer thickness. The increase in discharge gap distance in a powder-mixed dielectric has been suggested to change the flushing effects in the discharge gap [28] and to facilitate the presence of more powder additives in the gap which reduces discharge intensity [133]. These changes may

consequently affect the resulting recast layer thickness. To determine the gap distance, a reference height corresponding to the vertical location at which the tool electrode came into contact with the workpiece was defined. Next the tool electrode was retracted by a distance of 50μm from the reference height and the required dielectric was poured into the tank before the electrode was advanced towards the workpiece until electrical discharges occurred. Then the vertical location of the tool electrode measured from the reference height was recorded as the gap distance.

In the preparation of the powder-mixed dielectric, the required amount of powder additive and dielectric were measured separately before being mixed together and homogenised in an ultrasonic bath. In addition, the pre-mixed dielectric was ultrasonically agitated prior to the machining of each hole to ensure de-agglomeration and uniform dispersion of powder additives.

6.3 Results and discussion

The effects of tool electrode rotation on average recast layer thickness in micro-EDM are first compared. Following which, the effects of tool electrode rotation on average recast layer thickness in PMD micro-EDM are covered. Finally, observations on discharge gap enlargement and recast layer thickness caused by varying powder concentrations are discussed. The experimental results captured are shown in Appendix C.

6.3.1 Tool electrode rotation without powder additives

The recast layer thickness for each parametric condition was estimated with reference to the measured area of recast layer at the base of the blind micro-holes. The floor was chosen as it is the surface subjected to continuous machining throughout the micro-hole drilling process and possibly the surface where the effects of flushing and powder additives are most predominant. Figure 6.2 shows the recast layer thickness generated in a powder-free dielectric at pulse on time durations of 166 ns, 362 ns and 606 ns and electrode rotation speeds of 1000 rev/min and 3000 rev/min.

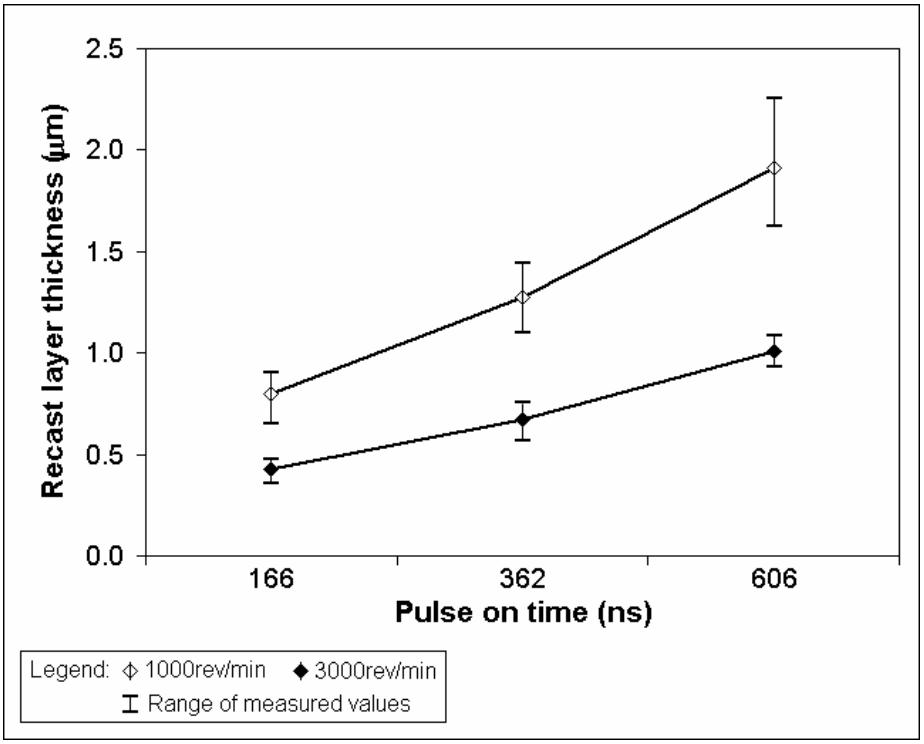

Figure 6.2 Average recast layer thickness under micro-EDM conditions

The results show that the rotation speed of 3000 rev/min generated a thinner recast layer than the rotation speed of 1000 rev/min. This may suggest that the stronger flushing effects caused by a faster electrode rotation speed in micro-EDM not only promotes debris flushing, it also reduces the amount of molten material retained within the crater and subsequently resolidified on the machined surface. This relationship between tool electrode rotation and flushing effects is consistent with the findings of a study that investigated the effects of tool electrode rotation on recast layer thickness in EDM [217]. Moreover, the influence of flushing on the removal of molten material was proposed in another study that employed a constant flushing pressure and various discharge energies to study the resulting recast layer thickness in EDM [138]. Thus, while more molten material is produced at larger pulse on time durations due to the greater discharge energies, the amount of molten material removed by the flushing effects of tool electrode rotation remains relatively constant and results in a net increase in recast layer thickness. The flushing effects from tool electrode rotation may also be a reason for the larger deviation in recast layer thickness at the rotation speed of 1000 rev/min compared to that at 3000 rev/min. The weaker flushing effects at 1000 rev/min may not provide adequate flushing to maintain a consistent discharge gap condition and cause unstable process conditions that lead to a larger deviation in recast layer thickness. On the other hand, the

smaller deviation in recast layer thickness at 3000 rev/min may suggest that the machining conditions across different micro-holes are relatively stable.

6.3.2 Tool electrode rotation with powder additives

The experiment was conducted to investigate the influence of flushing effects from tool electrode rotation on the presence of powder additives in the discharge gap and to assess the effectiveness of employing nano-powder additives for PMD micro-EDM. Figure 6.3 gives a pictorial comparison of the recast layers generated with an electrode rotation speed of 3000 rev/min.

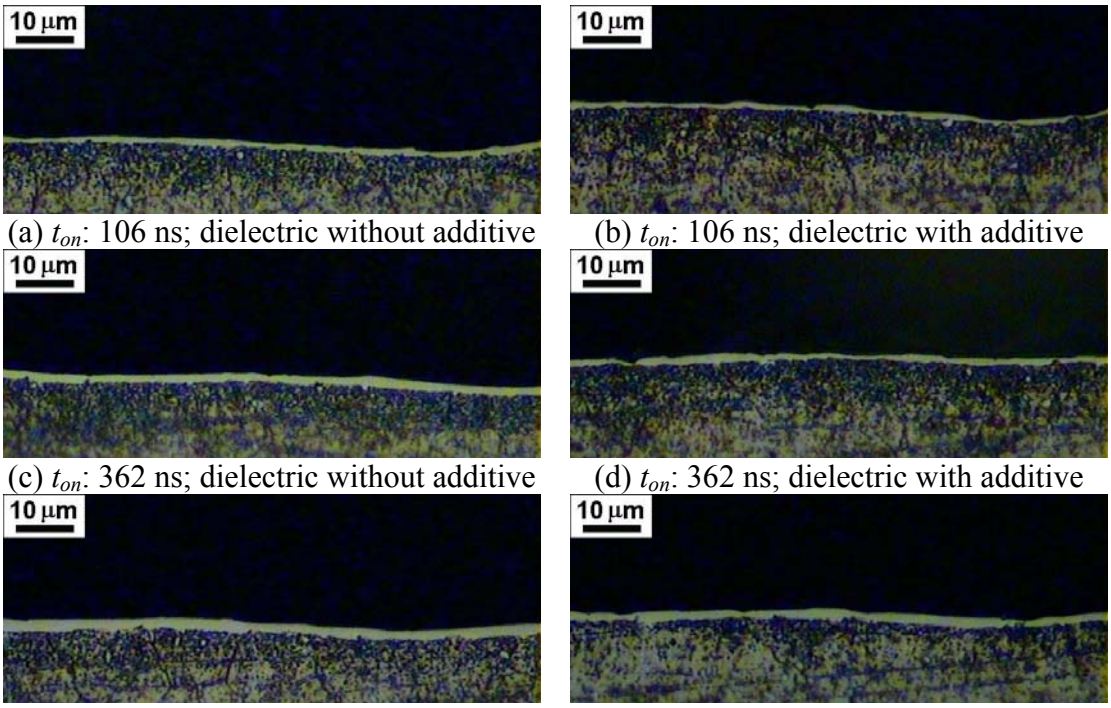

(a) t_{on}: 106 ns; dielectric without additive (b) t_{on}: 106 ns; dielectric with additive

(c) t_{on}: 362 ns; dielectric without additive (d) t_{on}: 362 ns; dielectric with additive

(e) t_{on}: 606 ns; dielectric without additive (f) t_{on}: 606 ns; dielectric with additive

Figure 6.3 Recast layers generated using electrode rotation speed of 3000 rev/min

Figure 6.4 shows that the stronger flushing effects at 3000 rev/min electrode rotation speed caused a thinner recast layer in both the powder-mixed dielectric and the powder-free dielectric. Also, it is evident that the recast layer thickness generated in the powder-mixed dielectric is smaller than that in powder-free dielectric. This observation may be attributed the presence of nano-powder additives in the discharge gap which caused changes to the distribution of discharge energy such that a larger fraction is consumed by the dielectric while a smaller fraction is transferred to the workpiece as suggested in findings from PMD-EDM [156, 158].

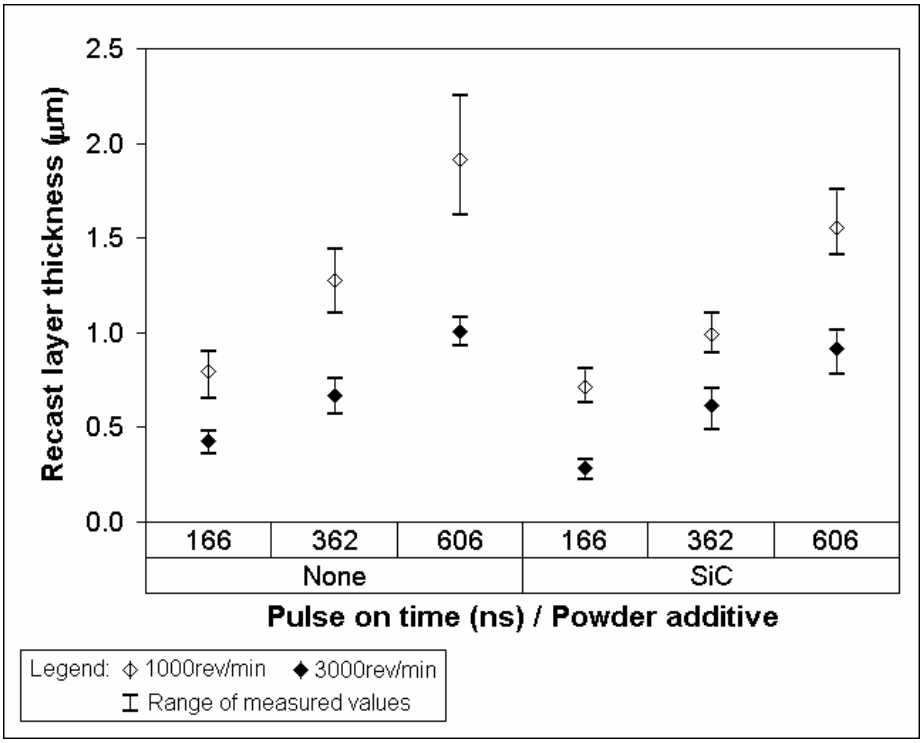

Figure 6.4 Average recast layer thickness under PMD micro-EDM conditions

The reduction in recast layer thickness caused by the presence of powder additives is generally more significant at the electrode rotation speed of 1000 rev/min than 3000 rev/min, especially at longer pulse on time durations. This may suggest that flushing effects and pulse on time durations have an effect on the reduction of recast layer thickness caused by the presence of powder additives. The more evident reduction in recast layer thickness at 1000 rev/min may suggest that the weaker flushing effects aided the accumulation of a larger amount of powder additives in the discharge gap which then caused a considerable reduction in fraction of discharge energy transferred to the workpiece and a significant reduction in recast layer thickness.

6.3.3 Concentration of powder additive

The experiment was conducted as observations from the earlier experiment revealed that the SiC nano-powder additive in the dielectric had flocculated towards the end of the machining process. The flocculation of powder additives, which may be due to the high powder concentration and absence of external agitation forces [218], also caused a deterioration in machining process stability. The deterioration in machining stability may point to changes in the discharge gap condition and affect recast layer thickness. Thus, the powder concentration was increased by incremental steps from 0 g/l to 0.02 g/l, 0.05 g/l, 0.1 g/l and 0.2 g/l to investigate its effect on discharge gap enlargement and recast layer

thickness. The electrode rotation speed was also set at 1000 rev/min as it facilitated a more significant change in recast layer thickness. Figure 6.5 shows the variation in discharge gap distance with powder concentration for pulse on time durations of 166 ns, 362 ns and 606 ns.

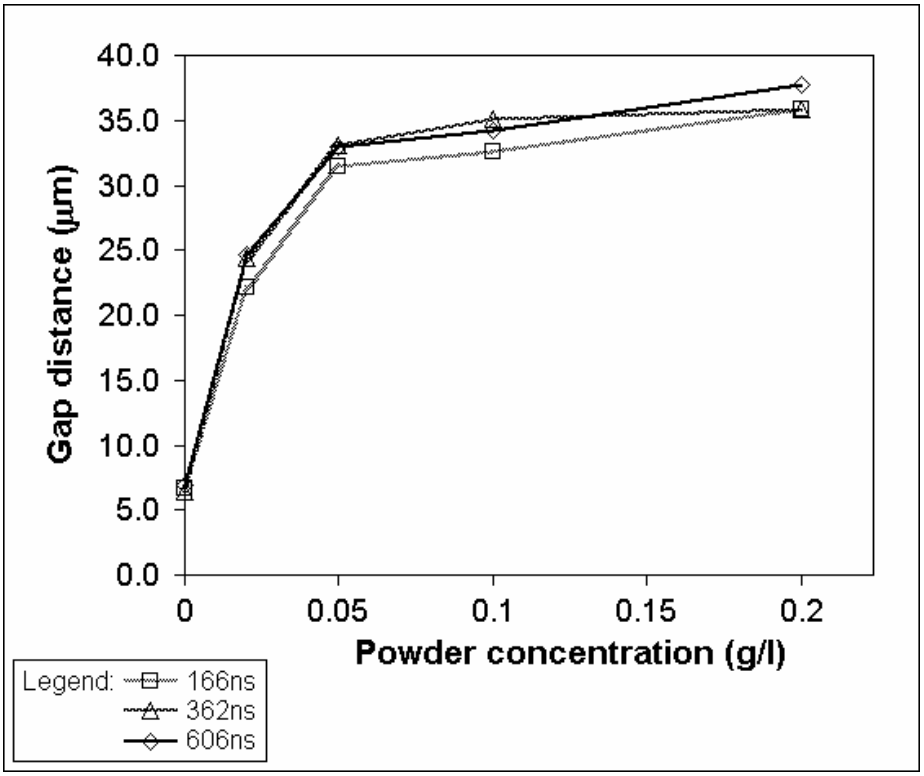

Figure 6.5 Gap distance at various powder concentration and pulse on time

The gap distance did not vary significantly with pulse on time duration. On the other hand, as powder concentration was increased gap distance enlarged significantly and tended towards saturation. This is consistent with suggestions that discharge gap distance is dependent on open-circuit voltage and concentration of suspended particles [22]. This increase in gap distance may initiate changes in flushing effects and quantity of powder additives within the discharge gap, thereby affecting recast layer thickness.

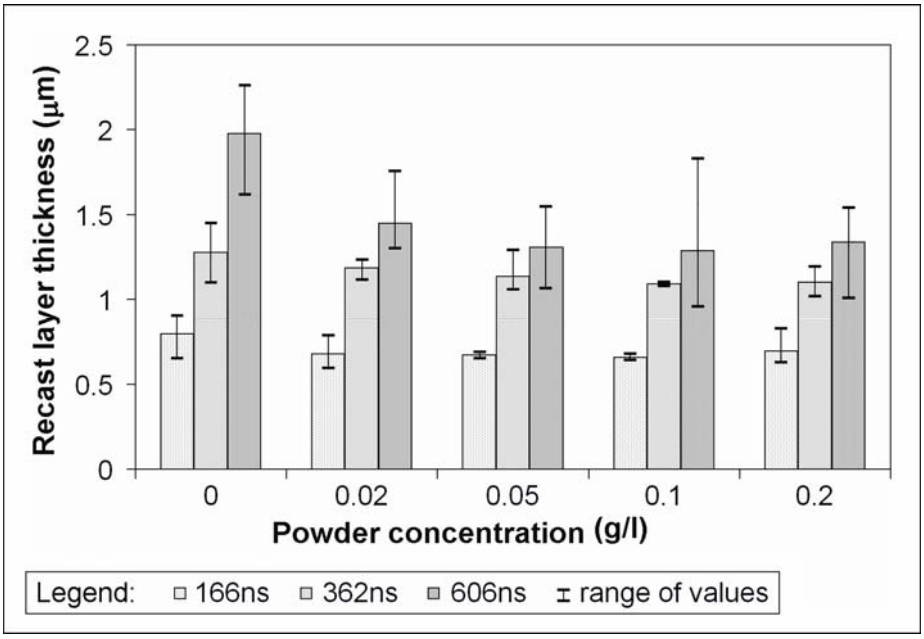

Figure 6.6 Average recast thickness and the associated range of measured values

The reduction in recast layer thickness was evident for all pulse on time durations and powder concentrations as shown in Figure 6.6. There was, however, a tendency for the range of measured recast thickness values generated at pulse on time durations of 362 ns and 606 ns and powder concentrations above 0.05 g/l to overlap. This was mainly due to the wider range of measured values for 606 ns pulse on time. To determine whether there was a significant reduction in recast layer thickness due to the presence of powder additives, the average recast layer thickness values were plotted with error bars as shown in Figure 6.7. The larger the separation between the lower error bar at 0 g/l and the upper error bar at other powder concentrations, the greater is the likelihood that a reduction in recast layer thickness exists. Thus, according to the error bar plots, the reduction was more significant for initial increases in powder concentrations than subsequent increases. The most significant reduction in recast layer thickness occurred at a powder concentration of 0.1 g/l and ranged between 15 % and 35 %. Figure 6.5 and Figure 6.7 showed that increases in gap distance and decreases in recast layer thickness followed a similar trend with increasing powder concentration. Based on this observation, a mechanism of recast layer formation in PMD micro-EDM will be proposed. The mechanism takes into account the influence of gap distance on the presence of powder additives within the discharge gap and their subsequent effect on recast layer thickness.

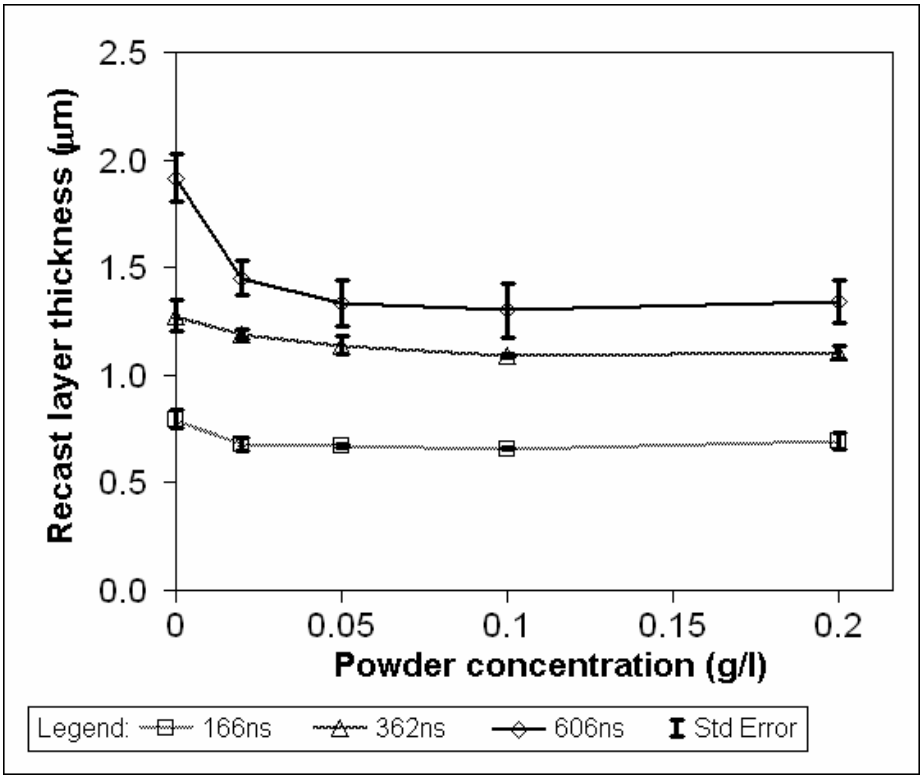

Figure 6.7 Average recast thickness values and the associated standard error ranges

The maximum reduction in recast layer thickness occurred at a powder concentration of 0.1 g/l and was most evident for the pulse on time duration of 606 ns. The more apparent reduction in recast layer thickness may be attributed to the space and time available for energy transfer interactions between the plasma channel and powder additives. In modelling the plasma channel, it was proposed that the expanding plasma channel vaporizes, disassociates and ionizes the dielectric at the plasma channel and dielectric interface [106]. In a study on PMD-EDM, it was observed that powder additives affected the extent of plasma channel expansion and that the powder additives stored energy absorbed from the plasma channel [156]. These observations may suggest that the absorption of energy from the plasma channel by the powder additives occurs at the plasma channel and dielectric interface. Thus, with a longer pulse on time duration the interface is larger in size as the plasma channel expands further and the time available for energy transfer also lengthens. As a result, a greater fraction of discharge energy may be absorbed by the powder additives and a smaller fraction is transferred to the workpiece, thereby forming a significantly thinner recast layer.

6.3.4 Mechanism of recast layer generation in PMD micro-EDM

The results shown in Figure 6.6 and Figure 6.7 indicated that the use of PMD micro-EDM with SiC nano-powder additive brought about a reduction in recast layer thickness. Furthermore, the concentration of nano-powder additive influenced the resulting recast layer thickness. To explore the mechanism of recast layer generation in PMD micro-EDM, a qualitative description of the process was proposed based on experimental observations of this research and reported findings of selected references. Next, a quantitative analysis of the process was performed using finite element methods (FEM) in support of the proposed mechanism of recast layer generation.

6.3.4.1 Qualitative description of recast layer generation in PMD micro-EDM

With reference to Figure 6.8, the recast layer may be viewed as a collection of recast regions from individual craters. Thus, the mechanism of recast region formation in a crater may be considered in order to explain the effects of powder concentration on recast layer thickness. During an electrical discharge, the border separating the melt pool and solid material defines the boundary of the recast region. The boundary becomes shallower as heat flux is reduced due to a decrease in discharge energy density or a reduction in fraction of heat flux distributed to the electrode. A fraction of the molten material in the melt pool is removed by flushing effects [138], pushed out of the melt pool by the overpressure of the plasma channel [137] and also expelled by the collapsing plasma channel at the end of discharge. Then the overflowed molten material and retained molten material within the melt pool resolidify as the recast region. The overflowed molten material produce overlapping recast layers which also contributes to recast layer thickness [216].

The amount of molten material removed during the electrical discharge is partly influenced by the pressure within the plasma channel. The overpressure within the plasma channel affects the amount of superheated molten material that may be boiled away at the end of discharge [103]. The magnitude of overpressure within the plasma channel is affected by the plasma channel size.

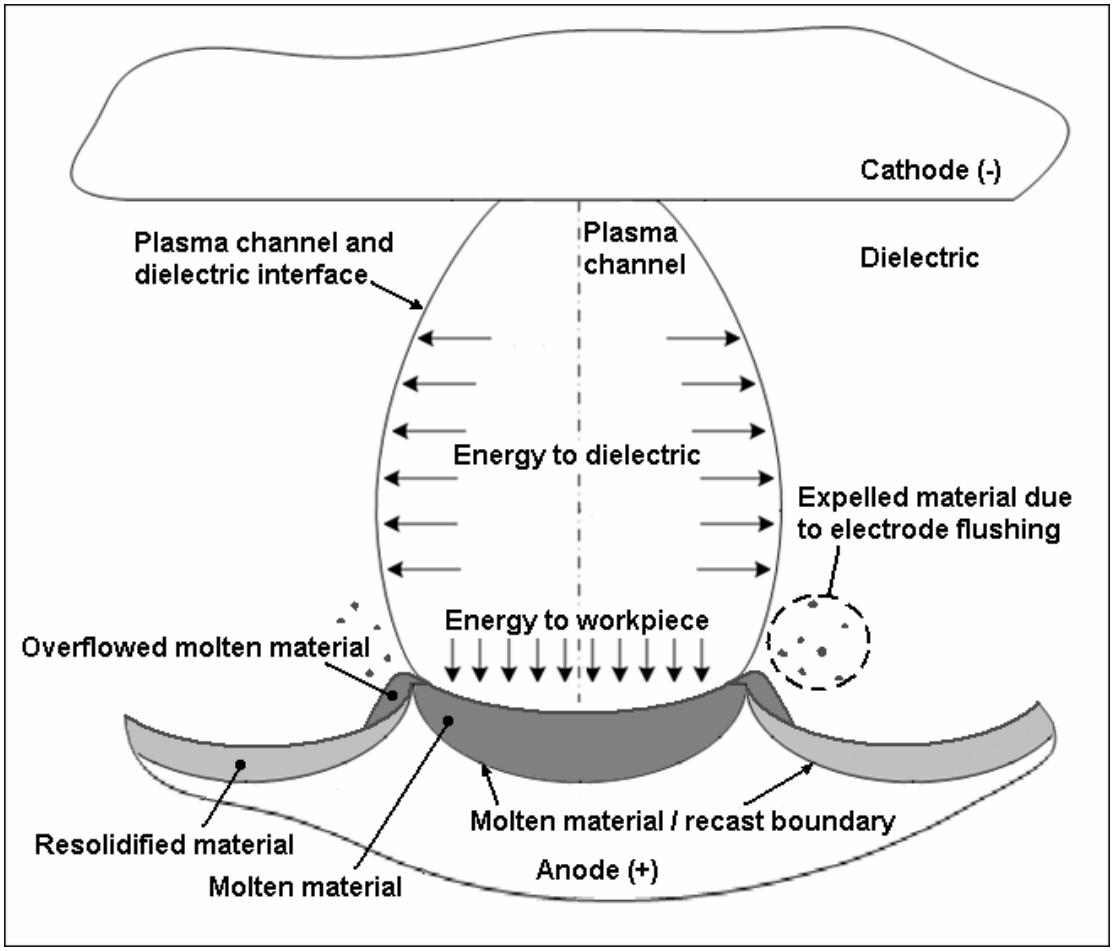

Figure 6.8 Mechanism of recast layer generation

With reference to the measurements of gap distance and recast layer thickness variation with powder concentration shown in Figure 6.5 and Figure 6.7, respectively, the following mechanism is proposed. At powder concentrations below 0.05 g/l, the significant gap enlargement suggested an increase in electrical conductivity of the dielectric brought about by the presence of nano-powder additives. The increase in dielectric conductivity would also enable a larger plasma channel expansion. This would cause a reduction in discharge energy density and result in the generation of a shallower melt pool. With a larger plasma channel, the overpressure within it would also decrease and result in a smaller plasma flushing efficiency (PFE). The decrease in recast layer thickness suggested that the decrease in depth of the shallower melt pool was more significant than the increase in height caused by an increase in molten material retention. At powder concentrations above 0.05 g/l, gap enlargement was not as significant as that below 0.05 g/l. This suggested that the increase in plasma channel expansion was not as significant as that below 0.05 g/l powder concentrations. Nevertheless, the larger plasma channel still decreased its overpressure and resulted in more molten material retention.

The larger plasma channel also decreased discharge energy density which was augmented by a smaller fraction of heat flux distributed to the workpiece arising from the presence of more nano-powder additives. Therefore, the depth of melt pool generated would still be shallower than that below 0.05 g/l powder concentrations. The relatively unchanged recast layer thickness suggested that the decrease in depth of the shallower melt pool was becoming less significant than the increase in height caused by the increase in molten material retention. In other words, the decrease in melt pool depth was offset by the increase in molten material height.

6.3.4.2 Quantitative analysis of recast layer generation in PMD micro-EDM

The quantitative explanation of the mechanism of recast layer generation in PMD micro-EDM was based on experimental results for 362 ns pulse on time. These experimental results included discharge voltage and current characteristics, crater radius, machined surface roughness and recast layer thickness. Using these results, a thermal analysis was conducted using FEM to estimate process constants such as fraction of heat flux distributed to the workpiece, plasma flushing efficiency and extent of plasma expansion. The experimental machining performance measures of machined surface roughness and recast layer thickness were then compared with their respective simulated performance measure values to ascertain the validity of the proposed recast layer thickness generation mechanism. The flow chart shown in Figure 6.9 illustrates the sequence of steps taken in the quantitative analysis process.

At the start of analysis, the average discharge voltage and current values generated in a powder-free dielectric were determined as 35.0 V and 0.92 A, respectively, for the pulse on time duration of 362 ns. These discharge characteristics were assumed to be constant for all powder concentrations. The heat flux incident on the workpiece was assumed to have a Gaussian distribution described by the following equation.

$$q(r) = q_0 \cdot \exp\left[-u\left(\frac{r}{R}\right)^2\right] \qquad (6.1)$$

where $q(r)$ represents the heat flux at radial coordinate r, q_0 the maximum heat flux at r = 0, u the distribution parameter that determines the concentration of the heat source and R the time-independent heat source radius. In simulating the heat flux distribution for the EDM process a u value of 4.5 has been used [144, 179, 219]. The magnitude of q_0 was

determined by equating the total heat energy of the Gaussian-distributed heat flux to the total heat energy distributed to the workpiece.

$$\int_{r=0}^{r=R} q_0 \cdot \exp\left[-4.5\left(\frac{r}{R}\right)^2\right] \cdot 2\pi r \cdot dr = F \cdot V_{av} \cdot I_{av} \qquad (6.2)$$

where F represents the fraction of heat distributed to the workpiece, V_{av} the average discharge voltage and I_{av} the average discharge current.

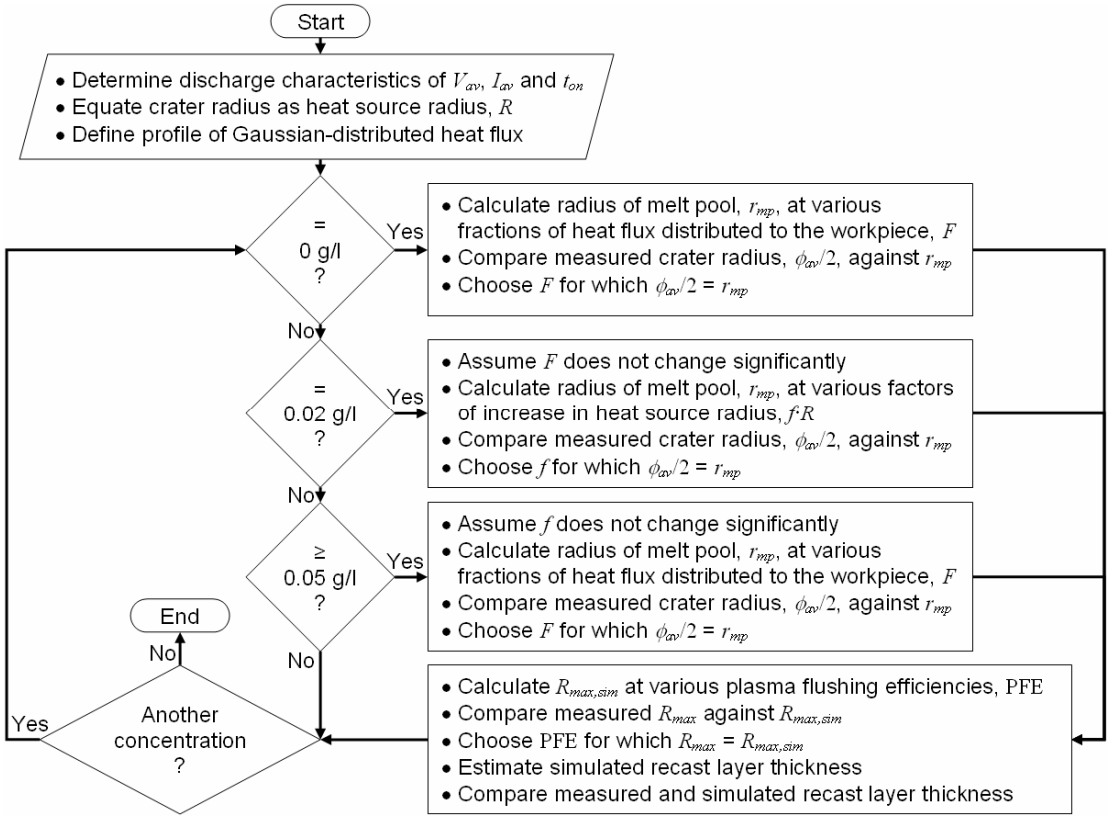

Figure 6.9 Process of quantitative analysis for recast layer generation in PMD micro-EDM

Solving Equation (6.2), as shown in Appendix C, the following relationship was established.

$$q_0 = \frac{4.55 \cdot F \cdot V_{av} \cdot I_{av}}{\pi \cdot R^2} \qquad (6.3)$$

Thus, combining Equations (6.1) and (6.3), the Gaussian-distributed heat flux incident on the workpiece may be described by the following expression.

$$q(r) = \frac{4.55 \cdot F \cdot V_{av} \cdot I_{av}}{\pi \cdot R^2} \cdot \exp\left[-4.5\left(\frac{r}{R}\right)^2\right] \qquad (6.4)$$

where the time-independent heat source radius, R, was assumed to be equal to the crater radius as proposed by Erden [204].

The crater radius used to represent the heat source radius was determined by taking the average of 6 crater radius measurements from the machined surface, as shown in Appendix C. Figure 6.10 shows the crater radii generated at 362 ns pulse on time and for all powder concentrations used in the quantitative analysis.

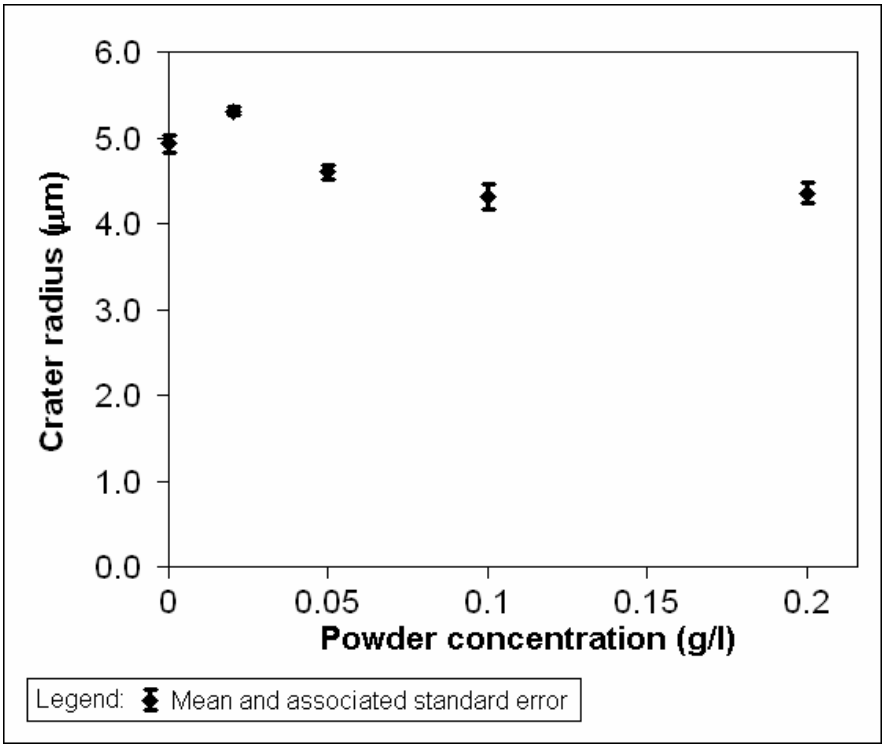

Figure 6.10 Crater radii at various powder concentrations

Since the crater radius ($\phi_{av}/2$) was considered a good indication of heat source radius (R), its change with respect to powder concentration would be a good gauge of the extent of plasma channel expansion in the powder-mixed dielectric ($f \cdot R$). Moreover, to analyse other changes in the PMD micro-EDM process, process constants such as fraction of heat flux distributed to the workpiece (F) and plasma flushing efficiency (PFE) were also determined. The decrease in fraction of heat flux distributed to the workpiece would indicate the increase in heat flux absorbed by the nano-powder additives. Similarly, the reduction in plasma flushing efficiency would point to the loss in overpressure within the plasma channel due to its larger expansion in the powder-mixed dielectric. Although the changes in F and PFE are useful indicators of process changes, only process performance measures, such as surface roughness and recast layer thickness, could be used in the comparison of measured and simulated results. Thus, simulated surface roughness ($R_{max,sim}$) and simulated recast layer thickness had to be determined for comparison with experimental results. The simulated process performance measures were estimated based on the F and PFE determined for PMD micro-EDM.

The changes in F and heat source radius (R) would occur simultaneously as powder concentration was increased, leading to greater complexity in analysing the mechanism of recast layer generation. Therefore, to address this, only one of the two process constants will be changed at each powder concentration.

At 0 g/l, F was determined based on equating the simulated melt pool radius (r_{mp}) and measured crater radius ($\phi_{av}/2$). PFE was determined by equating $R_{max,sim}$ and R_{max}. The recast layer thickness was then estimated. At 0.02 g/l, the decrease in F was assumed to be less significant than the increase in plasma channel expansion. This was because while the low powder concentration might contribute nano-powder additives to absorb the heat flux, the increase in crater radius shown in Figure 6.10 suggested that a more significant increase in plasma channel expansion occurred. Thus, the value of F determined at 0 g/l and a larger heat source radius ($f \cdot R$) were used in the simulation of melt pool radius (r_{mp}). The factor of increase in heat source radius (f) was estimated by equating the simulated melt pool radius (r_{mp}) and measured crater radius ($\phi_{av}/2$). Then PFE was again determined by equating $R_{max,sim}$ to R_{max} and the resulting recast layer thickness was also estimated. For powder concentrations of 0.05 g/l and above, the decrease in F was assumed to be more significant than the increase in plasma channel expansion. This was because while a higher powder concentration might promote a larger increase in plasma channel expansion, the decrease in crater radius shown in Figure 6.10 suggested that a more significant decrease in F occurred. Thus, the heat source radius ($f \cdot R$) determined at 0.02 g/l and a smaller value of F were used in the simulation of melt pool radius (r_{mp}). The various values of F for the different powder concentrations were estimated by equating the simulated melt pool radius (r_{mp}) and measured crater radius ($\phi_{av}/2$). Once again, PFE and recast layer thickness were estimated using the same method as the previous powder concentrations. The variations of f and F with powder concentration are shown in Figure 6.11. As illustrated, the factor of increase in heat source radius was unity at 0 g/l powder concentration and 1.07 at the other powder concentrations, which translated to an increase in heat source radius from 4.9 μm to 5.3 μm. On the other hand, the fraction of heat flux distributed to the workpiece remained at 0.24 for 0.02 g/l powder concentration, dropped to 0.14 for 0.05 g/l powder concentration and ranged between 0.1 and 0.11 for higher powder concentrations.

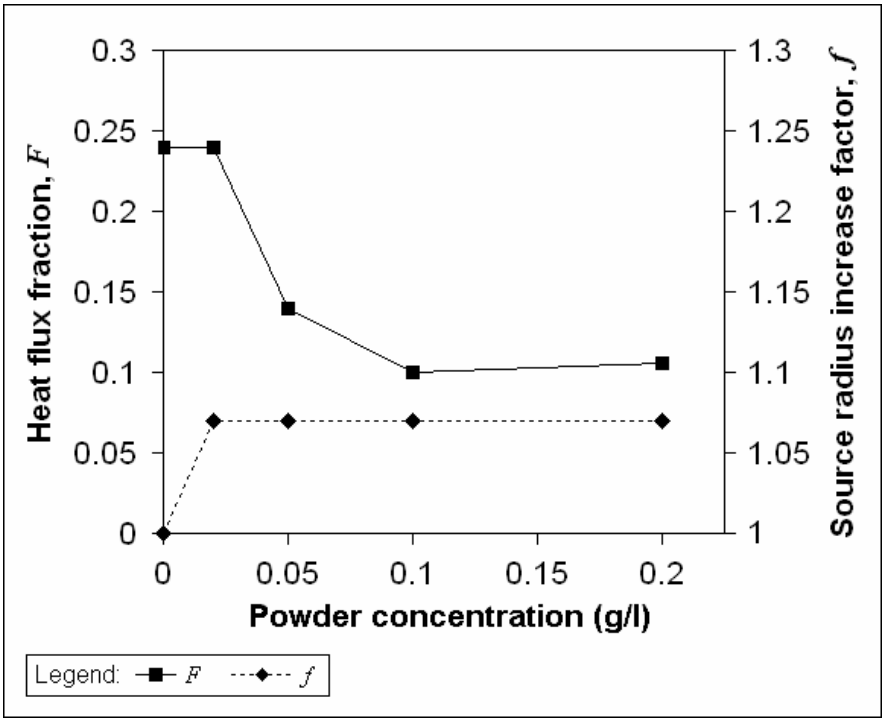

Figure 6.11 Variations of f and F with powder concentration

To ascertain the validity of the proposed recast layer thickness generation mechanism, the values of $R_{max,sim}$ and simulated recast layer thickness were compared with their respective measured values, as shown in Appendix C. At each powder concentration, the determination of $R_{max,sim}$ and simulated recast layer thickness used a common PFE value, which represented an interdependence between surface roughness and recast layer thickness. Figure 6.12 shows a typical result of FEM simulation from which the values of $R_{max,sim}$ and simulated recast layer thickness were measured.

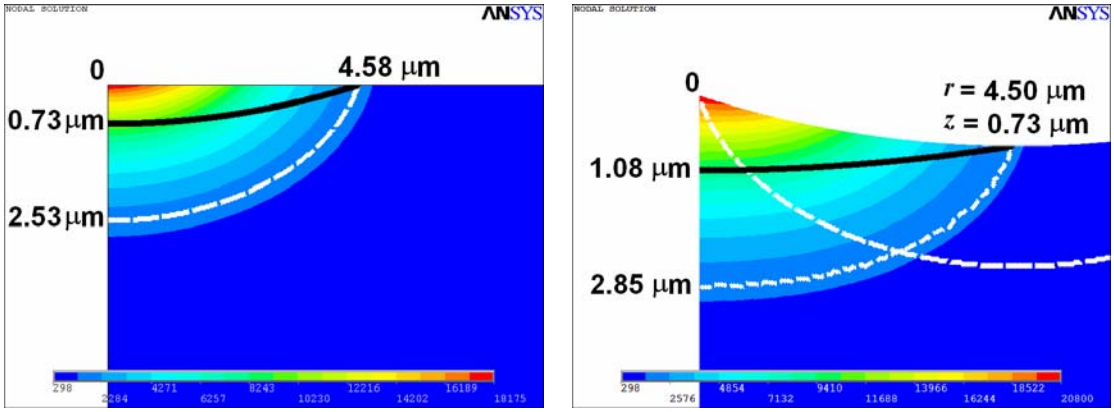

(a) First layer crater (b) Second layer crater

Figure 6.12 Typical results of FEM simulation

Generally, the results were drawn from the simulation of two consecutive layers of craters as it better represented the overlapping nature of craters on the machined surface. Two layers were chosen since it was assumed that if material removal occurred most readily at

highest points on the workpiece surface, then a layer by layer material removal process involving a coexistence of two layers of craters would occur. Figure 6.12(a) shows the results of thermal analysis conducted to determine the crater and melt pool generated for the first layer. The crater was represented by the solid black line while the boundary of the melt pool was represented by the dotted white line. Figure 6.12(b) shows the thermal analysis results for the crater and melt pool of the second layer. The second thermal analysis was performed by using the crater profile of the first layer as the initial boundary profile. The resulting crater for the second layer was represented by the solid black line while the boundaries of the melt pools for the first and second layers were represented by the dotted white lines.

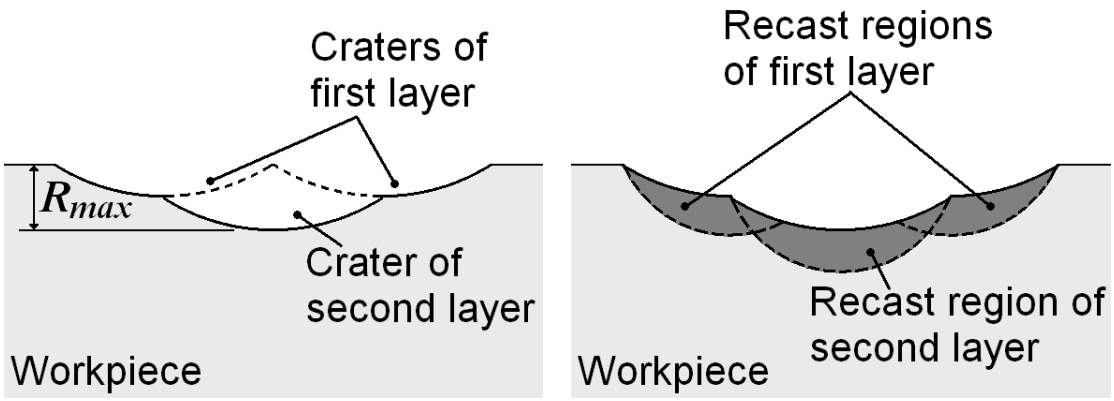

(a) R_{max} (b) Recast layer thickness

Figure 6.13 Determination of simulated process performance measures

Referring to Figure 6.13(a), the value of $R_{max,sim}$ was defined as the height between the apex of the crater in the first layer to the trough of the crater in the second layer. Furthermore, referring to Figure 6.13(b), the simulated recast layer thickness was determined by dividing the area of the dark-coloured region with the horizontal distance spanning the same region. A schematic illustration of the effects of powder concentration on process characteristics is shown in Figure 6.14. The illustration shows three states of powder concentration, namely, no powder, low concentration and high concentration. At low powder concentration, the plasma channel expands to a larger extent compared to that at powder-free condition which is represented by the dotted line within the dielectric. At high powder concentration, the extent of plasma channel expansion does not increase as much compared to that at low powder concentration. As a result of an electrical discharge on the workpiece, a melt pool is formed which is separated from the solid workpiece by the dotted curve. At the end of discharge, a portion of the molten material is expelled as represented by the lighter coloured region above the solid curve. The solid curve also

represents a crater surface. Thus, a recast region is formed as represented by the darker coloured region bounded by the solid curve and dotted curve.

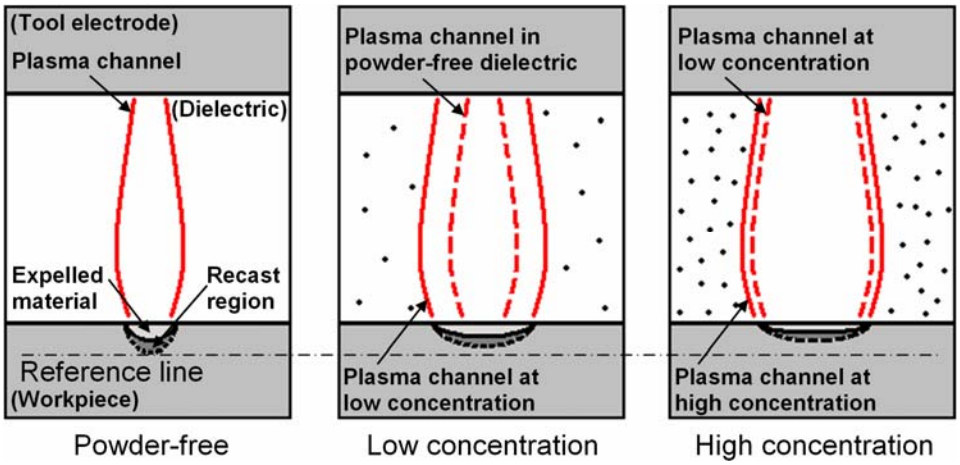

Figure 6.14 Illustration of process changes due to powder concentration

The comparison of simulated and measured results of R_{max} and recast layer thickness is presented in Figure 6.15.

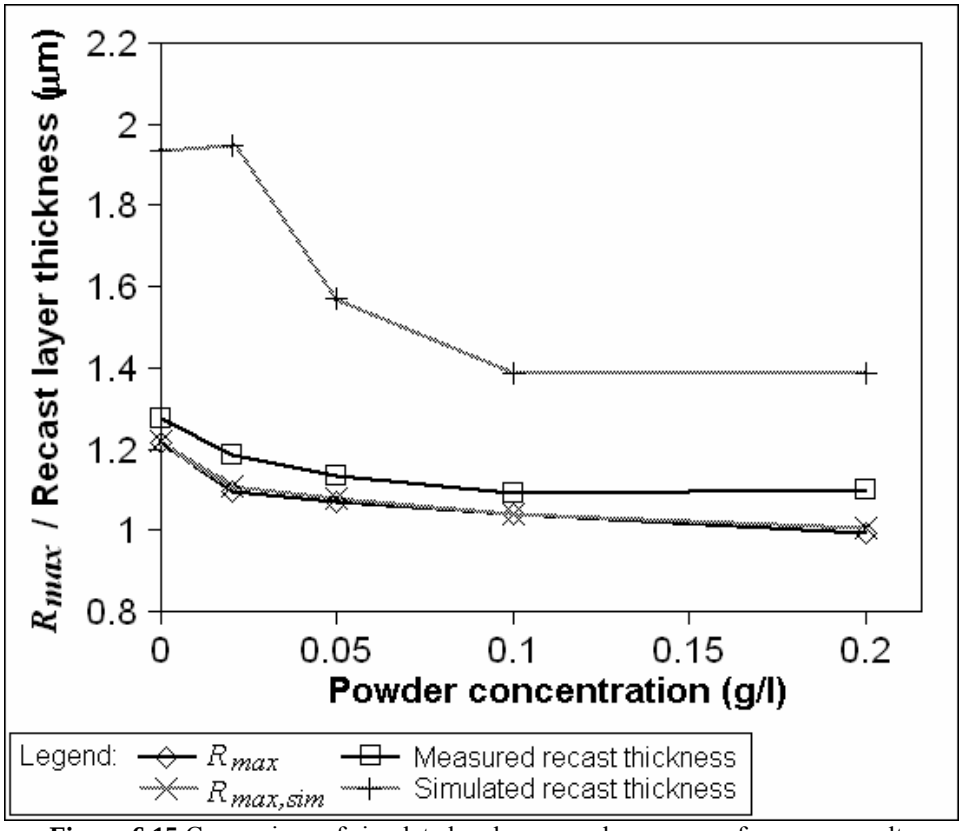

Figure 6.15 Comparison of simulated and measured process performance results

According to the results, the simulated and measured R_{max} results were closely matched since $R_{max,sim}$ and R_{max} were equated to determine the PFE values at each powder concentration. The decreasing R_{max} value shown in Figure 6.15 is correspondingly

depicted in Figure 6.14. The decrease in R_{max} was attributed to the decrease in overpressure within the plasma channel due to the channel's increased expansion. The results in Figure 6.15 showed a large deviation between simulated and measured recast layer thickness values. Nevertheless, the deviation was one-sided and the general trend of both sets of results was similar. This suggested that the proposed mechanism of recast layer generation in PMD micro-EDM was fundamentally sound. Nevertheless, owing to the complexities of describing the electro-thermal material removal mechanism, further refinement of process constants might be needed to provide better accuracy. According to the trend of decreasing recast layer thickness shown in Figure 6.15, the recast layer thickness approaches a constant value. As depicted in Figure 6.14, the decrease in recast layer thickness was attributed to a shallower melt pool due to a decrease in heat flux on the workpiece. The decrease in heat flux is due to the increase in heat source radius and a smaller fraction of heat flux distributed to the workpiece. The smaller fraction of heat flux resulted as more discharge energy was absorbed by the powder additives.

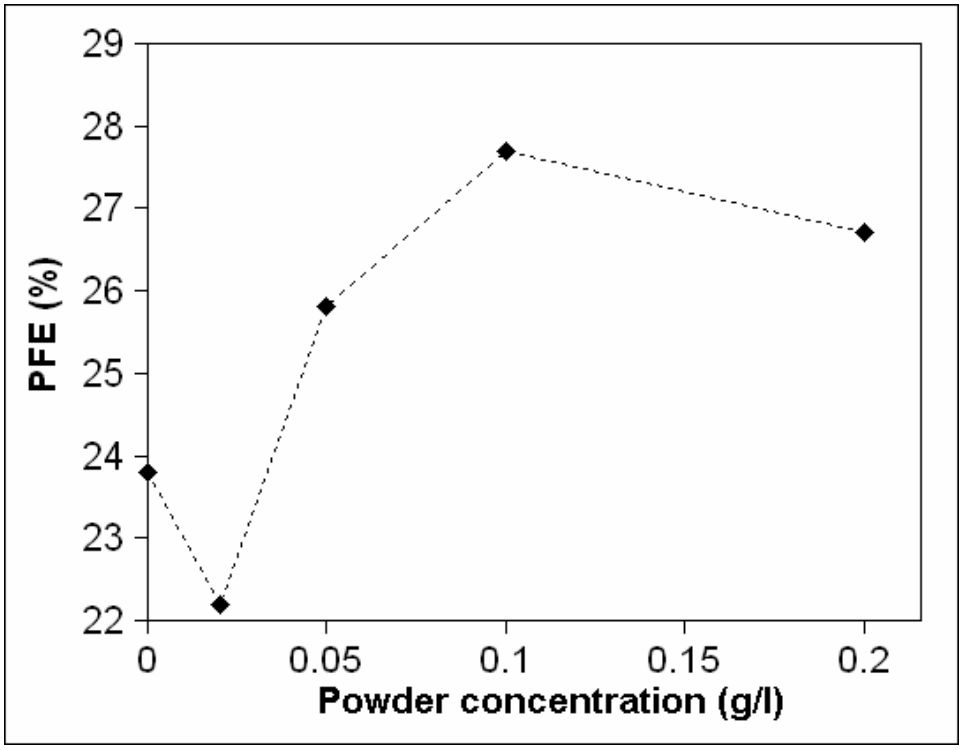

Figure 6.16 Variation of PFE values with powder concentration

The variations in PFE with powder concentration ranged between 22 % and 28 % as shown in Figure 6.16. Since PFE is the ratio of amount of expelled material to amount of material in the melt pool, the decrease in PFE from 0 g/l to 0.02 g/l indicated a decrease in amount of expelled material due to a decrease in plasma channel overpressure. The higher PFE values between powder concentrations of 0.05 g/l and 0.2 g/l compared to

0.02 g/l were attributed to a decrease in amount of material in the melt pool due to a decrease in fraction of heat flux distributed to the workpiece.

6.4 Summary

The recast layer thickness generated in micro-EDM and PMD micro-EDM processes were studied. The investigation employed machining parameters typical of the micro-EDM process, such as tool electrode rotation speed of 1000 rev/min and 3000 rev/min, peak discharge current of 1.45 A and pulse on time durations of 166 ns, 362 ns and 606 ns. Based on the results obtained, the following remarks can be made regarding the PMD micro-EDM process:

- The use of nano-sized SiC powder additives in small concentrations of less than 0.5 g/l was able to effect a reduction in recast layer thickness under micro-EDM process conditions.
- The flushing effects from a rotating tool electrode with rotation speed of 1000 rev/min generated a thicker recast layer than 3000 rev/min.
- The reduction in recast layer thickness due to the presence of powder additives was more evident for a pulse on time duration of 606 ns compared to 362 ns, when peak discharge current was maintained at 1.45 A.
- The increase in gap distance due to the presence of powder additives changed significantly for powder concentrations below 0.05 g/l. For powder concentrations between 0.05 g/l and 0.2 g/l, the increase in gap distance was relatively constant.
- At 606 ns pulse on time, the reduction in recast layer thickness due to an increase in powder concentration was more evident for initial increases in concentration up to 0.05 g/l. For powder concentrations between 0.05 g/l and 0.2 g/l, a relatively constant recast layer thickness was generated.
- The maximum reduction in recast layer thickness occurred at a concentration of 0.1 g/l and ranged between 15 % and 35 %.
- The changes in fraction of heat flux distributed to the workpiece (F) and heat source radius (R) are both affected by powder concentration. However, changes to R are more significant at lower concentrations while changes to F are more significant at higher concentrations.
- The mechanism of recast layer generation has been supported by FEM analysis. There was agreement in the general trend of simulated and measured results.

However, the magnitudes of simulated and measured recast layer thickness values showed a one-sided deviation.

- The deviation has been attributed to complexities in describing process constants like Gaussian profile, fraction of heat flux and heat source radius, which were used to model the electro-thermal material removal mechanism.

The reduction in recast layer thickness on a surface machined by the PMD micro-EDM process should be considered in surface quality improvement and surface modification applications. A reduction in recast layer thickness may represent one of the factors affecting the machined surface quality of micro-features while allowances for a reduced functional layer thickness should be given in surface modification applications.

Chapter 7
Process Modelling and Simulation

This chapter covers the results of numerical modelling and simulation conducted for the micro-EDM process. The purpose of models describing the micro-EDM process not only aids understanding of the material removal mechanism, it may also to serve as tools for process performance prediction. In the development of models to explain the material removal mechanism, a single crater generated by an electrical discharge is usually modelled. To enhance the single electrical discharge erosion model (SEDEM), a multiple discharge approach (MDA) is proposed. By adopting the MDA, a closer representation of the actual surface and sub-surface characteristics generated by the micro-EDM process may be achieved. In this chapter the purpose of developing the MDA for micro-EDM process modelling and simulation is explained. Following which the finite element method (FEM) used for modelling and simulation is presented. Then, the incorporation of MDA with the FEM solution for process modelling and simulation is explained. Finally, the modelling of surface roughness and recast layer thickness in the micro-EDM process to illustrate the MDA as well as model validation with data from machining experiments are covered. An overview of the chapter is shown in Figure 7.1.

Figure 7.1 Overview of Chapter 7

7.1 Process models for micro-EDM

Theoretical and empirical models have been developed for the EDM and micro-EDM processes. At its most basic, theoretical models describing the crater formation process due to a single electrical discharge have been developed [134, 190, 193]. These single electrical discharge erosion models (SEDEMs) have been used to elucidate the mechanism of crater formation as well as extended to the prediction of process performance measures. The methods used to extend the application of SEDEMs for process performance prediction included integration of Data Dependent Systems model with the SEDEM [142] and the use of surface factors to account for the effects of overlapping craters, pockmarks, micro-cracks and reattachment of debris on the actual machined surface [141]. A numerical procedure that incorporated a probability distribution of discharges occurring at various gap distances to predict the effects of successive discharges on material removal rate and surface roughness has also been proposed [202]. The availability of process models allows specific process performance measures to be related to a measurable or controllable machining parameter through mathematical expressions [47, 48] and can be adopted for actual machining operations. However, the stochastic nature of the EDM process presents difficulties in providing an exact match between predicted and measured results since the measured results itself display a degree of deviation. Thus, the objective of adopting the multiple discharge approach (MDA) for process performance prediction is to extend the application of SEDEMs to the determination of upper and lower limits of process performance measures. The MDA is adopted for the micro-EDM process since a key characteristic of the machined surface is the presence of overlapping craters.

7.2 Modelling with finite element method

The material removal phenomenon in EDM occurs under conditions which involves a combination of electrodynamic, thermodynamic and hydrodynamic effects [188]. Due to complexities arising from the multi-disciplined nature of the process, simplifications to

thermal loading and boundary conditions are usually made during the development of the material removal model, which are then solved by analytical or numerical methods. While the analytical approach requires specific thermal loading and boundary conditions to be applied, the numerical approach allows greater flexibility in the application of thermal loads, boundary conditions and material properties. As a result, wider ranging aspects of the electrical discharge erosion process may be included into the model to provide further insights into the material removal process. Some other benefits of the numerical approach include the ease of performing a time evolution of isothermal lines [101] and providing a concurrent display of various isothermal lines for an indication of different thermal affected zones [198]. One of the numerical analysis approaches commonly adopted for EDM is the finite element method.

7.2.1 Physical description

In the electro-thermal mode of material removal, the electrode material is removed through thermal melting and vaporisation as a result of a superheated and highly pressurised plasma channel formed between the electrodes during an electrical discharge. While the plasma channel has been modelled with a spherical shape and a cylindrical shape, the latter was used as it is considered to be the nearest geometry that approximated the actual barrel shape of the plasma channel [106]. The cylindrically-shaped plasma channel allows an axisymmetric consideration to be applied to the three-dimensional solution domain. As a result, the study was conducted on a two-dimensional model created in the radial and axial coordinates of the cylindrical coordinate system as shown in Figure 7.2.

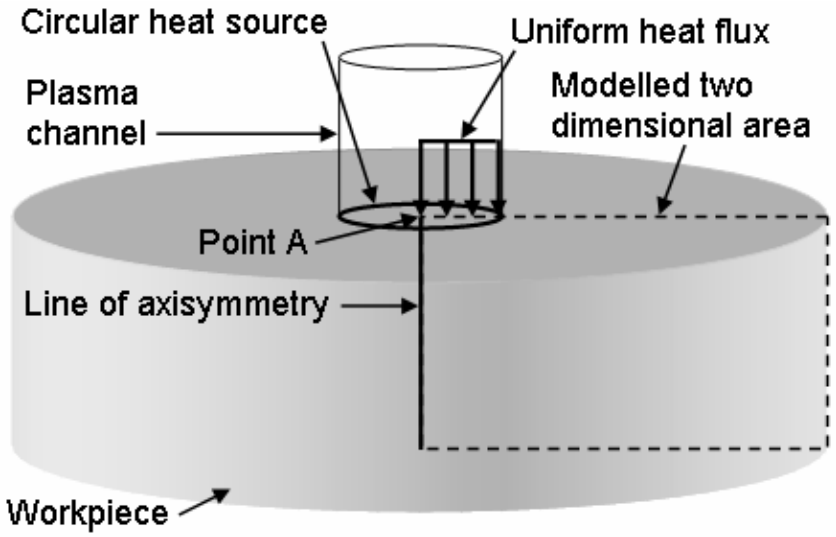

Figure 7.2 Schematic illustration of single electrical discharge erosion model

The growth of the plasma channel during electrical discharge is another characteristic that was considered in the model [103]. The expanding plasma channel causes a similar growth in the circular heat source, originating from point A, applied to the model. The heat flux associated with the heat source was also modelled with time dependence and derived from electrical discharge parameters of discharge voltage, discharge current and pulse on time. The heat flux was considered to be uniformly distributed about the heat source.

7.2.2 Mathematical description

The use of FEM for thermal analysis requires an underlying set of mathematical equations that represent various aspects of the electro-thermal material removal process. As described in Section 2.2.2, these equations include the thermal conduction model as well as expressions for heat source geometry and heat flux.

7.2.2.1 Thermal conduction model

The thermal conduction model adopted in the FEM analysis was the differential equation for heat transfer without internal heat generation. Written in cylindrical coordinates, the equation is

$$\frac{1}{r}\frac{\partial}{\partial r}\left(r\frac{\partial T}{\partial r}\right)+\frac{\partial^2 T}{\partial z^2}=\frac{\rho\cdot c}{k}\frac{\partial T}{\partial t} \qquad (7.1)$$

where T represents the temperature, r the radial coordinate, z the axial coordinate, t the time, k the thermal conductivity of the electrode material, ρ the mass density of the electrode material and c the specific heat capacity of the electrode material. Since the workpiece material for surface roughness modelling was stainless steel AISI 301 and that for recast layer thickness modelling was stainless mould steel AISI 420-MOD, the respective values of k, ρ and c used were 21.5 W/m·K, 8000 kg/m^3 and 500 J/kg·K for AISI 301 and 24.0 W/m·K, 7800 kg/m^3 and 460 J/kg·K for AISI 420-MOD.

In addition, the initial and boundary conditions associated with the model were expressed as follows

$$IC \quad : T(r,z,0) = T_0 \tag{7.2}$$

$$BCs \quad : -k\frac{\partial T(r,0,t)}{\partial z} = \begin{cases} q, & 0 < r \le R \\ 0, & r > R \end{cases} \tag{7.3}$$

$$: \frac{\partial T(0,z,t)}{\partial r} = 0, \qquad |z| > 0 \tag{7.4}$$

$$: T(\infty,\infty,t) = T_0 \tag{7.5}$$

where T_0 represents the ambient temperature, q the heat flux and R the heat source radius. The associated assumptions for the thermal conduction model are listed in Section 2.2.2.1.

7.2.2.2 Heat source

A variety of heat source characteristics have been used in the modelling of electrical discharges, such as shape, size and time-dependent growth. In this study, the time-dependent expanding circular heat source was used as it was suggested that the circular heat source is preferred for crater shape prediction and that the time-dependent heat source diameter growth should also be considered for more precise simulation of the electrical discharge erosion process [205]. The expression for the time dependent heat source radius was developed based on the measured crater radii from single discharge experiment since it has been proposed that measuring the crater shape was one approach to estimate the plasma channel diameter [189] and suggested that the crater radius was equal to the discharge radius [204]. Thus, re-writing equation (4.1), the time dependent heat source radius in a powder-free dielectric is expressed as

$$R(t) = 0.059 \cdot t^{0.79} \tag{7.6}$$

where $R(t)$ represents the time dependent heat source radius, measured in micrometers, and t the pulse on time, measured in nanoseconds. The pulse on time durations used in surface roughness modelling were 110 ns, 157 ns and 393 ns, while 106 ns, 362 ns and 606 ns were used in recast layer thickness modelling. The magnitudes of pulse on time for surface roughness modelling were a consequence of selecting capacitances of 500 pF, 1000 pF and 5000 pF for machining. On the other hand, the magnitudes of pulse on time for recast layer thickness modelling were determined by combinations of capacitance and inductance values that varied pulse on time duration while maintaining peak discharge current at 1.45 A. In general, the machining parameter magnitudes were chosen so that they were representative of those typical in micro-EDM and so that the resulting machining performance results at each machining condition were discernable.

7.2.2.3 Heat flux

The heat flux characteristics adopted in the modelling of electrical discharges include heat flux distribution within the heat source, time dependence of the heat flux and fraction of heat flux distributed to the cathode, anode and dielectric. The heat flux characteristics were empirically determined from discharge voltage, discharge current and pulse on time measurements. Considering a uniform heat flux distribution, the expression for the time dependent heat flux magnitude is written as

$$q(t) = \frac{F \cdot V(t) \cdot I(t)}{\pi \cdot R(t)^2} \qquad (7.7)$$

where $q(t)$ represents the time dependent heat flux, F the estimated fraction of heat flux distributed to the electrode, $V(t)$ the time dependent discharge voltage and $I(t)$ the time dependent discharge current.

The fraction of heat flux distributed to the electrode is an empirically determined constant, which has been suggested to be influenced by the dielectric condition as well as tool electrode and workpiece material combination. While a fraction of heat flux distributed to the anode of 0.48 was used in the model for surface roughness prediction for the EDM process [206], a set of fractions determined under micro-EDM conditions was used in the model for recast layer thickness prediction. The fractions were determined for a peak current of 1.45 A and pulse on time durations of 166 ns, 362 ns and 606 ns. By matching experimental and simulated crater radii results, the fractions for 166 ns, 362 ns and 606 ns were 0.33, 0.265 and 0.22, respectively. This trend is consistent with the suggestion that the fraction of heat flux distributed to the anode decreases as pulse on time increases [220]. The time dependent values of $V(t)$ and $I(t)$ were extracted from data captured by the oscilloscope which was capable of a sampling time interval of 0.5 ns.

7.2.2.4 Material properties

While performing the FEM study allows temperature-dependent material properties to be used, this study uses averaged material properties, which are typically employed when the heat conduction models are solved analytically. Furthermore, to account for the melting process, the adapted thermal diffusivity, defined by equation (2.10), is used. In addition, the following assumptions were made regarding the thermo-physical properties of the material:

- The thermo-physical properties of the electrode material are independent of temperature.
- The thermo-physical properties of the recast layer are similar to the base electrode material.

7.2.3 Numerical description

In the numerical description of the thermal conduction model, the weak form of the differential equation for heat transfer without internal heat generation and convective heat transfer for an elemental control volume may be expressed as:

$$\oint_{\Gamma^e} w q_n \, ds = 2\pi \int_{\Omega^e} \left[w\rho c \frac{\partial T}{\partial t} + k_r \frac{\partial w}{\partial r}\frac{\partial T}{\partial r} + k_z \frac{\partial w}{\partial z}\frac{\partial T}{\partial z} \right] r \cdot dr \cdot dz \qquad (7.8)$$

where

$$q_n = 2\pi r \left(k_r \frac{\partial T}{\partial r} n_r + k_z \frac{\partial T}{\partial z} n_z \right) \qquad (7.9)$$

and Ω^e represents a typical element, Γ^e the element boundary, w the weight function, q_n the heat flux normal to the element boundary, k_r and k_z the thermal conductivity in the r and z directions of the element, respectively, n_r and n_z the unit normal vectors in the r and z directions of the element, respectively.

Then, assuming that the time dependence and spatial variation are separable such that T is represented by the finite element approximation T^e over the element Ω^e,

$$T(r,z) \approx T^e(r,z) = \{N\}^T \{T^e\} \qquad (7.10)$$

where $\{N\}^T$ represents the transpose of the element shape function vector $\{N\}$ and $\{T^e\}$ the nodal temperature vector of the element.

Substituting $w = \{N\}$ and Eq. (7.10) into Eq. (7.8), the heat flow matrices in the finite element form is

$$\left[C^e\right]\left\{\dot{T}^e\right\} + \left[K^e\right]\left\{T^e\right\} = \left\{q^e\right\} \qquad (7.11)$$

where

$$\left[C^e\right] = \rho \cdot c \int_{\Omega^e} \{N\}\{N\}^T \, r \cdot dr \cdot dz = \text{element specific heat matrix}$$

$$\left[K^e\right] = \int_{\Omega^e} [B]^T [K][B] r \cdot dr \cdot dz = \text{element diffusion conductivity matrix}$$

$\{q^e\} = \oint_{\Gamma^e} \{N\} q_n \, ds$ = element heat flux vector

$\{T^e\}$ = element nodal temperature vector

$\{\dot{T}^e\}$ = time derivative of element nodal temperature vector

$\{N\}$ = element shape function vector

$[B] = \{L\}\{N\}^T$ = shape function derivative matrix evaluated at integration points

$[K] = \begin{bmatrix} k_r & 0 \\ 0 & k_z \end{bmatrix}$ = conductivity matrix

$\{L\} = \begin{Bmatrix} \dfrac{\partial}{\partial r} \\ \dfrac{\partial}{\partial z} \end{Bmatrix}$ = vector operator

The FEM model was created using ANSYS, a commercially available software for FEM modelling and analyses. With the assumption that the heat source and resulting crater are axisymmetric about the centre of the circular heat source, a two-dimensional model was developed as shown in Figure 7.3.

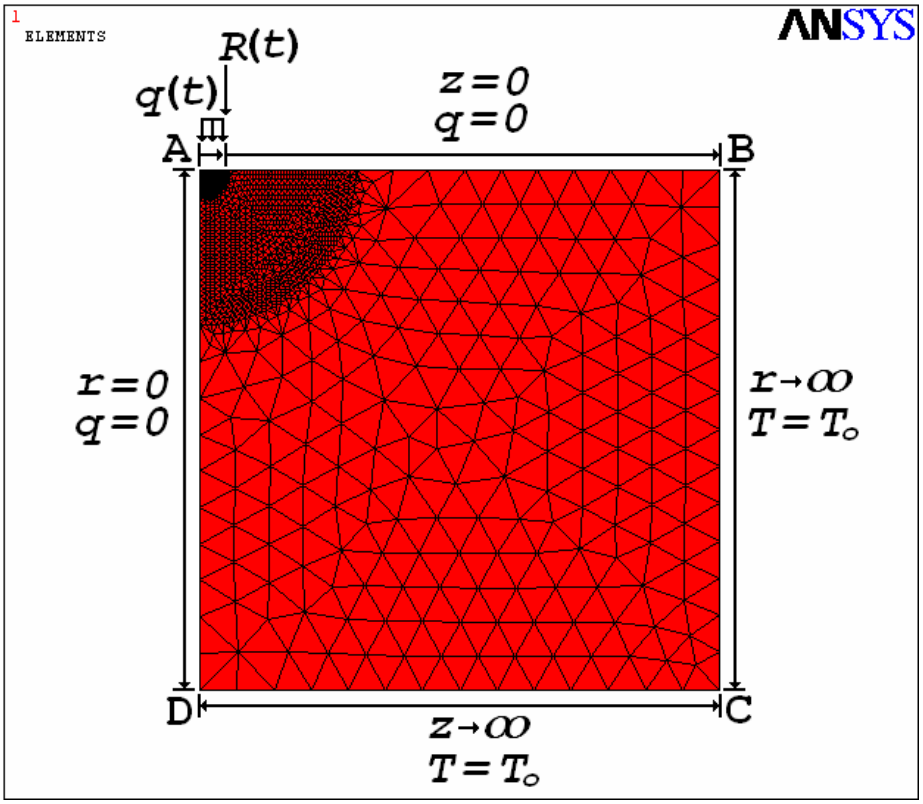

Figure 7.3 FEM model and assigned boundary conditions

The mesh was made up of triangular elements with varying sizes such that the smallest elements were located at the region of heat source application. A time varying boundary condition was applied on boundary AB, which consisted of two components. The first was an expanding heat source originating from Point A and equal to a heat source radius at a specified time. The second was an adiabatic condition along the remainder of the boundary. The adiabatic condition was applied as it was assumed that convective and radiation heat transfers from the machined surface were negligible given the short discharge time duration. The boundary conditions on boundaries BC and CD were assigned to be at ambient temperature and located at an infinite distance from the heat source. This was because the size of the heat source was considered to be much smaller than the size of the electrodes. The boundary condition along the line of axisymmetry, labelled as boundary DA, was also considered adiabatic.

The consideration of time dependent heat source radius and heat flux requires thermal loading to be applied in separate time steps within the pulse on time duration, as illustrated by the flowchart shown in Figure 7.4. The number of time steps is calculated as

$$n = \frac{t_{on}}{\Delta t} \tag{7.12}$$

where n represents the total number of time steps, t_{on} the pulse on time and Δt the duration of the time step. The duration of each time step was set at 1 ns so that the number of time steps was equivalent to the pulse on time. Furthermore, the heat source radius and heat flux at each time step can be estimated from the discretized form of equations (7.7) and (7.9), which are respectively shown as

$$R_i = 0.059 \cdot (i \cdot \Delta t)^{0.79} \tag{7.13}$$

$$q_i = \frac{F \cdot V_i \cdot I_i}{\pi \cdot R_i^2} \tag{7.14}$$

where R_i represents the heat source radius, q_i the heat flux, V_i the discharge voltage and I_i the discharge current at the i^{th} time step. These empirically obtained values are shown in Appendix D.

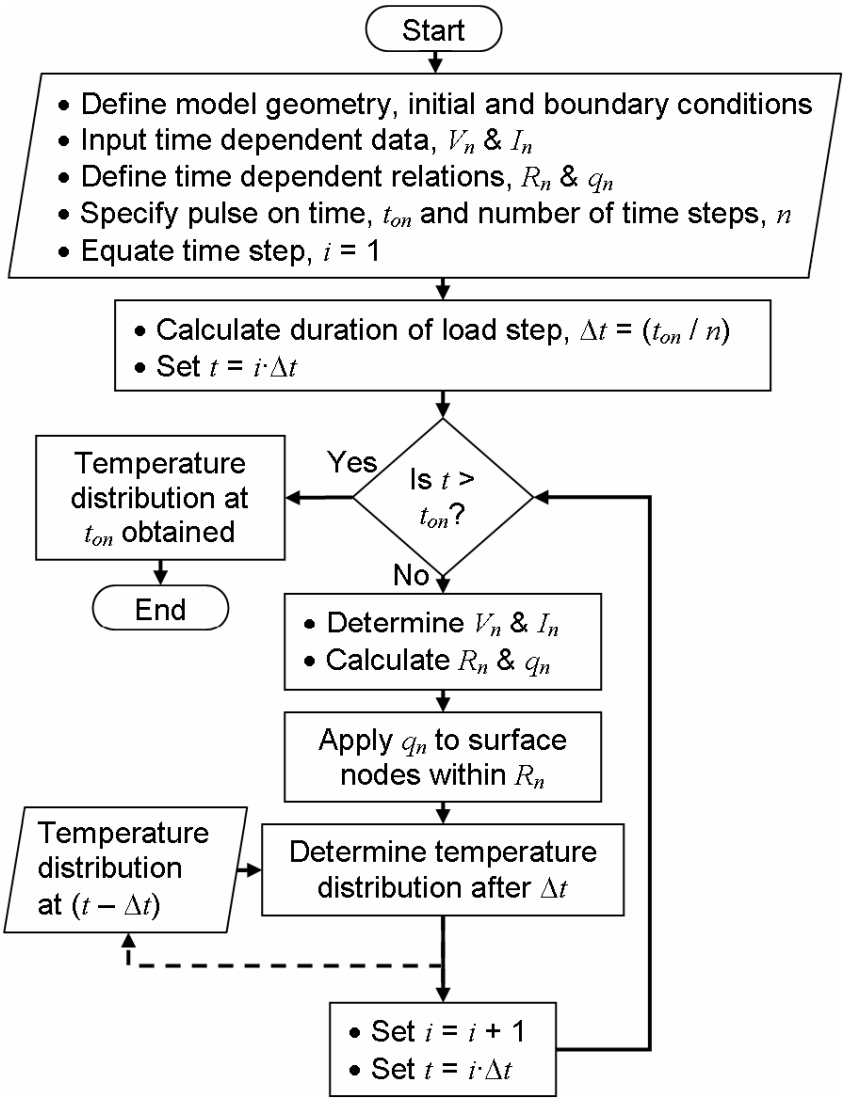

Figure 7.4 Flowchart illustrating the application of the time vary thermal load

7.2.4 Simulation process

The simulation process adopted in the multiple discharge approach (MDA) utilised a generic and repetitive two-stepped procedure that comprised a numerical analysis of thermal distribution and a geometrical determination of crater profile. As shown in Figure 7.5, the first step involved a numerical determination of the thermal distribution on a workpiece that was subjected to a heat flux from a single electrical discharge. Next, the crater profile was estimated by considering that a fraction of the molten material, bounded by the isothermal line corresponding to the melting temperature of the workpiece material, was expelled at the end of the electrical discharge. The fraction of expelled molten material is termed as the plasma flushing efficiency (PFE) and defined as the ratio of actual volume of material removed to the total volume of predicted melt pool in the

electrode [104]. Subsequently, the retained molten material was assumed to resolidify within the melting isotherm with a hemispherical-capped top profile, thereby forming the recast region of the crater.

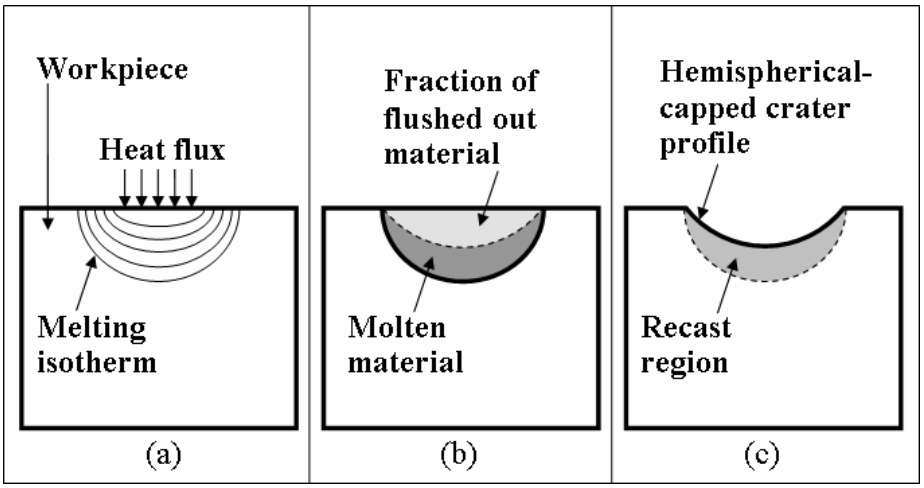

Figure 7.5 Generic simulation process in the multiple discharge approach

The two-stepped procedure was utilised in conjunction with the following assumptions:

- The magnitude of heat flux incident on the workpiece is independent of the affected surface profile.
- The effects of discharge gap variations on discharge characteristics are negligible.
- The effects of machining depth on plasma flushing efficiency are negligible.
- The molten material remains within the boundary of the crater.

To model the machined surface profile two-dimensionally in the MDA, considerations on the suitability of the modelled surface profile in representing the actual surface profile were required. These considerations were influenced by the machining performance measure which the model was developed to study. In modelling the surface roughness, the shape of a body subjected to the thermal influence of a heat flux was taken into consideration while the modelling of recast layer thickness considered the change in surface profile after a discharge at the apex of neighbouring craters. Furthermore, due to the stochastic nature of the EDM process the isotropic machined surface possesses numerous configurations of machined surface profile which may be modelled. Therefore, instead of modelling every possible machined surface profile, two extreme configurations were modelled to allow an upper and lower bound of a specified machining performance measure to be predicted. Then the range of values within the bounding limits may serve

as a gauge for the machining performance measure, which when measured would also display such deviations in values.

7.2.4.1 Modelling of surface roughness

In modelling the surface roughness with MDA, the two extreme configurations of machined surface profile were chosen based on the shape of a body subjected to the thermal influence of a heat flux. Since heat energy is consumed during melting of a material and also conducted away from the heat source by the material, the shape of the body subjected to the heat energy will affect the amount of molten material produced. The two factors used to define the body shape were the height and top surface area of the surface asperity subjected to the heat flux. Since the depth of a crater produced on a flat surface with zero surface asperity is theoretically the shallowest due to the availability of a larger heat conduction front, a heat flux applied to a surface asperity will generate a relatively deeper crater profile. The depth of the crater profile is considered since it directly affects the roughness of a machined surface. To determine the deepest crater profile, the highest surface asperity with a pointed top, defined as the maximum asperity condition, was used. The shallowest crater profile was determined using a top surface area equal to that of the heat source. This condition was chosen so that a consistent minimum asperity condition was maintained across various thermal loading scenarios.

The crater layout illustrated in Figure 7.6(a) was used to extract a machined surface profile for the maximum asperity condition since two neighbouring craters in contact at the crater rim would produce the surface asperity with a pointed top. To create a two-dimensional model for analysis, the extracted machined surface profile taken from line AA, as shown in Figure 7.6(b), was assumed to be axisymmetric about the contacting point of the neighbouring craters. As a result, the model of the machined surface profile is smaller in shape than the actual machined surface profile and was expected to generate a crater that was deeper than the actual case. Thus, half the machined surface profile shown in Figure 7.6(b) was modelled and solved by applying the depicted thermal loading condition.

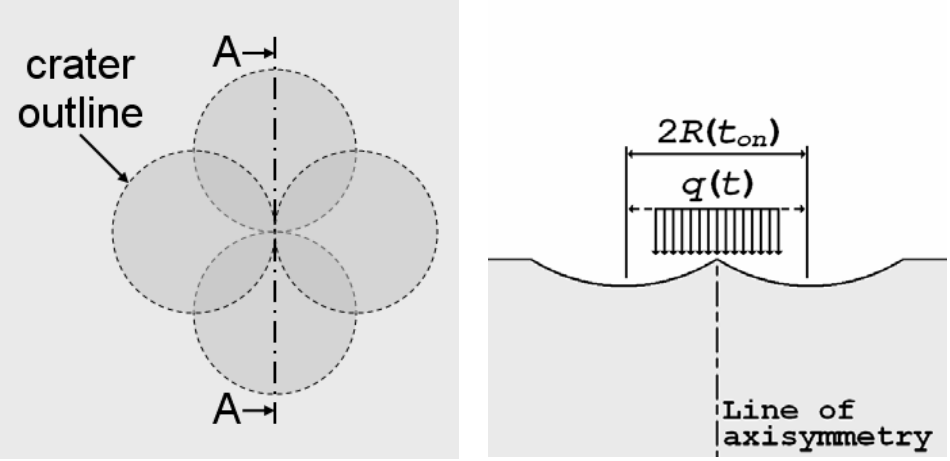

(a) Top view – layout of overlapping craters

(b) Side view – extracted machined surface profile along A-A

Figure 7.6 Extraction of machined surface profile for maximum asperity condition

The shallowest crater depth in the case of multiple discharges may not be equivalent to the crater depth predicted using the single discharge model. This is because the crater profile produced on a machined surface may be different from that produced on a flat surface due to the effects that neighbouring craters may have on the resulting thermal distribution from the heat source. Thus, to include the effects of neighbouring craters on thermal distribution, the largest top surface area was chosen as the heat source area. Considering the crater layout illustrated in Figure 7.7(a), it was noted that the machined surface profile extracted from line BB might be used to represent the general form of the minimum asperity condition since such a layout would result in the smallest surface roughness value. By applying the assumption of axisymmetry to the extracted surface profile about the midpoint of the distance between the neighbouring craters, the resulting modelled surface profile was larger in shape than the actual machined surface profile and was expected to generate a crater that was shallower than the actual case. Furthermore, to include the consideration of neighbouring craters in the extracted profile, the distance separating the two craters was assumed to be equal to the heat source diameter as shown in Figure 7.7(b). Thus, half of this machined surface profile was modelled and solved by applying the depicted thermal loading condition.

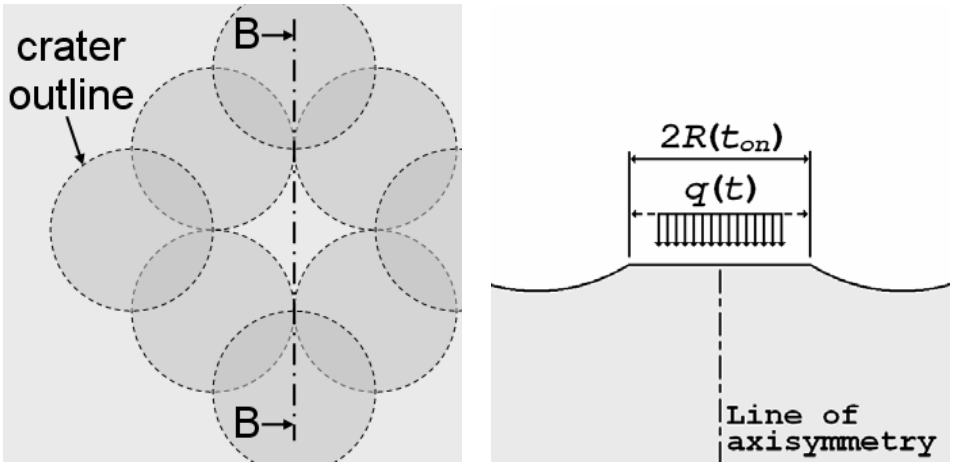

(a) Top view – layout of overlapping craters

(b) Side view – general machined surface profile along B-B

Figure 7.7 Extraction of machined surface profile for minimum asperity condition

7.2.4.2 Modelling of recast layer thickness

In modelling the recast layer thickness with MDA, a reference machined surface profile was generated so as to serve as a base for the simulation and prediction of the upper and lower limits of recast layer thickness. The process to generate the reference machined surface profile is schematically shown in Figure 7.8, while Figure 7.9 gives a flowchart representation of the complete simulation process for recast layer thickness modelling.

As shown in Figure 7.8(a) to Figure 7.8(c), the first three steps in the generation of the reference machined surface profile involved simulating the discharge on a flat surface. In the case of recast layer thickness modelling, the fraction of heat flux distributed to the workpiece was estimated for each pulse on time duration modelled by matching the simulated and measured crater radii. Furthermore, the PFE used was determined through an iterative process of comparing the simulated and measured recast layer thickness results and is termed the recast plasma flushing efficiency (recast PFE). The crater profile resulting from the simulation of discharge on a flat surface was arranged as neighbouring craters to create the first layer of craters shown in Figure 7.8(d). The subsequent discharge was then assumed to occur at the apex of neighbouring craters in the first crater layer since it is the location with the highest probability of discharge occurrence. Next, as shown in Figure 7.8(e) and (f), the recast PFE was used to determine the amount of material retained within the melting isotherm and to generate the hemispherical-capped crater profile.

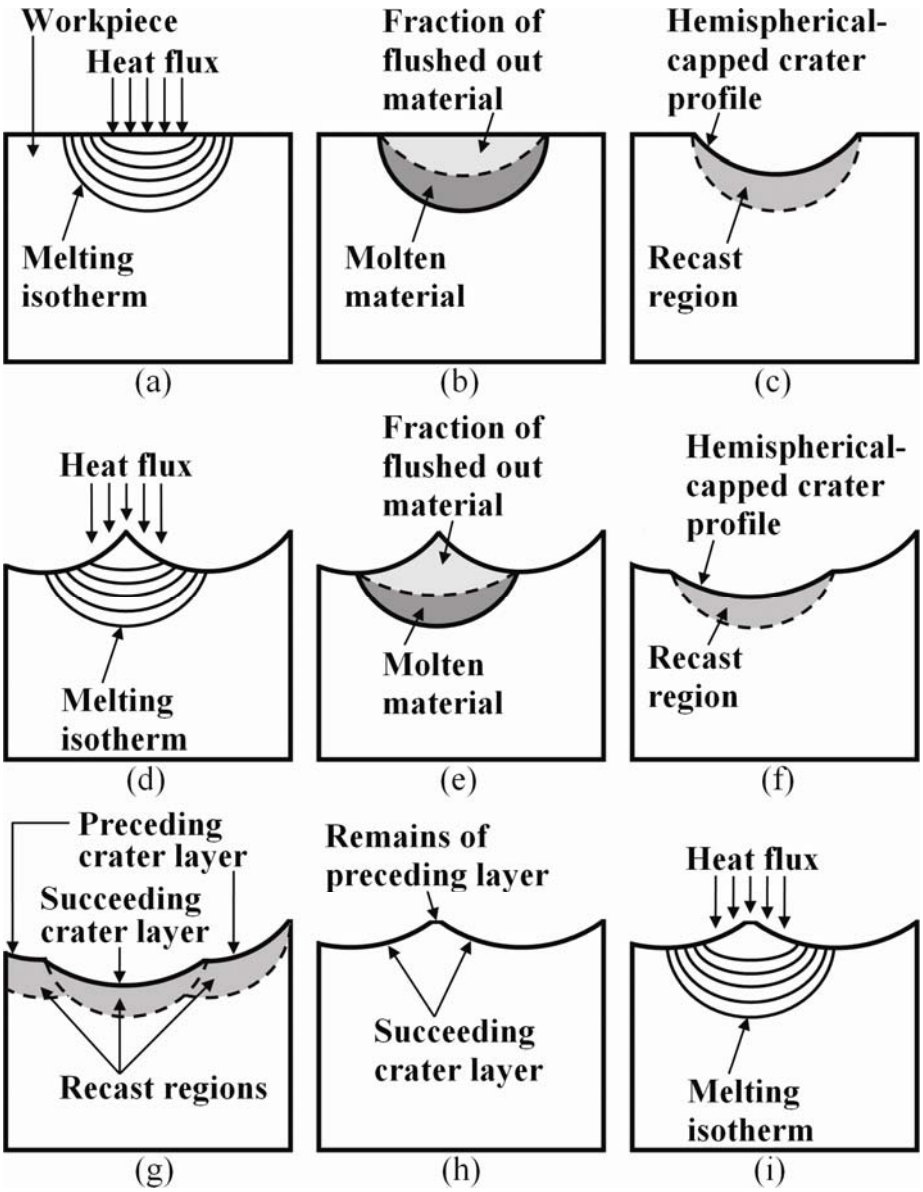

Figure 7.8 Generation of reference machined surface profile

Figure 7.8(g) shows the resulting overlapping crater profile, which comprised craters from preceding and succeeding layers. Considering that discharges continued to occur at the apex of neighbouring craters in the preceding layer, where gap width was the shortest, the resulting overlapping crater profile would consist of craters from the succeeding layer and remains of crater troughs from the preceding layer, as shown in Figure 7.8(h). When the resulting overlapping crater profile showed minimal changes compared to the earlier crater profile in terms of crater depth and remains of crater trough, the crater profile was used as the reference profile to determine the upper and lower limits of recast layer thickness. Else, another discharge was assumed to occur at the apex of neighbouring craters in the resulting crater layer, as shown in Figure 7.8(i), and the process was repeated. When a relatively steady state in machined surface profile is reached, the

boundary profile on which heat flux is applied and the resulting thermal distribution and recast region are also expected to shown minimal changes.

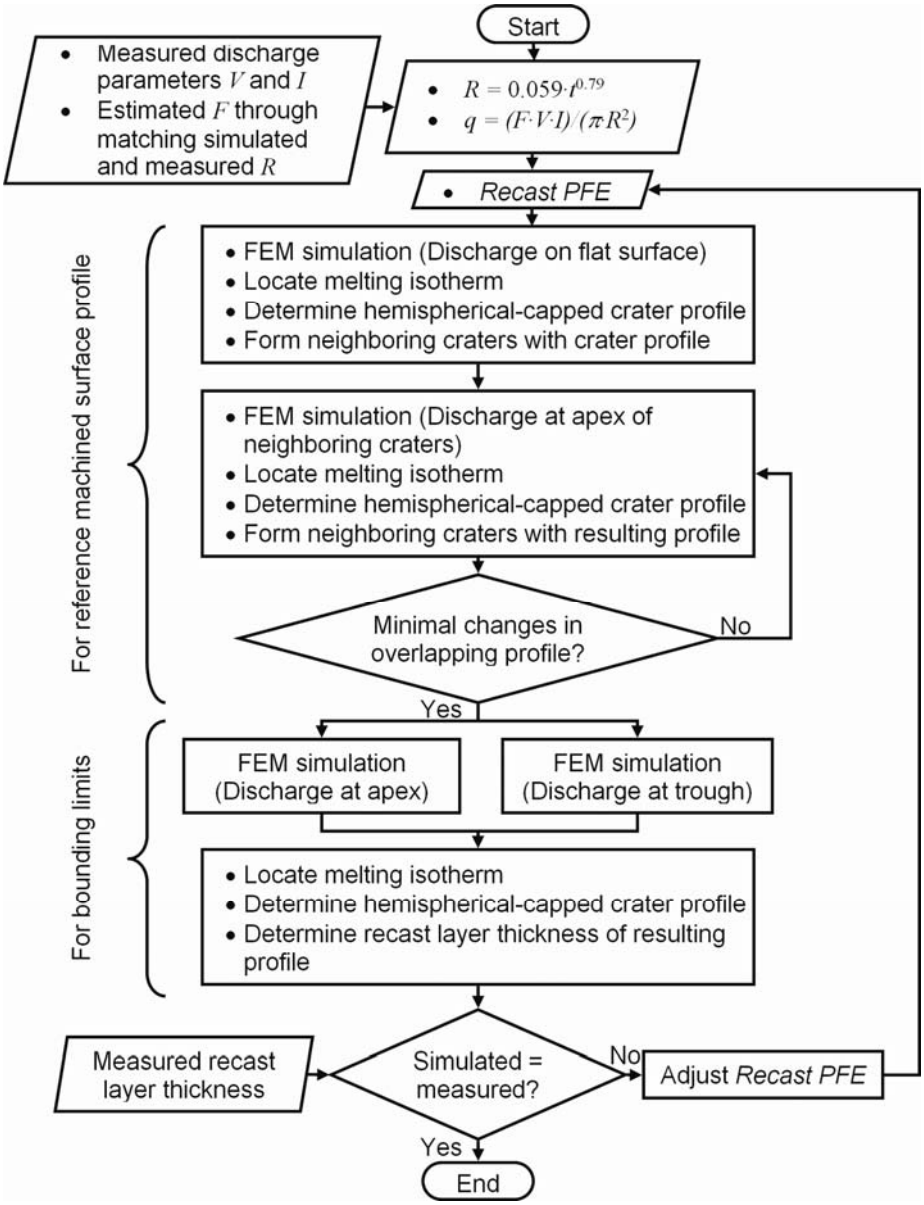

Figure 7.9 Flowchart of simulation process in recast layer thickness modelling

As shown in Figure 7.9, the determination of bounding limits for recast layer thickness began after the reference machined surface profile was established. The bounding limits were determined based on two extreme cases under which the recast layer may be formed. The first case considered the discharge to originate at the point represented by the apex of two neighbouring craters while the second case considered the discharge to originate at the trough of the crater as shown in Figure 7.10(a) and (b), respectively. As these two cases represented the two extreme surface profiles that may be subjected to an electrical discharge, the resulting thermal distribution and recast layer thickness were expected to

yield the bounding limits of recast layer thickness. The recast PFE was still used to determine the amount of molten material retained within the melting isotherm and to generate the hemispherical-capped crater profile and recast region. The recast layer thickness of the resulting profile was then compared with experimental data to determine the suitability of recast PFE value used. When the simulated and measured recast layer thickness values were in agreement, the simulation process was stopped. Else, the recast PFE value was adjusted and the simulation process was repeated.

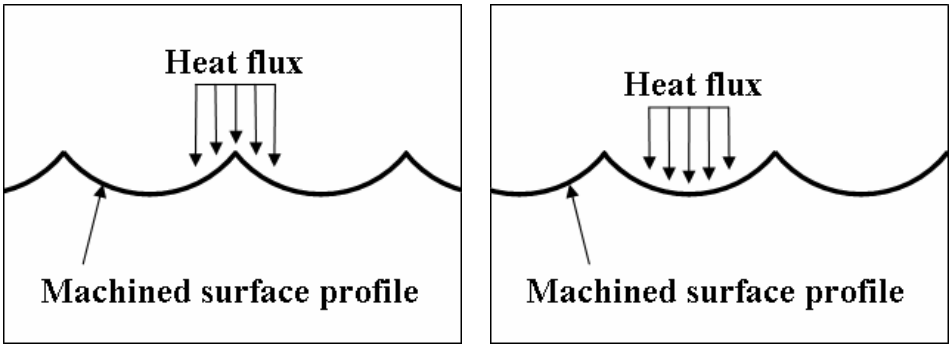

(a) At apex of neighbouring craters (b) At trough of a crater

Figure 7.10 Heat flux location for modelling bounding limits of recast layer thickness

7.3 Scope of numerical modelling and simulation

The numerical modelling and simulation were performed for conditions that were representative of the micro-EDM process. The average measured discharge energies studied ranged between 1.6 μJ and 21 μJ, while the time dependent voltage and current characteristics of electrical discharges from an RC pulse generator were modelled since the latter is commonly used in micro-EDM. In the modelling of surface roughness, results of single discharge experiment conducted with an RC pulse generator were used for model development. The subsequent model validation was performed by using the roughness of surfaces machined by a micro-EDM system that also employed the RC pulse generator. In the modelling of recast layer thickness, machining parameters from the RLC pulse generator were used so that pulse on time duration could be varied with minimal changes to peak discharge current.

7.3.1 Modelling of surface roughness

In developing the model for surface roughness estimation, results of the single discharge experiment were used to derive the empirical expression for growth of heat source radius. Furthermore, by comparing the measured geometries of craters to their corresponding predicted geometries, the plasma flushing efficiencies for average measured discharge energies of 1.6 μJ, 3.4 μJ and 14.6 μJ were estimated. The experiment was conducted on

the single discharge test rig with the machining conditions shown in Table 7.1. Moreover, the material properties of stainless steel AISI 301 were used in the FEM analysis of electrical discharge on the workpiece.

Table 7.1 Machining conditions for model development

Machining parameter	Value
Open circuit voltage, V_{OC} (V)	100
Capacitance, C (pF)	500; 1000; 5000
Input energy, E_{in} (μJ)	2.5; 5.0; 25.0
Measured discharge energy, E_m (μJ)	1.6; 3.4; 14.6
Workpiece material	Stainless steel, AISI 301
Tool electrode material	Tungsten
Tool electrode diameter (μm)	150
Gap distance (μm)	≈ 2.5

The estimated PFEs were then used in the generation of overlapping crater profiles, based on the multiple discharge approach and predefined maximum and minimum asperity conditions, for the three measured average discharge energies. The generated overlapping crater profiles were used to determine the upper and lower bounds of R_{max}. The surface parameter R_{max} is defined as the maximum peak to valley height of a profile within the sampling length. The surface parameter R_{max} was shown to be directly related to a free polishing depth, which was defined as the depth at which all surface craters would disappear [166]. It was also suggested that the knowledge of free polishing depth could aid in the removal of residual stress on the machined surface, which may be helpful in improving the fatigue strength of micro-components. Furthermore, the maximum peak to valley height of the machined surface profile may indicate the deviation in geometrical accuracy of a micro-feature since the relative size difference between a micro-feature and a discharge crater produced in micro-EDM may be very small [136]. Finally, the model developed using the MDA was validated through comparing the predicted R_{max} values with measured R_{max} values of surfaces machined by the micro-EDM system using machining conditions shown in Table 7.2. The results of validation experiments are shown in Appendix D.

Table 7.2 Machining conditions for model validation

Machining parameter	Value
Open circuit voltage, V_{OC} (V)	100
Capacitance, C (pF)	220; 1000; 2000; 3300
Measured discharge energy, E_m (μJ)	1.0; 3.2; 5.5; 10.4
Workpiece material	Stainless steel, AISI 301
Tool electrode material	Tungsten
Tool electrode diameter (μm)	300
Feature machined	300 μm deep blind hole

7.3.2 Modelling of recast layer thickness

In developing the model for recast layer thickness prediction, the fractions of heat flux distributed to the workpiece at different pulse on time durations were estimated by matching measured crater radii with simulated results for a range of fractions at a corresponding pulse on time duration. The fraction of heat flux was then used to generate overlapping crater profiles and interconnecting crater recast regions to determine the recast PFE and corresponding upper and lower bounds of recast layer thickness through an iterative process. By applying the MDA on prescribed reference machined surface profiles the simulated upper and lower bounds of recast layer thickness, at a specified recast PFE, were generated and compared with measured results. The recast PFE and simulated bounding limits were incorporated into the model when the simulated and measured results matched. Machining experiments conducted using the RLC pulse generator with the machining parameters shown in Table 7.3 generated the measured results used in model development. These results are shown in Appendix D.

Table 7.3 Machining conditions for model development

Machining parameter	Value
Open circuit voltage, V_{OC} (V)	100
Peak discharge current, I_{pk} (A)	1.45
Pulse on time, t_{on} (ns)	166; 362; 606
Measured discharge energy, E_m (μJ)	5.0; 11.7; 21.0
Workpiece material	Stainless mould steel, AISI 420-MOD
Tool electrode material	Tungsten
Tool electrode diameter (μm)	300
Feature machined	150 μm deep blind hole

The model consisted of bounding limits of recast layer thickness simulated at peak discharge current of 1.45 A and pulse on time durations of 166 ns, 362 ns and 606 ns. A constant peak discharge current was used in the model as it was reported that changes in pulse on time had a more significant influence on recast layer thickness than changes in peak current [118]. To validate the model, recast layer thickness values were measured from blind holes machined at conditions shown in Table 7.4. The results of validation experiments are shown in Appendix D.

Table 7.4 Machining conditions for model validation

Machining parameter	Value
Open circuit voltage, V_{OC} (V)	100
Peak discharge current, I_{pk} (A)	1.45
Pulse on time, t_{on} (ns)	244; 458
Measured discharge energy, E_m (μJ)	7.7; 15.1
Workpiece material	Stainless mould steel, AISI 420-MOD
Tool electrode material	Tungsten
Tool electrode diameter (μm)	300
Feature machined	150 μm deep blind hole

7.4 Results and discussion

The results obtained during model development as well as model validation are presented and discussed. Samples of simulated results are illustrated and comparisons between simulated and measured results are made.

7.4.1 Modelling of surface roughness

The results obtained during model development for surface roughness estimation included the estimation of plasma flushing efficiency, the simulated overlapping crater profile and the resulting bounding limits for R_{max}. In model validation, the measured R_{max} values are plotted with the simulated bounding limits.

7.4.1.1 Plasma flushing efficiency estimation

The thermal distribution resulting from FEM simulation of a single electrical discharge on a flat surface at discharge energies of 1.6 µJ, 3.4 µJ and 14.6 µJ are shown in Figure 7.11(a) to (c), respectively.

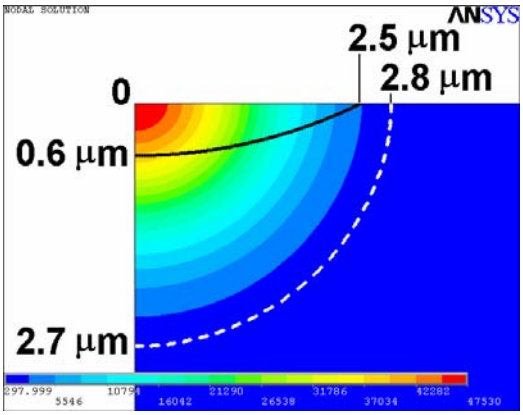

(a) Discharge energy: 1.6 µJ

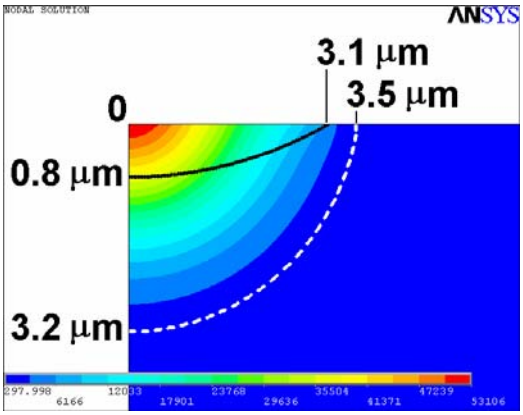

(b) Discharge energy: 3.4 µJ

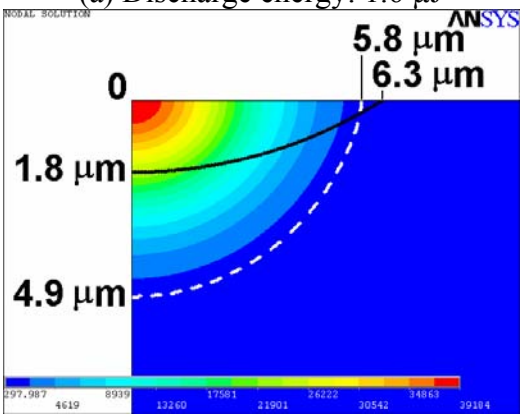

(c) Discharge energy: 14.6 µJ

Figure 7.11 Thermal distribution for heat flux on a flat surface

The dotted and solid lines show the simulated melting isotherms and estimated crater profiles obtained through the single discharge experiment, respectively. Since the empirical crater profile was assumed to be hemispherical-capped in shape, they are represented by circular arcs passing through the average measured radius and depth values. The comparison of simulated radius and depth values to the corresponding measured values, as shown in Figure 7.12(a) and (b), respectively, showed that the simulated radius values were within the range of measured values. However, the depths of melting isotherms were above the range of measured crater depth values illustrating the inability of collapsing plasma channel to expel all the molten material.

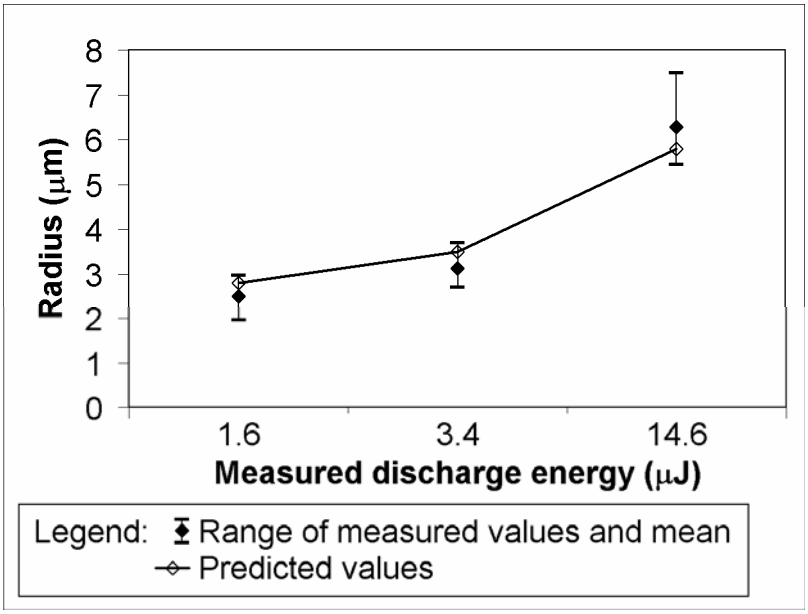

(a) Crater radius

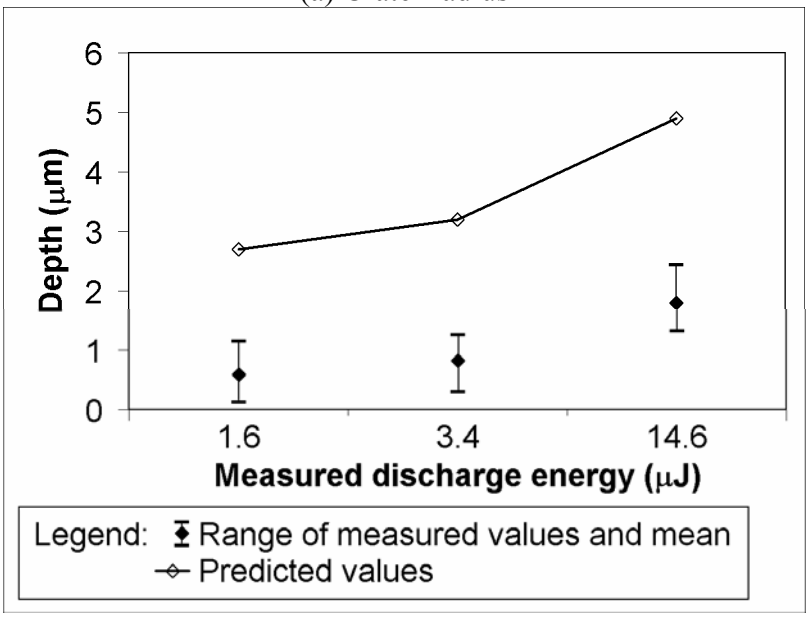

(b) Crater depth

Figure 7.12 Comparison of predicted and measured crater geometries

Thus, the plasma flushing efficiency may be estimated from the area of molten material and the area of crater cavity. The plasma flushing efficiencies were 19 %, 23 % and 33 % for measured average discharge energies of 1.6µJ, 3.4µJ and 14.6µJ, respectively. As these PFEs were determined under single discharge conditions they should represent the upper bound of PFEs experienced when employing machining conditions typically used in micro-EDM, since material removal in a single discharge was reported to be greater than the material removal per pulse in multiple discharges [221].

7.4.1.2 Overlapping crater profile

The various overlapping crater profiles were simulated based on the predefined maximum and minimum asperity conditions. The different asperity conditions were formed by arranging the crater profiles determined during the FEM analysis of single electrical discharge on a flat surface. The crater profile was defined by a circular arc through the simulated crater radius and the measured crater depth. The thermal distribution resulting from FEM simulation for the maximum and minimum asperity conditions are shown in Figure 7.13.

Maximum asperity condition | Minimum asperity condition

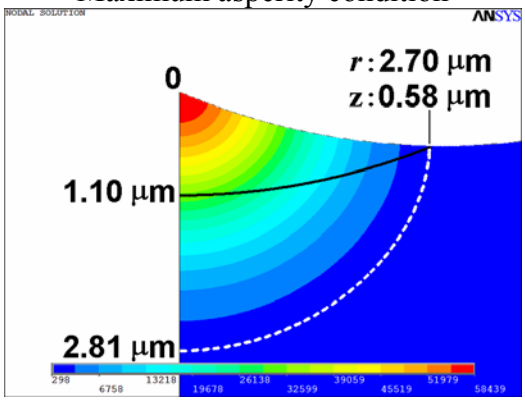

(a) Discharge energy: 1.6 µJ

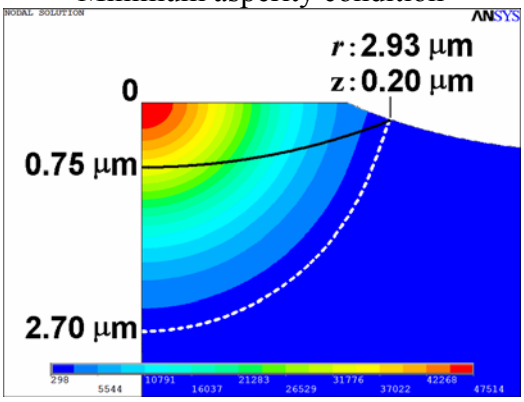

(b) Discharge energy: 1.6 µJ

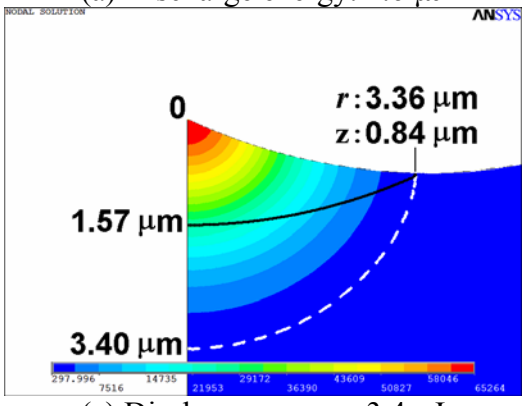

(c) Discharge energy: 3.4 µJ

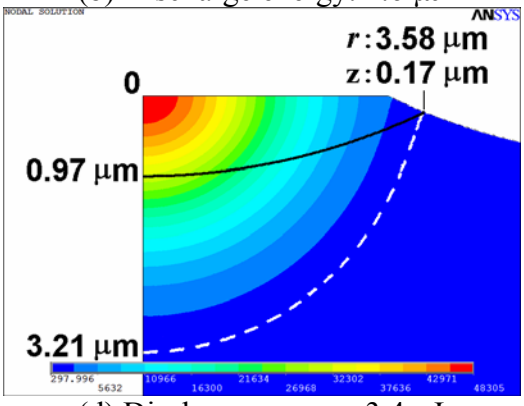

(d) Discharge energy: 3.4 µJ

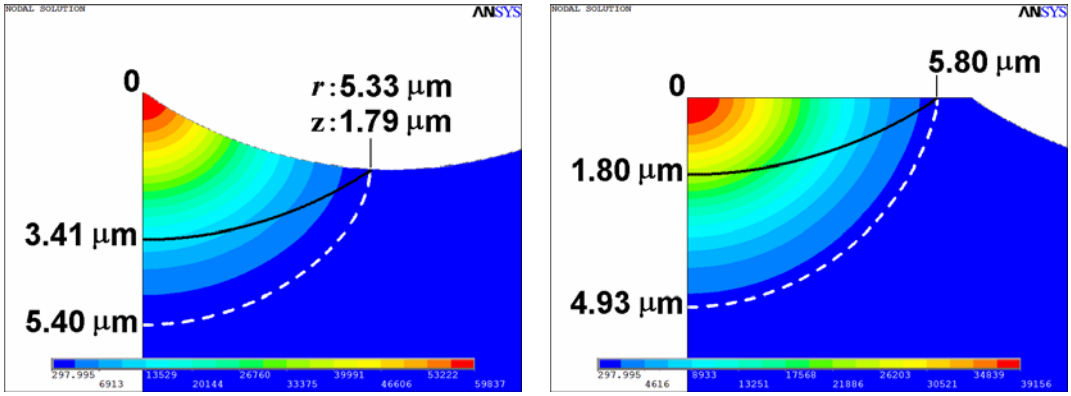

(e) Discharge energy: 14.6 µJ (f) Discharge energy: 14.6 µJ

Figure 7.13 Thermal distribution for heat flux on overlapping crater profile

The dotted line shows the melting isotherm while the estimated crater profile, shown by the solid line, was calculated using the estimated PFE and assuming that the crater radius corresponded to the melting isotherm radius. A comparison of the estimated crater profiles between the maximum and minimum asperity conditions showed that deeper craters are generated under the maximum asperity condition, which may be due to the smaller heat conduction front. In addition, a comparison of the estimated crater profiles under the minimum asperity condition showed that for the discharge energy of 14.6µJ the generated results were similar to that of the flat surface. This was because the melting isotherm did not propagate into the neighbouring crater profile and thus the resulting crater profile was not influenced by the neighbouring crater profile. On the other hand, the crater radius predicted for average discharge energies of 1.6µJ and 3.4µJ differed from those of the flat surface since the melting isotherm propagated into the neighbouring crater profile and consequently influenced its distribution. This resulted in a slight overlapping of crater profiles for average discharge energies of 1.6µJ and 3.4µJ.

7.4.1.3 Bounding limits for R_{max}

The bounding limits for R_{max} were determined from results of the overlapping crater profile analysis. Based on the multiple discharge approach, the value of R_{max} was defined as the distance between the unmachined crater rim of a crater in a preceding layer to the crater valley of a crater in a succeeding layer, as illustrated in Figure 7.14(a) and (b).

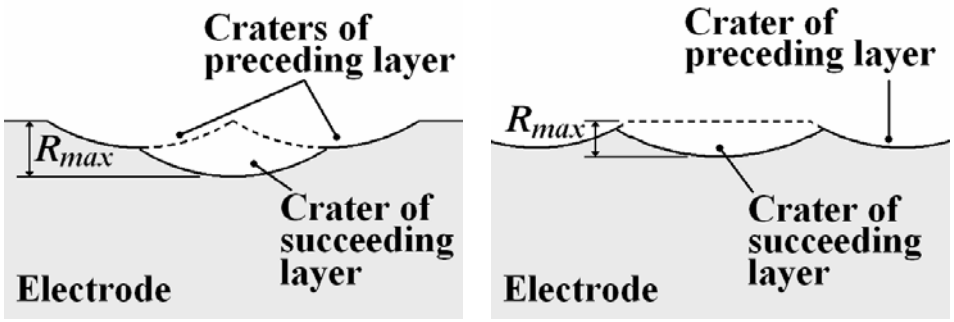

(a) Maximum asperity condition (b) Minimum asperity condition

Figure 7.14 Definition of R_{max} in multiple discharge approach

Two layers were chosen to represent the overlapping nature of craters since it was assumed that if material removal occurs most readily at highest points on the electrode surface, then a layer by layer material removal process involving a coexistence of two layers of craters occurs. In this material removal process, craters forming the preceding layer are sequentially eroded to form craters in the succeeding layer. When all craters forming the preceding layer have been eroded, craters in the succeeding layer now form the preceding layer in the next cycle of material removal. A qualitative examination of the machined surface as shown in Figure 7.15(a) and (b) revealed the occurrence of overlapping crater profiles similar to those depicted in Figure 7.14(a) and (b), respectively, thus supporting the choice of maximum and minimum asperity conditions and definition of R_{max}.

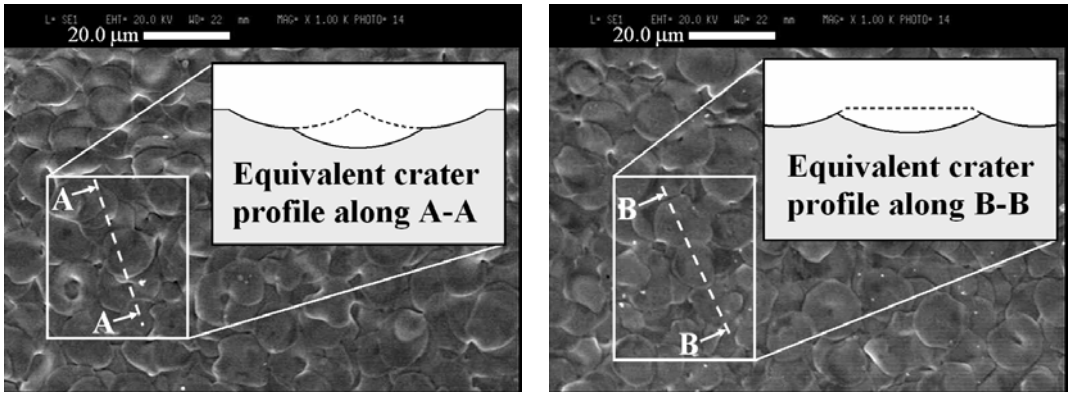

(a) Maximum asperity condition (b) Minimum asperity condition

Figure 7.15 Crater profiles on machined surface

Figure 7.16 shows the bounding limits of R_{max} simulated at discharge energies of 1.6 μJ, 3.4 μJ and 14.6 μJ. Since the simulated craters at the discharge energy of 14.6 μJ did not overlap, the lower bound of R_{max} at 14.6 μJ was taken as the crater depth.

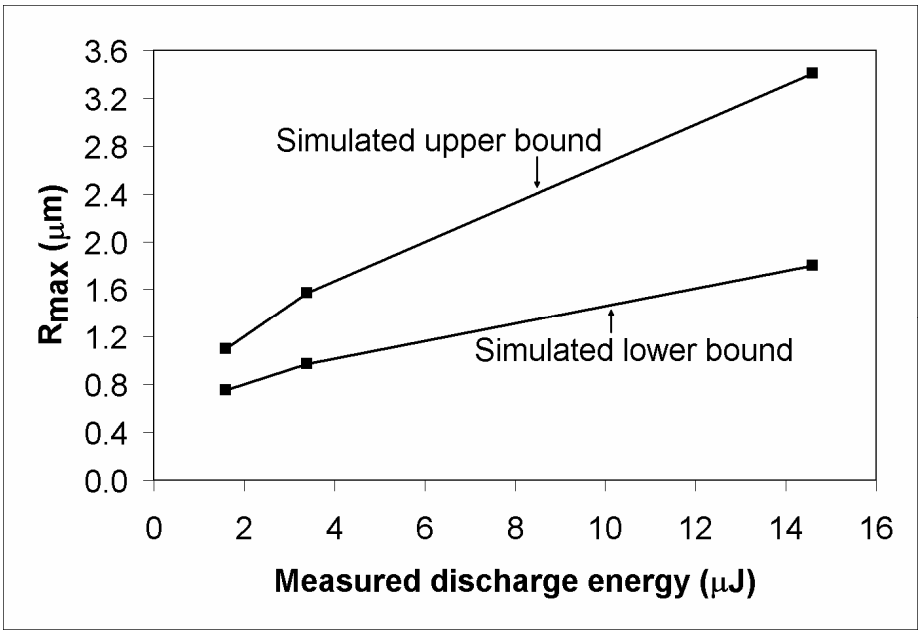

Figure 7.16 Bounding limits of R_{max}

Based on simulated results of the upper bound of R_{max} the expression of R_{max} as a function of discharge energy, having an R^2 coefficient of determination value of 0.999, may be expressed as

$$R_{\max} = 0.85 \cdot E_m{}^{0.51} \qquad (7.15)$$

This relationship is similar in form to that reported in related studies [166].

7.4.1.4 Experimental validation

To validate the model for R_{max} developed by the multiple discharge approach, machining experiments were conducted so that the R_{max} of machined surfaces could be compared to the bounding limits. The range of average measured values of R_{max} at discharge energies of 1.0 μJ, 3.2 μJ, 5.5 μJ and 10.4 μJ were plotted together with the range of simulated R_{max} values, as shown in Figure 7.17.

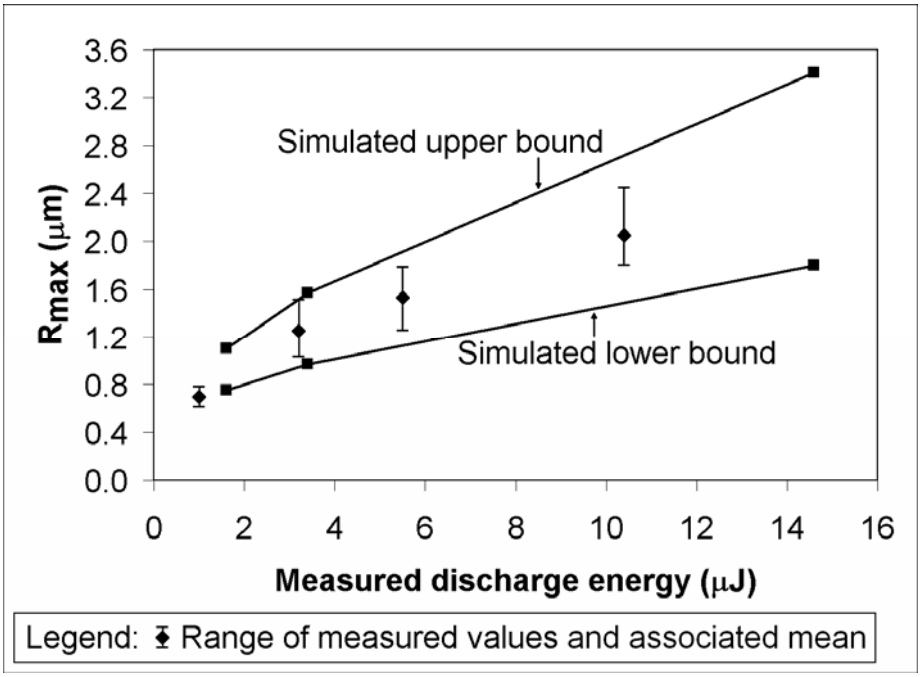

Figure 7.17 Comparison of measured and simulated R_{max}

The simulated R_{max} values within the bounding limits represented the range of R_{max} values that might exist on the machined surface. At the discharge energies of 3.2μJ, 5.5μJ and 10.4μJ, the range of average R_{max} values of the machined surface fell within the simulated bounding limits. Also, the range of measured R_{max} values increased with increasing discharge energy, which was similar to the trend of the simulated R_{max} values. However, the range of measured R_{max} values had a smaller band compared to the range of simulated R_{max} values at larger discharge energies. The deviation between measured and simulated R_{max} values may be attributed to the assumption of axisymmetry during the development of the modelled machined surface profile, which led to a difference in profile shape as described earlier. The smaller deviation in R_{max} at lower discharge energies may suggest that the modelled surface profile resulting from the assumption of axisymmetry was closer to the actual machined surface profile having smaller craters than that having larger craters produced at larger discharge energies. Finally, although the discharge energy of 1.0μJ used in the validation experiment was outside the range of discharge energies used in the FEM analysis, the R_{max} values measured from the machined surface may also fall within the simulated bound limits of R_{max}.

7.4.2 Modelling of recast layer thickness

The results obtained during model development for recast layer thickness estimation included the estimation of fraction of heat flux distributed to the workpiece, the recast

plasma flushing efficiency and corresponding simulated bounding limits of recast layer thickness. In model validation, the measured recast layer thickness values are plotted with the simulated bounding limits.

7.4.2.1 Fraction of heat flux estimation

To estimate the fraction of heat flux distributed to the workpiece during electrical discharge, crater radii were numerically simulated at fraction of heat flux values of 0.15, 0.25, 0.35 and 0.45 for each pulse on time setting. Figure 7.18 shows the fractions of heat flux versus simulated crater radii values which had been fitted with power function curves such that the R^2 coefficient of determination values for pulse on time settings of 166 ns, 362 ns and 606 ns were 0.997, 0.995 and 0.996, respectively. The curves provided a relationship between crater radius and fraction of heat flux for each of the three pulse on time durations.

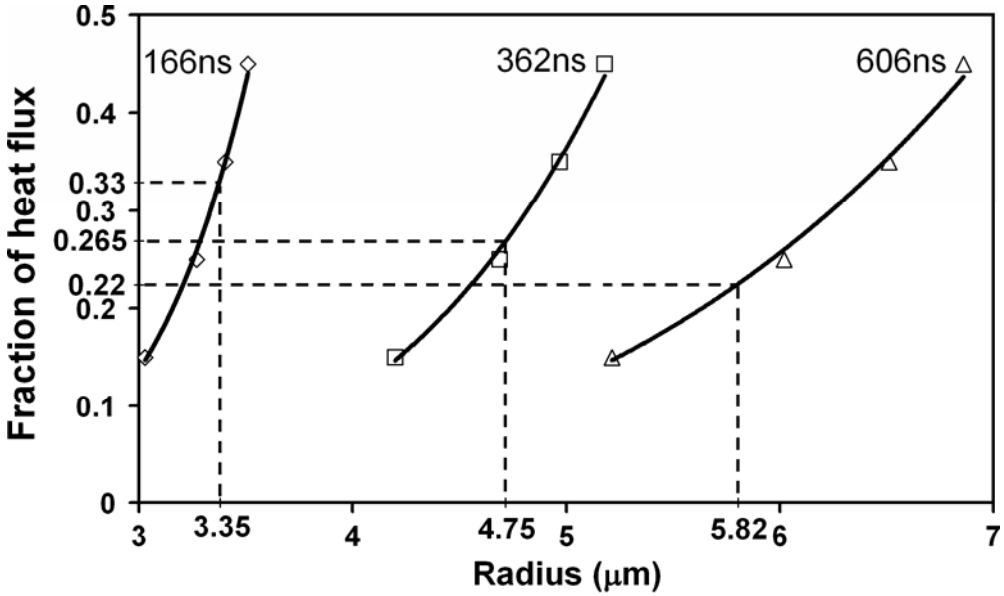

Figure 7.18 Simulated results of fraction of heat flux versus crater radii

Thus, assuming that the fraction of heat flux is constant for a given pulse on time and using the average radii of craters produced by single discharge experiment, the fraction of heat flux for each pulse on time was estimated from the corresponding curves. From the curve for 166 ns pulse on time, the fraction of heat flux corresponding to the measured single discharge crater radius of 3.35 μm is 0.33. Similarly, the curve for 362 ns pulse on time gives the fraction of heat flux corresponding to the crater radius of 4.75 μm as 0.265, while for 606 ns pulse on time the fraction of heat flux for crater radius of 5.82 μm is 0.22.

7.4.2.2 Recast plasma flushing efficiency estimation

The recast plasma flushing efficiency and corresponding bounding limits of recast layer thickness were estimated based on an iterative process in which the simulated bounding limits were matched with measured recast layer thickness values. The upper and lower bounds of recast layer thickness were estimated by simulating a single electrical discharge at the trough of a crater and at the apex of neighbouring craters, respectively. As shown in Figure 7.19, the simulated recast layer consisted of the crater recast regions in the succeeding layer and preceding layer. The crater profiles of the preceding layer form the boundary of the FEM model, while the crater profile of the succeeding layer is represented by the solid line. The melting isotherm of each individual discharge is depicted by dotted lines. The average recast layer thickness was calculated by averaging the vertical distances between the melting isotherm and crater profile of the combined recast region.

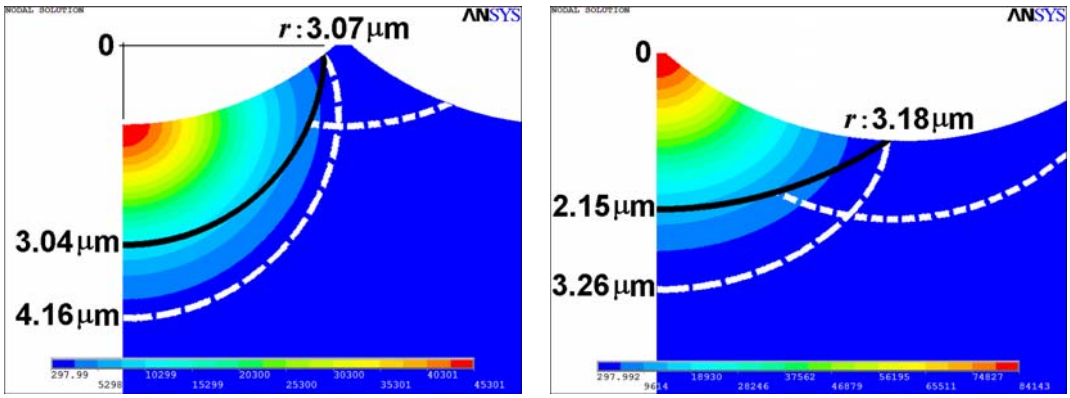

(a) Upper bound (b) Lower bound

Figure 7.19 Simulated recast layers for 166 ns pulse on time

The simulated bounding limits of recast layer thickness were compared with measured recast layer thickness values produced at the peak discharge current of 1.45 A and pulse on time durations of 166 ns, 362 ns and 606 ns to determine the suitability of recast PFE used in the simulation. Figure 7.20 shows the simulated bounding limits of recast layer thickness and the corresponding measured results. The estimated recast PFE value for 166 ns and 362 ns was 54 % while that for 606 ns was 50 %. The lower recast PFE value for 606 ns pulse on time may be attributed to the larger amount of molten material flowing to the immediate surroundings of the crater and contributing to the recast layer thickness, thereby lowering recast PFE.

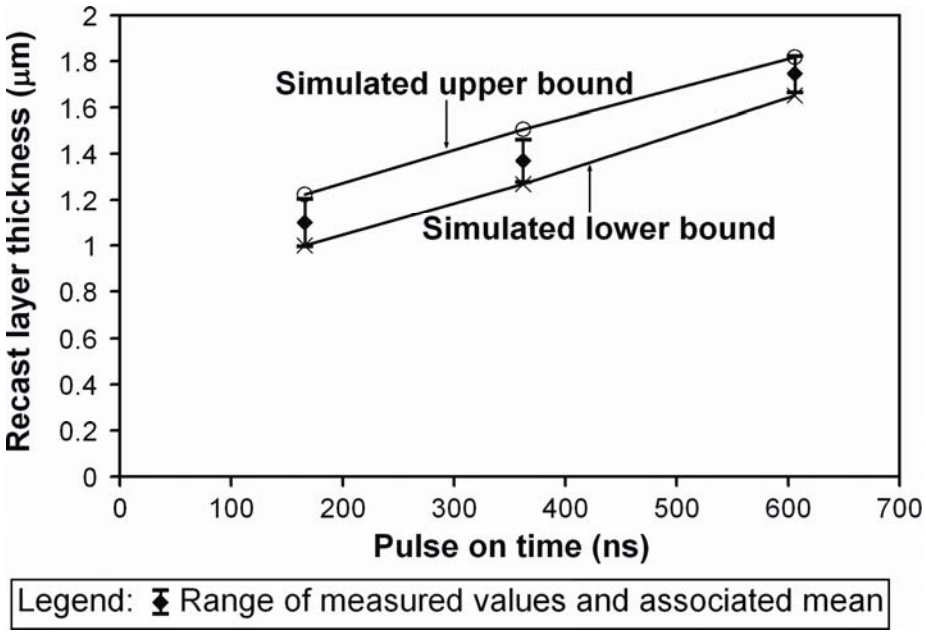

Figure 7.20 Measured and simulated recast layer thickness values

Based on the simulated results of upper bound recast layer thickness the expression of recast layer thickness as a function of pulse on time, having an R^2 coefficient of determination value of 0.992, may be expressed as

$$h_{recast} = 0.26 \cdot t_{on}{}^{0.30} \qquad (7.16)$$

where h_{recast} represents the recast layer thickness and t_{on} the pulse on time. This relationship is similar to that reported in a related study where the maximum depth of damaged layer thickness was expressed as a function of pulse on time duration [47].

7.4.2.3 Experimental validation

To validate the model for recast layer thickness developed by the MDA, machining experiments were conducted so that the recast layer thickness of machined surfaces could be compared to the bounding limits. The range of recast layer thickness values at discharge pulse on time durations of 244 ns and 458 ns were plotted together with the simulated bounding limits, as shown in Figure 7.21. The deviations in recast layer thickness from the validation experiment were smaller than those from model development. Nevertheless, the validation results were within the bounding limits of simulated recast layer thickness values.

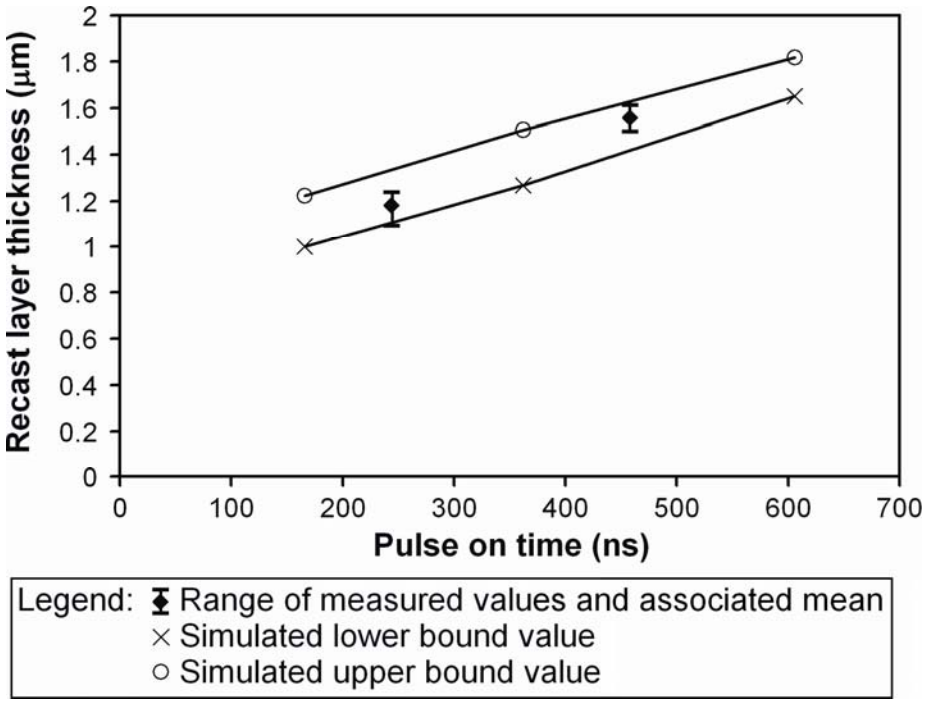

Figure 7.21 Comparison of measured and simulated results for model validation

7.5 Summary

A multiple discharge approach (MDA) was proposed and adopted for the theoretical modelling of sequential electrical discharges in the micro-EDM process. The consideration of multiple discharges allows overlapping craters to be modelled, which gives a better representation of the machining performance measures. The MDA involved numerical modelling and simulation of thermal conduction due to a time dependent heat source and heat flux acting on a machined surface profile. The simulated results provided information on melt isotherm and molten area which allowed a geometrical prediction of crater profile based empirically determined plasma flushing efficiencies. To address the deviations in performance measure values arising from the stochastic material removal mechanism, the MDA considered extremities in overlapping crater profiles and resulting temperature distributions to predict upper and lower bounds of performance measure values. The bounding limits defined the range of performance measure values that may be achieved for a given process parameter setting. The MDA was demonstrated through the modelling of R_{max} and recast layer thickness and validated by experimental results. It highlighted the influence of preceding crater profile and heat source location on resulting thermal distribution, crater profile and recast layer profile. Through the use of MDA for development of the theoretical model for R_{max}, plasma flushing efficiencies for discharge energies in the range of 1.6 μJ and 14.6 μJ were determined. In addition, the use of MDA

for recast layer thickness simulation enabled the recast plasma flushing efficiency (recast PFE) to be estimated for discharge energies in the range of 5 μJ and 21 μJ. The recast PFE was introduced to account for the flow of molten material into neighbouring craters, which increased recast layer thickness, during electrical discharge. The simulated bounding limits of machining performance measures, which were validated with experimental data, also allowed the formulation of expressions that related machining performance measure to controllable machining parameters. The specific findings from the study are as follows:

- The PFE for electrical discharges from an RC pulse generator were 19 %, 23 % and 33 % for discharge energies of 1.6 μJ, 3.4 μJ and 14.6 μJ, respectively.
- The recast PFE for recast layer thickness generation from an RLC pulse generator were 54 % for 166 ns and 362 ns pulse on time and 50 % for 606 ns pulse on time.
- The fractions of heat flux distributed to the anode were 0.33, 0.265 and 0.22 for pulse on time durations of 166 ns, 362 ns and 606 ns, respectively.
- The relationship between R_{max} and discharge energy is expressed as $R_{\max} = 0.85 \cdot E_m^{\,0.51}$.
- The relationship between recast layer thickness and pulse on time is expressed as $h_{recast} = 0.26 \cdot t_{on}^{\,0.30}$.

Chapter 8
Conclusion and Future Work

This chapter presents concluding remarks concerning investigations on the use of powder-mixed dielectric in micro-EDM (PMD micro-EDM). Observations from the single discharge experiment and machining experiments conducted on PMD micro-EDM are covered. Moreover, results of micro-EDM process modelling and simulation are summarized. In addition, potential research tracks that can improve the PMD micro-EDM process and extend the scope of the present study are presented as future work. An overview of the chapter is shown in Figure 8.1.

Chapter 8: Conclusion and Future Work
8.1 Conclusion
8.2 Future work
- 8.2.1 Further enhancements to the micro-EDM process
- 8.2.2 Applying PMD micro-EDM to surface modification processes
  - 8.2.2.1 Alloying of Ni and Ti in NiTi powder-mixed dielectric
  - 8.2.2.2 Machining of slot in NiTi powder-mixed dielectric

Figure 8.1 Overview of Chapter 8

8.1 Conclusion

The EDM technique possesses inherent process characteristics that make it a promising micro-machining technique. However, the micro-EDM technique has only established a niche in the fabrication of high aspect ratio micro-holes and manufacture of micro-moulds. This is partly due to the lack of an adequate knowledge base in micro-EDM, which arises due to the myriad of process parameter combinations available for machining, sensitivity of process performance to process parameters and conditions; and augmented by the stochastic nature of material removal. As a result complexities in addressing issues related to process reliability and controllability, which are amplified as feature size is reduced, arise. This shortfall is further compounded by differences in process parameters used and process conditions encountered in EDM and micro-EDM, which demand focused studies on micro-EDM to be conducted. The literature review has revealed unique process characteristics when powder-mixed dielectric is used in EDM, such as improvements in machined surface quality and enhancement of machined surface functional properties. The literature review has also underlined a striking knowledge gap in the application of

powder-mixed dielectric for micro-EDM. Furthermore, a review of process models for EDM and micro-EDM has highlighted a predominance of single electrical discharge erosion models and a limited number of theoretical process models that address the multiple discharge nature of the material removal mechanism. Thus, there is an inadequacy of models that can provide a new perspective in process understanding, control and performance prediction.

The knowledge gap in PMD micro-EDM has been addressed by first assessing process feasibility through single discharge experiments under the proposed process parameters of discharge energies less than 25 μJ, pulse on time durations in the sub-microsecond range, powder granularities in the nanometre range, powder concentrations less than 1 g/l and semi-conductive and non-conductive powder materials. Next machining experiments on PMD micro-EDM have been conducted to understand process characteristics, relate machining performance measures to experimental observations from the single discharge experiment and investigate the effectiveness of PMD micro-EDM in improving machined surface quality. The single discharge experiment results have shown a distinct difference in the morphology of craters produced in a powder-free and powder-mixed dielectric, which indicated that the proposed process parameters for PMD micro-EDM could change the material removal characteristics of an electrical discharge having discharge energies in the micro-joule range. Through the machining experiments on PMD micro-EDM, reductions in surface roughness have been achieved and attributed to the smaller peak-to-valley height of craters observed in the single discharge experiment. With input energies of 1.1 μJ and 16.5 μJ, reductions in *Ra* values ranging between 14 % and 24 % have been recorded. Furthermore, recast layer thicknesses have been found to decrease through performing PMD micro-EDM with rotary electrode for flushing. The maximum reduction in recast layer thickness has been achieved at a powder concentration of 0.1 g/l and ranged between 15 % and 35 %. Therefore, the feasibility of PMD micro-EDM technique has been demonstrated and applied to the improvement of machined surface quality.

A novel multiple discharge approach (MDA) has been proposed for micro-EDM process modelling and simulation; and has provided a new tool for understanding the mechanism of overlapping crater profile and interconnecting crater recast region formation. The theoretical model, solved through a numerical approach, incorporated the application of time dependent heat source and heat flux to non-linear boundaries that represented the

machined surface profile. Moreover, to address the deviations in performance measure values arising from the stochastic material removal mechanism, the MDA considered extremities in overlapping crater profiles and resulting temperature distributions to predict upper and lower bounds of performance measure values. The bounding limits defined the range of performance measure values that may be achieved for a given process parameter setting. The MDA has been demonstrated through the modelling of R_{max} and recast layer thickness and validated by experimental results. The findings have shown that the measured values are bounded by the simulated bounding limits. It has highlighted the influence of preceding crater profile and heat source location on resulting thermal distribution, crater profile and recast layer profile. Through this study, the range of values for PFE has been estimated as 19 % to 33 % for discharge energies between 1.6 μJ and 14.6 μJ. Furthermore, the range of values for fraction of heat flux distributed to the workpiece has been found to be 0.22 to 0.33 for pulse on time durations between 166 ns and 606 ns. In addition, expressions relating R_{max} and recast layer thickness to discharge energy and pulse on time, respectively, have also been formulated.

8.2 Future work

The investigations conducted on the PMD micro-EDM technique revealed unique process characteristics that may be used to enhance or create new applications for the micro-EDM process. While the application of PMD micro-EDM for reducing surface roughness and recast layer thickness have been demonstrated in this study, investigations on other machining performance measures such as material removal rate and tool wear ratio are also required. Furthermore, the use of powder-mixed dielectric may allow micro-EDM to be employed in surface modification processes such as micro-electrical discharge alloying and micro-electrical discharge coating. The directions of future work proposed for PMD micro-EDM were based on observations made during the course of investigations.

8.2.1 Further enhancements to the micro-EDM process

Micro-EDM is a precision machining process in which geometrical accuracy and speed of machining are important considerations. Investigations on the use of the semi-conductive SiC powder-mixed dielectric showed that the enlargement of discharge gap increased significantly and then tapered to a constant value for powder concentrations less than 0.2 g/l. The enlarged discharge gap has to be considered when accounting for the geometrical accuracy of machined features. On the other hand, the enlarged discharge gap may lead to

a reduction in abnormal discharges and improve the material removal rate and tool wear ratio of micro-EDM in a way similar to that observed in PMD-EDM processes. Moreover, although some similarities may be drawn between nano-sized and micro-sized powder additives, such as powder material and material properties, differences in their physical size and morphology may cause variations in performance characteristics. Thus, further explorations in PMD micro-EDM to enhance the micro-EDM process are still necessary.

8.2.2 Applying PMD micro-EDM to surface modification processes

Through the single discharge experiment on PMD micro-EDM, the plateau of resolidified material within the crater rim was observed. This highlighted a possible reduction in plasma flushing efficiency, which led to a greater amount of retained material in the crater. This material retention characteristic is potentially useful in the surface modification process since the retained material may form an alloyed functional layer on the machined surface. The process of surface modification in PMD micro-EDM may include micro electrical discharge alloying (micro-EDA) and micro electrical discharge coating (micro-EDC). These processes have been widely studied at the macro scale and have led to the application of EDA in the surface hardening of textured-rollers utilised in the automotive industry [172] and the application of EDC in the repair of aerospace components [154]. While the process of PMD micro-EDA has received limited attention, the process of PMD micro-EDC has been studied in relation to electrode configurations that promote high powder concentrations for deposition [30] and machining conditions for deposition and material removal [169]. However, the machining conditions used were in the PMD-EDM regime. In studies that employed discharge energies in the micro-EDM regime, the micro-EDC process was performed in air and did not involve powder-mixed dielectrics [222, 223]. Therefore, there is a need to conduct studies on PMD micro-EDM in surface modification applications to ascertain its feasibility and determine its scope of usability.

Preliminary experiments, with machining parameters shown in Table 8.1, on PMD micro-EDM using nano-powder additives of nickel-titanium (NiTi) material showed the alloying of nickel (Ni) and titanium (Ti) due to electrical discharges and also highlighted that a high powder concentration is required for adequate alloying onto the machined surface. The NiTi nano-powder additive is typically used in the fabrication of shaped-memory micro-structures. Besides this, NiTi has been alloyed onto the surface of stainless steels so as to improve the cavitation erosion resistance of the parent material [224]. It has also

been suggested that NiTi coatings can potentially be used to resist sliding wear and rolling fatigue [225]. An energy dispersive X-ray spectroscopy (EDX) of the NiTi nano-powder additive revealed the following elements as shown in Figure 8.2.

Table 8.1 Machining conditions for surface modification experiment

Machining parameter	Value
Open circuit voltage, V_{OC} (V)	100
Peak discharge current, I_{pk} (A)	1.45
Pulse on time, t_{on} (ns)	606
Measured discharge energy, E_m (μJ)	21
Powder material	Nickel-Titanium (NiTi)
Powder granularity (nm)	~100
Powder concentration (g/l)	2
Workpiece material	Stainless mould steel, AISI 420-MOD
Tool electrode material	Copper
Tool electrode diameter (μm)	300
Tool rotation speed (rev/min)	1000

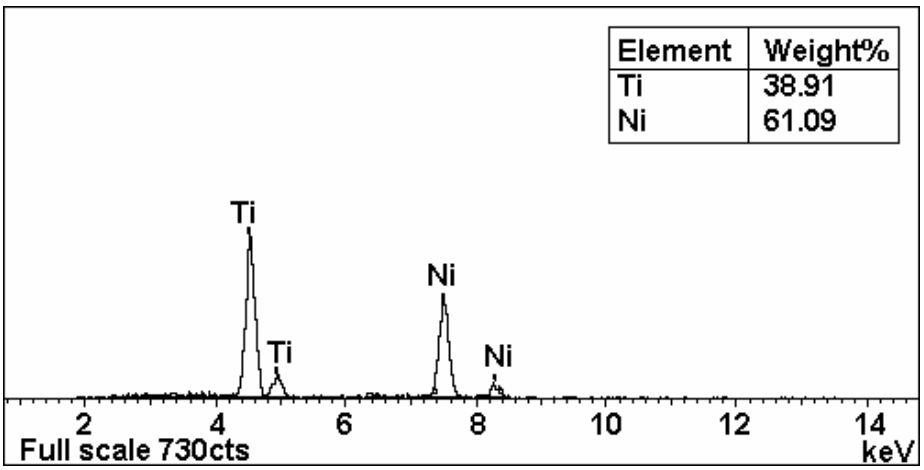

Figure 8.2 Energy dispersive X-ray element spectrum for NiTi nano-powder

8.2.2.1 Alloying of Ni and Ti in NiTi powder-mixed dielectric

The alloying of Ni and Ti onto the AISI 420-MOD stainless mould steel workpiece as a result of PMD micro-EDM with NiTi nano-powder additive was observed through the EDX analysis of the crater (Box A) and particle (Box B) shown in Figure 8.3.

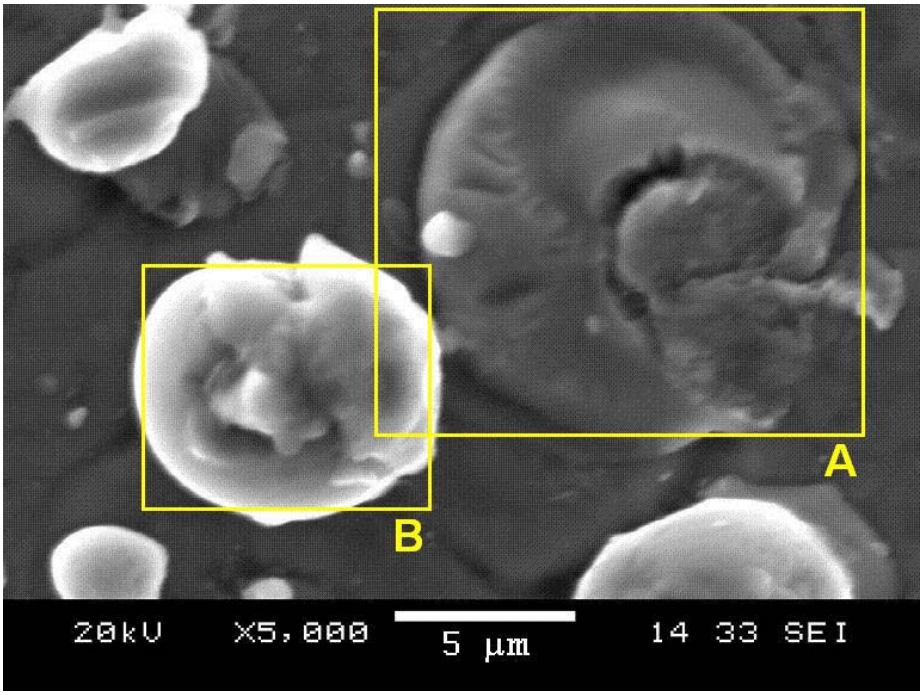

Figure 8.3 SEM of crater and particle

The EDX spectrum of elements from the workpiece, crater and particle, as shown in Figure 8.4(a) to (c), respectively, showed that apart from the elements of stainless mould steel, Ni and Ti were also found.

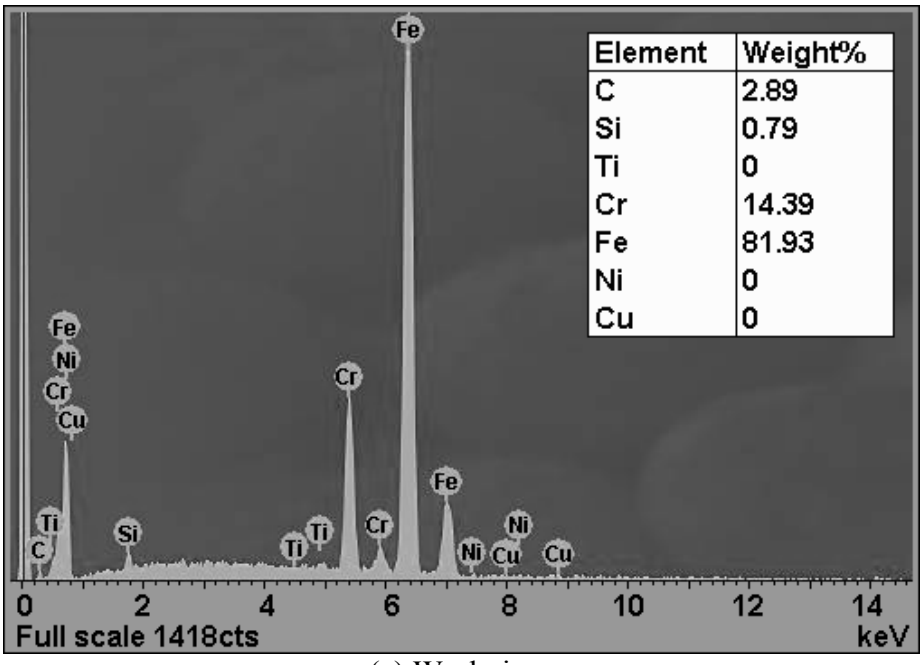

(a) Workpiece

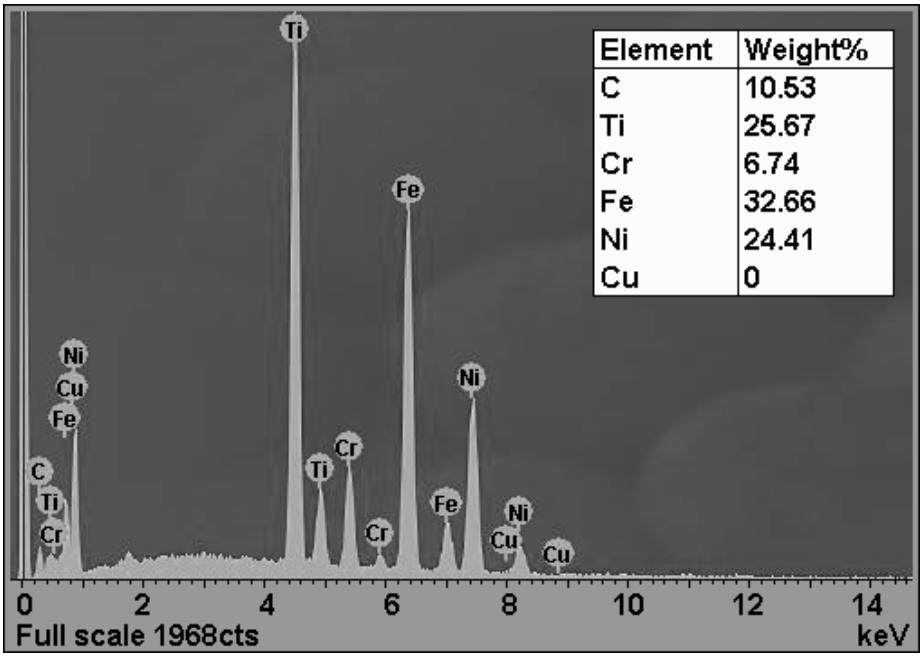

(b) Crater

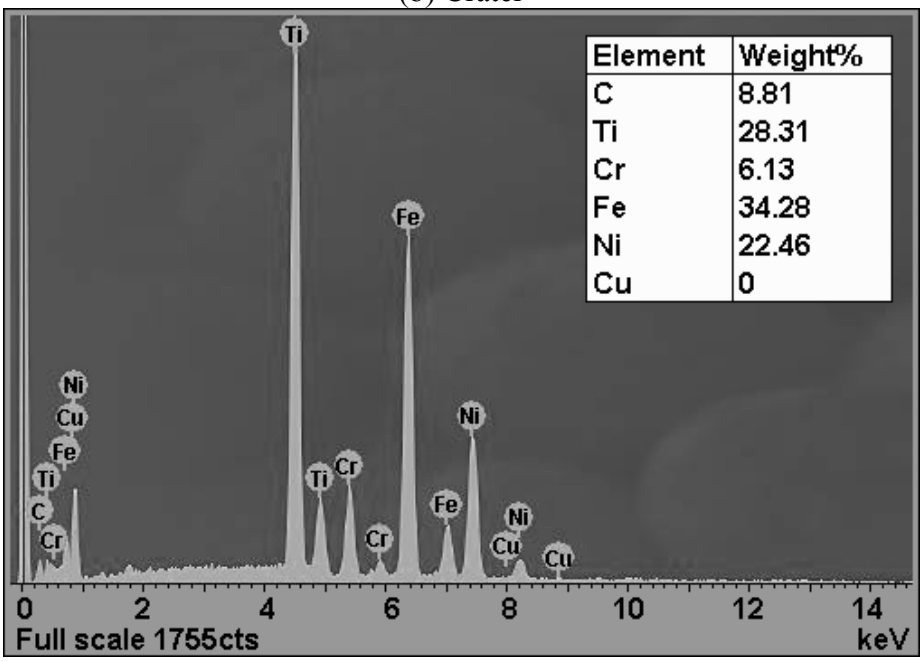

(c) Particle

Figure 8.4 Energy dispersive X-ray spectrum

8.2.2.2 Machining of slot in NiTi powder-mixed dielectric

A 600μm long slot was machined in NiTi powder-mixed dielectric, as shown in Figure 8.5. The EDX analysis was conducted at various locations of the slot to assess the uniformity of alloying.

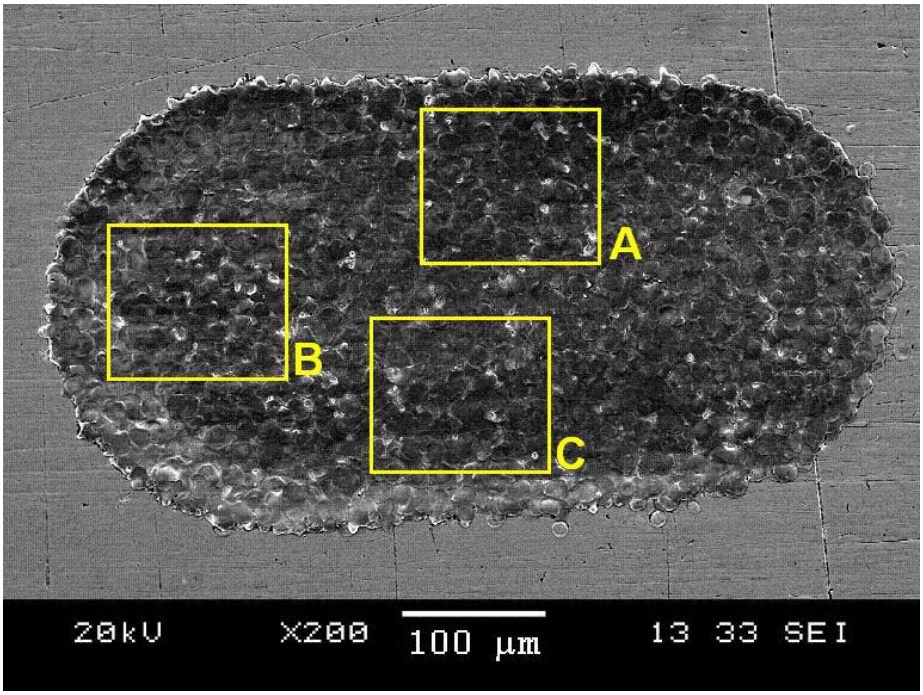

Figure 8.5 SEM image of slot

As shown in Figure 8.6(a) to (c), the concentration of Ti was highest at location A and lowest at location C. The variation in concentration may suggest that there was an inadequate amount of powder additives present in the discharge gap to ensure uniform alloying over the entire machined surface of the slot. Some factors that may influence the presence of powder additives within the discharge gap include powder concentration, homogeneity of powder suspension and flushing effects.

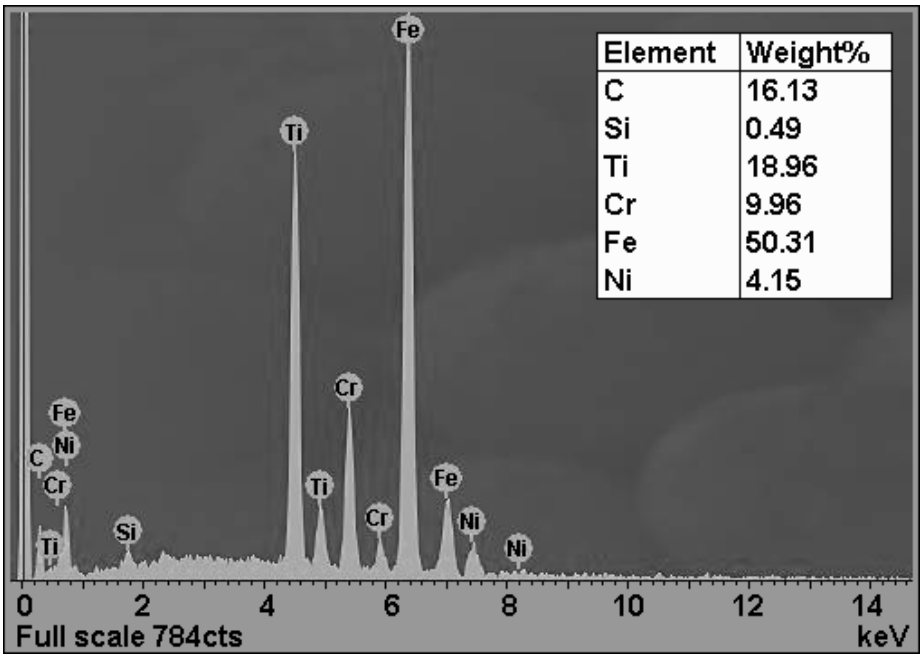

(a) Location A

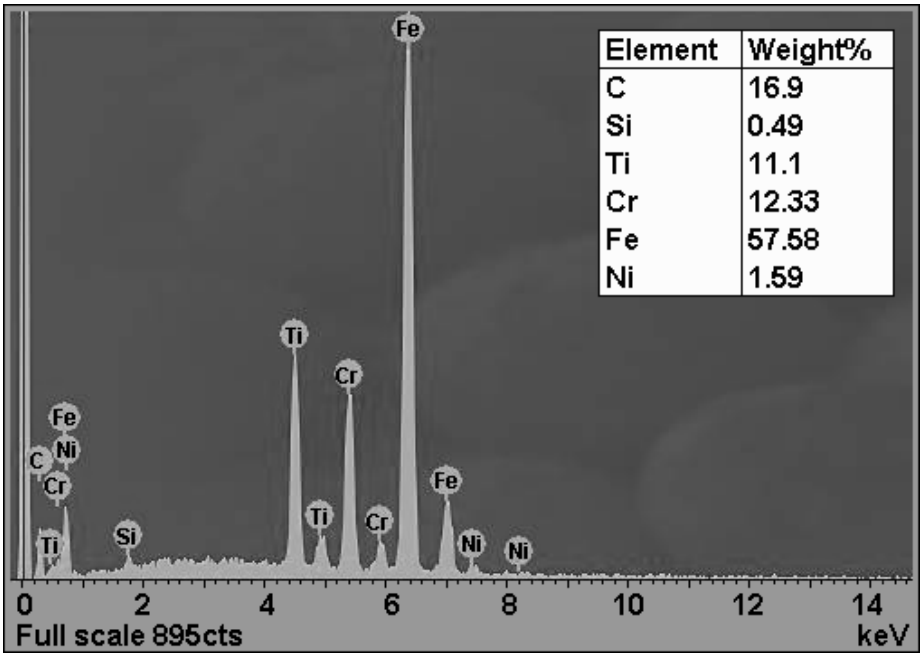

(b) Location B

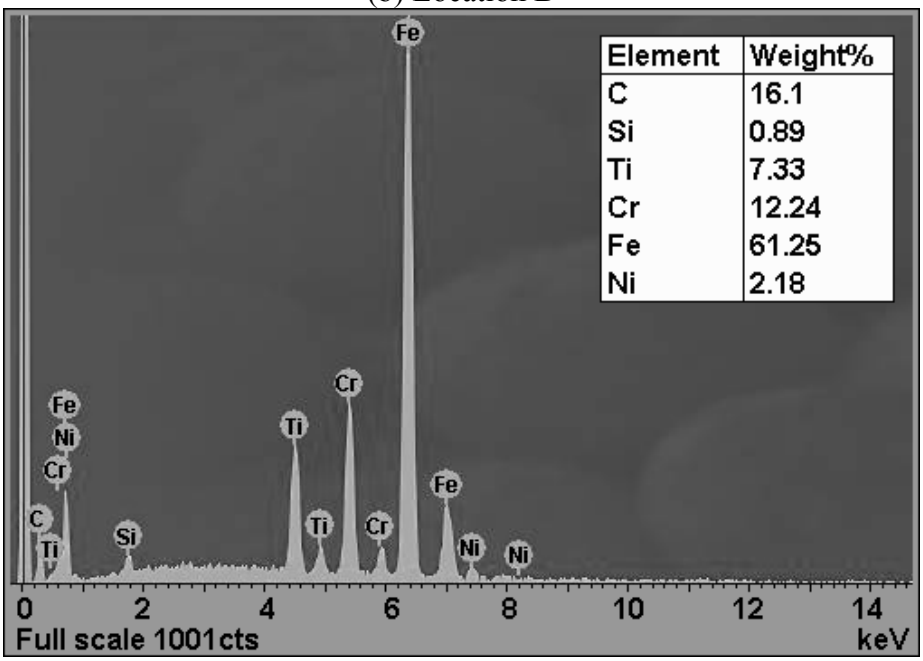

(c) Location C

Figure 8.6 Energy dispersive X-ray spectrum at various locations in slot

Thus, while preliminary results indicated the possibility of alloying powder materials onto the workpiece using PMD micro-EDM, further research is required to augment these findings and to develop the PMD micro-EDM process for surface modification purposes. In this way, the scope of micro-EDM applications may be widened.

References

[1] Dimov S.S., Matthews C.W., Glanfield A. and Dorrington P. 2006 A roadmapping study in multi-material micro manufacture. *Proceedings of Second International Conference on Multi-Material Micro Manufacture, 4M2006* (Grenoble, France, 20-22 Sep 2006) Elsevier, UK p. xi-xxv.

[2] Craven D. 1996 Photolithography challenges for the micromachining industry. *16th Annual Symposium on Photomask Technology and Management, Proceedings of the SPIE - The International Society for Optical Engineering* (Redwood City, CA, USA, 18-20 Sept 1996) SPIE-Int. Soc. Opt. Eng 2884 p. 498-507.

[3] Rahman M., Senthil Kumar A., Wong Y.S., Lim H.S. and Neo K.S. 2005 Tool - Based Micro / Nano Fabrication. *Innovating The Future Through Manufacturing*. (Narosa Publishing House) p. 234-243.

[4] Liu X., DeVor R.E., Kapoor S.G. and Ehmann K.F. 2004 The mechanics of machining at the microscale: Assessment of the current state of the science. *Journal of Manufacturing Science and Engineering, Transactions of the ASME*. **126**(4) p. 666-678.

[5] Denkena B., Hoffmeister H.-W., Reichstein M., Illenseer S. and Hlavac M. 2006 Micro-machining processes for microsystem technology. *Microsystem Technologies*. **12**(7) p. 659-664.

[6] Denkena B., Hoffmeister H.-W., Reichstein M. and Illenseer S. 2004 Process development in machining of micro guideways. *Colloquium Microproduction Microsystem Technologies*. **10**(3) p. 257-260.

[7] Hoffmeister H.-W. and Illenseer S. 2004 Burr formation and reduction in micro drilling of metals. *Production Engineering WGP*. **11**(1) p. 1-4.

[8] Lu Z. and Yoneyama T. 1999 Micro cutting in the micro lathe turning system. *International Journal of Machine Tools and Manufacture*. **39**(7) p. 1171-1183.

[9] Uhlmann E., Piltz S. and Schauer K. 2005 Micro milling of sintered tungsten-copper composite materials. *2005 International Forum on the Advances in Materials Processing, Journal of Materials Processing Technology*. **167**(2-3) p. 402-407.

[10] Chen W.K., Kuriyagawa T., Huang H. and Yosihara N. 2005 Machining of micro aspherical mould inserts. *Precision Engineering*. **29**(3) p. 315-23.

[11] Thornton A.G. and Wilks J. 1980 Wear of diamond tools turning mild steel. *Wear*. **65**(1) p. 67-74.

[12] El-Hofy H.A.-G. 2005 Nontraditional Machining. *Advanced machining processes : nontraditional and hybrid machining processes*. (New York : McGraw-Hill Professional, 2005) p. 8-13.

[13] Meijer J. 2004 Laser beam machining (LBM), state of the art and new opportunities. *Journal of Materials Processing Technology*. **149**(1-3) p. 2-17.

[14] Young R.J. 1993 Micro-machining using a focused ion beam. *Technology and Applications of Ion Beams: Conference of the Atomic Collisions in Solids Group of the Institute of Physics* (Loughborough, UK, 7-10 Apr 1992) 44 p. 353-356.

[15] Yu Z.Y., Rajurkar K.P. and Tandon A. 2004 Study of 3D micro-ultrasonic machining. *Journal of Manufacturing Science and Engineering, Transactions of the ASME*. **126**(4) p. 727-732.

[16] Masaki T., Kawata K. and Masuzawa T. 1990 Micro electro-discharge machining and its applications. *Proceedings. IEEE Micro Electro Mechanical Systems. An Investigation of Micro Structures, Sensors, Actuators, Machines and Robots* (Napa Valley, CA, USA, 11-14 Feb 1990) IEEE p. 21-26.

[17] Pham D.T., Dimov S.S., Bigot S., Ivanov A. and Popov K. 2004 Micro-EDM - Recent developments and research issues. *Journal of Materials Processing Technology*. **149**(1-3) p. 50-57.

[18] Ehrfeld W., Lehr H., Michel F., Wolf A., Gruber H.-P. and Bertholds A. 1996 Microelectro discharge machining as a technology in micromachining. *Micromachining and Microfabrication Process Technology II* (Austin, TX, USA, 14-15 Oct 1996) 2879 p. 332-337.

[19] Li X., Wang J. and Li W. 2007 Current state and prospect of micro-machining. *Proceedings of the IEEE International Conference on Automation and Logistics, ICAL 2007* (Jinan, China, 18-21 Aug 2007) Inst. of Elec. and Elec. Eng. Computer Society p. 1414-1419.

[20] Ho K.H. and Newman S.T. 2003 State of the art electrical discharge machining (EDM). *International Journal of Machine Tools and Manufacture*. **43**(13) p. 1287-300.

[21] Kansal H.K., Singh S. and Kumar P. 2007 Technology and research developments in powder mixed electric discharge machining (PMEDM). *Journal of Materials Processing Technology*. **184**(1-3) p. 32-41.

[22] Luo Y.F. 1997 Dependence of interspace discharge transitivity upon the gap debris in precision electrodischarge machining. *Journal of Materials Processing Technology*. **68**(2) p. 121-131.

[23] Jeswani M.L. 1981 Effect of the addition of graphite powder to kerosene used as the dielectric fluid in electrical discharge machining. *Wear*. **70**(2) p. 133-139.

[24] Mohri N., Saito N. and Higashi M. 1991 New process of finish machining on free surface by EDM methods. *41st General Assembly of CIRP* (Palo Alto, CA, USA, 18-24 Aug 1991) International Institute for Production Engineering Research, Berne, Switzerland 40 p. 207-210.

[25] Ming Q.Y. and He L.Y. 1995 Powder-suspension dielectric fluid for EDM. *Journal of Materials Processing Technology*. **52**(1) p. 44-54.

[26] Kozak J., Rozenek M. and Dabrowski L. 2003 Study of electrical discharge machining using powder-suspended working media. *Proceedings of the Institution of Mechanical Engineers, Part B: Journal of Engineering Manufacture*. **217**(11) p. 1597-02.

[27] Narumiya H., Mohri N., Saito N., Otake H., Tsnekawa Y., Takawashi T. and Kobayashi K. 1989 EDM by powder suspended working fluid. *9th International Symposium for Electro-Machining* (Nagoya, Japan, 5-8 Apr 1989) p. 5-8.

[28] Wong Y.S., Lim L.C., Rahuman I. and Tee W.M. 1998 Near-mirror-finish phenomenon in EDM using powder-mixed dielectric. *Journal of Materials Processing Technology*. **79**(1-3) p. 30-40.

[29] Uno Y., Okada A. and Cetin S. 2001 Surface modification of EDMed surface with powder mixed fluid. *Proc. of the 2nd Int. Conf. on Design and Production of Dies and Molds* (Kusadasi, Turkey, 21-23 Jun 2001)(CD-ROM).

[30] Furutani K., Saneto A., Takezawa H., Mohri N. and Miyake H. 2001 Accretion of titanium carbide by electrical discharge machining with powder suspended in working fluid. *Precision Engineering*. **25**(2) p. 138-144.

[31] Masuzawa T. and Toenshoff H.K. 1997 Three-dimensional micromachining by machine tools. *CIRP Annals - Manufacturing Technology*. **46**(2) p. 621-8.

[32] Nakazawa H. 1994 The Principle of Machining Units. *Principles of Precision Engineering*. (Oxford University Press: USA) p. 190-6.
[33] Okada A., Uno Y. and Hirao K. 2000 Formation of hard layer by EDM with carbon powder mixed fluid using titanium electrode. *Proceedings of 5th International Conference on Progress of Machining Technology* (Beijing, China, 16-20 Sep 2000) p. 464-469.
[34] Uno Y., Okada A., Hayashi Y. and Tabuchi Y. 1998 Surface integrity in EDM of aluminum bronze with nickel powder mixed fluid. *Journal of the Japan Society of Electrical Machining Engineers*. **32**(70) p. 24-31.
[35] Furutani K., Shiraki K. and Ohta M. 2001 Deposition of lubricant layer by electrical discharge machining during finishing process. *Journal of the Japan Society of Precision Engineering*. **67**(12) p. 2042-2047.
[36] Lim L.C., Lee L.C., Wong Y.S. and Lu H.H. 1991 Solidification microstructure of electrodischarge machined surfaces of tool steels. *Materials Science and Technology*. **7**(3) p. 239-248.
[37] Furutani K. and Shiraki K. 2002 Deposition of lubricant layer during finishing process by electrical discharge machining with molybdenum disulphide powder suspended in working fluid. *JSME/ASME International Conference on Materials and Processing 2002* (Honolulu, Hawaii, USA, 15-18 Oct 2002)10(2) p. 468-473.
[38] Lazarenko B.R. and Lazarenko N.I. 1947 Machining by erosion. *American Machinist*. **91**(26) p. 120-121.
[39] Sen B., Kiyawat N., Singh P.K., Mitra S., Ye J.H. and Purkait P. 2003 Developments in electric power supply configurations for electrical-discharge-machining (EDM). *Fifth International Conference on Power Electronics and Drive Systems* (Singapore, 17-20 Nov 2003) IEEE 1 p. 659-664.
[40] Smith G.V. 1967 Progress in spark-erosion machining. *Conference on Electrical Methods of Machining and Forming* (London, 1967) Institution of Electrical Engineers p. 119-124.
[41] Han F., Wachi S. and Kunieda M. 2004 Improvement of machining characteristics of micro-EDM using transistor type isopulse generator and servo feed control. *Precision Engineering*. **28**(4) p. 378-85.
[42] Han F., Chen L., Yu D. and Zhou X. 2007 Basic study on pulse generator for micro-EDM. *International Journal of Advanced Manufacturing Technology*. **33**(5-6) p. 474-479.
[43] Kunieda M., Hayasaka A., Yang X.D., Sano S. and Araie I. 2007 Study on nano EDM using capacity coupled pulse generator. *CIRP Annals - Manufacturing Technology*. **56**(1) p. 213-216.
[44] Jilani S.T. and Pandey P.C. 1983 Analysis of surface erosion in electrical discharge machining. *Wear*. **84**(3) p. 275-284.
[45] Lee H.T. and Yur J.P. 2000 Characteristic analysis of EDMed surfaces using the Taguchi approach. *Materials and Manufacturing Processes*. **15**(6) p. 781-806.
[46] Pandit S.M. and Rajurkar K.P. 1978 Mathematical model for electro-discharge machined surface roughness. *Proceedings of the 6th North American Metalworking Research Conference* (Gainesville, FL, USA, 16-19 Apr 1978) SME, Dearborn 00001500, Mich p. 339-345.
[47] Rajurkar K.P. and Pandit S.M. 1984 Quantitative expressions for some aspects of surface integrity of electro discharge machined components. *Journal of Engineering for Industry*. **106**(2) p. 171-177.

[48] Lee L.C., Lim L.C., Narayanan V. and Venkatesh V.C. 1988 Quantification of surface damage of tool steels after EDM. *International Journal of Machine Tools and Manufacture*. **28**(4) p. 359-372.

[49] Weck M. and Dehmer J.M. 1992 Analysis and adaptive control of EDM sinking process using the ignition delay time and fall time as parameter. *CIRP Annals*. **41**(1) p. 243-246.

[50] Rajurkar K.P. and Wang W.M. 1997 Improvement of EDM performance with advanced monitoring and control systems. *Transactions of the ASME. Journal of Manufacturing Science and Engineering*. **119**(4B) p. 770-775.

[51] Tarng Y.S., Tseng C.M. and Chung L.K. 1997 Fuzzy pulse discriminating system for electrical discharge machining. *International Journal of Machine Tools & Manufacture*. **37**(4) p. 511-522.

[52] Dauw D.F. and Coppenolle B.V. 1995 On the evolution of EDM research, part 2: From fundamental research to applied research. *Proceedings of the 11th International Symposium for Electro Machining (ISEM-11)* (Lausanne, Switzerland, 17-21 Apr 1995) p. 133-142.

[53] Masuzawa T., Fujino M., Kobayashi K. and Suzuki T. 1985 Wire electro-discharge grinding for micro-machining. *CIRP Annals 1985: Manufacturing Technology, Annals of the Int. Institution for Production Engineering Research. 35th General Assembly of CIRP.* (Palermo, Italy, 1985) Technische Rundschau, Berne, Switz 34 p. 431-34.

[54] Masuzawa T., Fujino M., Kobayashi K. and Suzuki T. 1986 Study on micro-hole drilling by EDM. *Bulletin of the Japan Society of Precision Engineering*. **20**(2) p. 117-120.

[55] Rajurkar K.P. and Yu Z.Y. 2000 Micro EDM can produce micro parts. *Manufacturing Engineering*. **125**(5) p. 68-70.

[56] Fukuzawa Y. 1995 Electrical discharge machining of insulating ceramics with a sheet of metal mesh. *Proceedings of the 11th International Symposium on Electromachining (ISEM-11)* (Lausanne, Switzerland, 17-21 Apr 1995) p. 173-179.

[57] Mohri N., Fukuzawa Y., Tani T., Saito N. and Furutani K. 1996 Assisting electrode method for machining insulating ceramics. *CIRP Annals - Manufacturing Technology*. **45**(1) p. 201-204.

[58] Mohri N., Fukuzawa Y., Tani T. and Sata T. 2002 Some considerations to machining characteristics of insulating ceramics - Towards practical use in industry. *CIRP Annals - Manufacturing Technology*. **51**(1) p. 161-164.

[59] Jia Z.-X., Zhang J.-H. and Ai X. 1997 Study on a new kind of combined machining technology of ultrasonic machining and electrical discharge machining. *International Journal of Machine Tools & Manufacture*. **37**(2) p. 193-199.

[60] Fleischer J., Schmidt J. and Haupt S. 2006 Combination of electric discharge machining and laser ablation in microstructuring of hardened steels. *Microsystem Technologies*. **12**(7) p. 697-701.

[61] Qu J., Shih A.J., Scattergood R.O. and Luo J. 2005 Abrasive micro-blasting to improve surface integrity of electrical discharge machined WC-Co composite. *Journal of Materials Processing Technology*. **166**(3) p. 440-448.

[62] Kunieda M., Yoshida M. and Taniguchi N. 1997 Electrical discharge machining in gas. *CIRP Annals - Manufacturing Technology*. **46**(1) p. 143-146.

[63] Kunieda M. and Furudate C. 2001 High precision finish cutting by dry WEDM. *CIRP Annals - Manufacturing Technology*. **50**(1) p. 121-124.

[64] Bo Y.Z., Kunieda M., Miyoshi Y., Takaya T., Nakajima N. and Yoshida M. 2003 High speed 3D milling by dry EDM. *CIRP Annals - Manufacturing Technology*. **52**(1) p. 147-150.

[65] Kunieda M., Takaya T. and Nakano S. 2004 Improvement of dry EDM characteristics using piezoelectric actuator. *CIRP Annals - Manufacturing Technology*. **53**(1) p. 183-186.

[66] Kao C.C., Tao J. and Shih A.J. 2007 Near dry electrical discharge machining. *International Journal of Machine Tools and Manufacture*. **47**(15) p. 2273-2281.

[67] Fujiki M., Ni J. and Shih A.J. 2009 Investigation of the effects of electrode orientation and fluid flow rate in near-dry EDM milling. *International Journal of Machine Tools & Manufacture*. **49**(10) p. 749-58.

[68] Muller M.A., Muller C., Forster R. and Menz W. 2005 Carbon paper flow fields made by WEDM for small fuel cells. *Microsystem Technologies*. **11**(4-5) p. 280-1.

[69] Qian J., Steegen S., Vander Poorten E., Reynaerts D. and Van Brussel H. 2002 EDM texturing of multicrystalline silicon wafer and EFG ribbon for solar cell application. *International Journal of Machine Tools and Manufacture*. **42**(15) p. 1657-1664.

[70] Konig W., Dauw D. and Levy G. 1988 EDM - A future step towards the machining of ceramics. *CIRP Annals 1988: Manufacturing Technology, Annals of the Int. Institution for Production Engineering Research. 38th General Assembly of CIRP.* (Tokyo, Japan, 22-27 Aug 1988) Technische Rundschau, Berne, Switz 37 p. 623-31.

[71] Yu Z.Y., Rajurkar K.P. and Shen H. 2002 High aspect ratio and complex shaped blind micro holes by micro EDM. *CIRP Annals - Manufacturing Technology*. **51**(1) p. 359-362.

[72] Zhao W., Yang Y., Wang Z. and Zhang Y. 2004 A CAD/CAM system for micro-ED-milling of small 3D freeform cavity. *Journal of Materials Processing Technology*. **149**(1-3) p. 573-578.

[73] Yeo S.H., Tan P.C., Aligiri E., Tor S.B. and Loh N.H. 2009 Processing of Zirconium-Based Bulk Metallic Glass (BMG) Using Micro Electrical Discharge Machining (Micro-EDM). *Materials and Manufacturing Processes*. **24**(12) p. 1242 - 1248.

[74] Ho K.H., Newman S.T., Rahimifard S. and Allen R.D. 2004 State of the art in wire electrical discharge machining (WEDM). *International Journal of Machine Tools and Manufacture*. **44**(12-13) p. 1247-1259.

[75] Muttamara A., Fukuzawa Y., Mohri N. and Tani T. 2003 Probability of precision micro-machining of insulating Si3N4 ceramics by EDM. *Journal of Materials Processing Technology*. **140**(1-3 SPEC) p. 243-247.

[76] Reynaerts D., Heeren P.-H. and van Brussel H. 1996 Microstructuring of silicon by electro-discharge machining (EDM) I Theory. *EUROSENSORS X, Sensors and Actuators A (Physical)* (Leuven, Belgium, 8-11 Sep 1996) Elsevier A60 p. 212-18.

[77] Heeren P.-H., Reynaerts D., Van Brussel H., Beuret C., Larsson O. and Bertholds A. 1996 Microstructuring of silicon by electro-discharge machining (EDM) II Applications. *EUROSENSORS X, Sensors and Actuators A (Physical)* (Leuven, Belgium, 8-11 Sep 1996) Elsevier A61 p. 379-86.

[78] Reynaerts D., Meeusen W. and van Brussel H. 1997 Machining of three-dimensional microstructures in silicon by electro-discharge machining. *EUROSENSORS XI, Sensors and Actuators A (Physical)* (Warsaw, Poland, 21-24 Sep 1997) Elsevier A67 p. 159-65.

[79] Reynaerts D. and Van Brussel H. 1997 Three-dimensional silicon microcomponents manufactured by micro-electro discharge machining. *Micromachined Devices and Components III, Proceedings of the SPIE - The International Society for Optical Engineering* (Austin, TX, USA, 29 Sep 1997) SPIE-Int. Soc. Opt. Eng 3224 p. 352-9.

[80] Li L., Diver C., Atkinson J., Giedl-Wagner R. and Helml H.J. 2006 Sequential laser and EDM micro-drilling for next generation fuel injection nozzle manufacture. *CIRP Annals - Manufacturing Technology*. **55**(1) p. 179-182.

[81] Sanha K., Bo Hyun K., Do Kwan C., Hong Shik S. and Chong Nam C. 2010 Hybrid micromachining using a nanosecond pulsed laser and micro EDM. *Journal of Micromechanics and Microengineering*. **20**(1) p. 015037 (8 pp.).

[82] Yeo S.H. and Murali M. 2003 A new technique using foil electrodes for the electro-discharge machining of micro grooves. *Journal of Micromechanics and Microengineering*. **13**(1) p. 1-5.

[83] Chaitanya C.R.A. and Takahata K. 2008 M3EDM: MEMS-enabled micro-electro-discharge machining. *Journal of Micromechanics and Microengineering*. **18**(10) p. 105009 (7 pp.).

[84] Sato T., Mizutani T. and Kawata K. 1985 Electro-discharge machine for micro-hole boring. *National Technical Report*. **31**(5) p. 725-33.

[85] Jahan M.P., Wong Y.S. and Rahman M. 2009 A study on the quality micro-hole machining of tungsten carbide by micro-EDM process using transistor and RC-type pulse generator. *Journal of Materials Processing Technology*. **209**(4) p. 1706-1716.

[86] Yu Z., Masuzawa T. and Fujino M. 1998 3D micro EDM with simple shape electrode Part 1: Machining of cavities with sharp corners and electrode wear compensation. *International Journal of Electrical Machining*. **3** p. 7-12 & 71-79.

[87] Hang G., Cao G., Wang Z., Tang J., Wang Z. and Zhao W. 2006 Micro-EDM milling of micro platinum hemisphere. *Proceedings of 1st IEEE International Conference on Nano Micro Engineered and Molecular Systems, 1st IEEE-NEMS* (Zhuhai, China, 18-21 Jan 2006) Institute of Electrical and Electronics Engineers Computer Society, Piscataway, NJ 08855-1331, United States p. 579-584.

[88] Luo Y.F., Chen C.G. and Tong Z.F. 1992 Investigation of silicon wafering by wire EDM. *Journal of Materials Science*. **27**(21) p. 5805-10.

[89] Schoth A., Forster R. and Menz W. 2005 Micro wire EDM for high aspect ratio 3D microstructuring of ceramics and metals. *Microsystem Technologies*. **11**(4-5) p. 250-253.

[90] Masuzawa T., Okajima K., Taguchi T. and Fujino M. 2002 EDM-lathe for micromachining. *CIRP Annals - Manufacturing Technology*. **51**(1) p. 355-358.

[91] Almond H. and Allen D.M. 2000 Influence of materials selection and quality on ink jet nozzles fabricated by micro-electrodischarge machining. *Proceedings of the SPIE - The International Society for Optical Engineering: Design, Test, Integration, and Packaging of MEMS/MOEMS* (Paris, France, 9-11 May 2000) SPIE-Int. Soc. Opt. Eng 4019 p. 446-455.

[92] Diver C., Atkinson J., Helml H.J. and Li L. 2004 Micro-EDM drilling of tapered holes for industrial applications. *Journal of Materials Processing Technology*. **149**(1-3) p. 296-303.

[93] Lee J.-L., Shen Y.-K., Lin Y., Teng P.-T. and Huang C.-M. 2009 Fabrication and analysis of microfluidic mold insert by micro electrical discharge machining. *4th IEEE International Conference on Nano/Micro Engineered and Molecular*

Systems, NEMS 2009 (Shenzhen, China, 5 - 8 Jan 2009) IEEE Computer Society p. 941-945.

[94] Rooks A. 2010 Sinker EDMing drives micro moldmaking. *MICROmanufacturing*. (Nelson, Don: Northbrook, IL) p. 7-11, 50.

[95] Schumacher B.M. 2004 After 60 years of EDM the discharge process remains still disputed. *Journal of Materials Processing Technology*. **149**(1-3) p. 376-381.

[96] Dhanik S., Joshi S.S., Ramakrishnan N. and Apte R. 2005 Evolution of EDM process modelling and development towards modelling of the micro-EDM process. *International Journal of Manufacturing Technology and Management*. **7**(2-4) p. 157-180.

[97] Snoeys R. and Van Dijck F.S. 1971 Investigation of electro discharge machining operations by means of thermo-mathematical model. *CIRP Annals*. **20**(1) p. 35-7.

[98] Van Dijck F.S. and Dutre W.L. 1974 Heat conduction model for the calculation of the volume of molten metal in electric discharges [discharge machining]. *Journal of Physics D (Applied Physics)*. **7**(6) p. 899-910.

[99] Lhiaubet C. and Meyer R.M. 1981 Method of indirect determination of the anodic and cathodic voltage drops in short high-current electric discharges in a dielectric liquid. *Journal of Applied Physics*. **52**(6) p. 3929-34.

[100] Benzerga L., Lhiaubet C. and Meyer R.M. 1985 Improvement of a proposed model for heat conduction in an electrode submitted to an electric discharge: application to the indirect determination of the anodic and cathodic voltage drops. *Journal of Applied Physics*. **58**(1) p. 604-6.

[101] Lhiaubet C., Benzerga L. and Boyer L. 1986 Simulation of the EDM process modeled as a semi-infinite solid. *Modeling, Sensing, and Control of Manufacturing Processes, Presented at the Winter Annual Meeting of the American Society of Mechanical Engineers* (Anaheim, CA, USA, 1986) ASME , New York, NY, USA 23 p. 109-27.

[102] Jilani S.T. and Pandey P.C. 1982 Analysis and modelling of EDM parameters. *Precision Engineering*. **4**(4) p. 215-21.

[103] Pandey P.C. and Jilani S.T. 1986 Plasma channel growth and the resolidified layer in EDM. *Precision Engineering*. **8**(2) p. 104-110.

[104] DiBitonto D.D., Eubank P.T., Patel M.R. and Barrufet M.A. 1989 Theoretical models of the electrical discharge machining process. I. A simple cathode erosion model. *Journal of Applied Physics*. **66**(9) p. 4095-103.

[105] Patel M.R., Barrufet M.A., Eubank P.T. and DiBitonto D.D. 1989 Theoretical models of the electrical discharge machining process. II. The anode erosion model. *Journal of Applied Physics*. **66**(9) p. 4104-11.

[106] Eubank P.T., Patel M.R., Burrufet M.A. and Bozkurt B. 1993 Theoretical models of the electrical discharge machining process. III. The variable mass, cylindrical plasma model. *Journal of Applied Physics*. **73**(11) p. 7900-9.

[107] Singh A. and Ghosh A. 1999 Thermo-electric model of material removal during electric discharge machining. *International Journal of Machine Tools & Manufacture*. **39**(4) p. 669-82.

[108] El-Hofy H.A.-G. 2005 Electrodischarge Machining: Mechanism of material removal. *Advanced machining processes : nontraditional and hybrid machining processes*. (New York : McGraw-Hill Professional, 2005) p. 116-118.

[109] Natsu W., Ojima S., Kobayashi T. and Kunieda M. 2004 Temperature distribution measurement in EDM arc plasma using spectroscopy. *JSME International Journal, Series C (Mechanical Systems, Machine Elements and Manufacturing)*. **47**(1) p. 384-90.

[110] Albinski K., Musiol K., Miernikiewicz A., Labuz S. and Malota M. 1996 Temperature of a plasma used in electrical discharge machining. *Plasma Sources Science and Technology*. **5**(4) p. 736-742.
[111] Shobert E.I.I. 1976 What Happens in EDM. *Manufacturing Engineering*. **77**(1) p. 38-39.
[112] Dhanik S. and Joshi S.S. 2005 Modeling of a single resistance capacitance pulse discharge in micro-electro discharge machining. *Transactions of the ASME. Journal of Manufacturing Science and Engineering*. **127**(4) p. 759-767.
[113] Kunieda M., Lauwers B., Rajurkar K.P. and Schumacher B.M. 2005 Advancing EDM through fundamental insight into the process. *CIRP Annals - Manufacturing Technology*. **54**(2) p. 599-622.
[114] Mamalis A.G., Vosniakos G.C., Vaxevanidis N.M. and Prohaszka J. 1987 Macroscopic and microscopic phenomena of electro-discharge machined steel surfaces: An experimental investigation. *Journal of Mechanical Working Technology*. **15**(3) p. 335-356.
[115] Guu Y.H., Hocheng H., Chou C.Y. and Deng C.S. 2003 Effect of electrical discharge machining on surface characteristics and machining damage of AISI D2 tool steel. *Materials Science & Engineering A (Structural Materials: Properties, Microstructure and Processing)*. **A358**(1-2) p. 37-43.
[116] Rebelo J.C., Dias A.M., Kremer D. and Lebrun J.L. 1998 Influence of EDM pulse energy on the surface integrity of martensitic steels. *Journal of Materials Processing Technology*. **84**(1-3) p. 90-96.
[117] Lee L.C., Lim L.C., Wong Y.S. and Lu H.H. 1990 Towards a better understanding of the surface features of electro-discharge machined tool steels. *Proceedings of the International Conference on Developments in Forming Technology, Journal of Materials Processing Technology*. **24** p. 513-523.
[118] Lee H.T. and Tai T.Y. 2003 Relationship between EDM parameters and surface crack formation. *Journal of Materials Processing Technology*. **142**(3) p. 676-683.
[119] Sarkar S., Mitra S. and Bhattacharyya B. 2005 Parametric analysis and optimization of wire electrical discharge machining of gamma-titanium aluminide alloy. *Journal of Materials Processing Technology*. **159**(3) p. 286-294.
[120] Ramakrishnan R. and Karunamoorthy L. 2008 Modeling and multi-response optimization of Inconel 718 on machining of CNC WEDM process. *Journal of Materials Processing Technology*. **207**(1-3) p. 343-349.
[121] Krishna Mohana Rao G., Rangajanardhaa G., Hanumantha Rao D. and Sreenivasa Rao M. 2009 Development of hybrid model and optimization of surface roughness in electric discharge machining using artificial neural networks and genetic algorithm. *Journal of Materials Processing Technology*. **209**(3) p. 1512-1520.
[122] Tsai K.-M. and Wang P.-J. 2001 Predictions on surface finish in electrical discharge machining based upon neural network models. *International Journal of Machine Tools and Manufacture*. **41**(10) p. 1385-403.
[123] Petropoulos G., Vaxevanidis N.M. and Pandazaras C. 2004 Modeling of surface finish in electro-discharge machining based upon statistical multi-parameter analysis. *Journal of Materials Processing Technology*. **155-156** p. 1247-51.
[124] Chiang K.-T. and Chang F.-P. 2007 Applying grey forecasting method for fitting and predicting the performance characteristics of an electro-conductive ceramic (Al2O3+30%TiC) during electrical discharge machining. *International Journal of Advanced Manufacturing Technology*. **33**(5-6) p. 480-8.

[125] Kaminski P.C. and Capuano M.N. 2003 Micro hole machining by conventional penetration electrical discharge machine. *International Journal of Machine Tools and Manufacture*. **43**(11) p. 1143-1149.
[126] Uhlmann E., Piltz S. and Doll U. 2005 Machining of micro/miniature dies and moulds by electrical discharge machining - Recent development. *2005 Int. Forum on the Advances in Materials Processing, J. of Materials Processing Technology*. **167**(2-3) p. 488-93.
[127] Masuzawa T. 2000 State of the art of micromachining. *CIRP Annals - Manufacturing Technology*. **49**(2) p. 473-488.
[128] Egashira K., Matsugasako A., Tsuchiya H. and Miyazaki M. 2006 Electrical discharge machining with ultralow discharge energy. *Precision Engineering*. **30**(4) p. 414-20.
[129] Sato T., Mizutani T., Yonemochi K. and Kawata K. 1986 The development of an electrodischarge machine for micro-hole boring. *Precision Engineering*. **8**(3) p. 163-168.
[130] Kawakami T. and Kunieda M. 2005 Study on factors determining limits of minimum machinable size in micro EDM. *CIRP Annals - Manufacturing Technology*. **54**(1) p. 167-70.
[131] Murali M. and Yeo S.H. 2004 A novel spark erosion technique for the fabrication of high aspect ratio micro-grooves. *Microsystem Technologies*. **10**(8-9) p. 628-632.
[132] Egashira K. and Mizutani K. 2005 EDM at low open-circuit voltage. *International Journal of Electrical Machining*. **10** p. 21-26.
[133] Zhao W.S., Meng Q.G. and Wang Z.L., *The application of research on powder mixed EDM in rough machining*, in *10th Int. Manufacturing Conf. in China (IMCC 2002)*. 2002, Elsevier Science Ltd: Fujian, China. p. 30-33.
[134] Yeo S.H., Kurnia W. and Tan P.C. 2007 Electro-thermal modelling of anode and cathode in micro-EDM. *Journal of Physics D: Applied Physics*. **40**(8) p. 2513-21.
[135] Xia H., Kunieda M. and Nishiwaki N. 1996 Removal amount difference between anode and cathode in EDM process. *International Journal of Electrical Machining*. **1**(1) p. 45-52.
[136] Han F., Yamada Y., Kawakami T. and Kunieda M. 2006 Experimental attempts of sub-micrometer order size machining using micro-EDM. *Precision Engineering*. **30**(2) p. 123-31.
[137] Ekmekci B., Sayar A., Opoz T.T. and Erden A. 2009 Geometry and surface damage in micro electrical discharge machining of micro-holes. *Journal of Micromechanics and Microengineering*. **19**(10) p. 105030 (16 pp.).
[138] Bhattacharyya B., Gangopadhyay S. and Sarkar B.R. 2007 Modelling and analysis of EDMed job surface integrity. *Journal of Materials Processing Technology*. **189**(1-3) p. 169-177.
[139] Katz Z. and Tibbles C.J. 2005 Analysis of micro-scale EDM process. *International Journal of Advanced Manufacturing Technology*. **25**(9-10) p. 923-928.
[140] Jeong Y.H. and Min B.-K. 2007 Geometry prediction of EDM-drilled holes and tool electrode shapes of micro-EDM process using simulation. *International Journal of Machine Tools and Manufacture*. **47**(12-13) p. 1817-26.
[141] Kurnia W., Tan P.C., Yeo S.H. and Tan Q.P. 2009 Surface roughness model for micro electrical discharge machining. *Proceedings of the Institution of Mechanical Engineers, Part B: Journal of Engineering Manufacture*. **223**(3) p. 279-287.

[142] Pandit S.M. and Rajurkar K.P. 1983 Stochastic approach to thermal modeling applied to electro-discharge machining. *Journal of Heat Transfer, Transactions ASME*. **105**(3) p. 555-62.
[143] Allen D.M., Almond H.J.A., Bhogal J.S., Green A.E., Logan P.M. and Huang X.X. 1999 Typical metrology of micro-hole arrays made in stainless steel foils by two-stage micro-EDM. *CIRP Annals - Manufacturing Technology*. **48**(1) p. 127-30.
[144] Yadav V., Jain V.K. and Dixit P.M. 2002 Thermal stresses due to electrical discharge machining. *International Journal of Machine Tools & Manufacture*. **42**(8) p. 877-888.
[145] Murali M.S. and Yeo S.H. 2005 Process simulation and residual stress estimation of micro-electrodischarge machining using finite element method. *Japanese Journal of Applied Physics, Part 1: Regular Papers and Short Notes and Review Papers*. **44**(7 A) p. 5254-5263.
[146] Lee L.C., Lim L.C. and Wong Y.S. 1992 Towards crack minimisation of EDMed surfaces. *Journal of Materials Processing Technology*. **32**(1-2) p. 45-54.
[147] Abu Zeid O.A. 1997 On the effect of electrodischarge machining parameters on the fatigue life of AISI D6 tool steel. *Journal of Materials Processing Technology*. **68**(1) p. 27-32.
[148] Bonny K., De Baets P., Vleugels J., Salehi A., Van der Biest O., Lauwers B. and Liu W. 2008 Influence of electrical discharge machining on tribological behavior of ZrO2-TiN composites. *Wear*. **265**(11-12) p. 1884-1892.
[149] Yan B.H., Lin Y.C., Huang F.Y. and Wang C.H. 2001 Surface modification of SKD 61 during EDM with metal powder in the dielectric. *Materials Transactions*. **42**(12) p. 2597-2604.
[150] Kurafuji H. and Suda K. 1965 Study on electrical discharge machining. *Journal of the Faculty of Engineering, University of Tokyo, Series B*. **28**(1) p. 1-18.
[151] Crookall J.R. and Khor B.C. 1974 Electro-discharge machined surfaces. *15th Int Mach Tool Design and Research Conf, Institutet for Verkstadsteknisk Forskning, IVF Resultat* (Birmingham, Engl, 18-20 Sep 1974) Halsted Press, Div of John Wiley, New York, NY 373-84.
[152] Meshcheriakov G.N. 1970 Electro-physical processes in electric pulse metal cutting from the point of view of efficiency and polarity of electrode wear. *Annals of the CIRP*. **18**(3) p. 491-9.
[153] Gangadhar A., Shunmugam M.S. and Philip P.K. 1991 Surface modification in electrodischarge processing with a powder compact tool electrode. *Wear*. **143**(1) p. 45-55.
[154] Ochiai H., Watanabe M., Arai M., Yoshizawa H. and Saitou Y. 2005 Development of coating and cladding technology, MScoating, using electro-discharge energy. *Ishikawajima-Harima Engineering Review*. **45**(2) p. 72-9.
[155] Erden A. and Bilgin S. 1981 Role of impurities in electric discharge machining. *Proceedings of the 21st International Machine Tool Design and Research Conference* (Swansea, Wales, 8-12 Sep1980) Univ Coll of Swansea, Dep of Mech Eng, Wales in Assoc with Macmillan Press, Ltd, London, Engl p. 345-350.
[156] Klocke F., Lung D., Antonoglou G. and Thomaidis D. 2004 The effects of powder suspended dielectrics on the thermal influenced zone by electrodischarge machining with small discharge energies. *14th Int. Symp. on Electromachining (ISEM XIV) J. Mater. Process. Technol. (Switzerland)* (Edinburgh, Scotland, UK, 30 Mar-1 Apr 2004) Elsevier 149 p. 191-7.
[157] Pecas P. and Henriques E. 2007 Effect of the powder concentration and dielectric flow in the surface morphology in electrical discharge machining with powder-

mixed dielectric (PMD-EDM). *The International Journal of Advanced Manufacturing Technology*. **37**(11-12) p. 1120-1132.

[158] Tzeng Y.-F. and Chen F.-C. 2005 Investigation into some surface characteristics of electrical discharge machined SKD-11 using powder-suspension dielectric oil. *Journal of Materials Processing Technology*. **170**(1-2) p. 385-91.

[159] Takawashi T., Kobayashi K., Ito H., Sakakibara T. and Saito N. 1983 Study on the mirror surface machining by planetary EDM. *Proceedings of the 7th International Symposium on Electromachining (ISEM-7)* (Birmingham, Engl, 12-14 Apr 1983) IFS (Publ) Ltd, Kempston, Bedfordshire, Engl p. 137-146.

[160] Schumacher B.M. 1990 About the Role of Debris in the Gap During Electrical Discharge Machining. *CIRP Annals - Manufacturing Technology*. **39**(1) p. 197-199.

[161] Kunieda M. and Yanatori K. 1997 Study on debris movement in EDM gap. *International Journal of Electrical Machining*. **2** p. 43-49.

[162] Pecas P. and Henriques E. 2003 Influence of silicon powder-mixed dielectric on conventional electrical discharge machining. *International Journal of Machine Tools and Manufacture*. **43**(14) p. 1465-71.

[163] Chow H.-M., Yan B.-H., Huang F.-Y. and Hung J.-C. 2000 Study of added powder in kerosene for the micro-slit machining of titanium alloy using electro-discharge machining. *J. of Materials Processing Technology*. **101**(1) p. 95-103.

[164] Tzeng Y.-F. and Lee C.-Y. 2001 Effects of powder characteristics on electrodischarge machining efficiency. *International Journal of Advanced Manufacturing Technology*. **17**(8) p. 586-92.

[165] Yan B.H. and Chen S.L. 1994 Characteristics of SKD11 by complex process of electrical discharge machining using liquid suspended with alumina powder. *Nippon Kinzoku Gakkaishi/Journal of the Japan Institute of Metals*. **58**(9) p. 1067-1072.

[166] Jeswani M.L. 1978 Roughness and wear characteristic of spark-eroded surfaces. *Wear*. **51**(2) p. 227-36.

[167] Wu K.L., Yan B.H., Huang F.Y. and Chen S.C. 2005 Improvement of surface finish on SKD steel using electro-discharge machining with aluminum and surfactant added dielectric. *International Journal of Machine Tools and Manufacture*. **45**(10) p. 1195-1201.

[168] Furutani K. and Shimizu Y. 2003 Experimental analysis of deposition process of lubricant surface by electrical discharge machining with molybdenum disulfide powder suspended in working oil. *Proceedings of the American Society for Precision Engineering* (Portland, Oregon, Oct 2003) American Society for Precision Engineering (ASPE) 30 p. 547-550.

[169] Furutani K., Sato H. and Suzuki M. 2009 Influence of electrical conditions on performance of electrical discharge machining with powder suspended in working oil for titanium carbide deposition process. *International Journal of Advanced Manufacturing Technology*. **40**(11) p. 1093-1101.

[170] Fukuzawa Y., Kojima Y., Tani T., Sekiguti E. and Mohri N. 1995 Fabrication of surface modification layer on stainless steel by electrical discharge machining. *Materials and Manufacturing Processes*. **10**(2) p. 195-203.

[171] Tsunekawa Y., Okumiya M., Mohri N. and Takahashi I. 1994 Surface modification of aluminum by electrical discharge alloying. *Materials Science & Engineering A (Structural Materials: Properties, Microstructure and Processing)*. **A174**(2) p. 193-8.

[172] Aspinwall D.K., Dewes R.C., Lee H.G. and Simao J. 2003 Electrical discharge surface alloying of Ti and Fe workpiece materials using refractory powder compact electrodes and Cu wire. *CIRP Annals - Manufacturing Technology*. **52**(1) p. 151-156.

[173] Wang Z.L., Fang Y., Wu P.N., Zhao W.S. and Cheng K. 2002 Surface modification process by electrical discharge machining with a Ti powder green compact electrode. *10th International Manufacturing Conference, Journal of Materials Processing Technology* (Xiamen, China, 11-13 Oct 2002) Elsevier 129 p. 139-42.

[174] Moro T., Mohri N., Otsubo H., Goto A. and Saito N. 2004 Study on the surface modification system with electrical discharge machine in the practical usage. *14th International Symposium on Electromachining (ISEM XIV) Journal of Materials Processing Technology* (Edinburgh, Scotland, UK, 30 Mar -1 Apr 2004) Elsevier 149 p. 65-70.

[175] Mohri N., Saito N., Tsunekawa Y. and Kinoshita N. 1993 Metal surface modification by electrical discharge machining with composite electrode. *CIRP Annals*. **42**(1) p. 219-222.

[176] Ho S.K., Aspinwall D.K. and Voice W. 2007 Use of powder metallurgy (PM) compacted electrodes for electrical discharge surface alloying/modification of Ti-6Al-4V alloy. *Journal of Materials Processing Technology*. **191**(1-3) p. 123-6.

[177] Chen Y.-F., Chow H.-M., Lin Y.-C. and Lin C.-T. 2008 Surface modification using semi-sintered electrodes on electrical discharge machining. *International Journal of Advanced Manufacturing Technology*. **36**(5-6) p. 490-500.

[178] Chow H.-M., Yang L.-D., Lin C.-T. and Chen Y.-F. 2008 The use of SiC powder in water as dielectric for micro-slit EDM machining. *Journal of Materials Processing Technology*. **195**(1-3) p. 160-70.

[179] Kansal H.K., Singh S. and Kumar P. 2008 Numerical simulation of powder mixed electric discharge machining (PMEDM) using finite element method. *Mathematical and Computer Modelling*. **47**(11-12) p. 1217-1237.

[180] Kansal H.K., Singh S. and Kumar P. 2005 Parametric optimization of powder mixed electrical discharge machining by response surface methodology. *Journal of Materials Processing Technology*. **169**(3) p. 427-36.

[181] Cogun C., Ozerkan B. and Karacay T. 2006 An experimental investigation on the effect of powder mixed dielectric on machining performance in electric discharge machining. *Proceedings of the Institution of Mechanical Engineers, Part B (Journal of Engineering Manufacture)*. **220**(B7) p. 1035-50.

[182] Ikawa N., Shimada S. and Tanaka H. 1992 Minimum thickness of cut in micromachining. *Nanotechnology*. **3**(1) p. 6-9.

[183] Kim C.-J., Bono M. and Ni J. 2002 Experimental analysis of chip formation in micro-milling. *NAMRI XXX* (West Lafayette, ID, 21-24 May 2002) Society of Manufacturing Engineers p. 1-8.

[184] Le Harzic R., Breitling D., Weikert M., Sommer S., Fohl C., Valette S., Donnet C., Audouard E. and Dausinger F. 2005 Pulse width and energy influence on laser micromachining of metals in a range of 100fs to 5ps. *Applied Surface Science*. **249**(1-4) p. 322-31.

[185] Wong Y.S., Rahman M., Lim H.S., Han H. and Ravi N. 2003 Investigation of micro-EDM material removal characteristics using single RC-pulse discharges. *6th Asia Pacific Conf. on Materials Processing (6th APCMP) J. Mater. Process. Technol.* (Taipei, Taiwan, 22-25 Sep 2003) Elsevier 140 p. 303-7.

[186] Habib S.S. 2009 Study of the parameters in electrical discharge machining through response surface methodology approach. *Applied Mathematical Modelling*. **33**(12) p. 4397-4407.
[187] Pradhan M.K., Das R. and Biswas C.K. 2009 Comparisons of neural network models on surface roughness in electrical discharge machining. *Proceedings of the Institution of Mechanical Engineers, Part B: Journal of Engineering Manufacture*. **223**(7) p. 801-808.
[188] Boothroyd G.G., *Fundamentals of Machining and Machine Tools*. 3rd ed. 2006, Boca Raton, FL: CRC/Taylor & Francis.
[189] Snoeys R., Van Dijck F.S. and Peters J. 1972 Plasma channel diameter growth affects stock removal in EDM. *CIRP Annals*. **21**(1) p. 39-40.
[190] Erden A. and Kaftanoglu B. 1981 Heat transfer modelling of electric discharge machining. *Proceedings of the 21st International Machine Tool Design and Research Conference* (Swansea, Wales, 1981) Univ Coll of Swansea, Dep of Mech Eng, Wales in Assoc with Macmillan Press, Ltd, London, Engl p. 351-358.
[191] Wang B.-J. and Saka N. 1993 Thermal analysis of electrode heating and melting due to a spark. *IEEE Transactions on Components, Hybrids, and Manufacturing Technology*. **16**(4) p. 456-66.
[192] Panda D.K. and Bhoi R.K. 2005 Analysis of spark eroded crater formed under growing plasma channel in electro-discharge machining. *Machining Science and Technology*. **9**(2) p. 239-61.
[193] Barrufet M.A., Patel M.R. and Eubank P.T. 1991 Novel computations of a moving boundary heat conduction problem applied to EDM technology. *Computers & Chemical Engineering*. **15**(8) p. 609-18.
[194] Shankar P., Jain V.K. and Sundararajan T. 1997 Analysis of spark profiles during EDM process. *Machining Science and Technology*. **1**(2) p. 195-217.
[195] Marafona J. and Chousal J.A.G. 2006 A finite element model of EDM based on the Joule effect. *International Journal of Machine Tools and Manufacture*. **46**(6) p. 595-602.
[196] Natsu W., Shimoyamada M. and Kunieda M. 2006 Study on expansion process of EDM arc plasma. *JSME International Journal, Series C: Mechanical Systems, Machine Elements and Manufacturing*. **49**(2) p. 600-5.
[197] Das S., Klotz M. and Klocke F. 2003 EDM simulation: finite element-based calculation of deformation, microstructure and residual stresses. *Journal of Materials Processing Technology*. **142**(2) p. 434-51.
[198] Schulze H.-P., Herms R., Juhr H., Schaetzing W. and Wollenberg G. 2004 Comparison of measured and simulated crater morphology for EDM. *14th International Symposium on Electromachining (ISEM XIV) J. Mater. Process. Technol.* (Edinburgh, Scotland, UK, 30 Mar -1 Apr 2004) Elsevier 149 p. 316-22.
[199] Panda D.K. 2008 Study of thermal stresses induced surface damage under growing plasma channel in electro-discharge machining. *Journal of Materials Processing Technology*. **202**(1-3) p. 86-95.
[200] Kurnia W., Tan P.C., Yeo S.H. and Wong M. 2008 Analytical approximation of the erosion rate and electrode wear in micro electrical discharge machining. *Journal of Micromechanics and Microengineering*. **18**(8) p. 085011 (8 pp.).
[201] Perez R., Carron J., Rappaz M., Walder G., Revaz B. and Flukiger R. 2007 Measurement and metallurgical modeling of the thermal impact of EDM discharges on steel. *15th International Symposium on Electromachining (ISEM XV)* (Pittsburgh, Pennsylvania - USA, 23-27 April 2007) p. 17-22.

[202] Izquierdo B., Sanchez J.A., Plaza S., Pombo I. and Ortega N. 2009 A numerical model of the EDM process considering the effect of multiple discharges. *International Journal of Machine Tools & Manufacture*. **49**(3-4) p. 220-9.
[203] Izquierdo B., Sanchez J.A., Plaza S., Ortega N. and Pombo I. 2009 Inverse determination of discharge properties based on surface finish and material removal rate predictions using thermal multi-spark modeling of the EDM process. *AIP Conference Proceedings. Third Manufacturing Engineering Society International Conference, MESIC-09* (Alcoy, Spain, 17-19 Jun 2009) American Institute of Physics 1181 p. 464-473.
[204] Erden A. 1983 Effect of materials on the mechanism of electric discharge machining (E.D.M.). *Journal of Engineering Materials and Technology, Transactions of the ASME*. **105**(2) p. 132-8.
[205] Erden A., Arinc F. and Kogmen M. 1995 Comparison of mathematical models for electric discharge machining. *Journal of Materials Processing and Manufacturing Science*. **4**(2) p. 163-76.
[206] Xia H., Hashimoto H., Kunieda M. and Nishiwaki N. 1996 Measurement of energy distribution in continuous EDM process. *Seimitsu Kogaku Kaishi/Journal of the Japan Society for Precision Engineering*. **62**(8) p. 1141-5.
[207] Salah N.B., Ghanem F. and Atig K.B. 2006 Numerical study of thermal aspects of electric discharge machining process. *International Journal of Machine Tools and Manufacture*. **46**(7-8) p. 908-911.
[208] Washko S.D. and Aggen G. *Properties and Selection: Irons, Steels, and High Performance Alloys*. In ASM engineered materials handbook desk edition [electronic resource] ASM International; 2003 [cited Aug 17, 2010]. Available from: ASM Handbooks Online. http://products.asminternational.org.
[209] Uddeholm, *STAVAX ESR Stainless mould steel Fact Sheet*. 2008.
[210] ASTM International, *Standard practice for microetching metals and alloys*. 2007.
[211] Sato K., Li J.-G., Kamiya H. and Ishigaki T. 2008 Ultrasonic dispersion of TiO2 nanoparticles in aqueous suspension. *Journal of the American Ceramic Society*. **91**(8) p. 2481-7.
[212] Ridler T.W. and Calvard S. 1978 Picture thresholding using an iterative selection method. *IEEE Transactions on Systems, Man and Cybernetics*. **8** p. 630-632.
[213] Schumacher B.M. 1983 EDM technology for precision workpieces with excellent surface quality. *Proceedings of the 7th International Symposium on Electromachining (ISEM-7)* (Birmingham, Engl, 12-14 Apr 1983) IFS (Publ) Ltd, Kempston, Bedfordshire, Engl p. 123-135.
[214] Rajurkar K.P. and Pandit S.M. 1986 Formation and ejection of EDM debris. *Journal of Engineering for Industry, Transactions ASME*. **108**(1) p. 22-6.
[215] Lu Z.-Z., Zhao F.-L. and Yang Y.-Y. 2008 Research on dielectric breakdown and discharge channel in powder-mixed EDM. *Dalian Ligong Daxue Xuebao/Journal of Dalian University of Technology*. **48**(3) p. 373-377.
[216] Ekmekci B. 2009 White layer composition, heat treatment, and crack formation in electric discharge machining process. *Metallurgical and Materials Transactions B: Process Metallurgy and Materials Processing Science*. **40**(1) p. 70-81.
[217] Soni J.S. and Chakraverti G. 1996 Experimental investigation on migration of material during EDM of die steel (T215 Cr12). *Journal of Materials Processing Technology (Proceedings of the 1993 International Conference on Advances in Material & Processing Technologies, AMPT'93, Aug 1993)*. **56**(1-4) p. 439-451.
[218] Timofeeva E.V., Gavrilov A.N., McCloskey J.M., Tolmachev Y.V., Sprunt S., Lopatina L.M. and Selinger J.V. 2007 Thermal conductivity and particle

agglomeration in alumina nanofluids: experiment and theory. *Physical Review E (Statistical, Nonlinear, and Soft Matter Physics)*. **76**(6) p. 061203-1.

[219] Joshi S.N. and Pande S.S. 2010 Thermo-physical modeling of die-sinking EDM process. *Journal of Manufacturing Processes*. **12**(1) p. 45-56.

[220] Arunachalam C. 1995 Modeling the electrical discharge machining process. Ph.D. dissertation. Texas A&M University.

[221] Natsu W., Kunieda M. and Nishiwaki N. 2004 Study on influence of inter-electrode atmosphere on carbon adhesion and removal amount. *International Journal of Electrical Machining*. **9**(1) p. 43-50.

[222] Jin B.D., Cao G.H., Wang Z.L. and Zhao W.S. 2007 A micro-deposition method by using EDM. *Key Engineering Materials*. **339** p. 32-36.

[223] Ori R.I., Itoigawa F., Hayakawa S., Nakamura T. and Tanaka S.-I. 2004 Micro-EDM deposition alloying process. *2004 ASME International Mechanical Engineering Congress and Exposition, IMECE 2004* (Anaheim, CA, United States, 13-19 Nov 2004) American Society of Mechanical Engineers, New York, NY 10016-5990, United States 15 p. 697-98.

[224] Chiu K.Y., Cheng F.T. and Man H.C. 2005 Cavitation erosion resistance of AISI 316L stainless steel laser surface-modified with NiTi. *Materials Science and Engineering A*. **392**(1-2) p. 348-358.

[225] He J.L., Won K.W., Chang C.T., Chen K.C. and Lin H.C. 1998 Cavitation-resistant TiNi films deposited by using cathodic arc plasma ion plating. *International Conference on Erosive and Abrasive Wear (ICEAW). incorporating the 9th International Conference on Erosion by Liquid and Solid Impact (ELSI IX)* (Cambridge, UK, 13-17 Sep 1998) Elsevier 233-235 p. 104-10.

Appendix A

Table A.1 Crater geometries produced in powder-free dielectric, 2.5μJ input energy

Crater	Input Energy = 2.5uJ							
	Outer diameter (um)			Inner diameter (um)			Rim ht	Pk-valley ht
	Direction 1	Direction 2	Average	Direction 1	Direction 2	Average	(um)	(um)
1	9.31	8.94	9.13	4.02	3.83	3.93	0.38	1.52
2	8.76	8.40	8.58	4.20	6.94	5.57	0.09	0.22
3	9.67	8.40	9.04	5.47	4.92	5.20	0.67	1.23
4	9.67	8.39	9.03	4.75	3.65	4.20	0.44	1.13
5	8.58	8.03	8.31	4.93	3.84	4.39	0.49	1.22
6	9.31	9.67	9.49	7.30	4.57	5.94	0.34	0.60
7	10.04	9.12	9.58	5.47	5.29	5.38	0.70	1.34
8	9.13	8.40	8.77	4.75	4.20	4.48	1.25	2.00
9	8.94	8.21	8.58	6.02	4.02	5.02	0.26	0.82
10	7.85	7.66	7.76	5.29	6.20	5.75	0.92	0.23
11	9.13	7.48	8.31	6.21	3.65	4.93	0.90	1.52
12	9.31	8.58	8.95	5.66	5.29	5.48	0.08	0.20
13	8.31	8.30	8.31	5.87	4.17	5.02	0.73	1.23
14	8.94	8.59	8.77	4.63	3.77	4.20	1.15	1.88
15	9.21	9.04	9.13	5.03	5.92	5.48	0.46	1.33
16	8.35	8.81	8.58	5.96	5.53	5.75	0.39	0.84
17	7.52	9.09	8.31	3.93	3.92	3.93	0.88	0.25
18	9.76	9.22	9.49	4.82	7.05	5.94	0.77	1.64
19	9.02	10.14	9.58	4.82	6.32	5.57	0.33	1.11
20	7.77	7.74	7.76	3.80	5.15	4.48	0.25	0.62
21	8.10	9.05	8.58	5.81	4.95	5.38	0.09	0.22
22	8.29	9.78	9.04	4.03	5.83	4.93	0.94	1.50
23	8.47	9.59	9.03	4.89	5.50	5.20	0.45	1.20
24	9.22	8.67	8.95	3.95	4.82	4.39	0.09	0.20
25	9.58	9.40	9.49	4.16	3.69	3.93	0.43	1.51
26	9.77	8.29	9.03	4.58	4.19	4.39	0.59	1.12
27	9.63	8.62	9.13	5.03	6.11	5.57	0.49	1.23
28	8.35	8.81	8.58	3.60	4.80	4.20	0.39	1.22
29	8.15	8.46	8.31	6.83	5.04	5.94	0.34	0.59
30	9.81	8.26	9.04	4.98	5.41	5.20	0.10	0.23
minimum			7.76			3.93	0.08	0.20
maximum			9.58			5.94	1.25	2.00
mean			8.82			4.99	0.51	1.00
std dev			0.49			0.66	0.32	0.54
std error			0.09			0.12	0.06	0.10

Table A.2 Crater geometries produced in powder-free dielectric, 5μJ input energy

Crater	Input Energy = 5uJ							
	Outer diameter (um)			Inner diameter (um)			Rim ht	Pk-valley ht
	Direction 1	Direction 2	Average	Direction 1	Direction 2	Average	(um)	(um)
1	12.05	10.77	11.41	5.84	5.66	5.75	0.43	1.40
2	10.59	12.23	11.41	6.93	5.11	6.02	0.78	1.79
3	11.50	10.95	11.23	7.11	5.29	6.20	1.92	3.00
4	11.13	12.59	11.86	6.39	4.93	5.66	1.31	2.51
5	10.22	8.76	9.49	4.75	6.76	5.76	0.34	0.89
6	10.22	10.04	10.13	6.39	6.39	6.39	0.56	0.99
7	11.13	10.77	10.95	6.38	6.94	6.66	0.37	0.98
8	11.68	11.50	11.59	5.84	8.03	6.94	1.37	2.43
9	11.86	12.05	11.96	6.57	5.29	5.93	0.35	1.29
10	10.95	11.32	11.14	7.48	4.93	6.21	0.42	0.71
11	11.32	10.77	11.05	7.12	6.93	7.03	0.32	0.68
12	11.50	10.40	10.95	6.20	6.94	6.57	0.29	0.63
13	12.96	11.86	12.41	5.11	5.66	5.39	0.83	1.75
14	12.05	10.95	11.50	6.75	5.66	6.21	0.28	1.01
15	11.68	12.05	11.87	5.84	6.02	5.93	0.71	1.95
16	11.13	11.13	11.13	7.30	6.75	7.03	0.42	1.14
17	11.13	11.50	11.32	7.67	6.75	7.21	0.58	1.30
18	11.13	12.05	11.59	7.12	3.83	5.48	1.82	3.00
19	12.41	10.95	11.68	5.29	5.65	5.47	1.07	2.01
20	10.95	10.04	10.50	7.12	7.66	7.39	0.65	1.71
21	10.40	10.04	10.22	5.35	7.06	6.21	0.24	1.20
22	15.70	10.40	13.05	7.06	6.26	6.66	0.56	1.35
23	11.12	11.33	11.23	6.23	5.09	5.66	0.34	0.97
24	11.64	11.18	11.41	5.97	5.53	5.75	0.44	1.00
25	11.97	9.93	10.95	6.57	6.21	6.39	0.55	1.38
26	10.43	9.83	10.13	6.93	5.47	6.20	1.31	2.43
27	11.40	11.78	11.59	7.79	6.08	6.94	0.36	0.90
28	8.89	10.09	9.49	6.43	5.43	5.93	1.89	2.77
29	11.25	12.47	11.86	6.55	5.49	6.02	1.37	2.50
30	11.92	10.90	11.41	4.98	6.53	5.76	0.81	2.02
minimum			9.49			5.39	0.24	0.63
maximum			13.05			7.39	1.92	3.00
mean			11.22			6.22	0.76	1.59
std dev			0.78			0.55	0.51	0.72
std error			0.14			0.10	0.09	0.13

Table A.3 Crater geometries produced in powder-free dielectric, 25μJ input energy

Crater	Input Energy = 25uJ							
	Outer diameter (um)			Inner diameter (um)			Rim ht	Pk-valley ht
	Direction 1	Direction 2	Average	Direction 1	Direction 2	Average	(um)	(um)
1	20.44	15.88	18.16	11.68	10.77	11.23	3.06	4.69
2	19.34	18.25	18.80	10.22	11.50	10.86	2.48	4.52
3	19.35	20.62	19.99	12.77	10.04	11.41	1.60	3.55
4	20.44	18.98	19.71	12.41	11.68	12.05	2.26	4.30
5	22.27	19.35	20.81	14.05	11.86	12.96	1.60	3.01
6	18.98	18.43	18.71	13.32	10.04	11.68	1.19	2.90
7	20.62	19.89	20.26	14.60	10.96	12.78	1.72	3.58
8	19.16	18.98	19.07	12.23	12.77	12.50	1.31	3.10
9	22.26	18.07	20.17	12.04	12.59	12.32	1.83	3.66
10	19.53	20.62	20.08	11.50	11.14	11.32	2.04	3.55
11	18.43	18.62	18.53	11.50	12.22	11.86	1.42	2.96
12	21.90	20.44	21.17	10.95	13.69	12.32	1.31	3.18
13	22.45	20.81	21.63	11.31	11.50	11.41	2.08	4.22
14	23.18	19.16	21.17	12.78	11.31	12.05	2.85	4.16
15	18.80	19.71	19.26	11.86	12.59	12.23	2.32	3.86
16	21.72	19.53	20.63	12.59	12.96	12.78	2.16	4.32
17	21.17	20.08	20.63	14.23	11.87	13.05	2.72	4.53
18	18.25	18.62	18.44	16.61	11.32	13.97	1.72	3.24
19	17.34	17.88	17.61	10.76	12.59	11.68	2.10	4.06
20	19.34	19.71	19.53	12.23	12.96	12.60	2.28	3.85
21	20.99	20.81	20.90	15.70	13.50	14.60	1.16	2.96
22	20.08	20.26	20.17	15.70	14.24	14.97	2.22	4.13
23	20.44	20.62	20.53	14.42	12.23	13.33	1.03	2.60
24	22.08	23.18	22.63	10.77	13.87	12.32	1.84	3.63
25	20.26	20.26	20.26	14.60	13.23	13.92	1.81	3.45
26	19.89	20.08	19.99	11.50	16.24	13.87	1.63	3.75
27	18.80	20.62	19.71	13.32	12.60	12.96	1.54	3.62
28	20.44	20.26	20.35	12.78	12.60	12.69	1.92	3.83
29	18.43	18.62	18.53	12.77	11.86	12.32	1.79	3.69
30	18.25	20.81	19.53	12.41	12.42	12.42	1.33	3.09
minimum			17.61			10.86	1.03	2.60
maximum			22.63			14.97	3.06	4.69
mean			19.90			12.55	1.88	3.67
std dev			1.11			0.99	0.51	0.55
std error			0.20			0.18	0.09	0.10

Table A.4 Crater geometries produced in powder-mixed dielectric, 2.5μJ input energy

Crater	Input Energy = 2.5uJ							
	Outer diameter (um)			Inner diameter (um)			Rim ht	Pk-valley ht
	Direction 1	Direction 2	Average	Direction 1	Direction 2	Average	(um)	(um)
1	8.40	8.76	8.58	6.02	5.30	5.66	0.10	0.24
2	8.40	8.21	8.31	4.93	5.11	5.02	0.32	1.08
3	8.58	8.21	8.40	5.66	6.76	6.21	0.19	0.92
4	8.40	8.21	8.31	4.93	4.20	4.57	0.15	0.33
5	8.40	10.04	9.22	5.84	5.11	5.48	0.33	0.80
6	8.76	8.40	8.58	6.02	5.84	5.93	0.23	0.54
7	8.76	8.76	8.76	6.20	6.76	6.48	0.29	1.05
8	8.03	8.03	8.03	4.38	5.47	4.93	0.26	0.54
9	8.03	8.21	8.12	5.66	6.75	6.21	0.12	0.24
10	8.58	8.58	8.58	5.47	5.48	5.48	0.29	0.64
11	9.31	8.40	8.86	6.21	6.57	6.39	0.50	1.17
12	8.40	8.40	8.40	6.21	5.84	6.03	0.35	0.76
13	8.03	8.03	8.03	5.48	5.85	5.67	0.14	0.28
14	8.21	8.03	8.12	5.84	6.21	6.03	0.17	0.42
15	7.48	8.03	7.76	5.47	5.66	5.57	0.09	0.19
16	8.21	8.21	8.21	5.66	5.29	5.48	0.13	0.28
17	7.30	7.85	7.58	5.47	6.75	6.11	0.09	0.11
18	7.96	8.10	8.03	5.48	5.85	5.67	0.13	0.33
19	8.50	9.21	8.86	5.58	5.37	5.48	0.35	1.10
20	8.58	8.21	8.40	6.21	6.21	6.21	0.35	0.81
21	8.50	8.11	8.31	6.10	6.31	6.21	0.12	0.24
22	8.32	8.84	8.58	6.50	6.46	6.48	0.29	0.65
23	8.01	8.05	8.03	6.02	4.93	5.48	0.25	0.54
24	8.40	8.76	8.58	5.34	6.71	6.03	0.10	0.24
25	8.31	9.21	8.76	5.40	4.45	4.93	0.23	0.92
26	8.03	8.21	8.12	5.84	5.48	5.66	0.33	0.76
27	8.34	8.46	8.40	4.55	4.58	4.57	0.15	0.28
28	9.80	8.64	9.22	4.88	5.16	5.02	0.48	1.15
29	9.00	8.16	8.58	6.47	6.31	6.39	0.30	1.04
30	8.20	8.41	8.31	5.70	6.16	5.93	0.19	0.54
minimum			7.58			4.57	0.09	0.11
maximum			9.22			6.48	0.50	1.17
mean			8.40			5.71	0.23	0.61
std dev			0.38			0.55	0.11	0.34
std error			0.07			0.10	0.02	0.06

Table A.5 Crater geometries produced in powder-mixed dielectric, 5μJ input energy

Crater	Input Energy = 5uJ							
	Outer diameter (um)			Inner diameter (um)			Rim ht (um)	Pk-valley ht (um)
	Direction 1	Direction 2	Average	Direction 1	Direction 2	Average		
1	9.67	9.86	9.77	6.75	7.12	6.94	0.15	0.31
2	10.95	10.77	10.86	8.03	7.67	7.85	0.44	0.90
3	11.13	10.77	10.95	7.67	7.30	7.49	0.47	1.11
4	10.59	10.59	10.59	7.12	7.12	7.12	0.14	0.29
5	11.32	11.86	11.59	7.30	7.30	7.30	0.35	1.27
6	9.67	10.59	10.13	7.12	7.66	7.39	0.27	0.65
7	9.67	9.85	9.76	6.93	7.30	7.12	0.09	0.18
8	10.04	10.04	10.04	6.93	8.21	7.57	0.14	0.30
9	9.67	10.04	9.86	6.76	7.12	6.94	0.19	0.46
10	9.85	9.85	9.85	6.93	7.85	7.39	0.21	0.48
11	10.04	10.40	10.22	6.93	7.30	7.12	0.13	0.30
12	9.12	10.95	10.04	6.56	7.12	6.84	0.54	0.98
13	10.04	10.04	10.04	7.12	7.49	7.31	0.14	0.39
14	10.22	10.04	10.13	7.12	7.12	7.12	0.20	0.39
15	8.94	9.31	9.13	6.76	6.75	6.76	0.24	0.50
16	9.12	9.13	9.13	7.48	7.85	7.67	0.18	0.33
17	10.22	10.22	10.22	7.12	7.30	7.21	0.24	0.54
18	10.22	10.04	10.13	7.48	7.66	7.57	0.35	0.75
19	9.49	9.85	9.67	6.93	8.03	7.48	0.21	0.46
20	9.49	9.49	9.49	6.76	6.94	6.85	0.13	0.24
21	10.04	10.22	10.13	6.93	6.57	6.75	0.21	0.45
22	10.22	10.22	10.22	7.66	7.67	7.67	0.26	0.62
23	10.22	10.04	10.13	7.12	7.67	7.40	0.20	0.42
24	11.13	10.95	11.04	7.30	7.12	7.21	0.33	0.74
25	10.40	10.40	10.40	7.85	7.85	7.85	0.32	0.78
26	10.95	10.22	10.59	6.94	7.12	7.03	0.44	1.10
27	11.13	10.58	10.86	7.85	7.12	7.49	0.26	0.55
28	10.77	10.59	10.68	7.31	6.93	7.12	0.24	0.48
29	10.59	10.95	10.77	7.49	6.93	7.21	0.32	0.84
30	11.86	11.13	11.50	6.94	7.48	7.21	0.35	0.76
minimum			9.13			6.75	0.09	0.18
maximum			11.59			7.85	0.54	1.27
mean			10.26			7.26	0.26	0.59
std dev			0.60			0.30	0.11	0.28
std error			0.11			0.06	0.02	0.05

Table A.6 Crater geometries produced in powder-mixed dielectric, 25μJ input energy

Crater	Input Energy = 25uJ							
	Outer diameter (um)			Inner diameter (um)			Rim ht	Pk-valley ht
	Direction 1	Direction 2	Average	Direction 1	Direction 2	Average	(um)	(um)
1	18.80	18.62	18.71	17.34	14.60	15.97	0.45	0.96
2	19.16	19.89	19.53	14.05	12.96	13.51	0.67	1.40
3	18.80	20.26	19.53	16.24	13.14	14.69	0.44	1.72
4	18.07	18.07	18.07	13.32	13.69	13.51	0.23	0.72
5	18.43	18.43	18.43	13.32	12.60	12.96	0.34	0.73
6	18.43	17.34	17.89	13.50	14.05	13.78	0.30	0.70
7	17.15	16.61	16.88	11.68	13.69	12.69	0.32	0.63
8	16.97	16.97	16.97	13.32	13.32	13.32	0.36	0.89
9	16.06	16.43	16.25	13.33	12.78	13.06	0.31	0.82
10	18.80	18.80	18.80	14.60	12.95	13.78	0.48	1.11
11	18.25	17.89	18.07	12.59	13.32	12.96	0.47	1.14
12	16.42	16.61	16.52	12.96	13.69	13.33	0.30	0.79
13	19.16	19.71	19.44	12.41	12.41	12.41	0.52	1.39
14	17.70	17.52	17.61	12.22	11.86	12.04	0.61	1.66
15	18.98	18.98	18.98	12.60	12.41	12.51	0.40	0.85
16	17.52	16.61	17.07	11.13	12.05	11.59	0.27	0.67
17	18.43	18.43	18.43	13.14	13.14	13.14	0.23	0.72
18	18.40	19.20	18.80	13.32	12.95	13.14	0.32	0.73
19	16.40	17.36	16.88	11.68	12.23	11.96	0.49	1.72
20	16.53	16.50	16.52	14.05	12.41	13.23	0.40	0.89
21	19.51	19.54	19.53	13.51	11.50	12.51	0.66	1.65
22	16.57	15.92	16.25	11.68	13.14	12.41	0.44	1.11
23	18.71	18.71	18.71	12.04	12.23	12.14	0.30	0.71
24	20.12	18.94	19.53	13.98	15.40	14.69	0.36	0.85
25	19.10	19.77	19.44	15.50	16.44	15.97	0.62	1.41
26	17.87	17.90	17.89	13.33	13.68	13.51	0.45	1.14
27	18.18	17.96	18.07	13.64	13.91	13.78	0.29	0.79
28	18.00	18.14	18.07	12.96	12.96	12.96	0.31	0.63
29	16.97	16.97	16.97	12.28	13.09	12.69	0.33	0.82
30	17.77	17.45	17.61	13.89	13.12	13.51	0.47	0.96
minimum			16.25			11.59	0.23	0.63
maximum			19.53			15.97	0.67	1.72
mean			18.05			13.26	0.40	1.01
std dev			1.07			1.03	0.12	0.35
std error			0.20			0.19	0.02	0.06

Table A.7 Peak current and pulse on time data at various machining conditions

Crater	Powder-free dielectric						Powder-mixed dielectric					
	Input energy = 2.5uJ		Input energy = 5uJ		Input energy = 25uJ		Input energy = 2.5uJ		Input energy = 5uJ		Input energy = 25uJ	
	Current (A)	On time (ns)	Current (A)	On time (ns)	Current (A)	On time (ns)	Current (A)	On time (ns)	Current (A)	On time (ns)	Current (A)	On time (ns)
1	1.13	107.5	1.59	160.5	3.78	365.0	1.03	112.5	1.50	170.0	3.53	435.0
2	1.09	105.0	1.59	167.5	3.66	373.0	1.03	110.0	1.50	173.0	3.66	452.5
3	1.13	107.5	1.56	157.5	3.75	390.0	1.06	117.5	1.31	163.0	3.53	395.5
4	1.19	110.5	1.19	140.5	3.78	398.0	1.06	112.5	1.44	168.0	1.97	347.5
5	1.09	105.0	1.44	153.0	2.78	338.0	0.97	112.5	1.38	160.5	3.31	393.0
6	1.19	125.5	1.53	157.5	3.75	375.0	0.94	117.5	1.38	160.5	3.50	420.5
7	1.19	112.5	1.59	152.5	3.75	378.0	1.00	102.5	1.44	170.5	3.63	430.0
8	1.13	122.5	1.59	157.5	3.53	365.0	0.94	115.0	1.44	160.5	3.38	425.0
9	0.91	92.5	1.44	155.0	3.69	368.0	1.03	112.5	1.19	157.5	3.38	415.5
10	1.22	95.0	1.59	150.5	3.53	368.0	1.03	110.0	1.44	162.5	3.59	400.5
11	1.13	107.5	1.59	155.0	3.75	395.0	1.06	117.5	1.25	167.5	3.59	422.5
12	1.09	105.0	1.59	168.0	3.81	372.5	1.06	112.5	1.38	162.5	3.59	402.5
13	1.13	107.5	1.59	158.0	3.75	380.0	0.97	112.5	1.50	165.0	3.50	413.0
14	1.19	110.5	1.59	158.0	3.69	373.0	0.94	117.5	1.47	163.0	3.31	388.0
15	1.09	105.0	1.59	158.0	3.66	375.0	1.00	102.5	1.44	172.5	3.25	368.0
16	1.19	125.5	1.31	140.5	3.78	393.0	0.94	115.0	1.44	163.0	3.13	410.5
17	1.19	112.5	1.63	163.0	3.75	378.0	1.03	112.5	1.50	170.0	3.25	395.5
18	1.13	122.5	1.63	160.5	3.78	388.0	1.03	110.0	1.50	173.0	2.72	345.0
19	0.91	92.5	1.59	162.5	3.75	395.0	1.06	117.5	1.31	163.0	3.38	395.0
20	1.22	95.0	1.31	138.0	3.69	378.0	1.06	112.5	1.44	168.0	2.84	367.5
21	1.13	107.5	1.69	177.5	3.81	405.0	0.97	112.5	1.38	160.5	3.13	395.5
22	1.09	105.0	1.59	160.5	3.59	373.0	0.94	117.5	1.38	160.5	3.44	393.0
23	1.13	107.5	1.59	167.5	3.75	388.0	1.00	102.5	1.44	170.5	2.88	367.5
24	1.19	110.5	1.56	157.5	3.81	393.0	0.94	115.0	1.44	160.5	3.53	435.0
25	1.09	105.0	1.19	140.5	3.84	392.5	1.03	112.5	1.19	157.5	3.66	452.5
26	1.19	125.5	1.44	153.0	3.81	403.0	1.03	110.0	1.44	162.5	3.53	395.5
27	1.19	112.5	1.53	157.5	3.78	395.0	1.06	117.5	1.25	167.5	1.97	347.5
28	1.13	122.5	1.59	152.5	3.78	365.0	1.06	112.5	1.38	162.5	3.31	393.0
29	0.91	92.5	1.59	157.5	3.66	373.0	0.97	112.5	1.50	165.0	3.50	420.5
30	1.22	95.0	1.44	155.0	3.75	390.0	0.94	117.5	1.47	163.0	3.63	430.0
minimum	0.91	92.50	1.19	138.00	2.78	338.00	0.94	102.50	1.19	157.50	1.97	345.00
maximum	1.22	125.50	1.69	177.50	3.84	405.00	1.06	117.50	1.50	173.00	3.66	452.50
mean	1.13	108.35	1.53	156.42	3.70	380.77	1.01	112.75	1.40	164.78	3.29	401.75
std dev	0.09	10.01	0.13	8.64	0.19	14.38	0.05	4.32	0.09	4.56	0.43	28.91
std error	0.02	1.83	0.02	1.58	0.03	2.63	0.01	0.79	0.02	0.83	0.08	5.28

Table A.8 ANOVA analysis for crater outer diameter

(a) Input energy: 2.5μJ

ANOVA						
Source of Variation	*SS*	*df*	*MS*	*F*	*P-value*	*F crit*
Dielectric condition	2.63132	1	2.63132	13.699	0.000479	4.006873
Within Groups	11.14071	58	0.192081			
Total	13.77203	59				

(b) Input energy: 5μJ

ANOVA						
Source of Variation	*SS*	*df*	*MS*	*F*	*P-value*	*F crit*
Dielectric condition	13.62314	1	13.62314	28.32992	1.73E-06	4.006873
Within Groups	27.89072	58	0.480875			
Total	41.51386	59				

(c) Input energy: 25μJ

ANOVA						
Source of Variation	*SS*	*df*	*MS*	*F*	*P-value*	*F crit*
Dielectric condition	50.15118	1	50.15118	42.10864	2.1E-08	4.006873
Within Groups	69.07771	58	1.190995			
Total	119.2289	59				

Table A.9 ANOVA analysis for crater inner diameter

(a) Input energy: 2.5μJ

ANOVA						
Source of Variation	*SS*	*df*	*MS*	*F*	*P-value*	*F crit*
Dielectric condition	7.73645	1	7.73645	20.95877	2.53E-05	4.006873
Within Groups	21.40937	58	0.369127			
Total	29.14582	59				

(b) Input energy: 5μJ

ANOVA						
Source of Variation	*SS*	*df*	*MS*	*F*	*P-value*	*F crit*
Dielectric condition	16.26042	1	16.26042	81.74422	1.13E-12	4.006873
Within Groups	11.53726	58	0.198918			
Total	27.79768	59				

(c) Input energy: 25μJ

ANOVA						
Source of Variation	*SS*	*df*	*MS*	*F*	*P-value*	*F crit*
Dielectric condition	7.550854	1	7.550854	7.393882	0.008619	4.006873
Within Groups	59.23134	58	1.02123			
Total	66.78219	59				

Table A.10 ANOVA analysis for crater rim height

(a) Input energy: 2.5μJ

ANOVA						
Source of Variation	*SS*	*df*	*MS*	*F*	*P-value*	*F crit*
Dielectric condition	1.17572	1	1.17572	20.5532	2.96E-05	4.006873
Within Groups	3.317817	58	0.057204			
Total	4.493537	59				

(b) Input energy: 5μJ

ANOVA						
Source of Variation	*SS*	*df*	*MS*	*F*	*P-value*	*F crit*
Dielectric condition	3.723049	1	3.723049	27.22601	2.54E-06	4.006873
Within Groups	7.931271	58	0.136746			
Total	11.65432	59				

(c) Input energy: 25μJ

ANOVA						
Source of Variation	*SS*	*df*	*MS*	*F*	*P-value*	*F crit*
Dielectric condition	32.57245	1	32.57245	238.2553	3.35E-22	4.006873
Within Groups	7.929319	58	0.136712			
Total	40.50177	59				

Table A.11 ANOVA analysis for crater peak-to-valley height

(a) Input energy: 2.5μJ

ANOVA						
Source of Variation	*SS*	*df*	*MS*	*F*	*P-value*	*F crit*
Dielectric condition	2.311236	1	2.311236	11.32899	0.001359	4.006873
Within Groups	11.83263	58	0.204011			
Total	14.14386	59				

(b) Input energy: 5μJ

ANOVA						
Source of Variation	*SS*	*df*	*MS*	*F*	*P-value*	*F crit*
Dielectric condition	15.08913	1	15.08913	50.60581	1.89E-09	4.006873
Within Groups	17.29386	58	0.29817			
Total	32.38299	59				

(c) Input energy: 25μJ

ANOVA						
Source of Variation	*SS*	*df*	*MS*	*F*	*P-value*	*F crit*
Dielectric condition	105.7885	1	105.7885	503.4459	2.82E-30	4.006873
Within Groups	12.18747	58	0.210129			
Total	117.976	59				

Appendix B

Table B.1 *Ra* measurements of micro-holes, 1.1μJ input energy

Additive	Concen (g/l)	Input energy = 1.1uJ										Ra (um)			
		Ra at location j (um)													
		1	2	3	4	5	6	7	8	9	10	Minimum	Maximum	Average	Std Dev	Std Error
Nil	0	0.054	0.060	0.066	0.055	0.056	0.058	0.075	0.076	0.065	0.089	0.054	0.089	0.065	0.011	0.004
	0	0.076	0.069	0.069	0.078	0.077	0.066	0.071	0.081	0.100	0.095	0.066	0.100	0.078	0.011	0.004
	0	0.064	0.063	0.063	0.079	0.086	0.075	0.063	0.063	0.059	0.063	0.059	0.086	0.068	0.009	0.003
SiC	0.02	0.084	0.069	0.063	0.081	0.077	0.067	0.052	0.066	0.055	0.080	0.052	0.084	0.069	0.011	0.003
	0.02	0.090	0.057	0.047	0.049	0.052	0.057	0.061	0.053	0.047	0.052	0.047	0.090	0.057	0.013	0.004
	0.02	0.053	0.040	0.039	0.043	0.046	0.048	0.069	0.066	0.053	0.087	0.039	0.087	0.054	0.015	0.005
	0.04	0.048	0.052	0.054	0.067	0.064	0.046	0.066	0.057	0.052	0.062	0.046	0.067	0.057	0.008	0.002
	0.04	0.052	0.046	0.063	0.061	0.055	0.057	0.049	0.069	0.058	0.053	0.046	0.069	0.056	0.007	0.002
	0.04	0.068	0.038	0.061	0.056	0.068	0.081	0.068	0.064	0.056	0.062	0.038	0.081	0.062	0.011	0.004
	0.08	0.043	0.055	0.056	0.077	0.071	0.049	0.052	0.056	0.067	0.053	0.043	0.077	0.058	0.011	0.003
	0.08	0.069	0.054	0.060	0.048	0.068	0.059	0.086	0.080	0.120	0.070	0.048	0.120	0.071	0.021	0.006
	0.08	0.053	0.068	0.061	0.069	0.057	0.057	0.068	0.073	0.091	0.093	0.053	0.093	0.069	0.014	0.004
Al2O3	0.02	0.041	0.043	0.050	0.047	0.044	0.095	0.055	0.064	0.057	0.050	0.041	0.095	0.055	0.016	0.005
	0.02	0.043	0.051	0.038	0.050	0.061	0.050	0.069	0.064	0.084	0.075	0.038	0.084	0.059	0.015	0.005
	0.02	0.085	0.077	0.078	0.095	0.074	0.115	0.086	0.087	0.062	0.099	0.062	0.115	0.086	0.015	0.005
	0.04	0.061	0.047	0.045	0.059	0.044	0.063	0.048	0.071	0.066	0.049	0.044	0.071	0.055	0.010	0.003
	0.04	0.050	0.056	0.040	0.039	0.043	0.044	0.037	0.056	0.041	0.046	0.037	0.056	0.045	0.007	0.002
	0.04	0.064	0.047	0.064	0.049	0.051	0.067	0.069	0.052	0.069	0.067	0.047	0.069	0.060	0.009	0.003
	0.08	0.060	0.061	0.053	0.065	0.071	0.070	0.057	0.062	0.061	0.083	0.053	0.083	0.064	0.009	0.003
	0.08	0.060	0.041	0.055	0.056	0.067	0.057	0.061	0.058	0.054	0.082	0.041	0.082	0.059	0.010	0.003
	0.08	0.065	0.063	0.066	0.094	0.081	0.072	0.069	0.069	0.065	0.074	0.063	0.094	0.072	0.009	0.003
	0.16	0.069	0.069	0.065	0.076	0.055	0.055	0.045	0.064	0.063	0.063	0.045	0.076	0.062	0.009	0.003
	0.16	0.066	0.076	0.053	0.081	0.076	0.086	0.077	0.069	0.089	0.092	0.053	0.092	0.077	0.012	0.004
	0.16	0.067	0.073	0.058	0.080	0.066	0.073	0.058	0.065	0.070	0.070	0.058	0.080	0.068	0.007	0.002

Table B.2 *Ra* measurements of micro-holes, 16.5μJ input energy

Additive	Concen (g/l)	Input energy = 16.5uJ										Ra (um)			
		Ra at location j (um)													
		1	2	3	4	5	6	7	8	9	10	Minimum	Maximum	Average	Std Dev	Std Error
Nil	0	0.272	0.221	0.216	0.211	0.194	0.312	0.254	0.217	0.188	0.243	0.188	0.312	0.233	0.038	0.012
	0	0.208	0.199	0.191	0.199	0.292	0.214	0.303	0.296	0.236	0.315	0.191	0.315	0.245	0.050	0.016
	0	0.233	0.216	0.279	0.182	0.192	0.220	0.216	0.245	0.279	0.254	0.182	0.279	0.232	0.033	0.010
SiC	0.02	0.290	0.232	0.216	0.160	0.243	0.230	0.216	0.205	0.248	0.247	0.160	0.290	0.229	0.034	0.011
	0.02	0.142	0.212	0.185	0.179	0.122	0.175	0.196	0.144	0.293	0.194	0.122	0.293	0.184	0.047	0.015
	0.02	0.216	0.258	0.175	0.190	0.211	0.188	0.123	0.205	0.243	0.227	0.123	0.258	0.204	0.038	0.012
	0.04	0.171	0.191	0.204	0.202	0.148	0.176	0.174	0.197	0.241	0.278	0.148	0.278	0.198	0.037	0.012
	0.04	0.198	0.179	0.108	0.146	0.173	0.172	0.246	0.206	0.214	0.223	0.108	0.246	0.187	0.040	0.013
	0.04	0.196	0.206	0.194	0.137	0.164	0.327	0.212	0.349	0.258	0.273	0.137	0.349	0.232	0.069	0.022
	0.08	0.316	0.273	0.252	0.264	0.287	0.210	0.225	0.212	0.202	0.239	0.202	0.316	0.248	0.037	0.012
	0.08	0.241	0.273	0.215	0.202	0.118	0.211	0.206	0.237	0.266	0.264	0.118	0.273	0.223	0.045	0.014
	0.08	0.233	0.219	0.161	0.179	0.227	0.310	0.284	0.230	0.207	0.291	0.161	0.310	0.234	0.048	0.015
Al2O3	0.02	0.179	0.228	0.219	0.170	0.208	0.312	0.223	0.262	0.305	0.204	0.170	0.312	0.231	0.048	0.015
	0.02	0.180	0.198	0.229	0.146	0.265	0.191	0.229	0.247	0.221	0.242	0.146	0.265	0.215	0.036	0.011
	0.02	0.145	0.176	0.264	0.274	0.175	0.193	0.224	0.177	0.166	0.264	0.145	0.274	0.206	0.047	0.015
	0.04	0.214	0.127	0.163	0.203	0.159	0.153	0.186	0.277	0.219	0.258	0.127	0.277	0.196	0.048	0.015
	0.04	0.194	0.194	0.186	0.215	0.307	0.269	0.298	0.216	0.164	0.188	0.164	0.307	0.223	0.050	0.016
	0.04	0.318	0.172	0.232	0.203	0.240	0.273	0.181	0.204	0.199	0.162	0.162	0.318	0.218	0.048	0.015
	0.08	0.202	0.195	0.124	0.162	0.251	0.192	0.157	0.193	0.170	0.255	0.124	0.255	0.190	0.040	0.013
	0.08	0.258	0.180	0.140	0.179	0.162	0.194	0.177	0.182	0.206	0.205	0.140	0.258	0.188	0.031	0.010
	0.08	0.221	0.147	0.192	0.164	0.176	0.191	0.168	0.169	0.240	0.367	0.147	0.367	0.204	0.064	0.020
	0.16	0.256	0.182	0.185	0.209	0.167	0.225	0.189	0.241	0.149	0.267	0.149	0.267	0.207	0.039	0.012
	0.16	0.270	0.227	0.162	0.262	0.178	0.285	0.279	0.180	0.275	0.215	0.162	0.285	0.233	0.047	0.015
	0.16	0.233	0.226	0.220	0.186	0.277	0.231	0.245	0.219	0.170	0.355	0.170	0.355	0.236	0.051	0.016

Table B.3 ANOVA analysis for *Ra* generated at input energy of 1.1 μJ

(a) Powder material and concentration: SiC, 0.02 g/l

ANOVA						
Source of Variation	*SS*	*df*	*MS*	*F*	*P-value*	*F crit*
Dielectric condition	0.001612	1	0.001612	9.449706	0.003217	4.006873
Within Groups	0.009894	58	0.000171			
Total	0.011506	59				

(b) Powder material and concentration: SiC, 0.04 g/l

ANOVA						
Source of Variation	*SS*	*df*	*MS*	*F*	*P-value*	*F crit*
Dielectric condition	0.002172	1	0.002172	20.22481	3.36E-05	4.006873
Within Groups	0.006229	58	0.000107			
Total	0.008401	59				

(c) Powder material and concentration: SiC, 0.08 g/l

ANOVA						
Source of Variation	*SS*	*df*	*MS*	*F*	*P-value*	*F crit*
Dielectric condition	0.000286	1	0.000286	1.445515	0.234135	4.006873
Within Groups	0.011476	58	0.000198			
Total	0.011762	59				

(d) Powder material and concentration: Al_2O_3, 0.02 g/l

ANOVA						
Source of Variation	*SS*	*df*	*MS*	*F*	*P-value*	*F crit*
Dielectric condition	0.00026	1	0.00026	0.951038	0.333505	4.006873
Within Groups	0.015882	58	0.000274			
Total	0.016142	59				

(e) Powder material and concentration: Al_2O_3, 0.04 g/l

ANOVA						
Source of Variation	*SS*	*df*	*MS*	*F*	*P-value*	*F crit*
Dielectric condition	0.004335	1	0.004335	35.46796	1.61E-07	4.006873
Within Groups	0.007089	58	0.000122			
Total	0.011424	59				

(f) Powder material and concentration: Al_2O_3, 0.08 g/l

ANOVA						
Source of Variation	*SS*	*df*	*MS*	*F*	*P-value*	*F crit*
Dielectric condition	0.000437	1	0.000437	3.52187	0.065598	4.006873
Within Groups	0.007203	58	0.000124			
Total	0.007641	59				

(g) Powder material and concentration: Al_2O_3, 0.16 g/l

ANOVA						
Source of Variation	*SS*	*df*	*MS*	*F*	*P-value*	*F crit*
Dielectric condition	3.38E-05	1	3.38E-05	0.268135	0.606555	4.006873
Within Groups	0.0073	58	0.000126			
Total	0.007334	59				

Table B.4 ANOVA analysis for *Ra* generated at input energy of 16.5 μJ

(a) Powder material and concentration: SiC, 0.02 g/l

ANOVA						
Source of Variation	*SS*	*df*	*MS*	*F*	*P-value*	*F crit*
Dielectric condition	0.014477	1	0.014477	8.387567	0.00532	4.006873
Within Groups	0.100109	58	0.001726			
Total	0.114586	59				

(b) Powder material and concentration: SiC, 0.04 g/l

ANOVA						
Source of Variation	*SS*	*df*	*MS*	*F*	*P-value*	*F crit*
Dielectric condition	0.014539	1	0.014539	6.632004	0.012588	4.006873
Within Groups	0.127153	58	0.002192			
Total	0.141692	59				

(c) Powder material and concentration: SiC, 0.08 g/l

ANOVA						
Source of Variation	*SS*	*df*	*MS*	*F*	*P-value*	*F crit*
Dielectric condition	3.08E-05	1	3.08E-05	0.017589	0.894949	4.006873
Within Groups	0.101617	58	0.001752			
Total	0.101648	59				

(d) Powder material and concentration: Al_2O_3, 0.02 g/l

ANOVA						
Source of Variation	*SS*	*df*	*MS*	*F*	*P-value*	*F crit*
Dielectric condition	0.005626	1	0.005626	3.193154	0.079173	4.006873
Within Groups	0.10219	58	0.001762			
Total	0.107816	59				

(e) Powder material and concentration: Al_2O_3, 0.04 g/l

ANOVA						
Source of Variation	*SS*	*df*	*MS*	*F*	*P-value*	*F crit*
Dielectric condition	0.008712	1	0.008712	4.389876	0.040529	4.006873
Within Groups	0.115107	58	0.001985			
Total	0.123819	59				

(f) Powder material and concentration: Al_2O_3, 0.08 g/l

ANOVA						
Source of Variation	*SS*	*df*	*MS*	*F*	*P-value*	*F crit*
Dielectric condition	0.027221	1	0.027221	14.58968	0.000328	4.006873
Within Groups	0.108216	58	0.001866			
Total	0.135438	59				

(g) Powder material and concentration: Al_2O_3, 0.16 g/l

ANOVA						
Source of Variation	*SS*	*df*	*MS*	*F*	*P-value*	*F crit*
Dielectric condition	0.001837	1	0.001837	0.975956	0.327303	4.006873
Within Groups	0.109175	58	0.001882			
Total	0.111012	59				

Appendix C

Table C.1 Recast layer thickness measurements at various machining conditions

Additive	Concen (g/l)	Rotation (rpm)	On time (ns)	Recast layer thickness (um)					Minimum	Maximum	Average	Std Dev	Std Error
				1	2	3	4	5					
Nil	0	1000	166	0.654	0.786	0.832	0.903	0.806	0.654	0.903	0.796	0.091	0.041
			362	1.115	1.100	1.442	1.354	1.370	1.100	1.442	1.276	0.158	0.070
			606	2.253	2.046	1.762	1.621	1.892	1.621	2.253	1.915	0.246	0.110
		3000	166	0.478	0.359	0.453	0.434	0.404	0.359	0.478	0.426	0.046	0.020
			362	0.755	0.668	0.636	0.570	0.721	0.570	0.755	0.670	0.073	0.032
			606	0.934	1.067	0.941	1.023	1.083	0.934	1.083	1.010	0.069	0.031
SiC	0.5	1000	166	0.671	0.629	0.650	0.807	0.809	0.629	0.809	0.713	0.088	0.039
			362	0.912	0.996	0.890	1.040	1.100	0.890	1.100	0.988	0.088	0.039
			606	1.493	1.656	1.754	1.441	1.415	1.415	1.754	1.552	0.147	0.066
		3000	166	0.224	0.277	0.334	0.304	0.305	0.224	0.334	0.289	0.041	0.018
			362	0.617	0.487	0.596	0.688	0.702	0.487	0.702	0.618	0.086	0.039
			606	0.780	0.815	0.979	1.015	0.978	0.780	1.015	0.913	0.108	0.048
	0.02	1000	166	0.781	0.595	0.658	0.693	0.661	0.595	0.781	0.678	0.068	0.030
			362	1.118	1.208	1.236	1.211	1.163	1.118	1.236	1.187	0.047	0.021
			606	1.386	1.358	1.305	1.751	1.455	1.305	1.751	1.451	0.176	0.079
	0.05		166	0.650	0.671	0.687	0.668	0.677	0.650	0.687	0.671	0.014	0.006
			362	1.060	1.060	1.287	1.166	1.112	1.060	1.287	1.137	0.095	0.042
			606	1.071	1.089	1.450	1.542	1.524	1.071	1.542	1.335	0.236	0.105
	0.1		166	0.642	0.677	0.655	0.648	0.671	0.642	0.677	0.658	0.015	0.007
			362	1.099	1.075	1.097	1.081	1.095	1.075	1.099	1.089	0.011	0.005
			606	1.592	1.001	1.215	1.606	1.086	1.001	1.606	1.300	0.283	0.127
	0.2		166	0.821	0.635	0.627	0.731	0.654	0.627	0.821	0.694	0.082	0.037
			362	1.092	1.193	1.020	1.156	1.054	1.020	1.193	1.103	0.071	0.032
			606	1.013	1.432	1.497	1.536	1.215	1.013	1.536	1.339	0.220	0.098

Table C.2 Discharge gap distance measurements at various machining conditions

Additive	Concen (g/l)	On time (ns)	Gap distance (um)					
			1	2	3	4	5	Average
Nil	0	166	7.3	5.5	6.4	6.9	7.5	6.7
		362	6.7	7.2	5.8	6.2	6.4	6.5
		606	7.6	6.9	7.3	5.8	6.7	6.9
SiC	0.02	166	23.4	21.9	21.2	23.1	21.2	22.2
		362	24.2	26.2	22.7	24.5	24.3	24.4
		606	24.2	24.7	24.7	25.2	24.8	24.7
	0.05	166	27.9	23.4	29.9	39.4	36.4	31.4
		362	38.7	26.7	28.4	38.7	32.7	33.1
		606	31.7	36.7	30.7	32.7	32.9	32.9
	0.1	166	31.9	30.4	35.4	34.4	30.8	32.6
		362	38.7	33.7	32.7	36.1	34.0	35.0
		606	39.7	28.2	33.7	34.2	35.0	34.2
	0.2	166	34.4	33.9	38.9	37.3	34.6	35.8
		362	40.7	37.2	29.7	33.7	38.0	35.9
		606	37.2	38.2	35.3	41.2	36.8	37.7

Table C.3 Crater radii measurements for 362 ns pulse on time and various powder concentrations

SiC conc (g/l)	Crater radius (um)							
	Direction 1	Direction 2	Average	Minimum	Maximum	Mean	Std dev	Std error
0	4.83	5.08	4.96	4.49	5.17	4.93	0.24	0.10
	5.00	5.34	5.17					
	4.66	5.00	4.83					
	5.08	5.08	5.08					
	5.17	4.92	5.04					
	4.49	4.49	4.49					
0.02	5.08	5.59	5.34	5.13	5.42	5.31	0.12	0.05
	5.08	5.76	5.42					
	5.17	5.51	5.34					
	5.59	5.25	5.42					
	5.34	5.08	5.21					
	5.00	5.25	5.13					
0.05	4.66	4.75	4.70	4.28	4.83	4.60	0.20	0.08
	4.58	4.92	4.75					
	4.92	4.75	4.83					
	4.66	4.32	4.49					
	4.24	4.32	4.28					
	4.32	4.75	4.53					
0.1	3.90	4.07	3.98	3.81	4.75	4.31	0.36	0.15
	3.73	3.90	3.81					
	4.24	4.32	4.28					
	4.81	4.41	4.61					
	4.49	4.41	4.45					
	4.75	4.75	4.75					
0.2	4.58	4.58	4.58	3.94	4.70	4.36	0.29	0.12
	3.90	3.98	3.94					
	4.92	4.49	4.70					
	4.66	4.15	4.41					
	3.90	4.32	4.11					
	4.32	4.49	4.41					

Table C.4 R_{max} measurements for 362 ns pulse on time and various powder concentrations

Concen (g/l)	Hole	Rmax at location j (um)										Overall Rmax (um)		
		1	2	3	4	5	6	7	8	9	Overall	Minimum	Maximum	Average
0	1	1.086	1.524	1.207	0.979	1.388	1.299	0.982	0.747	1.076	1.143			
0	2	1.173	0.584	1.417	1.002	1.422	0.686	1.442	1.705	1.803	1.248	1.143	1.259	1.217
0	3	0.997	1.204	1.813	0.915	0.856	0.853	2.290	0.852	1.547	1.259			
0.02	1	0.854	1.482	1.327	1.230	1.052	0.944	1.461	1.386	1.395	1.237			
0.02	2	1.355	1.233	1.102	0.576	1.009	0.925	0.830	0.615	1.150	0.977	0.977	1.237	1.095
0.02	3	1.358	1.069	0.851	0.866	1.119	0.899	1.177	1.113	1.182	1.070			
0.05	1	0.810	0.926	1.458	1.463	1.248	0.735	0.972	0.867	1.113	1.066			
0.05	2	1.271	0.815	1.156	0.855	0.785	1.002	0.746	1.053	1.172	0.984	0.984	1.164	1.071
0.05	3	1.226	0.973	0.903	1.231	1.501	0.650	1.363	1.436	1.197	1.164			
0.1	1	1.691	1.217	0.629	0.731	0.607	1.381	0.608	1.164	0.812	0.982			
0.1	2	1.030	1.296	1.054	1.226	1.476	0.966	1.223	1.071	1.504	1.205	0.935	1.205	1.041
0.1	3	1.463	1.184	1.123	0.751	0.632	0.687	1.029	0.936	0.606	0.935			
0.2	1	1.034	1.186	0.486	0.876	0.870	1.234	0.831	0.827	1.013	0.929			
0.2	2	0.927	1.074	1.240	1.182	0.952	0.930	0.865	0.990	1.054	1.024	0.929	1.024	0.992
0.2	3	0.854	0.633	1.087	0.999	1.299	1.100	0.837	1.149	1.251	1.023			

Derivation of the maximum heat flux (q_0) in a Gaussian-distributed heat flux

The Gaussian-distributed heat flux may be expressed by the following equation.

$$q(r) = q_0 \cdot \exp\left[-k\left(\frac{r}{R}\right)^2\right] \qquad (C.1)$$

where $q(r)$ represents the heat flux at radial coordinate r, q_0 the maximum heat flux at r = 0, k the distribution parameter that determines the concentration of the heat source and R the time-independent heat source radius. In simulating the heat flux distribution for the EDM process a k value of 4.5 has been used [144, 179, 219].

In EDM, the discharge energy is distributed between the tool electrode, workpiece and dielectric in the form of heat. The heat energy distributed to the workpiece may be expressed as:

$$Q_w = F \cdot V_{av} \cdot I_{av} \qquad (C.2)$$

where Q_w represents the heat absorption rate of the workpiece, F the fraction of heat distributed to the workpiece, V_{av} the average discharge voltage and I_{av} the average discharge current.

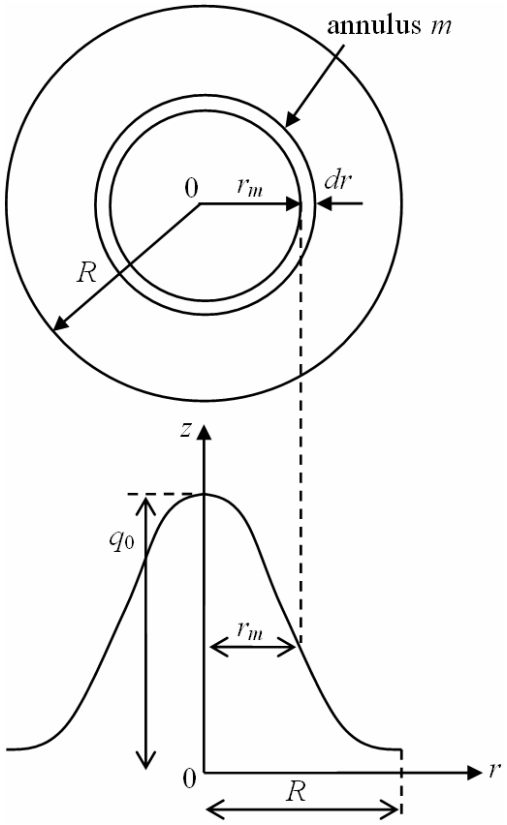

Figure C.1 Schematic diagram of a Gaussian-distributed heat flux

With reference to Figure C.1, the heat transmitted by an elemental annulus, *m*, having thickness Δr and located at a distance r_m from the origin may be expressed as:

$$Q_m = q_m \cdot 2\pi r_m \cdot \Delta r \qquad (C.3)$$

where

$$q_m = q_0 \cdot \exp\left[-4.5\left(\frac{r_m}{R}\right)^2\right] \qquad (C.4)$$

and represents the heat flux at distance r_m from the origin.

The total heat energy of the Gaussian-distributed heat flux may be obtained by summing the individual heat transmission rate from all the annuli. Furthermore, the total heat energy of the heat flux may be equated to the heat energy distributed to the workpiece due to the electrical discharge. Thus,

$$\sum_m q_0 \cdot \exp\left[-4.5\left(\frac{r_m}{R}\right)^2\right] \cdot 2\pi r_m \cdot \Delta r = Q_w \qquad (C.5)$$

Considering that Δr is infinitesimally small, Equation (C.5) can be written in the integral form as

$$\int_{r=0}^{r=R} q_0 \cdot \exp\left[-4.5\left(\frac{r}{R}\right)^2\right] \cdot 2\pi r \cdot dr = Q_w \qquad (C.6)$$

Solving Equation (C.6) by introducing a new variable, *v*, where

$$v = -4.5\frac{r^2}{R^2} \qquad (C.7)$$

and

$$dv = \frac{-9r}{R^2} \cdot dr \qquad (C.8)$$

Equation (C.6) may be expressed as:

$$\frac{-q_0 \cdot \pi \cdot R^2}{4.5}\int_{v=0}^{v=-4.5} \exp(v) \cdot dv = Q_w$$

$$\Rightarrow \frac{q_0 \cdot \pi \cdot R^2}{4.5}\left[1 - \exp(-4.5)\right] = Q_w \qquad (C.9)$$

Then, substituting Equation (C.2) into (C.9) and leaving only q_0 at the left hand side,

$$q_0 = \frac{4.5}{\left[1 - \exp(-4.5)\right]} \cdot \frac{F \cdot V_{av} \cdot I_{av}}{\pi \cdot R^2} \qquad (C.10)$$

Appendix D

Table D.1 Empirical discharge parameters for 110 ns pulse on time

Time step	Discharge time (ns)	Voltage (V)	Current (A)	Source radius (m)	Heat flux (W/m^2)
0	0.00E+00	--	--	--	--
1	1.00E-09	84.38	0.53	5.90E-08	1.97E+15
2	2.00E-09	75.78	0.44	1.02E-07	4.87E+14
3	3.00E-09	67.19	0.56	1.41E-07	2.92E+14
4	4.00E-09	58.59	0.53	1.76E-07	1.53E+14
5	5.00E-09	50.00	0.63	2.10E-07	1.08E+14
6	6.00E-09	47.59	0.56	2.43E-07	6.93E+13
7	7.00E-09	45.17	0.69	2.74E-07	6.30E+13
8	8.00E-09	42.76	0.63	3.05E-07	4.39E+13
9	9.00E-09	40.34	0.75	3.35E-07	4.13E+13
10	1.00E-08	37.93	0.69	3.64E-07	3.01E+13
11	1.10E-08	35.51	0.84	3.92E-07	2.98E+13
12	1.20E-08	33.10	0.75	4.20E-07	2.15E+13
13	1.30E-08	30.68	0.88	4.48E-07	2.05E+13
14	1.40E-08	28.27	0.84	4.75E-07	1.62E+13
15	1.50E-08	25.85	0.94	5.01E-07	1.47E+13
16	1.60E-08	23.44	0.88	5.27E-07	1.13E+13
17	1.70E-08	23.26	0.97	5.53E-07	1.13E+13
18	1.80E-08	23.09	0.94	5.79E-07	9.87E+12
19	1.90E-08	22.92	1.06	6.04E-07	1.02E+13
20	2.00E-08	22.74	0.97	6.29E-07	8.51E+12
21	2.10E-08	22.57	1.03	6.54E-07	8.32E+12
22	2.20E-08	22.40	1.03	6.78E-07	7.67E+12
23	2.30E-08	22.22	1.06	7.02E-07	7.31E+12
24	2.40E-08	22.05	1.03	7.26E-07	6.58E+12
25	2.50E-08	21.88	1.06	7.50E-07	6.31E+12
26	2.60E-08	21.70	1.06	7.74E-07	5.88E+12
27	2.70E-08	21.53	1.06	7.97E-07	5.50E+12
28	2.80E-08	21.35	1.06	8.21E-07	5.15E+12
29	2.90E-08	21.18	1.06	8.44E-07	4.83E+12
30	3.00E-08	21.01	1.06	8.67E-07	4.54E+12
31	3.10E-08	20.83	1.06	8.89E-07	4.28E+12
32	3.20E-08	20.66	1.06	9.12E-07	4.03E+12
33	3.30E-08	20.49	1.06	9.34E-07	3.81E+12
34	3.40E-08	20.31	1.06	9.57E-07	3.60E+12
35	3.50E-08	19.74	1.13	9.79E-07	3.54E+12
36	3.60E-08	19.18	1.06	1.00E-06	3.11E+12
37	3.70E-08	18.61	1.13	1.02E-06	3.06E+12
38	3.80E-08	18.04	1.13	1.04E-06	2.84E+12
39	3.90E-08	17.47	1.13	1.07E-06	2.64E+12
40	4.00E-08	16.90	1.13	1.09E-06	2.46E+12
41	4.10E-08	16.34	1.13	1.11E-06	2.28E+12
42	4.20E-08	15.77	1.13	1.13E-06	2.12E+12
43	4.30E-08	15.20	1.13	1.15E-06	1.97E+12
44	4.40E-08	14.63	1.09	1.17E-06	1.78E+12
45	4.50E-08	14.06	1.13	1.19E-06	1.70E+12
46	4.60E-08	14.06	1.06	1.21E-06	1.55E+12
47	4.70E-08	14.06	1.06	1.24E-06	1.50E+12
48	4.80E-08	14.06	1.06	1.26E-06	1.45E+12
49	4.90E-08	14.06	1.06	1.28E-06	1.40E+12
50	5.00E-08	14.06	1.06	1.30E-06	1.36E+12
51	5.10E-08	14.06	1.06	1.32E-06	1.31E+12
52	5.20E-08	14.06	1.00	1.34E-06	1.20E+12
53	5.30E-08	14.06	1.00	1.36E-06	1.16E+12
54	5.40E-08	14.06	0.94	1.38E-06	1.06E+12
55	5.50E-08	14.06	1.00	1.40E-06	1.10E+12
56	5.60E-08	14.06	0.94	1.42E-06	1.00E+12
57	5.70E-08	14.06	0.94	1.44E-06	9.73E+11
58	5.80E-08	14.06	0.94	1.46E-06	9.47E+11
59	5.90E-08	14.06	0.94	1.48E-06	9.21E+11
60	6.00E-08	14.06	0.88	1.50E-06	8.37E+11
61	6.10E-08	14.06	0.88	1.52E-06	8.16E+11
62	6.20E-08	14.06	0.84	1.54E-06	7.67E+11
63	6.30E-08	14.06	0.84	1.56E-06	7.48E+11
64	6.40E-08	14.06	0.81	1.58E-06	7.02E+11
65	6.50E-08	14.06	0.81	1.60E-06	6.85E+11
66	6.60E-08	14.06	0.81	1.62E-06	6.69E+11
67	6.70E-08	14.06	0.81	1.63E-06	6.53E+11
68	6.80E-08	14.06	0.75	1.65E-06	5.89E+11
69	6.90E-08	14.06	0.78	1.67E-06	6.00E+11
70	7.00E-08	14.06	0.75	1.69E-06	5.63E+11
71	7.10E-08	14.06	0.75	1.71E-06	5.50E+11
72	7.20E-08	12.50	0.66	1.73E-06	4.19E+11
73	7.30E-08	14.06	0.66	1.75E-06	4.61E+11
74	7.40E-08	12.50	0.63	1.77E-06	3.82E+11
75	7.50E-08	14.06	0.66	1.79E-06	4.41E+11
76	7.60E-08	14.06	0.63	1.81E-06	4.12E+11
77	7.70E-08	14.06	0.63	1.82E-06	4.03E+11
78	7.80E-08	12.50	0.59	1.84E-06	3.34E+11
79	7.90E-08	12.50	0.59	1.86E-06	3.27E+11
80	8.00E-08	10.94	0.56	1.88E-06	2.66E+11
81	8.10E-08	10.94	0.56	1.90E-06	2.61E+11
82	8.20E-08	7.81	0.53	1.92E-06	1.72E+11
83	8.30E-08	7.81	0.53	1.94E-06	1.69E+11
84	8.40E-08	4.69	0.44	1.95E-06	8.20E+10
85	8.50E-08	10.94	0.47	1.97E-06	2.01E+11
86	8.60E-08	7.81	0.44	1.99E-06	1.32E+11
87	8.70E-08	14.06	0.44	2.01E-06	2.33E+11
88	8.80E-08	10.94	0.41	2.03E-06	1.65E+11
89	8.90E-08	14.06	0.41	2.05E-06	2.09E+11
90	9.00E-08	14.06	0.34	2.06E-06	1.73E+11
91	9.10E-08	14.06	0.34	2.08E-06	1.70E+11
92	9.20E-08	14.06	0.28	2.10E-06	1.37E+11
93	9.30E-08	14.06	0.28	2.12E-06	1.35E+11
94	9.40E-08	14.06	0.25	2.14E-06	1.18E+11
95	9.50E-08	14.06	0.28	2.15E-06	1.30E+11
96	9.60E-08	14.06	0.25	2.17E-06	1.14E+11
97	9.70E-08	14.06	0.28	2.19E-06	1.26E+11
98	9.80E-08	12.50	0.19	2.21E-06	7.35E+10
99	9.90E-08	14.06	0.22	2.23E-06	9.49E+10
100	1.00E-07	12.50	0.16	2.24E-06	5.93E+10
101	1.01E-07	12.50	0.16	2.26E-06	5.84E+10
102	1.02E-07	10.94	0.16	2.28E-06	5.03E+10
103	1.03E-07	14.06	0.16	2.30E-06	6.37E+10
104	1.04E-07	12.50	0.09	2.31E-06	3.34E+10
105	1.05E-07	14.06	0.09	2.33E-06	3.71E+10
106	1.06E-07	14.06	0.09	2.35E-06	3.65E+10
107	1.07E-07	14.06	0.09	2.37E-06	3.60E+10
108	1.08E-07	14.06	0.03	2.38E-06	1.18E+10
109	1.09E-07	14.06	0.03	2.40E-06	1.16E+10
110	1.10E-07	14.06	0.03	2.42E-06	1.15E+10

Table D.2 Empirical discharge parameters for 157 ns pulse on time

Time step	Discharge time (ns)	Voltage (V)	Current (A)	Source radius (m)	Heat flux (W/m^2)
0	0.00E+00	--	--	--	--
1	1.00E-09	92.00	0.53	5.90E-08	2.15E+15
2	2.00E-09	85.00	0.44	1.02E-07	5.47E+14
3	3.00E-09	78.00	0.56	1.41E-07	3.39E+14
4	4.00E-09	71.00	0.53	1.76E-07	1.85E+14
5	5.00E-09	64.00	0.63	2.10E-07	1.38E+14
6	6.00E-09	61.36	0.56	2.43E-07	8.92E+13
7	7.00E-09	58.72	0.72	2.74E-07	8.55E+13
8	8.00E-09	56.08	0.63	3.05E-07	5.77E+13
9	9.00E-09	53.45	0.81	3.35E-07	5.92E+13
10	1.00E-08	50.81	0.72	3.64E-07	4.21E+13
11	1.10E-08	48.17	0.88	3.92E-07	4.19E+13
12	1.20E-08	45.53	0.81	4.20E-07	3.20E+13
13	1.30E-08	42.89	0.97	4.48E-07	3.17E+13
14	1.40E-08	40.25	0.88	4.75E-07	2.39E+13
15	1.50E-08	37.62	0.97	5.01E-07	2.22E+13
16	1.60E-08	34.98	0.94	5.27E-07	1.80E+13
17	1.70E-08	32.34	1.06	5.53E-07	1.71E+13
18	1.80E-08	29.70	0.97	5.79E-07	1.31E+13
19	1.90E-08	29.60	1.16	6.04E-07	1.43E+13
20	2.00E-08	29.51	1.06	6.29E-07	1.21E+13
21	2.10E-08	29.41	1.19	6.54E-07	1.25E+13
22	2.20E-08	29.31	1.16	6.78E-07	1.13E+13
23	2.30E-08	29.22	1.19	7.02E-07	1.07E+13
24	2.40E-08	29.12	1.19	7.26E-07	1.00E+13
25	2.50E-08	29.02	1.22	7.50E-07	9.59E+12
26	2.60E-08	28.93	1.19	7.74E-07	8.77E+12
27	2.70E-08	28.83	1.22	7.97E-07	8.44E+12
28	2.80E-08	28.73	1.19	8.21E-07	7.75E+12
29	2.90E-08	28.63	1.28	8.44E-07	7.88E+12
30	3.00E-08	28.54	1.22	8.67E-07	7.07E+12
31	3.10E-08	28.44	1.31	8.89E-07	7.21E+12
32	3.20E-08	28.34	1.28	9.12E-07	6.68E+12
33	3.30E-08	28.25	1.31	9.34E-07	6.49E+12
34	3.40E-08	28.15	1.31	9.57E-07	6.17E+12
35	3.50E-08	27.44	1.41	9.79E-07	6.15E+12
36	3.60E-08	26.72	1.31	1.00E-06	5.35E+12
37	3.70E-08	26.01	1.47	1.02E-06	5.58E+12
38	3.80E-08	25.30	1.41	1.04E-06	4.98E+12
39	3.90E-08	24.58	1.47	1.07E-06	4.85E+12
40	4.00E-08	23.87	1.47	1.09E-06	4.53E+12
41	4.10E-08	23.15	1.53	1.11E-06	4.41E+12
42	4.20E-08	22.44	1.47	1.13E-06	3.94E+12
43	4.30E-08	21.73	1.53	1.15E-06	3.84E+12
44	4.40E-08	21.01	1.53	1.17E-06	3.58E+12
45	4.50E-08	20.30	1.56	1.19E-06	3.40E+12
46	4.60E-08	20.25	1.53	1.21E-06	3.21E+12
47	4.70E-08	20.21	1.56	1.24E-06	3.16E+12
48	4.80E-08	20.16	1.53	1.26E-06	2.99E+12
49	4.90E-08	20.12	1.56	1.28E-06	2.95E+12
50	5.00E-08	20.07	1.53	1.30E-06	2.79E+12
51	5.10E-08	20.03	1.59	1.32E-06	2.81E+12
52	5.20E-08	19.98	1.56	1.34E-06	2.66E+12
53	5.30E-08	19.94	1.59	1.36E-06	2.63E+12
54	5.40E-08	19.89	1.56	1.38E-06	2.50E+12
55	5.50E-08	19.84	1.56	1.40E-06	2.42E+12
56	5.60E-08	19.80	1.53	1.42E-06	2.30E+12
57	5.70E-08	19.75	1.56	1.44E-06	2.28E+12
58	5.80E-08	19.71	1.53	1.46E-06	2.17E+12
59	5.90E-08	19.66	1.59	1.48E-06	2.19E+12
60	6.00E-08	19.62	1.56	1.50E-06	2.09E+12
61	6.10E-08	19.57	1.59	1.52E-06	2.07E+12
62	6.20E-08	19.53	1.59	1.54E-06	2.01E+12
63	6.30E-08	19.48	1.59	1.56E-06	1.96E+12
64	6.40E-08	19.43	1.56	1.58E-06	1.87E+12
65	6.50E-08	19.39	1.56	1.60E-06	1.82E+12
66	6.60E-08	19.34	1.53	1.62E-06	1.73E+12
67	6.70E-08	19.30	1.56	1.63E-06	1.72E+12
68	6.80E-08	19.25	1.53	1.65E-06	1.65E+12
69	6.90E-08	19.21	1.56	1.67E-06	1.64E+12
70	7.00E-08	19.16	1.53	1.69E-06	1.57E+12
71	7.10E-08	19.11	1.56	1.71E-06	1.56E+12
72	7.20E-08	19.07	1.53	1.73E-06	1.49E+12
73	7.30E-08	19.02	1.53	1.75E-06	1.46E+12
74	7.40E-08	18.98	1.50	1.77E-06	1.39E+12
75	7.50E-08	18.93	1.50	1.79E-06	1.36E+12
76	7.60E-08	18.89	1.47	1.81E-06	1.30E+12
77	7.70E-08	18.84	1.47	1.82E-06	1.27E+12
78	7.80E-08	18.80	1.44	1.84E-06	1.22E+12
79	7.90E-08	18.75	1.44	1.86E-06	1.19E+12
80	8.00E-08	14.05	1.41	1.88E-06	8.53E+11
81	8.10E-08	14.05	1.41	1.90E-06	8.37E+11
82	8.20E-08	12.50	1.38	1.92E-06	7.15E+11
83	8.30E-08	14.05	1.38	1.94E-06	7.88E+11
84	8.40E-08	12.50	1.34	1.95E-06	6.72E+11
85	8.50E-08	14.05	1.34	1.97E-06	7.41E+11
86	8.60E-08	12.50	1.31	1.99E-06	6.32E+11
87	8.70E-08	14.05	1.31	2.01E-06	6.98E+11
88	8.80E-08	12.50	1.28	2.03E-06	5.96E+11
89	8.90E-08	14.05	1.31	2.05E-06	6.73E+11
90	9.00E-08	12.50	1.28	2.06E-06	5.75E+11
91	9.10E-08	14.05	1.28	2.08E-06	6.35E+11
92	9.20E-08	14.05	1.22	2.10E-06	5.93E+11
93	9.30E-08	15.65	1.25	2.12E-06	6.66E+11
94	9.40E-08	14.05	1.19	2.14E-06	5.59E+11
95	9.50E-08	15.65	1.19	2.15E-06	6.12E+11
96	9.60E-08	14.05	1.19	2.17E-06	5.41E+11
97	9.70E-08	14.05	1.19	2.19E-06	5.32E+11
98	9.80E-08	14.05	1.13	2.21E-06	4.96E+11
99	9.90E-08	14.05	1.13	2.23E-06	4.88E+11
100	1.00E-07	14.05	1.06	2.24E-06	4.53E+11
101	1.01E-07	14.05	1.06	2.26E-06	4.46E+11
102	1.02E-07	14.05	1.06	2.28E-06	4.39E+11
103	1.03E-07	14.05	1.06	2.30E-06	4.32E+11
104	1.04E-07	14.05	1.03	2.31E-06	4.14E+11
105	1.05E-07	14.05	1.03	2.33E-06	4.08E+11
106	1.06E-07	14.05	0.94	2.35E-06	3.65E+11
107	1.07E-07	15.65	1.00	2.37E-06	4.27E+11
108	1.08E-07	14.05	0.94	2.38E-06	3.54E+11
109	1.09E-07	17.20	0.94	2.40E-06	4.28E+11
110	1.10E-07	15.65	0.88	2.42E-06	3.58E+11
111	1.11E-07	17.20	0.88	2.44E-06	3.88E+11
112	1.12E-07	17.20	0.84	2.45E-06	3.69E+11
113	1.13E-07	17.20	0.84	2.47E-06	3.63E+11
114	1.14E-07	15.65	0.81	2.49E-06	3.14E+11
115	1.15E-07	15.65	0.81	2.50E-06	3.09E+11
116	1.16E-07	14.05	0.75	2.52E-06	2.53E+11
117	1.17E-07	14.05	0.78	2.54E-06	2.60E+11
118	1.18E-07	14.05	0.75	2.56E-06	2.46E+11
119	1.19E-07	14.05	0.75	2.57E-06	2.43E+11
120	1.20E-07	14.05	0.69	2.59E-06	2.20E+11
121	1.21E-07	14.05	0.69	2.61E-06	2.17E+11
122	1.22E-07	14.05	0.63	2.62E-06	1.95E+11
123	1.23E-07	14.05	0.66	2.64E-06	2.02E+11
124	1.24E-07	14.05	0.59	2.66E-06	1.80E+11
125	1.25E-07	15.65	0.59	2.68E-06	1.98E+11
126	1.26E-07	14.05	0.56	2.69E-06	1.66E+11
127	1.27E-07	17.20	0.56	2.71E-06	2.01E+11
128	1.28E-07	15.65	0.53	2.73E-06	1.71E+11
129	1.29E-07	17.20	0.53	2.74E-06	1.88E+11
130	1.30E-07	15.65	0.50	2.76E-06	1.57E+11
131	1.31E-07	17.20	0.50	2.78E-06	1.70E+11
132	1.32E-07	15.65	0.44	2.79E-06	1.34E+11
133	1.33E-07	17.20	0.44	2.81E-06	1.46E+11
134	1.34E-07	15.65	0.41	2.83E-06	1.22E+11
135	1.35E-07	15.65	0.41	2.84E-06	1.20E+11
136	1.36E-07	12.50	0.38	2.86E-06	8.78E+10
137	1.37E-07	14.05	0.41	2.88E-06	1.05E+11
138	1.38E-07	14.05	0.34	2.89E-06	8.82E+10
139	1.39E-07	15.65	0.34	2.91E-06	9.72E+10
140	1.40E-07	14.05	0.28	2.93E-06	7.07E+10
141	1.41E-07	15.65	0.28	2.94E-06	7.79E+10
142	1.42E-07	14.05	0.28	2.96E-06	6.91E+10
143	1.43E-07	14.05	0.28	2.98E-06	6.84E+10
144	1.44E-07	14.05	0.28	2.99E-06	6.76E+10
145	1.45E-07	14.05	0.28	3.01E-06	6.69E+10
146	1.46E-07	14.05	0.19	3.02E-06	4.40E+10
147	1.47E-07	14.05	0.19	3.04E-06	4.35E+10
148	1.48E-07	12.50	0.16	3.06E-06	3.19E+10
149	1.49E-07	14.05	0.16	3.07E-06	3.55E+10
150	1.50E-07	12.50	0.16	3.09E-06	3.12E+10
151	1.51E-07	14.05	0.16	3.11E-06	3.48E+10
152	1.52E-07	14.05	0.09	3.12E-06	2.07E+10
153	1.53E-07	14.05	0.09	3.14E-06	2.04E+10
154	1.54E-07	10.95	0.06	3.15E-06	1.05E+10
155	1.55E-07	10.95	0.06	3.17E-06	1.04E+10
156	1.56E-07	9.40	0.06	3.19E-06	8.85E+09
157	1.57E-07	12.50	0.06	3.20E-06	1.17E+10

Table D.3 Empirical discharge parameters for 393 ns pulse on time

Time step	Discharge time (ns)	Voltage (V)	Current (A)	Source radius (m)	Heat flux (W/m^2)
0	0.00E+00	--	--	--	--
1	1.00E-09	95.31	0.56	5.90E-08	2.35E+15
2	2.00E-09	89.06	0.47	1.02E-07	6.13E+14
3	3.00E-09	89.06	0.63	1.41E-07	4.31E+14
4	4.00E-09	86.91	0.56	1.76E-07	2.40E+14
5	5.00E-09	84.77	0.69	2.10E-07	2.01E+14
6	6.00E-09	82.62	0.63	2.43E-07	1.34E+14
7	7.00E-09	80.47	0.81	2.74E-07	1.33E+14
8	8.00E-09	78.32	0.69	3.05E-07	8.84E+13
9	9.00E-09	76.17	0.91	3.35E-07	9.41E+13
10	1.00E-08	74.02	0.81	3.64E-07	6.94E+13
11	1.10E-08	71.88	0.97	3.92E-07	6.91E+13
12	1.20E-08	69.73	0.91	4.20E-07	5.47E+13
13	1.30E-08	67.58	1.06	4.48E-07	5.48E+13
14	1.40E-08	65.43	0.97	4.75E-07	4.30E+13
15	1.50E-08	63.28	1.13	5.01E-07	4.33E+13
16	1.60E-08	61.13	1.06	5.27E-07	3.57E+13
17	1.70E-08	58.98	1.25	5.53E-07	3.68E+13
18	1.80E-08	56.84	1.13	5.79E-07	2.92E+13
19	1.90E-08	54.69	1.31	6.04E-07	3.01E+13
20	2.00E-08	53.13	1.25	6.29E-07	2.56E+13
21	2.10E-08	53.13	1.38	6.54E-07	2.61E+13
22	2.20E-08	52.54	1.31	6.78E-07	2.29E+13
23	2.30E-08	51.95	1.44	7.02E-07	2.31E+13
24	2.40E-08	51.37	1.38	7.26E-07	2.04E+13
25	2.50E-08	50.78	1.44	7.50E-07	1.98E+13
26	2.60E-08	50.20	1.44	7.74E-07	1.84E+13
27	2.70E-08	49.61	1.50	7.97E-07	1.79E+13
28	2.80E-08	49.02	1.44	8.21E-07	1.60E+13
29	2.90E-08	48.44	1.56	8.44E-07	1.62E+13
30	3.00E-08	47.85	1.50	8.67E-07	1.46E+13
31	3.10E-08	47.27	1.63	8.89E-07	1.48E+13
32	3.20E-08	46.68	1.56	9.12E-07	1.34E+13
33	3.30E-08	46.09	1.72	9.34E-07	1.39E+13
34	3.40E-08	45.51	1.63	9.57E-07	1.23E+13
35	3.50E-08	44.92	1.84	9.79E-07	1.32E+13
36	3.60E-08	44.34	1.72	1.00E-06	1.16E+13
37	3.70E-08	43.75	1.91	1.02E-06	1.22E+13
38	3.80E-08	42.19	1.84	1.04E-06	1.09E+13
39	3.90E-08	42.19	1.97	1.07E-06	1.12E+13
40	4.00E-08	41.60	1.91	1.09E-06	1.02E+13
41	4.10E-08	41.02	2.06	1.11E-06	1.05E+13
42	4.20E-08	40.43	1.97	1.13E-06	9.52E+12
43	4.30E-08	39.84	2.09	1.15E-06	9.61E+12
44	4.40E-08	39.26	2.06	1.17E-06	9.00E+12
45	4.50E-08	38.67	2.13	1.19E-06	8.81E+12
46	4.60E-08	38.09	2.09	1.21E-06	8.26E+12
47	4.70E-08	37.50	2.22	1.24E-06	8.33E+12
48	4.80E-08	36.91	2.13	1.26E-06	7.60E+12
49	4.90E-08	36.33	2.22	1.28E-06	7.55E+12
50	5.00E-08	35.74	2.19	1.30E-06	7.10E+12
51	5.10E-08	35.16	2.34	1.32E-06	7.25E+12
52	5.20E-08	34.57	2.22	1.34E-06	6.55E+12
53	5.30E-08	34.38	2.34	1.36E-06	6.67E+12
54	5.40E-08	34.38	2.31	1.38E-06	6.39E+12
55	5.50E-08	34.38	2.47	1.40E-06	6.63E+12
56	5.60E-08	34.38	2.34	1.42E-06	6.12E+12
57	5.70E-08	34.38	2.47	1.44E-06	6.26E+12
58	5.80E-08	34.38	2.44	1.46E-06	6.02E+12
59	5.90E-08	34.38	2.56	1.48E-06	6.16E+12
60	6.00E-08	33.79	2.47	1.50E-06	5.68E+12
61	6.10E-08	33.20	2.59	1.52E-06	5.71E+12
62	6.20E-08	32.62	2.56	1.54E-06	5.40E+12
63	6.30E-08	32.03	2.66	1.56E-06	5.36E+12
64	6.40E-08	31.45	2.59	1.58E-06	5.01E+12
65	6.50E-08	30.86	2.72	1.60E-06	5.03E+12
66	6.60E-08	30.27	2.66	1.62E-06	4.71E+12
67	6.70E-08	29.69	2.78	1.63E-06	4.72E+12
68	6.80E-08	29.10	2.72	1.65E-06	4.42E+12
69	6.90E-08	28.52	2.88	1.67E-06	4.47E+12
70	7.00E-08	28.13	2.78	1.69E-06	4.17E+12
71	7.10E-08	28.13	2.88	1.71E-06	4.22E+12
72	7.20E-08	28.13	2.88	1.73E-06	4.13E+12
73	7.30E-08	28.13	2.91	1.75E-06	4.08E+12
74	7.40E-08	28.13	2.88	1.77E-06	3.95E+12
75	7.50E-08	27.54	3.00	1.79E-06	3.95E+12
76	7.60E-08	26.95	2.91	1.81E-06	3.67E+12
77	7.70E-08	26.37	3.00	1.82E-06	3.63E+12
78	7.80E-08	26.56	3.00	1.84E-06	3.58E+12
79	7.90E-08	26.56	3.06	1.86E-06	3.58E+12
80	8.00E-08	25.98	3.00	1.88E-06	3.37E+12
81	8.10E-08	25.39	3.13	1.90E-06	3.36E+12
82	8.20E-08	24.80	3.06	1.92E-06	3.16E+12
83	8.30E-08	24.22	3.16	1.94E-06	3.12E+12
84	8.40E-08	23.63	3.13	1.95E-06	2.95E+12
85	8.50E-08	23.05	3.19	1.97E-06	2.88E+12
86	8.60E-08	22.46	3.16	1.99E-06	2.73E+12
87	8.70E-08	21.88	3.25	2.01E-06	2.69E+12
88	8.80E-08	21.88	3.19	2.03E-06	2.59E+12
89	8.90E-08	21.88	3.25	2.05E-06	2.60E+12
90	9.00E-08	21.88	3.22	2.06E-06	2.53E+12
91	9.10E-08	21.88	3.28	2.08E-06	2.53E+12
92	9.20E-08	21.88	3.25	2.10E-06	2.46E+12
93	9.30E-08	21.88	3.31	2.12E-06	2.47E+12
94	9.40E-08	21.88	3.28	2.14E-06	2.40E+12
95	9.50E-08	21.88	3.38	2.15E-06	2.43E+12
96	9.60E-08	21.88	3.31	2.17E-06	2.35E+12
97	9.70E-08	21.29	3.38	2.19E-06	2.29E+12
98	9.80E-08	20.31	3.38	2.21E-06	2.15E+12
99	9.90E-08	20.31	3.44	2.23E-06	2.15E+12
100	1.00E-07	20.31	3.38	2.24E-06	2.08E+12
101	1.01E-07	20.31	3.47	2.26E-06	2.11E+12
102	1.02E-07	20.31	3.44	2.28E-06	2.05E+12
103	1.03E-07	20.31	3.53	2.30E-06	2.08E+12
104	1.04E-07	20.31	3.47	2.31E-06	2.01E+12
105	1.05E-07	20.31	3.53	2.33E-06	2.02E+12
106	1.06E-07	20.31	3.53	2.35E-06	1.99E+12
107	1.07E-07	20.31	3.53	2.37E-06	1.96E+12
108	1.08E-07	20.31	3.53	2.38E-06	1.93E+12
109	1.09E-07	20.31	3.59	2.40E-06	1.93E+12
110	1.10E-07	20.31	3.53	2.42E-06	1.87E+12
111	1.11E-07	20.31	3.63	2.44E-06	1.90E+12
112	1.12E-07	20.31	3.59	2.45E-06	1.85E+12
113	1.13E-07	20.31	3.66	2.47E-06	1.86E+12
114	1.14E-07	20.31	3.63	2.49E-06	1.82E+12
115	1.15E-07	20.31	3.66	2.50E-06	1.81E+12
116	1.16E-07	20.31	3.66	2.52E-06	1.78E+12
117	1.17E-07	20.31	3.66	2.54E-06	1.76E+12
118	1.18E-07	20.31	3.66	2.56E-06	1.74E+12
119	1.19E-07	20.31	3.69	2.57E-06	1.73E+12
120	1.20E-07	20.31	3.66	2.59E-06	1.69E+12
121	1.21E-07	20.31	3.69	2.61E-06	1.68E+12
122	1.22E-07	18.75	3.66	2.62E-06	1.52E+12
123	1.23E-07	20.31	3.69	2.64E-06	1.64E+12
124	1.24E-07	18.75	3.66	2.66E-06	1.48E+12
125	1.25E-07	20.31	3.69	2.68E-06	1.60E+12
126	1.26E-07	18.75	3.66	2.69E-06	1.44E+12
127	1.27E-07	18.75	3.69	2.71E-06	1.44E+12
128	1.28E-07	18.75	3.66	2.73E-06	1.41E+12
129	1.29E-07	18.75	3.75	2.74E-06	1.43E+12
130	1.30E-07	18.75	3.66	2.76E-06	1.38E+12
131	1.31E-07	18.75	3.75	2.78E-06	1.39E+12
132	1.32E-07	18.75	3.72	2.79E-06	1.37E+12
133	1.33E-07	18.75	3.78	2.81E-06	1.37E+12
134	1.34E-07	17.19	3.72	2.83E-06	1.22E+12
135	1.35E-07	17.19	3.78	2.84E-06	1.23E+12
136	1.36E-07	17.19	3.75	2.86E-06	1.20E+12
137	1.37E-07	17.19	3.78	2.88E-06	1.20E+12
138	1.38E-07	15.63	3.72	2.89E-06	1.06E+12
139	1.39E-07	17.19	3.78	2.91E-06	1.17E+12
140	1.40E-07	17.19	3.78	2.93E-06	1.16E+12
141	1.41E-07	17.19	3.78	2.94E-06	1.15E+12
142	1.42E-07	17.19	3.78	2.96E-06	1.13E+12
143	1.43E-07	17.19	3.78	2.98E-06	1.12E+12
144	1.44E-07	17.19	3.78	2.99E-06	1.11E+12
145	1.45E-07	17.19	3.78	3.01E-06	1.10E+12
146	1.46E-07	17.19	3.75	3.02E-06	1.08E+12
147	1.47E-07	17.19	3.78	3.04E-06	1.07E+12
148	1.48E-07	15.63	3.72	3.06E-06	9.50E+11
149	1.49E-07	17.19	3.78	3.07E-06	1.05E+12
150	1.50E-07	17.19	3.78	3.09E-06	1.04E+12
151	1.51E-07	17.19	3.78	3.11E-06	1.03E+12
152	1.52E-07	15.63	3.78	3.12E-06	9.26E+11
153	1.53E-07	15.63	3.78	3.14E-06	9.16E+11
154	1.54E-07	14.06	3.78	3.15E-06	8.16E+11
155	1.55E-07	14.06	3.78	3.17E-06	8.08E+11
156	1.56E-07	14.06	3.75	3.19E-06	7.93E+11
157	1.57E-07	14.06	3.78	3.20E-06	7.92E+11
158	1.58E-07	14.06	3.72	3.22E-06	7.71E+11
159	1.59E-07	14.06	3.78	3.24E-06	7.76E+11
160	1.60E-07	14.06	3.75	3.25E-06	7.62E+11
161	1.61E-07	14.06	3.75	3.27E-06	7.55E+11
162	1.62E-07	14.06	3.72	3.28E-06	7.41E+11
163	1.63E-07	14.06	3.75	3.30E-06	7.40E+11
164	1.64E-07	14.06	3.72	3.32E-06	7.27E+11
165	1.65E-07	14.06	3.75	3.33E-06	7.26E+11
166	1.66E-07	14.06	3.69	3.35E-06	7.07E+11
167	1.67E-07	14.06	3.69	3.36E-06	7.00E+11
168	1.68E-07	14.06	3.66	3.38E-06	6.88E+11
169	1.69E-07	14.06	3.69	3.40E-06	6.87E+11
170	1.70E-07	14.06	3.66	3.41E-06	6.75E+11
171	1.71E-07	14.06	3.69	3.43E-06	6.75E+11
172	1.72E-07	14.06	3.66	3.44E-06	6.63E+11
173	1.73E-07	14.06	3.66	3.46E-06	6.57E+11
174	1.74E-07	14.06	3.66	3.47E-06	6.51E+11
175	1.75E-07	14.06	3.66	3.49E-06	6.45E+11
176	1.76E-07	14.06	3.63	3.51E-06	6.34E+11
177	1.77E-07	14.06	3.63	3.52E-06	6.28E+11
178	1.78E-07	12.50	3.59	3.54E-06	5.49E+11
179	1.79E-07	14.06	3.63	3.55E-06	6.17E+11
180	1.80E-07	14.06	3.59	3.57E-06	6.06E+11
181	1.81E-07	14.06	3.63	3.58E-06	6.06E+11
182	1.82E-07	12.50	3.59	3.60E-06	5.30E+11
183	1.83E-07	14.06	3.59	3.62E-06	5.91E+11
184	1.84E-07	12.50	3.53	3.63E-06	5.11E+11
185	1.85E-07	12.50	3.53	3.65E-06	5.07E+11
186	1.86E-07	10.94	3.53	3.66E-06	4.40E+11
187	1.87E-07	14.06	3.53	3.68E-06	5.61E+11
188	1.88E-07	12.50	3.50	3.69E-06	4.90E+11
189	1.89E-07	14.06	3.50	3.71E-06	5.47E+11
190	1.90E-07	10.94	3.47	3.72E-06	4.18E+11
191	1.91E-07	10.94	3.50	3.74E-06	4.18E+11
192	1.92E-07	10.94	3.44	3.76E-06	4.07E+11
193	1.93E-07	10.94	3.44	3.77E-06	4.04E+11
194	1.94E-07	10.94	3.41	3.79E-06	3.97E+11
195	1.95E-07	14.06	3.41	3.80E-06	5.06E+11
196	1.96E-07	10.94	3.38	3.82E-06	3.87E+11
197	1.97E-07	10.94	3.38	3.83E-06	3.84E+11
198	1.98E-07	9.38	3.34	3.85E-06	3.23E+11
199	1.99E-07	10.94	3.38	3.86E-06	3.78E+11
200	2.00E-07	9.38	3.31	3.88E-06	3.15E+11
201	2.01E-07	10.94	3.31	3.89E-06	3.65E+11
202	2.02E-07	9.38	3.28	3.91E-06	3.08E+11
203	2.03E-07	10.94	3.28	3.92E-06	3.56E+11

Table D.4 Empirical discharge parameters for 393 ns pulse on time (continued)

Time step	Discharge time (ns)	Voltage (V)	Current (A)	Source radius (m)	Heat flux (W/m^2)
204	2.04E-07	9.38	3.25	3.94E-06	3.00E+11
205	2.05E-07	14.06	3.25	3.95E-06	4.46E+11
206	2.06E-07	9.38	3.25	3.97E-06	2.95E+11
207	2.07E-07	10.94	3.25	3.99E-06	3.42E+11
208	2.08E-07	9.38	3.19	4.00E-06	2.85E+11
209	2.09E-07	10.94	3.19	4.02E-06	3.30E+11
210	2.10E-07	9.38	3.16	4.03E-06	2.78E+11
211	2.11E-07	10.94	3.16	4.05E-06	3.22E+11
212	2.12E-07	9.38	3.13	4.06E-06	2.71E+11
213	2.13E-07	10.94	3.13	4.08E-06	3.14E+11
214	2.14E-07	7.81	3.13	4.09E-06	2.23E+11
215	2.15E-07	7.81	3.13	4.11E-06	2.21E+11
216	2.16E-07	7.81	3.13	4.12E-06	2.20E+11
217	2.17E-07	7.81	3.13	4.14E-06	2.18E+11
218	2.18E-07	7.81	3.03	4.15E-06	2.10E+11
219	2.19E-07	9.38	3.03	4.17E-06	2.50E+11
220	2.20E-07	7.81	3.00	4.18E-06	2.05E+11
221	2.21E-07	9.38	3.00	4.20E-06	2.44E+11
222	2.22E-07	9.38	3.00	4.21E-06	2.42E+11
223	2.23E-07	9.38	3.00	4.23E-06	2.41E+11
224	2.24E-07	7.81	2.94	4.24E-06	1.95E+11
225	2.25E-07	7.81	2.94	4.26E-06	1.94E+11
226	2.26E-07	7.81	2.91	4.27E-06	1.90E+11
227	2.27E-07	7.81	2.91	4.29E-06	1.89E+11
228	2.28E-07	7.81	2.84	4.30E-06	1.83E+11
229	2.29E-07	7.81	2.84	4.32E-06	1.82E+11
230	2.30E-07	7.81	2.81	4.33E-06	1.79E+11
231	2.31E-07	7.81	2.81	4.35E-06	1.78E+11
232	2.32E-07	7.81	2.78	4.36E-06	1.75E+11
233	2.33E-07	9.38	2.78	4.38E-06	2.08E+11
234	2.34E-07	7.81	2.75	4.39E-06	1.70E+11
235	2.35E-07	10.94	2.75	4.41E-06	2.37E+11
236	2.36E-07	9.38	2.72	4.42E-06	1.99E+11
237	2.37E-07	10.94	2.72	4.44E-06	2.31E+11
238	2.38E-07	9.38	2.69	4.45E-06	1.94E+11
239	2.39E-07	9.38	2.72	4.46E-06	1.95E+11
240	2.40E-07	9.38	2.63	4.48E-06	1.87E+11
241	2.41E-07	10.94	2.63	4.49E-06	2.17E+11
242	2.42E-07	9.38	2.63	4.51E-06	1.85E+11
243	2.43E-07	9.38	2.63	4.52E-06	1.84E+11
244	2.44E-07	7.81	2.59	4.54E-06	1.50E+11
245	2.45E-07	9.38	2.59	4.55E-06	1.79E+11
246	2.46E-07	7.81	2.53	4.57E-06	1.45E+11
247	2.47E-07	7.81	2.53	4.58E-06	1.44E+11
248	2.48E-07	7.81	2.50	4.60E-06	1.41E+11
249	2.49E-07	7.81	2.50	4.61E-06	1.40E+11
250	2.50E-07	7.81	2.47	4.63E-06	1.38E+11
251	2.51E-07	7.81	2.47	4.64E-06	1.37E+11
252	2.52E-07	7.81	2.44	4.66E-06	1.34E+11
253	2.53E-07	7.81	2.44	4.67E-06	1.33E+11
254	2.54E-07	7.81	2.41	4.68E-06	1.31E+11
255	2.55E-07	7.81	2.41	4.70E-06	1.30E+11
256	2.56E-07	7.81	2.38	4.71E-06	1.28E+11
257	2.57E-07	7.81	2.38	4.73E-06	1.27E+11
258	2.58E-07	7.81	2.31	4.74E-06	1.23E+11
259	2.59E-07	7.81	2.34	4.76E-06	1.24E+11
260	2.60E-07	7.81	2.28	4.77E-06	1.20E+11
261	2.61E-07	7.81	2.28	4.79E-06	1.19E+11
262	2.62E-07	7.81	2.22	4.80E-06	1.15E+11
263	2.63E-07	7.81	2.22	4.82E-06	1.14E+11
264	2.64E-07	7.81	2.22	4.83E-06	1.14E+11
265	2.65E-07	7.81	2.22	4.84E-06	1.13E+11
266	2.66E-07	7.81	2.16	4.86E-06	1.09E+11
267	2.67E-07	7.81	2.16	4.87E-06	1.08E+11
268	2.68E-07	7.81	2.13	4.89E-06	1.06E+11
269	2.69E-07	9.38	2.16	4.90E-06	1.29E+11
270	2.70E-07	7.81	2.13	4.92E-06	1.05E+11
271	2.71E-07	9.38	2.13	4.93E-06	1.25E+11
272	2.72E-07	9.38	2.09	4.94E-06	1.23E+11
273	2.73E-07	9.38	2.09	4.96E-06	1.22E+11
274	2.74E-07	7.81	2.03	4.97E-06	9.80E+10
275	2.75E-07	7.81	2.03	4.99E-06	9.75E+10
276	2.76E-07	7.81	2.00	5.00E-06	9.54E+10
277	2.77E-07	7.81	2.00	5.02E-06	9.49E+10
278	2.78E-07	4.69	1.97	5.03E-06	5.57E+10
279	2.79E-07	7.81	1.97	5.05E-06	9.23E+10
280	2.80E-07	7.81	1.97	5.06E-06	9.18E+10
281	2.81E-07	7.81	1.97	5.07E-06	9.13E+10
282	2.82E-07	7.81	1.91	5.09E-06	8.79E+10
283	2.83E-07	7.81	1.91	5.10E-06	8.74E+10
284	2.84E-07	7.81	1.88	5.12E-06	8.55E+10
285	2.85E-07	7.81	1.88	5.13E-06	8.50E+10
286	2.86E-07	7.81	1.81	5.14E-06	8.17E+10
287	2.87E-07	7.81	1.81	5.16E-06	8.13E+10
288	2.88E-07	4.69	1.78	5.17E-06	4.77E+10
289	2.89E-07	7.81	1.81	5.19E-06	8.04E+10
290	2.90E-07	7.81	1.78	5.20E-06	7.86E+10
291	2.91E-07	7.81	1.78	5.22E-06	7.82E+10
292	2.92E-07	7.81	1.75	5.23E-06	7.64E+10
293	2.93E-07	7.81	1.75	5.24E-06	7.60E+10
294	2.94E-07	4.69	1.69	5.26E-06	4.37E+10
295	2.95E-07	7.81	1.69	5.27E-06	7.25E+10
296	2.96E-07	4.69	1.66	5.29E-06	4.24E+10
297	2.97E-07	7.81	1.66	5.30E-06	7.04E+10
298	2.98E-07	4.69	1.63	5.31E-06	4.12E+10
299	2.99E-07	7.81	1.63	5.33E-06	6.83E+10
300	3.00E-07	4.69	1.59	5.34E-06	4.00E+10
301	3.01E-07	7.81	1.59	5.36E-06	6.63E+10
302	3.02E-07	4.69	1.53	5.37E-06	3.80E+10
303	3.03E-07	7.81	1.56	5.39E-06	6.43E+10
304	3.04E-07	7.81	1.50	5.40E-06	6.14E+10
305	3.05E-07	7.81	1.50	5.41E-06	6.11E+10
306	3.06E-07	7.81	1.47	5.43E-06	5.95E+10
307	3.07E-07	7.81	1.47	5.44E-06	5.92E+10
308	3.08E-07	7.81	1.44	5.46E-06	5.77E+10
309	3.09E-07	7.81	1.44	5.47E-06	5.74E+10
310	3.10E-07	7.81	1.41	5.48E-06	5.58E+10
311	3.11E-07	7.81	1.41	5.50E-06	5.55E+10
312	3.12E-07	7.81	1.38	5.51E-06	5.40E+10
313	3.13E-07	7.81	1.38	5.52E-06	5.38E+10
314	3.14E-07	7.81	1.31	5.54E-06	5.11E+10
315	3.15E-07	9.38	1.31	5.55E-06	6.10E+10
316	3.16E-07	7.81	1.31	5.57E-06	5.06E+10
317	3.17E-07	10.94	1.31	5.58E-06	7.04E+10
318	3.18E-07	9.38	1.25	5.59E-06	5.72E+10
319	3.19E-07	10.94	1.25	5.61E-06	6.64E+10
320	3.20E-07	10.94	1.25	5.62E-06	6.61E+10
321	3.21E-07	10.94	1.25	5.64E-06	6.58E+10
322	3.22E-07	10.94	1.19	5.65E-06	6.22E+10
323	3.23E-07	10.94	1.19	5.66E-06	6.19E+10
324	3.24E-07	10.94	1.16	5.68E-06	5.99E+10
325	3.25E-07	10.94	1.16	5.69E-06	5.96E+10
326	3.26E-07	9.38	1.09	5.71E-06	4.81E+10
327	3.27E-07	10.94	1.09	5.72E-06	5.59E+10
328	3.28E-07	7.81	1.09	5.73E-06	3.97E+10
329	3.29E-07	7.81	1.09	5.75E-06	3.95E+10
330	3.30E-07	4.69	1.06	5.76E-06	2.29E+10
331	3.31E-07	7.81	1.06	5.77E-06	3.80E+10
332	3.32E-07	4.69	1.00	5.79E-06	2.14E+10
333	3.33E-07	10.94	1.00	5.80E-06	4.96E+10
334	3.34E-07	7.81	0.97	5.82E-06	3.42E+10
335	3.35E-07	10.94	1.00	5.83E-06	4.92E+10
336	3.36E-07	9.38	0.94	5.84E-06	3.93E+10
337	3.37E-07	9.38	0.94	5.86E-06	3.91E+10
338	3.38E-07	9.38	0.91	5.87E-06	3.77E+10
339	3.39E-07	9.38	0.91	5.88E-06	3.75E+10
340	3.40E-07	9.38	0.84	5.90E-06	3.47E+10
341	3.41E-07	9.38	0.84	5.91E-06	3.46E+10
342	3.42E-07	7.81	0.81	5.93E-06	2.76E+10
343	3.43E-07	10.94	0.81	5.94E-06	3.85E+10
344	3.44E-07	9.38	0.81	5.95E-06	3.28E+10
345	3.45E-07	10.94	0.81	5.97E-06	3.81E+10
346	3.46E-07	9.38	0.78	5.98E-06	3.13E+10
347	3.47E-07	10.94	0.78	5.99E-06	3.63E+10
348	3.48E-07	9.38	0.72	6.01E-06	2.85E+10
349	3.49E-07	14.06	0.72	6.02E-06	4.26E+10
350	3.50E-07	9.38	0.69	6.03E-06	2.70E+10
351	3.51E-07	14.06	0.69	6.05E-06	4.04E+10
352	3.52E-07	12.50	0.66	6.06E-06	3.41E+10
353	3.53E-07	14.06	0.66	6.08E-06	3.82E+10
354	3.54E-07	10.94	0.59	6.09E-06	2.68E+10
355	3.55E-07	12.50	0.59	6.10E-06	3.04E+10
356	3.56E-07	10.94	0.56	6.12E-06	2.51E+10
357	3.57E-07	10.94	0.56	6.13E-06	2.50E+10
358	3.58E-07	9.38	0.56	6.14E-06	2.13E+10
359	3.59E-07	9.38	0.56	6.16E-06	2.13E+10
360	3.60E-07	7.81	0.53	6.17E-06	1.67E+10
361	3.61E-07	10.94	0.53	6.18E-06	2.32E+10
362	3.62E-07	7.81	0.50	6.20E-06	1.55E+10
363	3.63E-07	10.94	0.50	6.21E-06	2.17E+10
364	3.64E-07	10.94	0.44	6.22E-06	1.89E+10
365	3.65E-07	10.94	0.44	6.24E-06	1.88E+10
366	3.66E-07	9.38	0.41	6.25E-06	1.49E+10
367	3.67E-07	14.06	0.41	6.27E-06	2.22E+10
368	3.68E-07	9.38	0.38	6.28E-06	1.36E+10
369	3.69E-07	14.06	0.38	6.29E-06	2.04E+10
370	3.70E-07	12.50	0.34	6.31E-06	1.65E+10
371	3.71E-07	12.50	0.34	6.32E-06	1.64E+10
372	3.72E-07	10.94	0.28	6.33E-06	1.17E+10
373	3.73E-07	10.94	0.28	6.35E-06	1.17E+10
374	3.74E-07	10.94	0.28	6.36E-06	1.16E+10
375	3.75E-07	10.94	0.28	6.37E-06	1.16E+10
376	3.76E-07	10.94	0.25	6.39E-06	1.02E+10
377	3.77E-07	10.94	0.25	6.40E-06	1.02E+10
378	3.78E-07	9.38	0.22	6.41E-06	7.62E+09
379	3.79E-07	10.94	0.22	6.43E-06	8.85E+09
380	3.80E-07	9.38	0.16	6.44E-06	5.40E+09
381	3.81E-07	10.94	0.16	6.45E-06	6.27E+09
382	3.82E-07	10.94	0.16	6.47E-06	6.24E+09
383	3.83E-07	10.94	0.16	6.48E-06	6.22E+09
384	3.84E-07	10.94	0.13	6.49E-06	4.95E+09
385	3.85E-07	14.06	0.13	6.51E-06	6.34E+09
386	3.86E-07	10.94	0.06	6.52E-06	2.46E+09
387	3.87E-07	14.06	0.06	6.53E-06	3.15E+09
388	3.88E-07	10.94	0.06	6.55E-06	2.44E+09
389	3.89E-07	12.50	0.06	6.56E-06	2.77E+09
390	3.90E-07	10.94	0.03	6.57E-06	1.21E+09
391	3.91E-07	10.94	0.03	6.59E-06	1.20E+09
392	3.92E-07	10.94	0.03	6.60E-06	1.20E+09
393	3.93E-07	10.94	0.03	6.61E-06	1.19E+09

Table D.5 R_{max} measurements for model validation

Energy (uJ)	Hole	Rmax measured at location j (um)										Overall	Overall Rmax (um)		
		1	2	3	4	5	6	7	8	9	10		Minimum	Maximum	Average
1.0	1	0.645	0.515	0.632	0.883	0.651	0.595	0.473	0.957	0.468	0.399	0.622	0.609	0.779	0.693
	2	0.895	0.924	0.616	0.589	0.483	0.606	0.499	0.479	0.402	0.596	0.609			
	3	1.420	0.703	0.679	0.702	0.545	0.690	1.097	0.578	0.677	0.510	0.760			
	4	1.072	1.150	0.798	0.783	0.917	0.579	0.446	0.759	0.666	0.622	0.779			
3.2	1	1.547	1.625	1.627	1.426	1.478	1.742	1.380	1.265	1.542	1.478	1.511	1.026	1.511	1.252
	2	1.094	1.162	1.163	0.996	0.934	1.155	0.898	0.784	1.082	0.996	1.026			
	3	1.129	0.925	0.775	0.967	1.221	1.184	1.206	1.717	1.758	1.698	1.258			
	4	1.221	1.163	0.784	0.934	0.996	1.265	1.155	1.625	1.547	1.426	1.212			
5.5	1	1.578	1.800	2.270	1.240	1.566	1.182	1.415	1.756	1.691	1.504	1.600	1.251	1.785	1.535
	2	2.407	1.583	1.481	1.306	1.699	1.933	1.425	2.591	1.666	1.756	1.785			
	3	0.950	1.502	1.258	1.980	1.193	1.664	1.260	1.376	2.033	1.805	1.502			
	4	1.248	1.026	1.022	1.422	1.136	1.569	1.399	1.017	1.410	1.265	1.251			
10.4	1	2.255	2.368	2.540	1.644	2.541	1.313	1.721	2.322	1.890	1.131	1.973	1.800	2.444	2.054
	2	2.364	1.791	2.310	1.580	1.805	1.030	1.763	2.769	1.306	1.280	1.800			
	3	2.027	4.370	2.980	2.305	2.813	1.601	1.549	2.181	2.582	2.027	2.444			
	4	2.820	2.093	3.176	1.176	1.520	1.686	2.479	1.430	2.117	1.491	1.999			

Table D.6 Simulated R_{max} values for lower and upper bounds

Measured energy (uJ)	Simulated Rmax (um)	
	Lower bound	Upper bound
1.6	0.75	1.10
3.4	0.97	1.57
14.6	1.80	3.41

Table D.7 Recast layer thickness values for model development

	Recast layer thickness (um)							
On time (ns)	1	2	3	4	5	Minimum	Maximum	Average
166	1.203	0.995	1.061	1.080	1.176	0.995	1.203	1.103
362	1.462	1.344	1.310	1.277	1.454	1.277	1.462	1.369
606	1.665	1.823	1.704	1.727	1.811	1.665	1.823	1.746

Table D.8 Simulated recast layer thickness values for lower and upper bounds

	Simulated thickness (um)	
On time (ns)	Lower bound	Upper bound
166	1.00	1.22
362	1.27	1.51
606	1.65	1.82

Table D.9 Recast layer thickness values for model validation

	Recast layer thickness (um)							
On time (ns)	1	2	3	4	5	Minimum	Maximum	Average
244	1.237	1.173	1.189	1.092	1.213	1.092	1.237	1.181
458	1.591	1.502	1.613	1.595	1.499	1.499	1.613	1.560